====== MAGNETIC CONFINEMENT ======
====== SYSTEMS ======

Quasi-Stellarator Magnetic Substructures in a Magnetized Toroidal Plasma with Electric Current

I. S. Danilkin

Prokhorov Institute of General Physics, Russian Academy of Sciences, ul. Vavilova 38, Moscow, 119991 Russia
Received April 22, 2004; in final form, May 31, 2004

Abstract—The X-ray tomography of plasmas in large tokamaks made it possible to observe large single-mode magnetic substructures similar to the global structures of the stellarator magnetic configurations. This similarity can serve as the basis for developing a simplified, helically symmetric model that would provide a qualitative description of such substructures and a determination of some thresholds for their possible bifurcation. © *2005 Pleiades Publishing, Inc.*

1. INTRODUCTION

In recent years, it has become frequent practice to monitor tokamak plasmas by means of X-ray tomography, which makes it possible to visualize the structure of the confining magnetic field [1–3]. In some cases, the tomographically observed resonant substructures (magnetic islands) turn out to be surprisingly similar to the global structure of the magnetic field produced by helical windings in certain types of stellarators (Fig. 1) [4]. By the global structure here is meant the entire structure of the magnetic field, namely, the internal magnetic field structure in which the plasma is confined and the magnetic field structure outside the radius of the helical windings.

In most cases, the systems of magnetic islands revealed tomographically in tokamaks have little resemblance to the "classical" structures with alternating X and O points occurring at different radial rays on the same resonant magnetic surface, such as the magnetic structure obtained analytically by the method of expansion in the vicinity of a given magnetic surface [5]. In a recent paper by Chudnovskiy [6], however, it was pointed out that such classical island structures usually arise from the plasma current perturbations whose amplitude is nearly constant in a radial direction across the island. Earlier, in my paper [7], devoted to analyzing the effects of different magnetic structure imperfections that result from defects in the assembly of the stellarator magnetic system, it was also mentioned that conventional magnetic islands arise only under the action of external perturbations whose amplitudes vary slightly across the internal magnetic field configuration. However, strongly localized perturbations (such as those produced by the filamentary electric currents flowing within magnetic islands) can change the structure of some islands so as to stretch
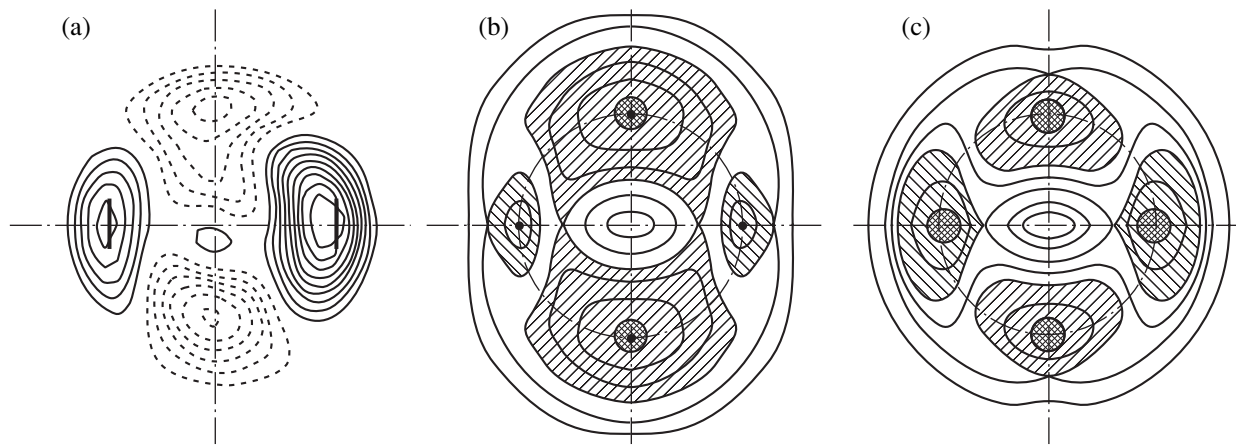

Fig. 1. Tomographic image of a JET plasma (a) and general characteristic patterns of the global magnetic structures in stellarators: (b) a torsatron with long-pitch ($\alpha r \ll 1$) helical windings and (c) a classical stellarator with oppositely directed currents in each pair of helical windings.
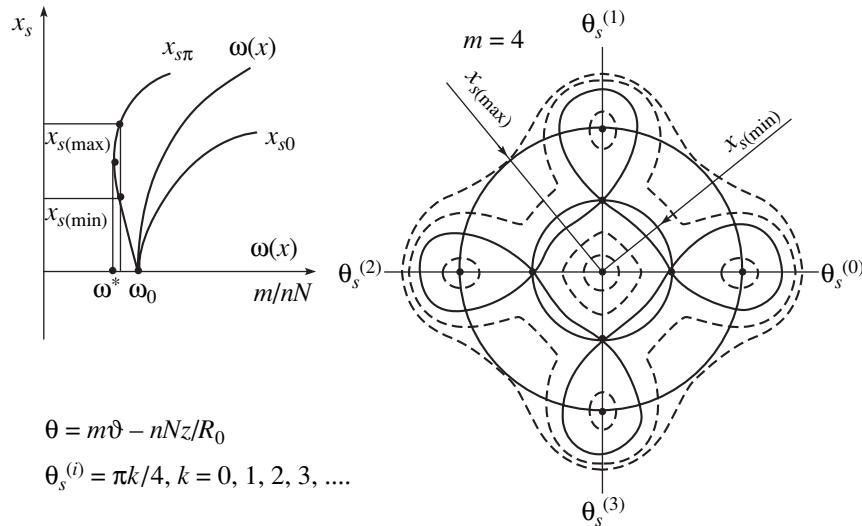
$$\theta = m\vartheta - nNz/R_0$$

$$\theta_s^{(i)} = \pi k/4, \, k = 0, 1, 2, 3, \dots.$$

Fig. 2. Example of the rearrangement of a resonant magnetic substructure in a stellarator in which the amplitude of a localized helical perturbation decreases toward the center more rapidly than $\omega(x) - \omega_0$, where $\omega(x) = t(x)/2\pi N$ (with N being the number of periods of the helical winding along the major circumference of the torus), $x_s = l\alpha r_s$ (with l being the helical winding multipoparity), and $\alpha = 2\pi/L$ (with L being the pitch of the helical windings). The case is shown in which the poloidal (m) and toroidal (n) harmonic numbers of the perturbation satisfy the condition $\omega^* < m/nN < \omega_0$. Singular points of both types (the X and O points) lie in pairs on the same radial rays and the magnetic islands are stretched in the radial direction [7].

them in the radial direction and to displace the corresponding pairs of the singular (X and O) points to the same radial rays (Fig. 2). In particular, in tokamak-like toroidal confinement systems, these processes can lead to an effect similar to the formation of the so-called positive magnetic islands [6, 8].

The similarity of the single-mode magnetic structures observed by X-ray tomography of tokamak plasmas to the global structures of some stellarator magnetic configurations suggests that they can be calculated in terms of a relatively simple, helically symmetric model in a way analogous to the calculations of a stellarator magnetic configuration to the lowest order in the toroidicity. As will be clear later, this approach makes it possible not only to verify that such single-mode magnetic configurations have a topological structure fairly close to that of the tomographically visualized configurations but also to obtain some estimates of the parameter values corresponding to their possible bifurcation. Looking at the structures shown in Fig. 1, a careful reader, however, would have already noticed that the global structure of the stellarator magnetic configuration is in essence an island structure produced by the helical winding currents flowing within the magnetic islands. At the same time, it should be emphasized that the present study deals only with the formal similarity that exists between the single-mode structures observed in tokamaks and the global structures of the magnetic configurations in several types of stellarators, specifically, *torsatrons with long-pitch helical windings*, and the questions about the equilibrium of actual tokamak plasmas are completely set aside. It may well be, however, that the surprising similarity between the actually observed structures and the structures of the quasi-stellarator magnetic configurations points to a similarity between the distributions of the currents that produce these two types of magnetic structures.

2. BASIC TOPOLOGICAL MODEL

In order to construct the calculation model, we consider a helically symmetric system in which the role of the "topological" torus is played by a straight cylinder of length $2\pi R_0$ with identified ends (where R_0 is the major radius of the "torus"). We introduce a cylindrical coordinate system (r, ϑ, z) and assume that, inside the cylinder, there is a strong "toroidal" magnetic field $\mathbf{B}_0 = B_0 \mathbf{e}_z$, where $\mathbf{e}_z$ is a unit vector pointing in the z direction. Let an electric current I_0 with the density $\mathbf{j}_z = j_z \mathbf{e}_z$, which is assumed to be uniform along the angular coordinate ϑ, flow along the z axis within a cylinder of radius r_0. This current creates a poloidal magnetic field $\mathbf{B}_\vartheta^0 = B_\vartheta^0 \mathbf{e}_\vartheta$ such that

$$B_\vartheta^0 = \frac{2I(r)}{cr} = \frac{2}{cr}\int_0^r j_z(r)r\,dr \oint_\vartheta d\vartheta \quad \text{for} \quad r \leq r_0,$$

$$B_\vartheta^0 = \frac{2I_0}{cr} \quad \text{for} \quad r \geq r_0. \tag{1}$$

Together with the toroidal magnetic field $\mathbf{B}_0$, the poloidal magnetic field produces a quasi-tokamak magnetic configuration corresponding to the limit of large aspect ratios. Obviously, this configuration possesses a family

of magnetic surfaces in the form of nested cylinders (tori) and exhibits translational symmetry in the ϑ and z directions. We consider a resonant magnetic surface of radius $r = r_{ss}$ at which the safety factor $q(r)$ takes on a resonant value q_s,

$$q(r) = \frac{r_{ss}B_0}{R_0 B_\vartheta^0} = q(r_{ss}) = q_s = m/n,$$

where m and n are integers. We introduce helical electric currents at this surface that flow along the magnetic field lines of the original magnetic configuration (produced by the magnetic field components B_0 and B_ϑ^0), i.e., along helices with a pitch of $L = R_0 q(r_{ss}) = R_0 q_s$. The resulting system does not exhibit translational symmetry of the original magnetic configuration but keeps helical symmetry along the helices $\theta = \vartheta - \alpha z$, where $\alpha = 2\pi/L = 2\pi/R_0 q_s$.

We thus have constructed the resulting quasi-tokamak system involving a quasi-stellarator substructure produced by long-pitch ($q > 1$) helical currents. Note by the way that the substructure of the helical currents introduced above, namely, those flowing along the magnetic field lines of the original quasi-tokamak magnetic configuration, is a force-free substructure. The explicit expressions for the magnetic field components $B_{hr}(r, \theta)$, $B_{h\vartheta}(r, \theta)$, and $B_{hz}(r, \theta)$ produced by these helical currents can be specified in terms of their Fourier expansions in helical harmonics. However, the formulas describing the structure of the magnetic surfaces in a system possessing the above helical symmetry can also be derived in the most general case without obtaining explicit expressions for the components of the helical magnetic field. Since such general formulas will be used in further analysis, they will be derived in the next section in order to make the description more complete.

3. GENERAL STRUCTURE OF MAGNETIC SURFACES IN A HELICALLY SYMMETRIC SYSTEM WITH A LONGITUDINAL CURRENT

We assume that the magnetic field has the components

$$B_r = B_{hr}(r, \theta), \quad B_\vartheta = B_\vartheta^0(r) + B_{h\vartheta}(r, \theta),$$
$$B_z = B_0(r) + B_{hz}(r, \theta),$$
(2)

where $\theta = \vartheta - \alpha z$ and, in accordance with expressions (1), the field component B_ϑ^0 is produced by the toroidal current. The magnetic field lines are described by the set of equations

$$\frac{dr}{B_r} = \frac{r\,d\vartheta}{B_\vartheta} = \frac{dz}{B_z},$$
(3)

where the magnetic field components B_r, B_ϑ, and B_z are given by expressions (2). Switching to the helical coordinate $\theta = \vartheta - \alpha z$ in Eqs. (3) yields

$$\frac{dr}{d\theta} = \frac{B_r}{B_z\left(\dfrac{B_\vartheta}{rB_z} - \alpha\right)} = \frac{rB_r}{B_\vartheta - \alpha rB_z}.$$
(4)

Taking into account the equation $\nabla \cdot \mathbf{B} = 0$, we obtain from Eqs. (4) the following equation in differentials:

$$d\psi = (B_\vartheta - \alpha rB_0)dr - rB_r d\theta.$$
(5)

The solution $\psi(r, \theta)$ to this equation describes a family of magnetic surfaces $\psi(r, \theta) = \text{const}$:

$$\psi(r, \theta) = \int_{(r)} [B_\vartheta^0(r) - \alpha rB_0(r)]dr - \int_{(\theta)} rB_r d\theta.$$
(6)

By virtue of the properties assigned to the θ-independent magnetic field components B_θ^0 and B_0, formula (6) can be rewritten in the following final form:

$$\psi(r, \theta) = \frac{1}{2\pi}\int_{(r)} dr \oint_\vartheta (B_\vartheta - \alpha rB_z)d\vartheta - \int_{(\theta)} rB_r d\theta.$$
(6a)

For helically symmetric currents that create the magnetic field given by general expressions (2), formula (6a) is an exact integral of field line equations (3) and describes the magnetic surfaces of the field configuration produced by these currents. In other words, all the parameters in formula (6a) are free of any restrictions. Hence, formula (6a) describes all possible structures of magnetic surfaces in a helically symmetric system with a toroidal electric current.

We also present the set of equations for determining the positions of the singular points of the function $\psi(r, \theta)$ in the plane of the variables r and θ. These points will be denoted by the subscript s (a double subscript is used only for the subsystem of helical currents, the centers of whose cross sections are, by construction, center-type singular points). Using formulas (6) and (6a), we obtain

$$\frac{\partial\psi}{\partial\theta} = 0 = r_s B_{hr}(r_s, \theta_s),$$

$$\frac{\partial\psi}{\partial r} = 0 = \left\{ \frac{\partial}{\partial r}\left[\int_{(r)} (B_\vartheta^0 - \alpha rB_0)dr - \int_{(\theta)} rB_{hr}d\theta \right] \right\}_{r = r_s, \theta = \theta_s}.$$
(7)

With allowance for the condition $\nabla \cdot \mathbf{B} = 0$, the second of Eqs. (7) can be transformed to

$$\frac{\partial\psi}{\partial r} = (B_\vartheta - \alpha rB_z)_{r = r_s, \theta = \theta_s}.$$
(7a)

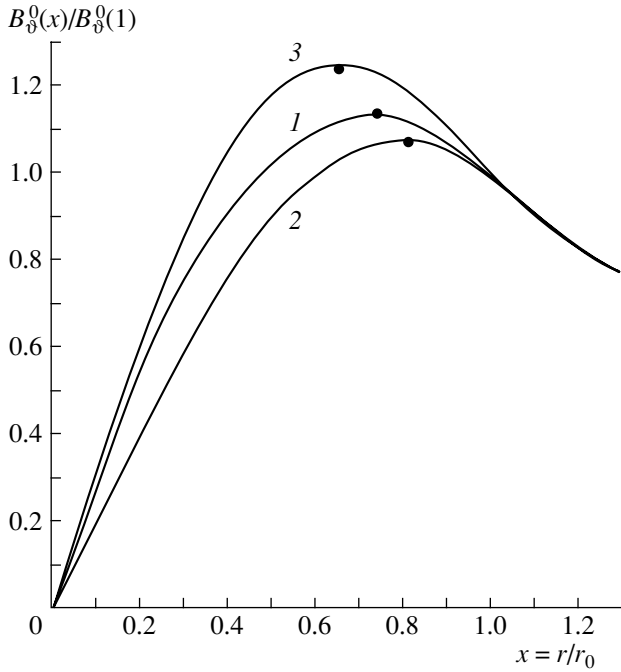**Fig. 3.** Poloidal magnetic field B_ϑ^0 vs. normalized radius $x = r/r_0$ for the three current density profiles j_z under consideration: (1) $j_z \sim (1-x)$, (2) $j_z \sim (1-x^2)$, and (3) $j_z \sim (1-x^2)^2$. The closed circles denote the maximal values of the poloidal magnetic field, $B_\vartheta^0 (1) = 2I_0/cr_0$.

The right-hand side of Eq. (7a) contains the components of the total magnetic field, which are given by expressions (2). An analysis of these equations shows that the first of them describes the ray $\theta = \theta_s$ on which the radial magnetic field component B_r vanishes. The second equation determines the radius of the helix $\theta_s = $ const having the same period as that of the original helical structure, $L = R_0 q_s$. Hence, the complete set of equations (7) and (7a) describes the helical lines in the vicinities of which two independent magnetic field components orthogonal to them vanish, i.e., the lines that, in the cross section $z = $ const, correspond to the center-type singular points (O points) or to hyperbolic singular points (X points). We now proceed to an analysis of different examples of magnetic structures. To do this, it is of course necessary to transform the general formulas obtained in this section into the corresponding particular expressions for the magnetic field components and the electric current density.

4. EXAMPLES OF QUASI-STELLARATOR SUBSTRUCTURES

We begin with specifying the explicit expressions for the magnetic field components. First, we consider the nonhelical components B_ϑ^0 and B_0, which deter-

mine the original quasi-tokamak structure. Without any serious loss of generality, we can assume that the toroidal magnetic field B_0 is independent of radius. As for the poloidal magnetic field B_ϑ^0 produced by the toroidal current, we will consider the following three radial profiles of j_z:

$$j_z = j_0^{(1)}(1 - r/r_0), \tag{8a}$$

$$j_z = j_0^{(2)}(1 - r^2/r_0^2), \tag{8b}$$

$$j_z = j_0^{(3)}(1 - r^2/r_0^2)^2, \tag{8c}$$

where, for the same total current

$$I_0 = \int_0^{r_0} dr \int_0^{2\pi} r j_z d\vartheta \tag{9}$$

the amplitudes $j_0^{(1, 2, 3)}$ are equal to

$$j_0^{(1)} = \frac{3I_0}{\pi r_0^2}, \quad j_0^{(2)} = \frac{2I_0}{\pi r_0^2}, \quad j_0^{(3)} = \frac{3I_0}{\pi r_0^2}. \tag{10}$$

As is seen, the first and third cases correspond to peaked current density profiles, while the second profile is relatively more uniform over the cross sections $z = $ const and decreases abruptly only near the boundary $r = r_0$.

The toroidal current I_0 with density profiles (8a), (8b), and (8c) creates the poloidal magnetic field B_ϑ^0:

$$B_\vartheta^0 = \begin{cases} \dfrac{6I_0 r}{cr_0^2}\left(1 - \dfrac{2}{3}\dfrac{r}{r_0}\right) & \text{for} \quad r \le r_0 \\[2mm] \dfrac{2I_0}{cr} & \text{for} \quad r \ge r_0, \end{cases} \tag{11a}$$

$$B_\vartheta^0 = \begin{cases} \dfrac{4I_0 r}{cr_0^2}\left(1 - \dfrac{1}{2}\dfrac{r^2}{r_0^2}\right) & \text{for} \quad r \le r_0 \\[2mm] \dfrac{2I_0}{cr} & \text{for} \quad r \ge r_0, \end{cases} \tag{11b}$$

$$B_\vartheta^0 = \begin{cases} \dfrac{6I_0 r}{cr_0^2}\left(1 - \dfrac{r^2}{r_0^2} + \dfrac{1}{3}\dfrac{r^4}{r_0^4}\right) & \text{for} \quad r \le r_0 \\[2mm] \dfrac{2I_0}{cr} & \text{for} \quad r \ge r_0, \end{cases} \tag{11c}$$

respectively.

The plots of the poloidal magnetic field B_ϑ^0 calculated as a function of the variable $x = r/r_0$ and normalized to its boundary value at $r = r_0$, which is the same

for a given longitudinal current I_0 in all three cases at hand, are displayed in Fig. 3. Formulas (11) and the plots shown in Fig. 3 obviously imply that, in these three cases, the magnetic field component B_ϑ^0 has a maximum inside the region $r \le r_0$. We denote by the subscript m the values of the coordinate r or x at which the component B_ϑ^0 is maximal. For the above current density profiles $j_z \sim (1-x)$, $j_z \sim (1-x^2)$, and $j_z \sim (1-x^2)^2$, these coordinate values are equal to

$$x_m = r_m/r_0 = 3/4, \tag{12a}$$

$$x_m = \sqrt{2/3} \approx 0.816, \tag{12b}$$

$$x_m = \sqrt{(9 - \sqrt{21})/10} \approx 0.665, \tag{12c}$$

respectively, and the corresponding maximal values of the component B_ϑ^0 (normalized to $B_\vartheta^0(r_0) = 2I_0/cr_0$) are equal to

$$\frac{B_{\vartheta m}^0}{B_\vartheta^0(r_0)} = (9/8), \tag{13a}$$

$$\frac{B_{\vartheta m}}{B_\vartheta^0(r_0)} \approx 1.089, \tag{13b}$$

$$\frac{B_{\vartheta m}^0}{B_\vartheta^0(r_0)} \approx 1.243, \tag{13c}$$

respectively. We thus obtained all the expressions required to calculate the mean (nonoscillating) part of the function $\psi(r, \theta)$, which will be denoted below by the superscript 0:

$$\psi^0(r) = \frac{1}{2\pi}\oint d\theta \int_{(r)} (B_\vartheta - \alpha r B_z)\,dr$$

$$= \int_0^r (B_\vartheta - \alpha r B_0)\,dr = r_0 q_0 B_\vartheta^0(r_0)\int_0^x \left(\frac{1}{q(x)} - \frac{1}{q_s}\right)x\,dx, \tag{14}$$

where the poloidal magnetic field component $B_\vartheta^0(r)$ is expressed in terms of the safety factor $q(r) = \dfrac{r B_0}{R_0 B_\vartheta^0(r)}$, whose value at the boundary $r = r_0$ is indicated by q_0. It is also convenient to introduce the form factor

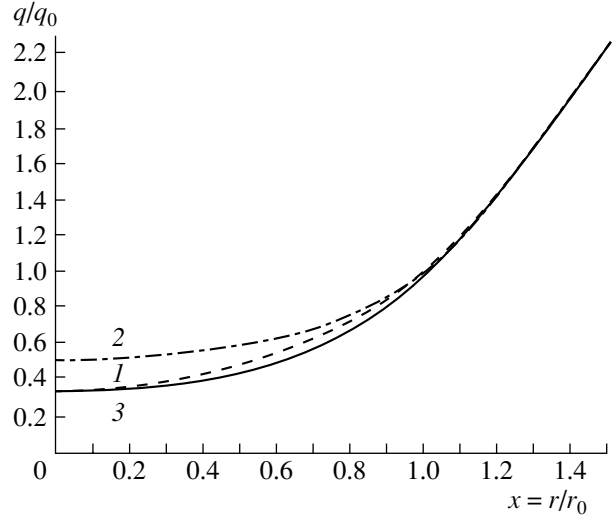$$f(x) = q_0/q(x), \tag{15}$$

Fig. 4. Ratio $q(x)/q_0$ vs. normalized radius $x = r/r_0$ for the same three j_z profiles.

which accounts for the dependence on the current density profiles j_z given by expressions (8). In this case, expression (14) reduces to

$$\psi^0 = r_0 q_0 B_\vartheta^0(r_0)\int_0^x \left(\frac{f(x)}{q_0} - \frac{1}{q_s}\right)x\,dx$$

$$= r_0 B_\vartheta^0(r_0)F(x), \tag{16}$$

$$F(x) = \int_0^x \left[f(x) - \frac{q_0}{q_s}\right]x\,dx,$$

where the form factor $f(x)$ for the chosen current density profiles (8a), (8b), and (8c) is determined by the relationships

$$f(x) = \begin{cases} 3(1 - 2x/3) & \text{for } x \le 1 \\ 1/x^2 & \text{for } x \ge 1, \end{cases} \tag{17a}$$

$$f(x) = \begin{cases} 2(1 - x^2/2) & \text{for } x \le 1 \\ 1/x^2 & \text{for } x \ge 1, \end{cases} \tag{17b}$$

$$f(x) = \begin{cases} 3(1 - x^2 + x^4/3) & \text{for } x \le 1 \\ 1/x^2 & \text{for } x \ge 1, \end{cases} \tag{17c}$$

respectively.

The profiles of the safety factor $q(x) = q_0/f(x)$ calculated from these relationships are depicted in Fig. 4.

For the current density profiles j_z given by expressions (8a), (8b), and (8c), substituting relationships (17)
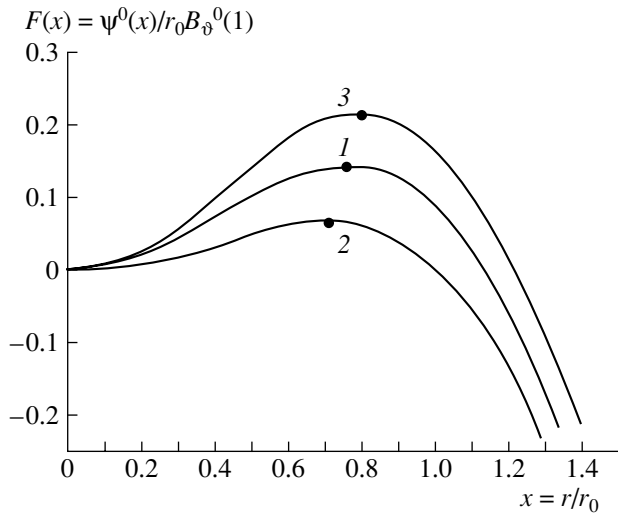
$F(x) = \psi^0(x)/r_0 B_\vartheta{}^0(1)$

Fig. 5. Magnetic flux function $\psi^0(x)$ averaged over the helical variable $\theta = \vartheta - \alpha z$ for $q_0/q_s = 3/2$ and for the same j_z profiles as in Figs. 3 and 4.

into expression (16) yields the following formulas for the function $F(x) = \psi^0/r_0 B_\vartheta^0 (r_0)$:

$$F(x) = \begin{cases} \dfrac{x^2}{2}\left[(3 - q_0/q_s) - \dfrac{4}{3}x\right] & \text{for} \quad x \le 1 \\[2ex] \dfrac{5}{6} + \ln x - \dfrac{x^2}{2}\dfrac{q_0}{q_s} & \text{for} \quad x \ge 1, \end{cases} \quad (18a)$$

$$F(x) = \begin{cases} \dfrac{x^2}{2}\left[(2 - q_0/q_s) - \dfrac{x^2}{2}\right] & \text{for} \quad x \le 1 \\[2ex] \dfrac{3}{4} + \ln x - \dfrac{x^2}{2}\dfrac{q_0}{q_s} & \text{for} \quad x \ge 1, \end{cases} \quad (18b)$$

$$F(x) = \begin{cases} \dfrac{x^2}{2}\left[(3 - q_0/q_s) - \dfrac{3}{2}x^2 + \dfrac{x^4}{3}\right] & \text{for} \quad x \le 1 \\[2ex] \dfrac{11}{12} + \ln x - \dfrac{x^2}{2}\dfrac{q_0}{q_s} & \text{for} \quad x \ge 1, \end{cases} \quad (18c)$$

respectively.

The plots of the functions $F(x)$ calculated for the particular case of $q_0 = 3$ and $q_s = 2$ are given in Fig. 5. Obviously, the function $F(x)$ introduced above is just the sought mean (nonoscillating) part of the magnetic flux function ψ^0 expressed in units of $r_0 B_\vartheta^0 (r_0)$. Below, it will also be clear that the amplitude of variations in the function $F(x)$ over the interval $0 < x < 1$ plays an important role in the topological stability of the resulting resonant magnetic substructures.

We now consider the helical magnetic field components $B_{hr}(r, \theta)$, $B_{h\vartheta}(r, \theta)$, and $B_{hz}(r, \theta)$, which determine the helical part of the magnetic flux function,

$$\psi_h(r, \theta) = \int_{(\theta)} r B_{hr} d\theta. \qquad (19)$$

The configuration of the helical currents at the resonant magnetic surface can naturally be represented in terms of Fourier expansions in helical harmonics, as is done in calculating a stellarator magnetic configuration produced by helical windings. Ignoring the toroidal effects (i.e., for the topological torus introduced above), the components of the helical magnetic field $\mathbf{B}_h = -\nabla\Phi_h$ can be specified in terms of the scalar potential [9, 10]

$$\Phi = \Phi^{(i)} = \sum_m \Phi_m^{(i)} = \alpha^{-1}\sum_m B_m^{(i)} I_m(m\alpha r)\sin m\theta,$$
$$\theta = \vartheta - \alpha z, \quad r \le r_{ss} \qquad (20)$$

for the region enclosed by the helical currents and

$$\Phi = \Phi^{(e)} = \sum_m \Phi_m^{(e)} = \alpha^{-1}\sum_m B_m^{(e)} K_m(m\alpha r)\cos m\theta,$$
$$r \ge r_{ss}, \qquad (21)$$

for the region outside them. Here, $\alpha = 2\pi/L = 2\pi/q_s R_0$, $I_m(m\alpha r)$ and $K_m(m\alpha r)$ are the modified Bessel functions of the first and second kinds, respectively; $m\alpha r$ is their argument; $B_m^{(i, e)} = \varepsilon_m^{(i, e)} B_0$; and m is the number of the harmonic in the helical coordinate θ. The amplitude coefficients $\varepsilon_m^{(i, e)}$ are given by the formulas [4]

$$\varepsilon_m^{(i)} = \frac{8 I_h \alpha}{B_0 c} f_h(m\gamma_h, \Delta r_h) K_m'(m\alpha r),$$
$$\varepsilon_m^{(e)} = \varepsilon_m^{(i)} \frac{I_m'(m\alpha r_{ss})}{K_m'(m\alpha r_{ss})}, \qquad (22)$$

where I_h is the electric current in the pole of the helical winding (in the case at hand, this pole plays the role of a magnetic island carrying the same current), the form factor f_h takes into account the shape of the pole conductor (i.e., its azimuthal width $2\gamma_h$ and radial thickness Δr_h), and the prime denotes the derivative with respect to the argument.

Experience gained in calculating stellarator helical magnetic configurations [7] shows that, for the lowest harmonic numbers m, the form factor f_h usually depends only slightly on the shape and dimensions of a helical conductor and is nearly equal to unity. As was shown in [11], the dependence on the azimuthal width $2\gamma_h$ of the pole conductor is described by a fairly weak function $(\sin m\gamma_h)/(m\gamma_h)$, which is close to unity for small m and γ_h values. As for the radial thickness Δr_h, it

leads to corrections in the form of a power series in even powers of the parameter $\Delta r_h/2r_h \ll 1$ (where r_h is the mean radius of the cross section of the conductor), the first term of the series being quadratic. This is why the form factor f_h can be approximated by the formula

$$f_h \approx \frac{\sin m\gamma_0}{m\gamma_0}\left\{1 + O\left[\left(\frac{\Delta r_h}{2r_h}\right)^2\right]\right\},$$

which implies that, in the first approximation, the radial thickness of a helical conductor can be ignored. If, in addition, the magnetic island carrying the helical current has a sufficiently small width along the azimuthal coordinate ϑ, then the form factor f_h is certainly close to unity and the amplitudes (22) of the helical harmonics (21) of the magnetic field are determined by the global parameters of the helical conductor (island): the current I_h flowing within it and the pitch ($R_0 q_{ss} = \alpha^{-1}$) and radius (r_{ss}) of the helix.

Note also that the higher current harmonics associated with the complex shape of the helical conductor generate magnetic fields whose amplitudes decrease rapidly in space according to the law $|K_m'(m\alpha r_{ss})|$. Consequently, these fields do not significantly change the positions of the singular points (in the plane of the variables r and θ) that govern the global magnetic structure. As a result, it turns out that this structure is almost completely determined by the lowest (fundamental) helical field harmonic, the amplitude of which depends weakly on the shape of the conductor, whereas the higher harmonics of the helical magnetic field lead merely to small corrections and thus do not substantially alter the magnetic configuration. A striking example of this situation is the magnetic configuration of the American Advanced Toroidal Facility (ATF) torsatron, equipped with complex helical windings having a radial size of $\Delta r_h \approx 25$ cm (the mean radius being $r_h = 45$ cm) and approximately the same width. It was found that the magnetic configuration of such a complex device can be modeled, with an accuracy of several percent, as being produced by a filamentary helical current flowing around a torus with an appropriately chosen minor radius (≈ 47 cm) [12]. This apparently stems from the fact that the exact model of a finite-size helical conductor and the model of a filamentary helical current gave almost the same amplitudes of the fundamental harmonic of the magnetic field.

Hence, in accordance with the aforesaid, we can assume for simplicity that, in formulas (22) for the coefficient $\varepsilon_m^{(i,\,e)}$ of the fundamental field harmonic, the form factor f_h is equal to unity. As for the higher field harmonics, they can be ignored in the first approximation, in which we are working here. Note, however, that they can be included in the analysis in order to correct the final results.

Using representations (20) and (21), we arrive at the following explicit expressions for the helical part ψ_h of the magnetic flux function:

$$\psi_h = \int_{(\theta)} r B_{hr} d\theta = \sum_m \varepsilon_m^{(i)} B_0 r I_m'(m\alpha r)\cos m\theta \quad (23a)$$

for the region enclosed by the helical currents ($r \leq r_{ss}$) and

$$\psi_h = \sum_m \varepsilon_m^{(e)} B_0 K_m'(m\alpha r)\cos m\theta \qquad (23b)$$

for the region outside them ($r \geq r_{ss}$). Combining the expressions for ψ^0 and ψ_h yields the resulting magnetic flux function:

$$\psi(r,\theta) = r_0 B_\vartheta^0(r_0)\left[F(x) + \sum_m b_m^{(i)} x^* I_m'(x^*)\cos m\theta\right]$$
$$\text{for} \quad x^* \leq x_{ss}^*, \qquad\qquad (24a)$$

$$\psi(r,\theta) = r_0 B_\vartheta^0(r_0)\left[F(x) + \sum_m b_m^{(e)} x^* K_m'\cos m\theta\right]$$
$$\text{for} \quad x^* \geq x_{ss}^*, \qquad\qquad (24b)$$

where $x_{ss}^* = m\alpha r_{ss} = m\dfrac{1}{q_s R_0}r_{ss}$ and, instead of the amplitude coefficients $\varepsilon_m^{(i,\,e)}$, we have introduced the coefficients

$$b_m^{(i)} = 4\frac{I_h}{I_0}x_{ss}^* K_m'(x_{ss}^*), \quad b_m^{(e)} = 4\frac{I_h}{I_0}x_{ss}^* I_m'(x_{ss}^*), \quad (25)$$

in order for the functions ψ^0 and ψ_h to have the common normalizing factor, which is taken outside the square brackets of formulas (24a) and (24b).

In order to specify the problem, we choose the values of the remaining free parameters to be close to the parameter values of the JET tokamak, on which the sharpest tomographic images were obtained [1]. We set the aspect ratio of the torus equal to $A = R_0/r_0 = 3$ and consider two operating modes with $q_0 = 3$ and 4. We also set $q_s = 2$, which indicates that we will be interested in a perturbation in the form of a quadrupole helical current (i.e., that with the harmonic numbers $m = 2$ and $n = 1$). The reason for this is twofold. First, the corresponding tomographic image was taken in the JET tokamak. Second, the quadrupole current mode is peculiar in that, in the internal region, it creates a so-called negative magnetic shear, which can cancel the initial positive shear and can disrupt the topological stability of the forming magnetic substructure.
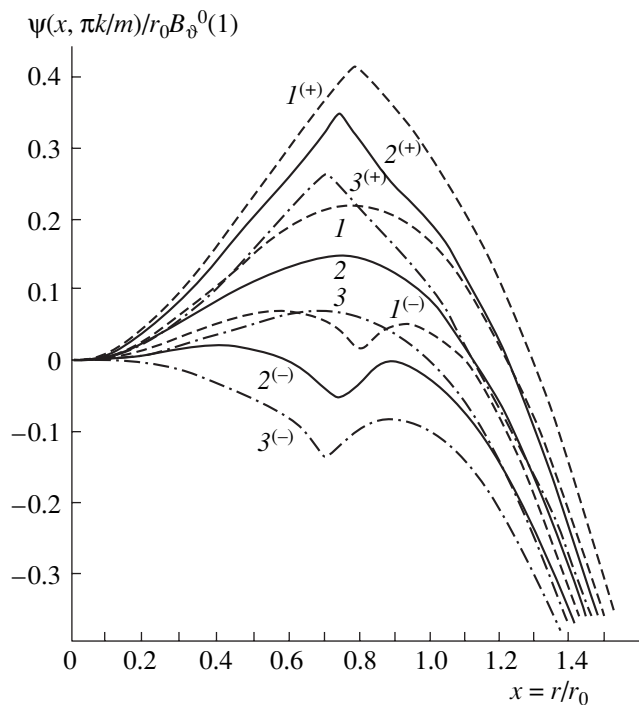
$\psi(x, \pi k/m)/r_0 B_\vartheta^0(1)$

Fig. 6. Profiles of the magnetic flux function $\psi(x, \theta)$ along the characteristic radial rays such that $m\theta_s = k\pi$ ($k = 0, 1, 2, \ldots$) for $q_0/q_s = 3/2$, for the relative helical current amplitude $I_h/I_0 = 0.1$, and for three different current density profiles j_z: $j_z \sim (1-x)$ (curves 2, $2^{(\pm)}$), $j_z \sim (1-x^2)$ (curves 3, $3^{(\pm)}$), and $j_z \sim (1-x^2)^2$ (curves 1, $1^{(\pm)}$). The superscript plus and minus signs indicate the positive and negative values of $\cos m\theta_s$, respectively.

For the above three profiles of the current density j_z, we, using formula (15), can easily obtain the values of the radial coordinate at which $q_s = 2$:

$$x_{ss} = r_{ss}/r_0 = 3/4 \quad \text{for} \quad j_z \sim (1-x), \quad (26a)$$

$$x_{ss} = 1/\sqrt{2} \approx 0.707 \quad \text{for} \quad j_z \sim (1-x^2), \quad (26b)$$

$$x_{ss} = \sqrt{3 - \sqrt{3}}/\sqrt{2} \approx 0.799 \quad \text{for} \quad j_z \sim (1-x^2)^2. \quad (26c)$$

It can be seen that, in accordance with the definition (16) of the function $F(x)$, these values of x_{ss} coincide with the coordinates at which $F(x)$ has a maximum. Consequently, for $x < x_{ss}$, the derivative of $F(x)$ is positive and, for $x > x_{ss}$, it is negative. As will be clear later, this circumstance largely governs the positions of the singular points in the (r, θ) plane.

Let us now investigate the behavior of the magnetic flux function $\psi(r, \theta)$ along the characteristic rays $\theta_s =$ const at which this function has singularities. In the particular case under consideration, Eqs. (7) and (7a) for

determining the singular points in the internal region ($x^* \leq x_{ss}^*$) have the form

$$\frac{\partial \psi}{\partial \theta} = 0 = \sum_m m b_m^{(i)} x_s^* I_m'(x_s^*) \sin m\theta_s, \quad (27)$$

$$\frac{\partial \psi}{\partial r} = 0 = \left[F_x' \frac{1}{r_0} + \sum_m m\alpha b_m^{(i)} (x_s^* I_m'(x_s^*))' \cos m\theta_s \right].$$

The singular points in the external region ($x^* \geq x_{ss}^*$) are determined by the same equations with the coefficients $b_m^{(i)}$ replaced with $b_m^{(e)}$ and the Bessel function $I_m(x)$ replaced with $K_m(x)$. The first of Eqs. (27), as well as the first of the more general equations (7), yields the following solution for θ_s:

$$m\theta_s = \pi k, \quad k = 0, 1, 2, 3\ldots. \quad (28)$$

The second of Eqs. (27) determines the extreme points at the rays θ_s in the internal region ($x^* \leq x_{ss}^*$):

$$\frac{F_x'(x_s)}{x_s} \pm \sum_m (m\alpha r_0)^2 b_m^{(i)} \frac{m^2 + (x_s^*)^2}{(x_s^*)^2} I_m(x_s^*). \quad (29)$$

The extreme points at the rays in the external region ($x^* \geq x_{ss}^*$) are determined by the same equation with the coefficients $b_m^{(i)}$ replaced with $b_m^{(e)}$ and the Bessel function $I_m(x)$ replaced with $K_m(x)$. Here, we take into account the relationship $\cos m\theta = \cos \pi k = \pm 1$. For the internal region ($r < r_0$), the first term in Eqs. (29) is given by the following explicit expressions:

$$\frac{1}{x} F_x'(x) = 3 - \frac{q_0}{q_s} - 2x \quad \text{for} \quad j_z \sim (1-x), \quad (30a)$$

$$\frac{1}{x} F_x'(x) = 2 - \frac{q_0}{q_s} - x^2 \quad \text{for} \quad j_z \sim (1-x^2), \quad (30b)$$

$$\frac{1}{x} F_x'(x) = 3 - \frac{q_0}{q_s} - 3x^2 + x^4 \quad \text{for} \quad j_z \sim (1-x^2)^2. \quad (30c)$$

For the external region ($r > r_0$), the first term has the same form for each of the three current density profiles j_z:

$$\frac{1}{x} F_x'(x) = \frac{1}{x} - \frac{q_0}{q_s} x. \quad (30d)$$

Since the amplitude coefficients $b_m^{(i)}$ and $b_m^{(e)}$ are of opposite signs, and since the first term in Eq. (29) has opposite signs in the regions corresponding to these coefficients, the ray at which the function $\psi(r, \theta)$ has extremes is characterized by the same coordinate $m\theta = m\theta_s = \pi(2l + 1)$, $l = 0, 1, 2\ldots$ in both internal and exter-
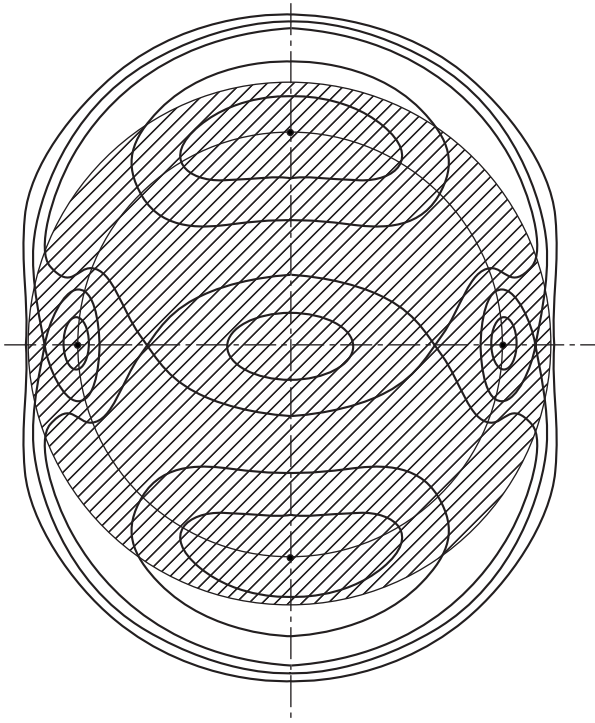
Fig. 7. Example of a magnetic substructure for $q_0/q_s = 3/2$, for the relative quadrupole helical current perturbation amplitude $I_h/I_0 = 0.1$, and for the current density profile $j_z \sim (1 - x^2)^2$.
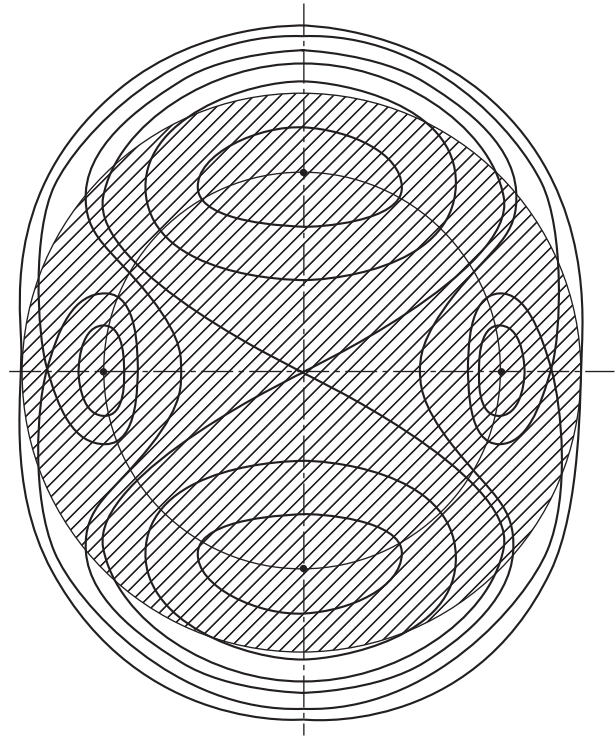

Fig. 8. The same as in Fig. 7, but for $j_z \sim (1 - x^2)$. The negative magnetic islands touch one another to form a figure-eight separatrix.

nal regions, i.e., for $\cos m\theta_s = -1$. In this respect, the situation in question differs from that in conventional (classical) stellarator with purely multipolar helical windings, where the singular points of the global magnetic field structure in the internal and the external region lie in pairs at different rays $m\theta_s$, shifted by π relative to one another (see Fig. 1). This case, however, corresponds to another type of stellarator, namely, to the torsatron [4].

The profiles of the function $\psi(r, \theta)$ along the rays $\theta_s = 0, \pi$, and $\pm\pi/2$, as well as along the rays $\theta = \pm\pi/4 + \pi$ (where $\psi(r, \theta)$ coincides with $F(x)$ are shown in Fig. 6 for the case of a quadrupole helical current ($m = 2$ and $n = 1$ at a radius at which $q_s = 2$). In the approximation at hand, only the fundamental harmonic in the helical term of the function $\psi(r, \theta)$ was retained for simplicity. The magnetic structures corresponding to these profiles are plotted in Figs. 7–9, in which we clearly see the presence of the so-called positive islands (the conditions for their onset were considered earlier in [6, 8]).

On the one hand, Eqs. (27)–(29) for the singular points make it possible to infer the type of magnetic substructure. On the other hand, these equations are of interest because they provide estimates of the critical amplitude $b_m^{(i, e)}$ (and, accordingly, the relative fraction of the current, I_h/I_0, captured by the island) at which the

internal ($x \leq x_{ss}$) substructure acquires a figure-eight shape. Thus, we must resolve Eq. (29) in $b_m^{(i)}$ and take the limit $x_s \longrightarrow 0$. As a result, for the chosen parameter values $q_0/q_s = 3/2$ and $r_0/R_0 = 1/3$, we obtain

$$b_m^{(i)} \longrightarrow \approx 27 \quad \text{for} \quad j_z \sim (1 - x), \quad j_z \sim (1 - x^2)^2,$$
$$b_m^{(i)} \longrightarrow \approx 9 \quad \text{for} \quad j_z \sim (1 - x^2). \tag{31}$$

Hence, when $b_m^{(i)}$ becomes larger than ≈ 27 for the above two peaked profiles of j_z and larger than ≈ 9 for the parabolic current density profile, the internal separatrix of the magnetic substructure contracts into a point and a figure-eight separatrix forms that encloses the regions in which the amplitude of the current density j_z is negative. This threshold corresponds to the following threshold amplitude of the current captured by the island:

$$I_h/I_0 = 0.21 \quad \text{for} \quad j_z \sim (1 - x), \quad j_z \sim (1 - x^2)^2,$$
$$I_h/I_0 = 0.07 \quad \text{for} \quad j_z \sim (1 - x^2). \tag{31a}$$

It can be seen from these estimates that, for the parabolic profile of j_z, the threshold current amplitude is not as large as that for the peaked profiles. The magnetic
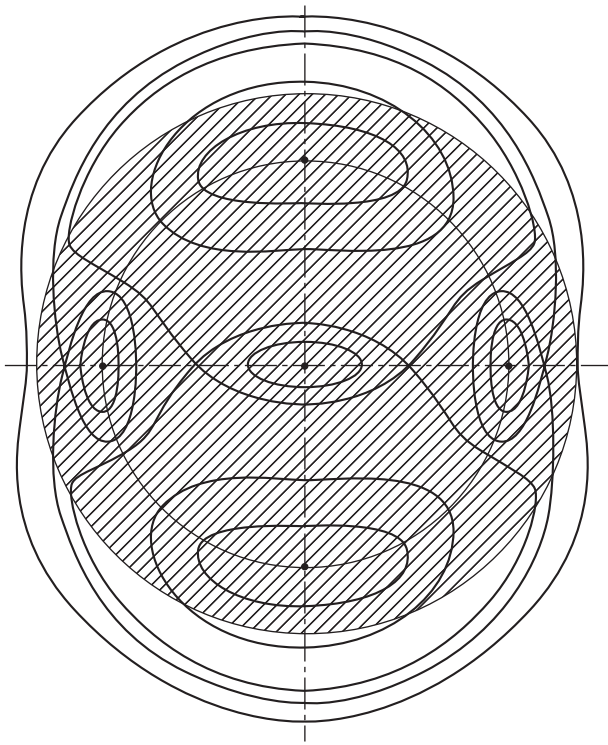
Fig. 9. The same as in Figs. 7 and 8, but for $j_z \sim (1-x)$. It is clearly seen that the substructure formed by negative islands is depressed by a pair of positive islands having their centers at the radial rays $\theta = 0$ and $\theta = \pi$.
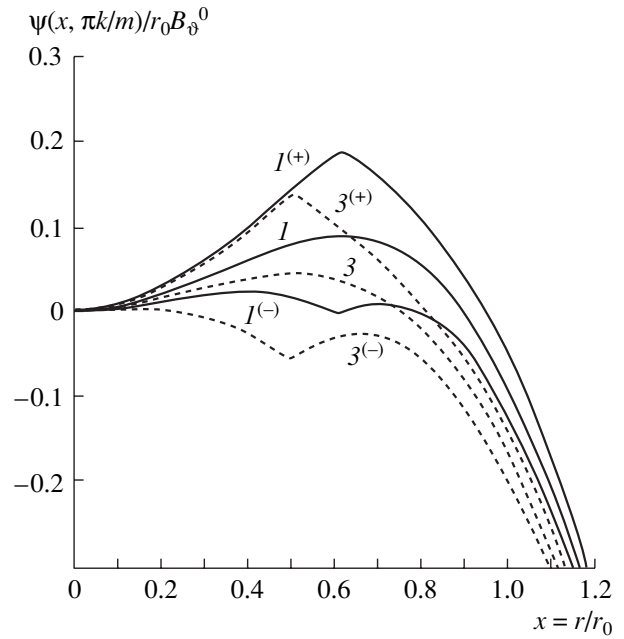

Fig. 10. Profiles of the magnetic flux function $\psi(x)$ along the characteristic radial rays such that $m\theta_s = k\pi$ ($k = 0, 1, 2, \ldots$) for $q_0/q_s = 4/2$, for the relative helical current amplitude $I_h/I_0 = 0.05$, and for two different current density profiles j_z: $j_z \sim (1-x^2)^2$ (curves 1, $1^{(\pm)}$) and $j_z \sim (1-x)$ (curves 3, $3^{(\pm)}$).
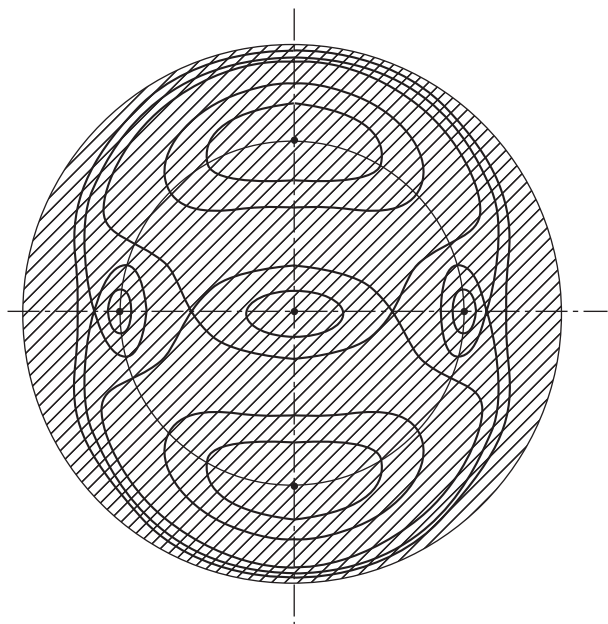

Fig. 11. Example of a magnetic substructure corresponding to $q_0/q_s = 4/2$ and to the profiles of the magnetic flux function for the case from Fig. 10 with $j_z \sim (1-x^2)^2$ and $I_h/I_0 = 0.05$.
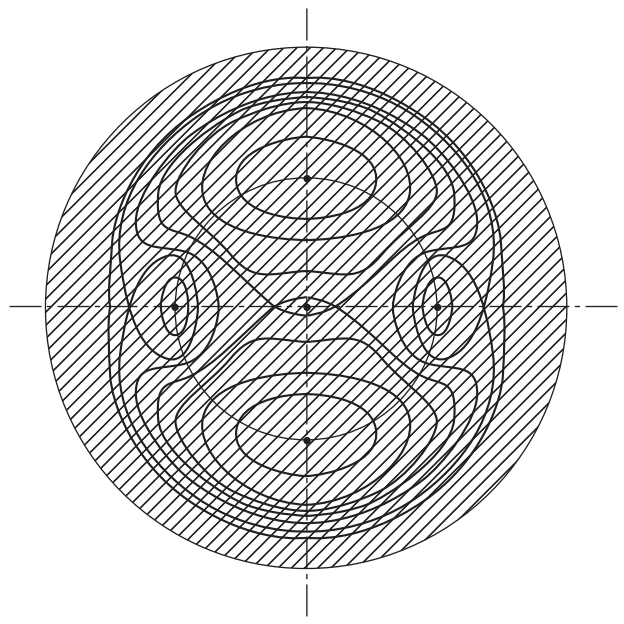

Fig. 12. The same as in Fig. 11, but for $j_z \sim (1-x)$. The magnetic substructure is near the threshold for its transformation into a figure-eight shape.
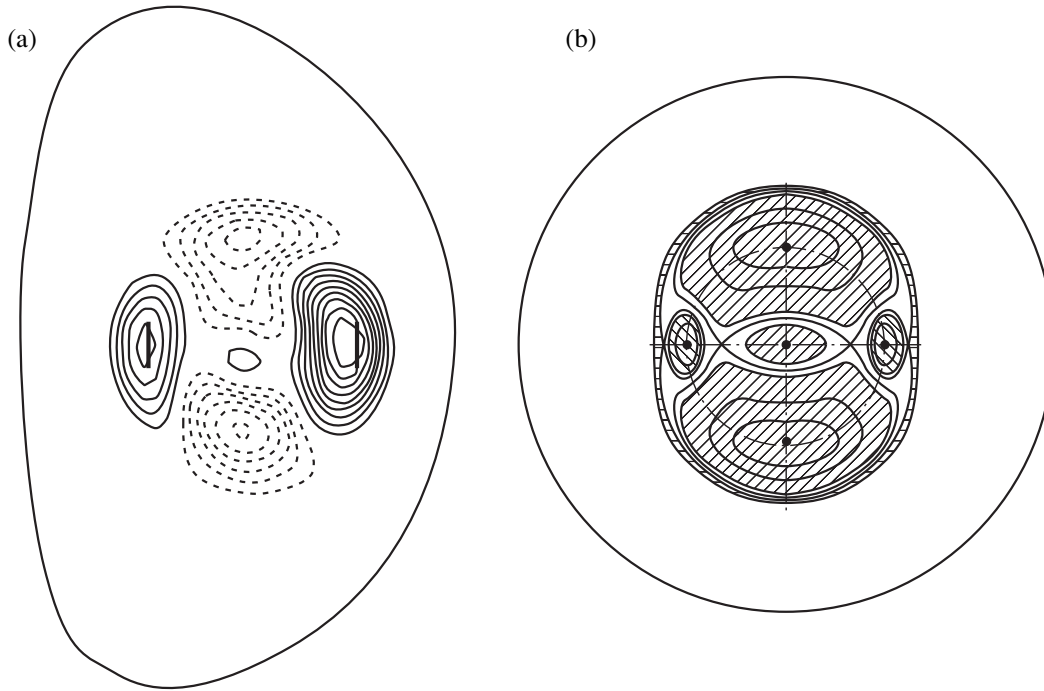
Fig. 13. Comparison between a helically symmetric model configuration with parameters close to those of the JET tokamak and an actual JET configuration: (a) tomographic image of a JET plasma and (b) helically symmetric model configuration calculated for the chosen parameter values. Explanations are given in the body of the text.

configurations shown in Figs. 7–9 were calculated for $I_h/I_0 = 0.1$. For the two peaked profiles of the current density j_z (for which the current has a large poloidal component in the region where $q_s = 2$), the calculations yield fairly stable structures with positive magnetic islands. For the parabolic current density profile, however, this value of the ratio I_h/I_0 turned out to be overcritical; this, in accordance with estimates (31) and (31a), led to the formation of a large figure-eight separatrix that results from the touching of two negative magnetic islands.

Figure 10 shows the profiles of the function $\psi(r, \theta)$ along all the characteristic rays for $q_0/q_s = 4/2$. In this case, the resonant ($q_s = 2$) magnetic surface lies deeper in the region $r < r_0$, where the poloidal magnetic field component B_ϑ^0 is weaker. As a result, the maximum value of the function $F(x_{ss})$ is lower, as well as the critical (limiting) current I_h that is captured by the island and at which the figure-eight structure forms. In this case, it turns out for the parabolic profile of j_z that the safety factor takes on the resonant value $q_s = 2$ at the center of the cross section of the current-carrying island and a figure-eight structure arises at an arbitrary value of the ratio $I_h/I_0 > 0$. For the more peaked j_z profiles, the torsatron-like magnetic structures still persist (Figs. 11, 12). Note, however, that, for the peaked distribution $j_z \sim (1 - x)$ and for the ratio I_h/I_0 as small as 0.05, the struc-

ture is seen to be very near the threshold for its bifurcation into a figure-eight shape.

Finally, Fig. 13 displays the tomographic image of a magnetic configuration that was recorded in one of the operating modes of the JET tokamak (and that has already been shown in Fig. 1) and the single-mode configuration calculated for $q_s = 2$ in terms of the helically symmetric ideal model developed here. The calculated configuration is seen to be fairly close in structure to the image. The computations were carried out for a somewhat larger boundary value of the safety factor, $q_0 = 4.5$, in order to obtain the magnetic substructure with $q_s = 2$ at the minor radius of the cross section of the current-carrying island close to that in the JET shot in question. In this case, we have $r_{ss} = 3/8r_0$; this value, being somewhat smaller than the radius of the substructure in JET, is nonetheless fairly close to it. It can be seen from Fig. 13 that, although the above two configurations have slightly different geometric parameters, their topological properties are essentially the same. In particular, this is true of the characteristic shape of the cross sections of negative magnetic islands, which are seen as if they were "depressed" by the positive islands, having a relatively smooth, round shape. It is evident that the geometric similarity between the two configurations could be even closer if the model incorporated the vertical elongation of the plasma column (as is the case in JET) and the two nearest helical satellite har-

monics $m = 2 \pm 1$, which are related to the small aspect ratio of the JET tokamak. In addition, the significant difference between the widths of the magnetic islands in the azimuthal direction can be reduced by taking into account the second helical harmonic of the magnetic field.

5. CONCLUSIONS

The results obtained demonstrate that the main geometric features of the magnetic structures observed in tomographic images of tokamak plasmas can be derived in terms of a relatively simple, single-mode, helically symmetric model. A comparison of the calculated structures with the tomographic images shows that the toroidicity and the vertical elongation of the plasma column manifest themselves only in details of the magnetic substructures under consideration and slightly affect their geometric shapes and topological properties. At the same time, taking these effects into account can, of course, help to refine the thresholds for the bifurcation of the forming magnetic substructures into a purely multipolar rosette structure enclosing the axial region of the plasma column.

With regard to the disruption of the topological stability of the forming magnetic substructures and their possible bifurcation into multipolar rosette structures as the parameter q_0/q_s increases, one point must be kept in mind. Although an increase in the parameter q_0/q_s displaces the resonant substructures toward the center, thereby worsening their stability because the poloidal magnetic field near the axis is weak, the region of the plasma column where the magnetic substructure bifurcates into a multipolar rosette structure (in the case at hand, a figure-eight structure) can be much smaller than that in the original situation, in which the values of the parameter q_0/q_s are smaller. This indicates that the global structure of the magnetic configuration is characterized by a comparatively thick radial layer of weakly perturbed external magnetic surfaces near the boundary $r = r_0$ of the plasma column. As a consequence, the resulting zone where the magnetic field lines are mixed by multipolar bifurcation, which can occur at large values of the parameter q_0/q_s, can turn out to be small; therefore, globally, the operating modes with large q_0/q_s values can be even more stable.

The calculations of magnetic configurations by means of the simplified single-mode model also show that the so-called positive magnetic islands are produced by local current perturbations with arbitrarily small amplitudes. The only condition for the onset of the positive islands is that the dimensions of the zone where the helical current perturbations are localized be smaller than the characteristic spatial scale of the current density profile j_z. However, for a perturbed helical current captured partially by the islands, this condition is satisfied automatically because the perturbation is localized on a spatial scale of $\leq r_s/m$, while the charac-

teristic spatial scale of the current density profile is on the order of r_0. As for the type of the quasi-stellarator substructure, which, in the case at hand, is essentially similar to the global torsatron configuration (all the hyperbolic singular points (X points) lie on the same radial ray), it is governed by the negative derivative of the function $F(x)$ at $x > x_{ss}$ in Eq. (29), i.e., is eventually associated with an abrupt decrease in the poloidal magnetic field B_ϑ^0 in the vicinity of the boundary of the current-carrying plasma column.

It should be noted that analogous magnetic substructures were recently obtained by Martynov and Medvedev [13], who analytically studied possible force-free configurations of a current-carrying plasma. However, they investigated the parameter range corresponding to small pitches of the helical structures and small safety factors $q < 1$, in which the formation of positive islands is virtually impossible. At the same time, the island structures obtained in [13] are topologically similar to a torsatron with a short-pitch ($\alpha r > 1$) helical winding [4].

Finally, it is necessary to outline some of the drawbacks of the calculation model used here. The main drawback is that the model is steady-state and does not take into account the toroidal effects associated with the poloidal nonuniformity of the magnetic structure. Because of its steady-state character, the model cannot be used to investigate the evolution of the magnetic structures and can serve solely to predict possible final structures in a system that has already relaxed to a state with prescribed parameters. Because of its idealized geometry, the model is incapable of describing possible, more complicated, responses of the toroidal system to helical current perturbations. The toroidal effects give rise to additional helical satellite harmonics with the numbers $m \pm 1$, $m \pm 2$, $m \pm 3$, ... in the subsequent terms of an expansion in powers of the inverse aspect ratio $A^{-1} = r_0/R_0$. In this case, the harmonics with higher numbers m can describe additional resonant responses at the magnetic surfaces with $q_s = m + 1$, $m + 2$, ..., while the lower harmonics break the symmetry in the positions of magnetic islands, making them partially overlapping. This leads to the destruction of the zone with hyperbolic singular points and gives rise to local error magnetic fluxes, which, in particular, result in the stochastization of the magnetic field lines in certain layers enclosing different parts of the magnetic island structures. Such effects, however, go beyond the scope of the present study and should be addressed in a separate paper.

REFERENCES

1. R. S. Granetz and P. S. Smeulders, Nucl. Fusion **28**, 457 (1988).
2. N. R. Sauthoff, S. von Goeler, and W. Stodiek, Nucl. Fusion **18**, 1445 (1978).
3. V. Schittenhelm and H. Zohm, Nucl. Fusion **37**, 1255 (1997).
4. I. S. Danilkin and O. E. Khadin, Fiz. Plazmy **15**, 155 (1989) [Sov. J. Plasma Phys. **15**, 86 (1989)].
5. B. B. Kadomtsev, Fiz. Plazmy **1**, 710 (1975) [Sov. J. Plasma Phys. **1**, 389 (1975)].
6. A. N. Chudnovskiy, Fiz. Plazmy **30**, 976 (2004) [Plasma Phys. Rep. **30**, 907 (2004)].
7. I. S. Danilkin, Tr. FIAN **65**, 26 (1973).
8. S. V. Mirnov, Fiz. Plazmy **24**, 875 (1998) [Plasma Phys. Rep. **24**, 813 (1998)].
9. A. I. Morozov and L. S. Solov'ev, in *Reviews of Plasma Physics*, Ed. by M. A. Leontovich (Gosatomizdat, Moscow, 1963; Consultants Bureau, New York, 1966), Vol. 2.
10. I. S. Danilkin and I. K. Karpenko, Zh. Tekh. Fiz. **39**, 1959 (1969) [Sov. Phys. Tech. Phys. **14**, 1477 (1969)].
11. I. S. Danilkin and O. E. Khadin, Preprint No. 343 (Inst. of General Physics, USSR. Acad. Sci., Moscow, 1985).
12. J. F. Harris, private communication (1989).
13. A. A. Martynov and A. Yu. Medvedev, Fiz. Plazmy **28**, 291 (2002) [Plasma Phys. Rep. **28**, 259 (2002)].

Translated by O.E. Khadin

Dust Acoustic Solitons in the Dusty Plasma
of the Earth's Ionosphere

S. I. Kopnin*, I. N. Kosarev*, S. I. Popel*, and M. Y. Yu**

*Institute of Geosphere Dynamics, Russian Academy of Sciences, Leninskiĭ pr. 38-1, Moscow, 119334 Russia
e-mail: s_i_popel@mtu-net.ru
**Institute for Theoretical Physics I, Ruhr University Bochum, D-44780 Bochum, Germany
Received May 11, 2004

Abstract—Stratified structures that are observed at heights of 80–95 km in the lower part of the Earth's ionosphere are known as noctilucent clouds and polar mesosphere summer echoes. These structures are thought to be associated with the presence of vast amounts of charged dust or aerosols. The layers in the lower ionosphere where there are substantial amounts of dust are called the dusty ionosphere. The dust grains can carry a positive or a negative charge, depending on their constituent materials. As a rule, the grains are ice crystals, which may contain metallic inclusions. A grain with a sufficiently large metallic content can acquire a positive charge. Crystals of pure ice are charged negatively. The distribution of the dust grains over their charges has a profound impact on the ionizational and other properties of dust structures in the dusty ionosphere. In the present paper, a study is made of the effect of the sign of the dust charge on the properties of dust acoustic solitons propagating in the dusty ionosphere. It is shown that, when the dust charge is positive, dust acoustic solitons correspond to a hill in the electron density and a well in the ion density. When the dust is charged negatively, the situation is opposite. These differences in the properties of dust acoustic solitons can be used to diagnose the plasmas of noctilucent clouds and polar mesosphere summer echoes. © 2005 Pleiades Publishing, Inc.

1. INTRODUCTION

In present-day plasma physics, an important place is occupied by the study of the so-called complex (dusty) plasma, which consists of electrons, ions, neutrals, and charged dust grains. In nature, an example of such a medium is the lower part of the Earth's ionosphere (at heights of 80–95 km). The stratified structures that are observed from mid-May to mid-August at sufficiently high latitudes in the lower ionosphere are known as noctilucent clouds and polar mesosphere summer echoes. These structures are thought to be associated with the presence of vast amounts of fine charged dust, in which the grains are usually less than 1 μm in size. The investigation of noctilucent clouds and polar mesosphere summer echoes is of considerable interest in connection with their possible effect on the global warming processes. Hence, studying dust structures in the lower ionosphere is an important task for specialists working in the fields of plasma physics, atmospheric and ionospheric sciences, ecology, micro- and nanogeophysics, and others.

It is generally considered that noctilucent clouds consist of ice grains. They occasionally form in summer at heights of 80–85 km at polar and mid-latitudes when the temperature falls below 155 K (see, e.g., [1]). In such circumstances, the atmospheric water vapor freezes into ice crystals. Polar mesosphere summer echoes, which are strong radar echoes, are also associated with the presence of dust [2]. They arise in a fairly narrow range of heights, from 80 to 95 km [3]. The fact that noctilucent clouds and polar mesosphere summer echoes occur during the same season of the year and at the same heights in the lower ionosphere allows one to suggest that these two phenomena are precisely of the same nature. The summer polar ionosphere layer at heights of 80–95 km, at which (possibly dusty) ice crystals form, is often called the dusty ionosphere.

The noctilucent clouds and polar mesosphere summer echoes are macroscopic ionospheric formations. Their vertical heights range from 10 to 1000 m, which is much less than the vertical scale of the atmosphere, $H \approx 7$ km. Many questions concerning these stratified formations still lack adequate answers. In particular, their structure is not yet completely understood. It seems that the structure of these formations is significantly affected by the sign of the charges of their constituent dust grains. This suggestion is confirmed by observations of noctilucent clouds and polar mesosphere summer echoes [2, 4–6]. Direct measurements [2, 5] verified that a sharp decrease in the electron density within macroscopic ionospheric formations is accompanied by the production of a great amount of negatively charged dust. That positively charged dust may be present in the dusty ionosphere was proved the *Dusty 2* [2] observations, their most noteworthy result being that a comparatively thin (about 200 m) negatively charged dust layer was observed upon a positively charged dust layer with a thickness of about 1.4 km.

The positive charge of the dust grains is explained by electron ejection from their surfaces due to the photoelectric effect with solar light [7]. The solar radiation spectra are sharply cut off at wavelengths approximately equal to 170 nm (which corresponds to a photon energy of 7.3 eV); consequently, in the range of heights under consideration, there are no photons with energies higher than 7.3 eV [8]. For pure ice, the photoelectric work function is about 8.9 eV. Hence, the photoelectric effect does not influence the processes of icy grain charging. This indicates that all the grains of pure ice are charged negatively; therefore, the electron density near the noctilucent clouds and polar mesosphere summer echoes should be reduced in comparison to the background electron density. That the increased electron density, too, was observed near these objects can be explained by the fact that the icy grains can contain impurities. In this case, the work function of the dust grain material can turn out to be lower than 7.3 eV, so the photoelectric effect can play an important (and even governing) role in the grain charging processes and can charge the grains positively.

The chemical composition of the dust grains in the dusty ionosphere is unknown. An indirect way of determining possible impurities is to measure the electron and ion densities within the noctilucent clouds and polar mesosphere summer echoes. The objective of the present paper is to consider dust acoustic solitons in the cases of positively and negatively charged dust in the plasma of the Earth's dusty ionosphere. We show that, in these two cases, the solitons have different properties. Consequently, such nonlinear solitons can be used to infer the sign of the dust charge and to determine whether the grains contain impurities.

The reasons for considering dust acoustic solitons in the Earth's dusty ionosphere are as follows:

(i) The dust acoustic perturbations are slow enough to be detected by observations.

(ii) Among the steady-state dust acoustic structures propagating with a constant velocity, solitons are especially noteworthy [9].

(iii) Solitons have been observed in geophysical experiments. In particular, lower hybrid envelope solitons in the Earth's magnetosphere were observed from the *Freja* satellite [10–12].

Our paper is organized as follows. In Section 2, we describe the properties and parameters of the dusty ionosphere, make the basic assumptions, and present the basic equations for dust acoustic solitons propagating in a complex (dusty) plasma with positively or negatively charged dust grains. In Section 3, we investigate dust acoustic solitons and the conditions for their existence in the Earth's dusty ionosphere. In Section 4, we summarize the main results and conclusions.

2. DESCRIPTION OF THE MODEL

In the model to be developed here, the noctilucent clouds and polar mesosphere summer echoes are considered as the layers of complex (dusty) plasma irradiated by solar light. The calculations are carried out for the following parameters of the dusty ionosphere at a height of 84 km [13]: the density of the atmospheric gases is $\rho_0 \approx 1.23 \times 10^{-8}$ g/cm^3, the water vapor pressure is $P_{H_2O} \approx 6.319 \times 10^{-5}$ g/(s^2 cm) (which corresponds to a partial water vapor density of $\rho_{H_2O} \approx 4.68 \times 10^{-14}$ g/cm^3), and the temperatures of the neutral gas (T_n), electrons (T_e), and ions (T_i) have the same value: $T_n = T_e = T_i = 141.1$ K.

The mean radius a of the dust grains is calculated by using the data derived from measurement. In the visible dust detected by lidar measurements, the mean radius of the dust grains is about 50 nm, the mean dust density being approximately equal to 100 cm^{-3}, whereas, in the invisible dust detected by rocket experiments, the grain radii are about 10–30 nm, the dust density being about several thousand grains per cubic centimeter [7]. The dust grain radii that are derived by the analysis of the water vapor density at heights of 80–95 km agree fairly well with those measured in experiments. For the above parameters [13] of the dusty ionosphere (a gas density of $\rho_0 \approx 1.23 \times 10^{-8}$ g/cm^3, a neutral gas temperature of $T_n = 141.1$ K, and a water vapor pressure of $P_{H_2O} \approx 6.319 \times 10^{-5}$ g/(s^2 cm)), condensation nuclei with a mean radius of 2.57 nm form in the initial stage of the process. The water vapor then condenses onto the nuclei until the pressure of the supersaturated vapor reduces to the saturated pressure. If the number density of the condensation nuclei (and, accordingly, the number density of the dust grains that compose the ionospheric structures) is $n_d = 100$ cm^{-3}, then the mean grain radius is $a = 61$ nm, which corresponds to visible dust and noctilucent clouds. Analogously, for $n_d = 1000$ cm^{-3}, we obtain $a = 28$ nm, which corresponds to invisible dust and polar mesosphere summer echoes. In what follows, these values of the radii and number densities of the dust grains will be used to investigate the nonlinear structures under consideration.

The impurities in the dust grains are characterized by the work function $\hbar\omega_R$, where $\hbar$ is Planck's constant. Recall that the work function of the grains of pure ice is 8.9 eV. The values of the work function of several materials [14] are presented in the table. In further analysis, we will use the value $\hbar\omega_R = 4.0$ eV, which is fairly close to the work functions of some refractory materials.

The dust grain charge changes as a result of absorption of the electrons and ions of the ambient plasma on the grain surface and also due to the photoelectric effect, which gives rise to the electron photocurrent from the grain surface. The dust grain charging process is described in terms of the so-called orbit motion lim-

Table

Substance	Li	Na	K	Rb	Cs	Be	Mg	Ca	Sr	Ba	Cu	Zn	Cb	Hg	Sn	Pd	Mo	W	U
Work function, eV	2.38	2.35	2.22	2.16	1.81	3.92	3.64	2.80	2.35	2.49	4.4	4.24	4.1	4.52	4.38	4.0	4.3	4.5	3.3

ited approach [15, 16]. In this approach, the mean dust grain charge $q_d = -Z_d e$ is calculated by the formula

$$d_t q_d = I_e(q_d) + I_i(q_d) + I_{ph}(q_d), \tag{1}$$

where $-e$ is the charge of an electron, I_e and I_i are the electron and ion macroscopic currents to the grain surface, and I_{ph} is the photocurrent.

For positively charged dust grains, the electron and ion macroscopic currents have the form

$$I_e \approx -\pi a^2 e \left(\frac{8T_e}{\pi m_e}\right)^{1/2} n_e \left(1 + \frac{eq_d}{aT_e}\right), \tag{2}$$

$$I_i \approx \pi a^2 e \left(\frac{8T_i}{\pi m_i}\right)^{1/2} n_i \exp\left(-\frac{eq_d}{aT_i}\right), \tag{3}$$

where $m_{e(i)}$ is the mass of an electron (ion) and $n_{e(i)}$ is the electron (ion) density.

For negatively charged dust grains, the electron and ion macroscopic currents are given by the expressions

$$I_e \approx -\pi a^2 e \left(\frac{8T_e}{\pi m_e}\right)^{1/2} n_e \exp\left(\frac{eq_d}{aT_e}\right), \tag{4}$$

$$I_i \approx \pi a^2 e \left(\frac{8T_i}{\pi m_i}\right)^{1/2} n_i \left(1 - \frac{eq_d}{aT_i}\right). \tag{5}$$

The expressions for the electron and ion currents, I_e and I_i, in the cases of a positive and a negative dust charge are different for the following reason. For positive q_d values, only ions with velocities such that $|\mathbf{v}| > (2eq_d/am_i)^{1/2}$ can reach the grain surfaces, while the electrons are free of this constraint, and vice versa for a negative dust charge.

The expression for the photocurrent has the form [8]

$$I_{ph} = \frac{\pi \beta e a^2}{\hbar} \int\limits_{\omega_R - (e^2 Z_d/a\hbar)}^{\infty} \frac{\Phi(\omega)}{\omega} d\omega, \tag{6}$$

where $\Phi(\omega)$ is the solar spectrum at the heights in question, $\Phi = \int \Phi(\omega) d\omega$ is the solar radiation flux, and β is the probability for a dust grain to emit an electron when a photon strikes its surface. The lower limit of integration is determined by the fact that only photons with frequencies $\omega > \omega_R - (e^2 Z_d/a\hbar)$ can give rise to the photoelectric effect. In the case under consideration, the work function $\hbar\omega_R$ is equal to several electronvolts (see table); on the other hand, we have $e^2 Z_d/a \sim T_n \sim 0.01$ eV $\ll \hbar\omega_R$. This is why the value of the integral in expres-

sion (6) depends insignificantly on the lower integration limit.

The characteristic electron densities in the dusty ionosphere vary between 10 and 10^3 cm^{-3} at night and between 10^3 and 10^5 cm^{-3} during the day [7, 17]. For definiteness, we choose the value $n_e = 3 \times 10^4$ cm^{-3}.

There is a fairly wide variety of ions in the dusty ionosphere [18], among which are positive and negative ions of different species. In further analysis, we will take into account only the contribution from positive ions, such as O_2^+ ions, which play an important role in dust charging processes [8]. The role of negative ions in the dusty ionosphere can be estimated as follows. The main primary negative ions are O_2^- ions, which are produced in the three-body attachment reactions $e + 2O_2 \longrightarrow O_2^- + O_2$ (the reaction rate constant being $k_{att} \simeq 5 \times 10^{-31}$ cm^6 s^{-1}). The O_2^- ions are lost in the photodetachment processes ($O_2^- + \hbar\omega \longrightarrow O_2 + e$, the rate constant being $k_{photo} \sim 0.3$ s^{-1}) and in the charge-exchange reactions $O_2^- + M \longrightarrow M^- + O_2$; they are also destroyed in collisions with atomic oxygen ($O_2^- + O \longrightarrow O_2 + O + e$, the reaction rate constant being $k_{det} \simeq 3 \times 10^{-10}$ cm^3 s^{-1}). The most efficient process is charge exchange with water molecules, the charge-exchange rate constant being $k_{ct}^{H_2O} \simeq 10^{-11}$ cm^3 s^{-1}. The kinetics of O_2^- ions in the dusty ionosphere can be described by the equation [8]

$$\frac{\partial n_{O_2^-}}{\partial t} \approx k_{att} n_e [O_2]^2 - k_{det}[O_2^-][O]$$
$$- k_{photo}[O_2^-] - k_{ct}^{H_2O}[O_2^-][H_2O], \tag{7}$$

where the square brackets stand for the densities of the corresponding molecules. Equating the terms that describe the production and loss of O_2^- ions, we can estimate their equilibrium density by $[O_2^-] \simeq k_{att} n_e [O_2]^2/(k_{photo} + k_{det}[O] + k_{ct}^{H_2O}[H_2O]) \simeq 0.1-1$ cm^{-3}. This density is much lower than that of the positive ions in the dusty ionosphere, $n_i \sim n_e \approx 10-10^5$ cm^{-3}. Consequently, the effect of negative ions on the dust charging processes can be ignored. In what follows, we will also ignore the contribution from positive proton–hydrate ions ($H^+(H_2O)_n$, $n \leq 10$). These ions are responsible for nucleation processes in the lower ionosphere [19], which are not considered in our paper. In the absence of

perturbations, the density of the positive ions is determined from the quasineutrality condition

$$n_{i0} \simeq n_{e0} + Z_{d0}n_{d0}, \tag{8}$$

where n_d is the dust density and the subscript 0 denotes unperturbed quantities.

The equilibrium dust charge is described by time-independent equation (1) in which the term with the time derivative on the left-hand side is replaced by zero. The photocurrent was determined using the computations of the solar spectrum in the dusty ionosphere that were done with the PHODIS code [8]. The results of calculating the equilibrium grain charges correspond to the data reported in [7]. According to these data, the dust grains of pure ice acquire a negative charge equal to several electron charges, whereas the charge of icy dust grains contaminated with impurities can be positive and can amount to several hundreds of electron charges. For a complex (dusty) plasma with positive O_2^+ ions and with the parameters $T_e = T_i = 141.1$ K, $n_{e0} = 3 \times 10^4$ cm^{-3}, $n_{d0} = 100$ cm^{-3}, $a = 61$ nm, $\hbar\omega_R = 4$ eV, and $\beta = 0.1$, we find $Z_{d0} = -139.8$. For the same parameter values, but for the grains of pure ice ($\hbar\omega_R \approx 8.9$ eV), we obtain $Z_{d0} = 2.28$. These Z_{d0} values will be used in further analysis of the solitons.

Here, we are considering solitons occurring on dust acoustic time scales. A soliton forms as a result of the cancellation of the nonlinear wave steepening by dispersion, which acts to widen the perturbation, thereby stopping the steepening. The dust charging process turns out to be far faster than the remaining processes that take part in the formation and propagation of a nonlinear dust acoustic wave. This indicates that the dust charge at each point of a dust acoustic soliton is fixed: it is determined by the plasma parameters at this particular point. Generally, the dust charges at different points of the soliton are different.

The dust acoustic solitons are described by a set of equations in which the electrons and ions obey Boltzmann distributions and which includes the hydrodynamic equations (namely, the continuity equation and the momentum conservation equation) for the dust grains, Poisson's equation for the electrostatic potential, and the time-independent equation relating the dust charge to the plasma parameters (cf. [9]):

$$\frac{\partial n_d}{\partial t} + \frac{\partial(n_d v_d)}{\partial x} = 0, \quad \frac{\partial v_d}{\partial t} + v_d\frac{\partial v_d}{\partial x} = \frac{Z_d e}{m_d}\frac{\partial\varphi}{\partial x}, \tag{9}$$

$$n_e = n_{e0}\exp\left(\frac{e\varphi}{T_e}\right), \quad n_i = n_{i0}\exp\left(-\frac{e\varphi}{T_i}\right), \tag{10}$$

$$\frac{\partial^2\varphi}{\partial x^2} = 4\pi e(n_e + Z_d n_d - n_i), \tag{11}$$

$$I_e(q_d) + I_i(q_d) + I_{ph}(q_d) = 0,$$

where v_d is the dust velocity, m_d is the mass of a grain, and φ is the electrostatic potential.

3. SOLITON SOLUTIONS

We seek such soliton solutions to Eqs. (9)–(11) that correspond to localized wave structures propagating with a constant velocity M along the x axis. In this way, all the quantities dependent on x and t are functions of only one variable $\xi = (x - Mt)/\lambda_{De}\sqrt{\tau}$, where $\lambda_{De} = \sqrt{T_e/4\pi n_e e^2}$ is the electron Debye radius and $\tau = T_i/T_e$. It is assumed that the amplitudes of all perturbations vanish at $\xi \longrightarrow \pm\infty$. Is solving Eqs. (9)–(11), we also assume that the dust charge within the soliton does not change. This latter assumption was checked for each specific solution to Eqs. (9)–(11).

Using the standard method of the Sagdeev potential [20], we can reduce Poisson's equation to a form similar to the energy conservation law in mechanics:

$$\frac{1}{2}(\varphi_\xi)^2 + V(\varphi) = 0, \tag{12}$$

where

$$V(\varphi) = \frac{1}{\tau}[1 - \exp(\varphi\tau) + (1 + Z_{d0}d)\tau(1 - \exp(-\varphi))$$
$$+ |M|\tau d(|M| - \sqrt{M^2 + 2Z_{d0}\varphi})]. \tag{13}$$

Equation (12) and expression (13) are written in terms of the dimensionless quantities φ and M, which are obtained from their dimensional analogues by the replacement

$$\frac{e\varphi}{T_i} \longrightarrow \varphi, \quad \frac{M}{c_d} \longrightarrow M, \tag{14}$$

and also contain the parameters $d = n_{d0}/n_{e0}$ and $c_d \equiv \sqrt{T_i/m_d}$. Expression (13) implies that $V(0) = 0$.

The necessary conditions for the existence of dust acoustic solitons are the condition that the Sagdeev potential $V(\varphi)$ have a local maximum at the point $\varphi = 0$ and the condition that the equation $V(\varphi) = 0$ have a non-zero real solution $\varphi = \varphi_0 \neq 0$, which determines the amplitude of the soliton, φ_0, as a function of M.

The condition for the Sagdeev potential to have a local maximum $V(\varphi) = 0$ at the point $\varphi = 0$ has the form

$$M^2 > \frac{Z_{d0}^2 d}{1 + \tau + Z_{d0}d}, \tag{15}$$

which is a consequence of the inequality $d^2V/d\varphi^2|_{\varphi=0} < 0$. The dust acoustic speed in a complex plasma is given by the formula

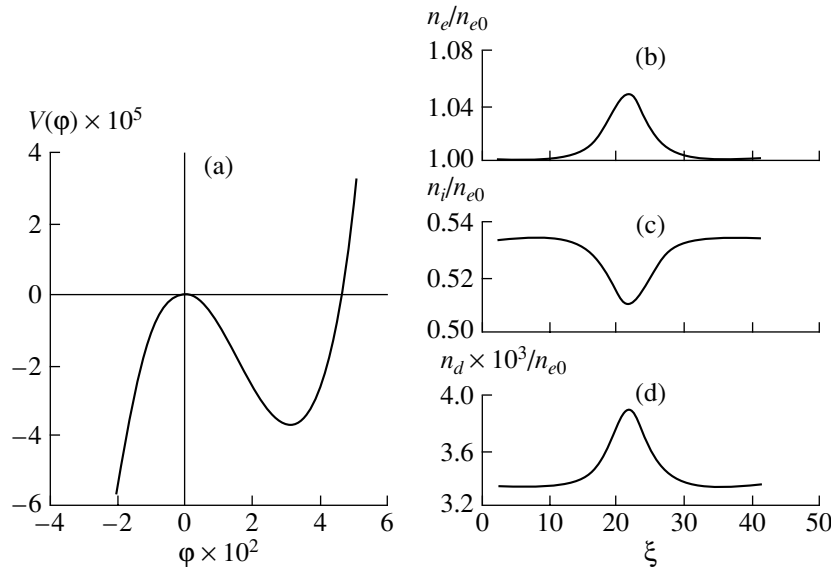$$c_{DA} = \sqrt{\frac{Z_{d0}^2 d}{1 + \tau + Z_{d0}d}}c_d. \tag{16}$$

Fig. 1. Sagdeev potential $V(\varphi)$ in the case of a positively charged dust (a) and the density profiles of (b) electrons, (c) ions, and (d) dust grains in the soliton solution for $M = 7$, $Z_{d0} = -139.8$ $(q_d > 0)$, $n_{d0} = 10^2$ cm^{-3}, $n_{e0} = 3 \times 10^4$ cm^{-3}, $T_e = T_i = 141.1$ K, and $a = 61$ nm. It is assumed that the main contribution comes from O_2^+ ions. All the densities are expressed in units of n_{e0}.

Consequently, condition (15) implies that the only solitons that can exist on dust acoustic time scales in a complex plasma are supersonic solitons.

Note that, for conditions typical of plasmas in the dusty ionosphere, the equation $V(\varphi) = 0$ with M values satisfying inequality (15) has nonzero real solutions such that the electrostatic potential φ may have opposite signs, depending on the sign of Z_{d0}. Figure 1a shows the dependence of the Sagdeev potential $V(\varphi)$ on the dimensionless electrostatic potential φ for $M = 7$, $Z_{d0} = -139.8$ $(q_d > 0)$, $n_{d0} = 10^2$ cm^{-3}, $n_{e0} = 3 \times 10^4$ cm^{-3}, $T_e = T_i = 141.1$ K, and $a = 61$ nm. In this case, the main ion contribution to the dust charging processes is assumed to come from O_2^+ ions. Figures 1b–1d show the density profiles of the electrons, ions, and dust grains, respectively, in a dust acoustic soliton whose amplitude corresponds to a nonzero solution to the equation $V(\varphi) = 0$. Figure 2a shows the dependence of the Sagdeev potential on the normalized electrostatic potential for $M = 0.1$, $Z_{d0} = 2.28$ $(q_d < 0)$, $n_{d0} = 10^2$ cm^{-3}, $n_{e0} = 3 \times 10^4$ cm^{-3}, $T_e = T_i = 141.1$ K, and $a = 61$ nm. In this case, the main ion contribution to the dust charging processes is also assumed to come from O_2^+ ions. The profiles corresponding to the soliton solution at hand are shown in Figs. 2b–2d.

It is generally impossible to determine how the sign of the dust charge in dust acoustic solitons depends on the sign of the amplitude of the electrostatic potential. Nevertheless, numerical analysis shows that this dependence can be determined for the parameter values typical of the dusty ionosphere ($T_e = T_i = 135$–155 K, $n_{d0} =$

100–1150 cm^{-3}, and $n_{e0} = 10^3$–10^5 cm^{-3}) [7, 13]. The analysis was carried out in the following way: For different parameter values, we calculated the radii and charges of the dust grains on the basis of a model incorporating the water vapor condensation. We also calculated the dependence of the radii of the dust grains on their densities. Using the results of these calculations, we obtained the profiles of the amplitudes of the solitons, φ_0, as functions of the velocity M (in the range of its possible values) and the unperturbed dust density n_{d0}. Examples of such profiles for a positive and a negative dust charge are presented in Figs. 3 and 4, respectively. We can see that, for a positively charged dust (Fig. 3), the soliton amplitude φ_0 is positive over the entire range of M values and the unperturbed dust density varies in the range $n_{d0} = 100$–620 cm^{-3}. For higher dust densities, soliton solutions do not exist. For a negatively charged dust (Fig. 4), the soliton amplitude φ_0 is negative over the entire range of M values and we have $n_{d0} = 100$–1150 cm^{-3}. The positive (negative) soliton amplitude φ_0 corresponds to a positive (negative) value $\delta n_e \equiv n_e - n_{e0}$ and a negative (positive) value $\delta n_i \equiv n_i - n_{i0}$. This indicates that, in the case of a negatively charged dust, dust acoustic solitons correspond to a hill in the electron density and a well in the ion density. The situation with a positively charged dust is opposite: the soliton shows up as a hill in the ion density and a well in the electron density. In both these cases, the dust density behaves in the same way: specifically, it increases above its unperturbed value.

Figures 3 and 4 were obtained for particular values of the plasma parameters, namely, $T_e = T_i = 141.1$ K and
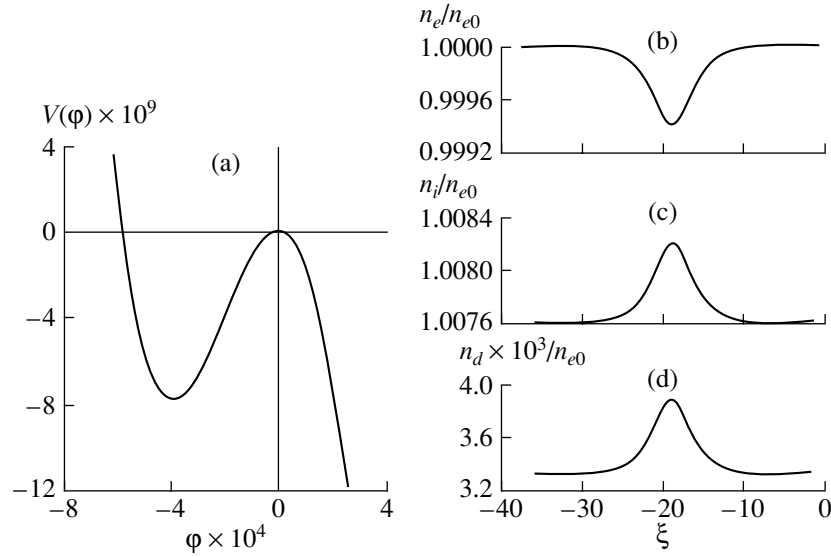
Fig. 2. Sagdeev potential $V(\varphi)$ in the case of a negatively charged dust (a) and the density profiles of (b) electrons, (c) ions, and (d) dust grains in the soliton solution for $M = 0.1$, $Z_{d0} = 2.28$ ($q_d < 0$), $n_{d0} = 10^2$ cm^{-3}, $n_{e0} = 3 \times 10^4$ cm^{-3}, $T_e = T_i = 141.1$ K, and $a = 61$ nm. It is assumed that the main contribution comes from O_2^+ ions. All the densities are expressed in units of n_{e0}.

$n_{e0} = 3 \times 10^4$ cm^{-3}. Numerical analysis shows, however, that the conclusion about the correlation between the sign of the dust charge and the amplitude of the electrostatic potential φ_0 of the dust acoustic solitons also remain valid for the parameters $T_e = T_i = 135$–155 K and $n_{e0} = 10^3$–10^5 cm^{-3}. This indicates that, in the dusty ionosphere, the properties of dust acoustic solitons in the case of dust grains contaminated with impurities (which act to decrease the work function of the grain material to values less than 7.3 eV) are quite different from those in the case of dust grains of pure ice. It is expected that, in the first case, the electron density will increase while the ion density will decrease, and vice versa in the second case. Note also that, in the case of impurity-contaminated dust grains, dust acoustic solitons can be far more intense (Fig. 3) than those in the case of dust grains of pure ice (Fig. 4).

An analysis of how the dust charge varies in a dust acoustic soliton that can propagate in the dusty ionosphere shows that the maximum relative amplitude of these variations is much less than one percent and cannot exceed the relative amplitudes of variations in the electron and ion densities within the soliton. This confirms the validity of the assumption that variations in the dust charge within dust acoustic solitons in the dusty ionosphere can be ignored.

From Figs. 3 and 4 we can see that, for any value of the dust density, there is a very strong restriction on the
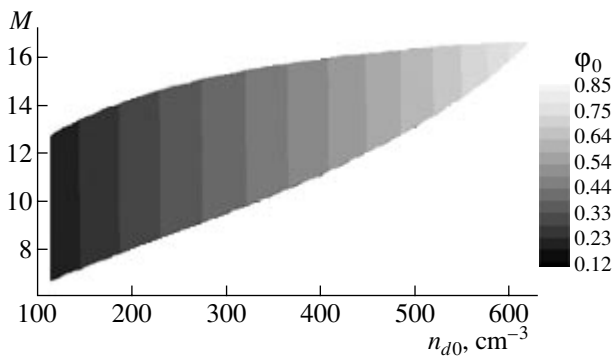

Fig. 3. Soliton amplitude φ_0 as a function of M and n_{d0} in the case of a positively charged dust (the photoelectric effect is important) for $T_e = T_i = 141.1$ K and $n_{e0} = 3 \times 10^4$ cm^{-3}.

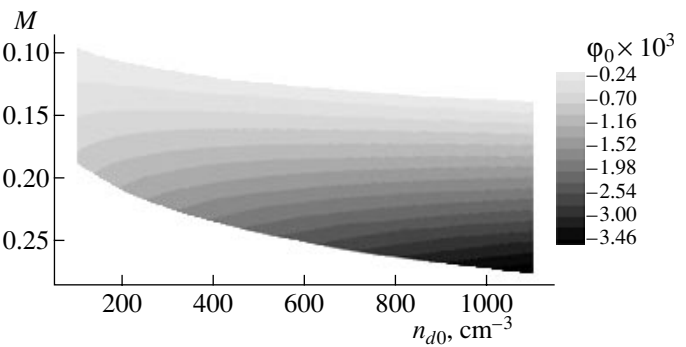**Fig. 4.** Soliton amplitude φ_0 as a function of M and n_{d0} in the case of a negatively charged dust ($\hbar\omega_R > 7.3$ eV) for $T_e = T_i = 141.1$ K and $n_{e0} = 3 \times 10^4$ cm^{-3}.

absolute values of the maximum amplitudes of the solitons, $|\varphi_0|$. This restriction stems from the fact that the equation $V(\varphi) = 0$ can have solutions corresponding to dust acoustic solitons not only under inequality (15) but also under the condition

$$V(\varphi_{max}) \geq 0, \tag{17}$$

where $\varphi_{max} = -M^2/2Z_{d0}$ (see expression (13)). Note that $|\varphi_{max}|$ is the maximal absolute value of the soliton amplitude. Condition (17), which can be rewritten as

$$1 - \exp(M^2\tau/2|Z_{d0}|) \\ + (1 + Z_{d0}d)\tau(1 - \exp(M^2/2Z_{d0})) + M^2\tau d \geq 0, \tag{18}$$

turns out to be satisfied for both positively and negatively charged dust grains.

Nonlinear dust acoustic waves can be investigated analytically only under the assumption that their amplitudes are small. Under this assumption, the evolutionary equation for the waves can easily be derived by expanding the Sagdeev potential $V(\varphi)$ in powers of the electrostatic potential φ and retaining terms up to the third order (φ^3) in this potential. Using expression (13), we obtain

$$\frac{d^2\varphi}{d\xi^2} + \left\{ -1 - \tau - Z_{d0}d + \frac{Z_{d0}^2 d}{M^2} \right\} \varphi \\ + \left\{ 1 + Z_{d0}d - \tau^2 - \frac{3Z_{d0}^3 d}{M^4} \right\} \frac{\varphi^2}{2} = 0. \tag{19}$$

Equation (19) has the localized solution

$$\varphi = \frac{3M^2[M^2 + M^2\tau + M^2 Z_{d0}d - Z_{d0}^2 d]}{M^4 + M^4 Z_{d0}d - M^4\tau^2 - 3Z_{d0}^3 d} \\ \times \cosh^{-2}\left(\frac{\xi}{2} \left\{ 1 + \tau + Z_{d0}d - \frac{Z_{d0}^2 d}{M^2} \right\}^{1/2} \right), \tag{20}$$

which describes a dust acoustic soliton. Note that analytical solution (20) deviates by no more than 1 percent from the solutions to Eqs. (9)–(11) that were calculated numerically for a dusty plasma with O_2^+ ions and with the parameters $M = 7$, $Z_{d0} = -139.8$ ($q_d > 0$), $n_{d0} = 10^2$ cm^{-3}, $n_{e0} = 3 \times 10^4$ cm^{-3}, $T_e = T_i = 141.1$ K, and $a = 61$ nm and for a dusty plasma with O_2^+ ions and with the parameters $M = 0.1$, $Z_{d0} = 2.28$ ($q_d < 0$), $n_{d0} = 10^2$ cm^{-3}, $n_{e0} = 3 \times 10^4$ cm^{-3}, $T_e = T_i = 141.1$ K, and $a = 61$ nm. Hence, analytical solution (20) may be helpful in describing small-amplitude ($\varphi \ll 1$) dust acoustic solitons in the plasma of the Earth's dusty ionosphere.

4. CONCLUSIONS

In the present paper, we have shown that dust acoustic solitons can propagate in a complex plasma of the dusty ionosphere in summer at heights of 80–85 km in the polar regions and at mid-latitudes. The properties of the solitons depend substantially on the sign of the dust charge along their paths. The dust consists of nanometer-size icy grains. If the grains contain impurities that lower the grain's photoelectric work function to less than 7.3 eV, then they can be charged positively by the photoelectric effect with solar light at heights of 80–95 km. The work function of the grains of pure ice is too high (8.9 eV) for the photoelectric effect to play a significant role (such high-energy photons are absent in the solar radiation spectrum), so the dust grains acquire a negative charge. In dust acoustic solitons propagating in a plasma layer with positively charged dust grains, the electron density is higher than its unperturbed value (a hill in the electron density) while the ion density is lower (a well in the ion density). The situation with negatively charged dust grains is the opposite: the soliton shows up as a hill in the ion density and a well in the electron density. In both cases, the dust density behaves in the same way: specifically, it increases above its unperturbed value regardless of whether the grains carry a negative or a positive charge. In a dusty ionospheric layer with positively charged grains, the dust acoustic solitons are more intense than those in a layer of negatively charged dust. Observations of dust acoustic solitons in the dusty mesosphere can be useful for diagnosing the plasma of the dusty ionosphere, noctilucent clouds, and polar mesosphere summer echoes as well as for determining the constituent substances and materials of the dust grains.

REFERENCES

1. J. N. Cho and J. Röttger, J. Geophys. Res. **102**, 2001 (1997).
2. O. Havnes, J. Trøim, T. Blix, *et al.*, J. Geophys. Res. **101**, 10839 (1996).
3. V. Nussbaumer, K.-H. Fricke, M. Langer, *et al.*, J. Geophys. Res. **101**, 19161 (1996).
4. O. Havnes, U. de Angelis, R. Bingham, *et al.*, J. Atmos. Terr. Phys. **52**, 637 (1990).

5. O. Havnes, L. I. Næsheim, T. W. Hartquist, *et al.*, Planet. Space Sci. **44**, 1191 (1996).

6. B. A. Klumov, G. E. Morfill, and S. I. Popel, Zh. Éksp. Teor. Fiz. **127** (1), 171 (2005) [JETP **100**, 152 (2005)].

7. O. Havnes, T. Aslaksen, and A. Brattli, Phys. Scr. **T89**, 133 (2001).

8. V. A. Klumov, S. I. Popel, and R. Bingham, Pis'ma Zh. Éksp. Teor. Fiz. **72**, 524 (2000) [JETP Lett. **72**, 364 (2000)].

9. A. V. Ivlev and G. Morfill, Phys. Rev. E **63**, 026412 (2001).

10. H. L. Pécseli, B. Lybekk, J. Trulsen, and A. Eriksson, Plasma Phys. Controlled Fusion **39**, A227 (1997).

11. S. H. Kjus, H. L. Pécseli, B. Lybekk, *et al.*, J. Geophys. Res. **103**, 26633 (1998).

12. S. I. Popel, Fiz. Plazmy **27**, 475 (2001) [Plasma Phys. Rep. **27**, 448 (2001)].

13. V. V. Adushkin, V. P. Kudryavtsev, and A. B. Khrustalev, in *Physical Processes in Geospheres: Their Manifesta-tions and Interactions* (IDG RAN, Moscow, 1999), p. 217.

14. A. G. Khrapak and I. T. Yakubov, *Electrons in Dense Gases and Plasmas* (Nauka, Moscow, 1981).

15. F. F. Chen, in *Plasma Diagnostic Techniques*, Ed. by R. H. Huddlestone and S. L. Leonard (Academic, New York, 1965).

16. M. S. Barnes, J. H. Keller, J. C. Forster, *et al.*, Phys. Rev. Lett. **68**, 313 (1992).

17. G. von Cossart, J. Fiedler, U. von Zahn, *et al.*, Geophys. Res. Lett. **24**, 1635 (1997).

18. G. C. Reid, J. Geophys. Res. **94**, 14653 (1989).

19. T. Sugiyama, J. Geophys. Res. **99**, 3915 (1994).

20. R. Z. Sagdeev, in *Reviews of Plasma Physics*, Ed. by M. A. Leontovich (Atomizdat, Moscow, 1964; Consultants Bureau, New York, 1968), Vol. 4.

Translated by I.A. Kalabalyk

==
DUSTY
PLASMA
==

Effect of Microwave Radiation on a Dusty Plasma

A. N. Starostin and Yu. V. Petrushevich

Troitsk Institute for Innovation and Fusion Research, Troitsk, Moscow oblast, 142092 Russia
Received May 24, 2004; in final form, July 22, 2004

Abstract—The effect of microwave radiation on a complex plasma produced by an external ionizer is studied using numerical simulations. It is shown that, as the radiation intensity increases, the scattering of the incident radiation by charged metal grains is enhanced and radiation at the second harmonic of the incident radiation appears in the scattered spectrum. This effect is associated with the grain charge oscillations caused by the nonlinear action of the microwave field. It is found that, under the action of strong microwave radiation, the grain charge can increase by one order of magnitude. It is shown that, when the microwave intensity is high enough, the distribution of the electric field near a dust grain is shown to change so radically that the field component normal to the grain surface can even change its sign. © 2005 Pleiades Publishing, Inc.

1. INTRODUCTION

In experimental studies of dusty (or complex) plasmas [1], the plasma is produced by various means, such as glow and RF discharges and ionizing radiation sources. A variety of phenomena related to the effect of radiation have been observed in such plasmas. So, it is of interest to study the combined action of various factors on the plasma under these conditions. The aim of this study is to investigate the effect of a microwave field on a complex plasma produced by an external ionizer (e.g., by an electron beam) over a wide range of microwave intensities: from the minimal detectable value up to the breakdown intensity. Particular attention is given to the scattering of microwave radiation in a dusty plasma and to the nonlinear interaction of radiation with such plasmas.

2. FORMULATION OF THE PROBLEM AND THE BASIC EQUATIONS DESCRIBING THE DYNAMICS OF CHARGED PARTICLES IN A LOW-TEMPERATURE COMPLEX PLASMA

We study processes in a complex plasma containing solid metal grains. Let us consider a single grain surrounded by a plasma. We assume that the plasma consists of the electron component and one positive ion component. It is also assumed that the microwave pulse is short enough for the temperature of the dust grain to remain unchanged during irradiation. The grain is assumed to be a sphere of a given radius. Our time-dependent model includes the processes of charge transport in plasma and plasma generation under the action of an external ionizer.

Since the microwave wavelength (~1 cm) far exceeds the diameter of the dust grain and the size of the plasma region and under consideration, the action of the microwave field on the complex plasma can be considered in a quasistatic approximation. The self-consistent electrostatic (potential) electric field is the sum of the electric field of the incident microwave and the fields produced by the plasma particles and the charged dust grain.

Taking into account the axisymmetric geometry of the problem, we use spherical coordinates with the polar axis directed along the axis of symmetry. The model of a low-temperature plasma used in this paper and the numerical algorithm are described in detail in [2]. The basic set of equations has the form

$$\frac{\partial n_e}{\partial t} + \nabla \cdot (\mathbf{w}_e n_e) = \nabla \cdot (D \cdot \nabla n_e) + Q_e,$$

$$\frac{\partial n_i}{\partial t} + \nabla \cdot (\mathbf{w}_i n_i) = Q_i, \tag{1}$$

$$\Delta\varphi = 4\pi e(n_e - n_i).$$

Here, n_e and n_i are the densities of the electrons and positive ions, respectively; $\mathbf{w}_e$ and $\mathbf{w}_i$ are their drift velocities; Q_e and Q_i are the terms describing charge kinetics (the generation and loss of charged particles in plasmochemical reactions); D is the electron diffusion coefficient; and φ is the electric field potential.

We use a spherical coordinate system whose origin coincides with the center of the spherical dust grain of radius R_d. The set of Eqs. (1) should be supplemented with boundary conditions at the grain surface. The boundary condition for ions depends on the direction of the ion drift velocity. If this velocity is directed away from the grain surface, then the ion density is set at zero at the grain surface, because there is no ion source. If the ion drift velocity is directed toward the sphere (as is the case with a negatively charged grain), then no boundary conditions for ions are imposed at the grain surface.

The electron transport equation contains a diffusion term; therefore, the boundary condition for electrons at

the grain surface must be imposed for any sign of the grain charge. Taking into account that the known mechanisms for electron production at the surface of a room-temperature grain surrounded by a low-temperature plasma are inefficient, we assume that the electron density near the sphere is zero. At infinity, the ion and electron densities are assumed to be equal to their equilibrium values determined by plasmochemical processes.

The electric field at infinity is assumed to be equal to the given electric field $E_0(r)$ of the incident microwave. Since we consider a metal grain, its surface must be equipotential. Summarizing all the assumptions, we arrive at the following set of the boundary conditions:

$$n_i(r = R_d) = 0 \quad \text{for} \quad E(r = R_d) > 0,$$

$$n_i(r \longrightarrow \infty) = n_i^{(eq)},$$

$$n_e(r = R_d) = 0, \tag{2}$$

$$n_e(r \longrightarrow \infty) = n_e^{(eq)};$$

$$\varphi(r = R_d) = \varphi_0,$$

$$\nabla \varphi(r \longrightarrow \infty) = -\mathbf{E}_0(r). \tag{3}$$

3. SIMULATION RESULTS

For the sake of definiteness, we must specify the terms describing the charge kinetics in the set of Eqs. (1). We chose nitrogen as a plasma-forming medium, because its kinetics has been investigated rather well. Low-temperature nitrogen plasma can be considered two-component. The rates of charge kinetics in a nitrogen plasma can be written as

$$Q_e = Q_i = q - \beta n_e n_i, \tag{4}$$

where q is the rate of ionization by an electron beam and β is the recombination coefficient, which depends on the electric field and is on the order of $\beta \sim 10^{-6}$ cm^3/s. In calculations, we used the known dependence of the plasma recombination coefficient on the electric field in argon; a similar charge kinetics model is described in [3].

Dust grains were metal spheres of radius $R_d = 12$ μm. We considered a gas at normal pressure ($p = 1$ atm) and room temperature ($T = 300$ K). The dust density was assumed to be low enough for the charge transferred onto the grains not to affect the density of charged plasma particles. Thus, we ignored a decrease in the plasma density due to the charging of dust grains.

The dust grain charge was calculated from the balance of the currents produced by different plasma components; the computations continued until the currents reached their quasi-steady values.

It was assumed that low-temperature nitrogen plasma is produced by an electron beam ionizing the gas. The beam power and, accordingly, the ionization rate were varied. We performed calculations for ioniza-
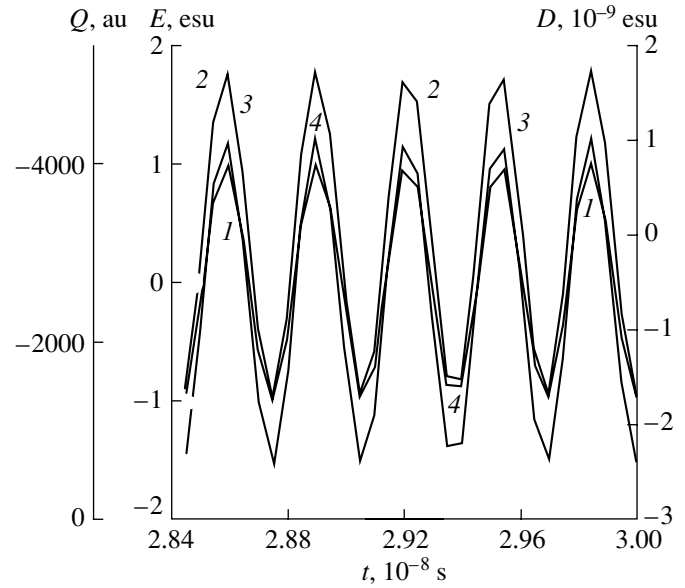

Fig. 1. Time dependences of some quantities in the quasi-steady stage of the process for a microwave intensity of 120 W/cm^2: (*1*) electric field strength, (*2*) grain charge, (*3*) dipole moment of the grain–plasma system, and (*4*) dipole moment of the grain according to the Mee theory.

tion rates of $q_1 = 10^{14}$ s^{-1} cm^{-3} and $q_2 = 10^{15}$ s^{-1} cm^{-3}. Under these conditions, the maximal electron density attained $\sim 5 \times 10^{10}$ and 2×10^{11} cm^{-3}, respectively.

The microwave frequency was chosen to satisfy the requirements of our quasistatic model and to be higher than the plasma frequency, because at lower frequencies, the microwave field is screened by the plasma.

We performed calculations for different intensities of the incident microwave radiation. At the lower electron-beam power (which corresponded to the ionization rate q_1), the microwave intensity was varied from 0.1 to 120 W/cm^2, and at the higher power (i.e., at $q = q_2$), it was varied from 0.1 to 1 MW/cm^2.

It was found that the dust grain charge increased substantially with increasing microwave intensity: as the intensity increased from 0.1 to 120 W/cm^2, the negative grain charge increased from 3400 to 5100 au. In these calculations, the plasma density was rather low, the electron density being $\sim 6 \times 10^{10}$ cm^{-3}.

The calculated time dependences of some quantities for a microwave intensity of 120 W/cm^2 are shown in Fig. 1. The time interval presented in the figure (28.4–30.0 ns) refers to the quasi-steady phase of the process, when the grain charge has already reached its steady-state value. It can be seen that the oscillations of the external field are accompanied by oscillations of the dipole moments of both the dust grain and the surrounding plasma. These oscillations, in turn, induce electromagnetic radiation; this effect can be interpreted as the scattering of the incident microwave field.
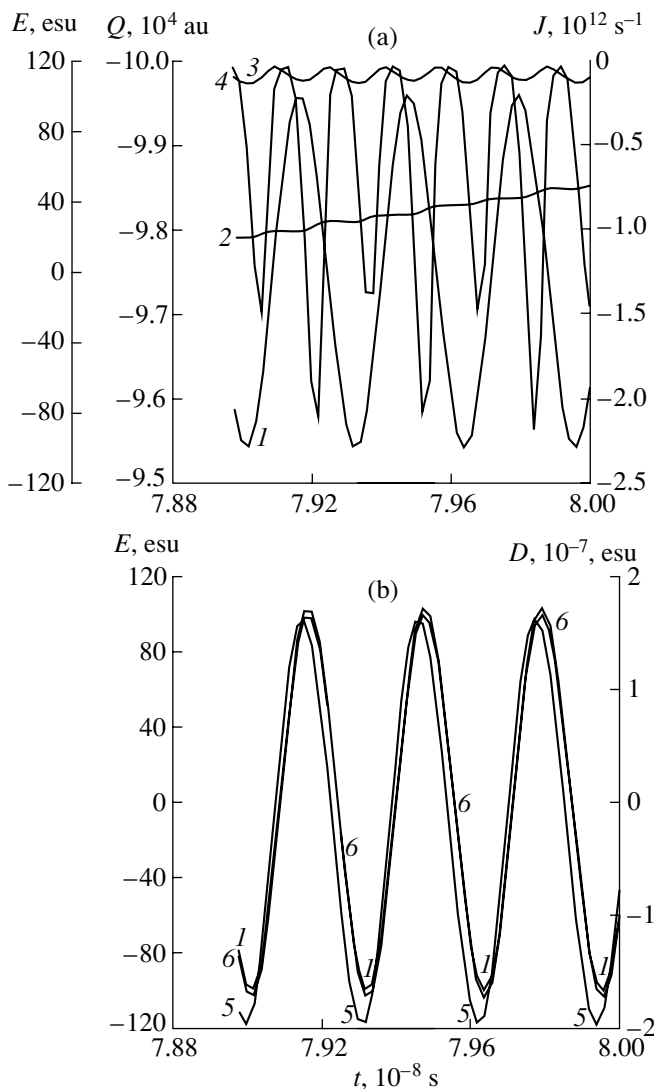
Fig. 2. Time dependence of some quantities in the quasi-steady stage of the process for a microwave intensity of ~1.2 MW/cm^2: (*1*) electric field strength, (*2*) grain charge, (*3*) electron flux, (*4*) ion flux, (*5*) dipole moment of the grain–plasma system, and (*6*) dipole moment of the grain according to the Mee theory.

To estimate the intensity of the scattered radiation, we consider the diffraction of radiation by a conducting sphere in the Mee theory [4]. This theory applies to an uncharged metal sphere embedded in a nonconducting medium, and the radiation is considered in terms of the wave theory for an arbitrary radius of the sphere. When the radiation wavelength far exceeds the radius of the sphere, $\kappa = 2\pi R_d/\lambda \ll 1$ (as is in the case under consideration), the electric field of the scattered radiation in the Mee theory is described by the radiation field of an electric dipole with a moment $p = p_0 \exp\{-i\omega t\}$. Here, ω is the radiation frequency, $p_0 = E_0 R_d^3$, and E_0 is the electric field of the incident wave. This solution corresponds to the first electric partial wave at a large dis-

tance r from the sphere, $\lambda \ll r$. The other components of the electric field (partial scattered waves of the *l*th order) are small in the parameter κ^{2l}. Note that the dipole moment for the first partial wave in the Mee theory corresponds to the dipole moment of a metal sphere in the electric field of strength E_0.

Thus, according to the Mee theory, the radiation scattered by the spherical grain coincides with the radiation from an identical sphere placed in an alternating electrostatic field oscillating with the frequency of the incident radiation. Therefore, our quasistatic model can be used not only to study the action of a microwave field on a dusty plasma but also to calculate the intensity of the scattered radiation. It is quite reasonable to assume that the scattered radiation corresponds to the dipole radiation of the system consisting of the charged dust grain and the surrounding plasma. The value and time dependence of this dipole moment can be found from numerical simulations.

The dipole moment of the grain–plasma system is not a mere result of the polarization of an uncharged metal sphere under the action of an external field, as is in the Mee theory. In our model, we take into account both the polarization of the charged spherical grain and the polarization of the surrounding plasma. The dipole moment that determines the scattered radiation in the Mee theory is only a part of the total dipole moment of the system. Its value is easy to estimate: the dipole moment calculated by the Mee theory for a microwave intensity of 120 W/cm^2 is equal to $p_0 = 1.7 \times 10^{-9}$ esu, which differs insignificantly from the calculated value of the total dipole moment (see Fig. 1). Under these conditions, the contribution from the polarization of the surrounding plasma to the total dipole moment is small and comprises ~10% of the total dipole moment.

The simulation results show that the external field can also cause the oscillations of the grain charge; however, this occurs at a considerably higher intensity of the incident radiation. Figure 2 demonstrates the calculated time dependences of some quantities for a microwave intensity of ~1.2 MW/cm^2. The intensity of the ionizer in these calculations is ten times higher than in Fig. 1; accordingly, the plasma electron density is ~2 × 10^{11} cm^{-3}.

It can be seen that the ion and electron fluxes onto the grain oscillate at a frequency twice as high as the frequency of the external electric field. This can be explained as follows: Over two half-periods of the external field oscillations, the total fluxes of charged plasma particles onto the dust grain are the same, but the particles fall onto the different hemispheres of the grain, depending on the direction of the electric field vector.

It can also be seen that the grain charge oscillates at a frequency that is also twice as high as the microwave frequency. The simulation results show that oscillations of the grain charge are observed when the microwave

intensity exceeds a threshold intensity of ~10 kW/cm². As the intensity increases, the oscillation amplitude of the dipole moment (Fig. 2b) also increases in comparison to the that in Fig. 1. This is explained by not only the plasma polarization under the action of the external alternating electric field but also the oscillations of the grain charge. However, even at such a high microwave intensity as in Fig. 2b, the total dipole moment is close to that calculated by the Mee theory. Therefore, the simulation results allow us to conclude that the scattering of microwave radiation by a complex plasma is primarily determined by the field-induced dipole moments of metal grains, whereas the contribution from the polarization of the ambient plasma is relatively small.

Nevertheless, the oscillations of the grain charge at the frequency 2ω (at the second harmonic of the incident radiation) lead to a qualitatively new effect that does not follow from the Mee theory: the appearance of the second harmonic in the scattered spectrum. Since the amplitude of the charge oscillations is small, the 2ω component of the dipole moment is hardly detectable against the background of the oscillations of the total dipole moment. The intensity of the scattered radiation at the frequency 2ω can be estimated as follows:

The simulation results (see Fig. 2a) show that, at a microwave intensity of ~1 MW/cm², the relative oscillation amplitude of the grain charge Q_d is $\Delta Q/Q_d = 10^{-3}$. In our quasistatic model, the dipole moment caused by the polarization of the grain charge is proportional to the charge itself; therefore, we have $\Delta D_d/D_d = \Delta Q/Q_d$. Since the dipole radiation intensity is equal to $I_n = \frac{4\omega^4 n^4}{3c^3}D_n^2$, the ratio between the intensities of scattered radiation at the second and first harmonics is $I_{2\omega}/I_\omega \sim 10^{-7}$. When obtaining this estimate, we took into account that the dipole moment caused by the polarization of the grain charge comprises ~10% of the total dipole moment of the system.

It should also be noted that the average charge of the dust grain in Fig. 2 is much larger than in Fig. 1 and amounts to nearly 10^5 au at a microwave intensity of ~1 MW/cm². As is known [5, 6], the dust grain charge determines the coupling parameter of a complex plasma and, consequently, the properties of the possible crystal dusty structures. Therefore, an important result of our simulations is the demonstration of the possibility of controlling the dust grain charge with the help of an external electric field.

A considerable number of studies are devoted to calculating the dust grain charge in complex plasma. A review of theoretical models of the charging processes is presented in [1]. Analytical studies usually employ a model in which the electric field distribution is described by the Debye–Hückel potential. Based on numerical simulations of dust grain charging in the absence of an external electric field, Pal' *et al.* [3]

arrived at the conclusion that, when the Debye approximation is used to describe the potential near the grain surface, it is necessary to replace the electron Debye length with a considerably greater length, because the ion distribution near the grain differs substantially from a Boltzmann one. This result was confirmed by Zobnin *et al.* [7], who also proved that the hydrodynamic plasma model is applicable even in the immediate vicinity of the grain surface, at least when the inequality $R_d/\lambda_i > 3$ (where λ_i is the ion mean free path) is satisfied. Vranies *et al.* [8] showed that, for dusty plasmas with a very large grain charge, the formula for the screened potential is more complicated; this result was obtained, however, under the assumption that the plasma particles obey a Boltzmann distribution near the grain surface. They also noted that the polarization of a metal grain in an external electric field should be taken into account when calculating the spatial distribution of the field.

Theoretical models suitable for analytical considerations turn out to be too simplified when calculating the electric field distribution near the grain surface. The problem under consideration here is even more complicated by the presence of a strong external electric field. This field leads to the redistribution of the charged particle density and the electric field, which increases sharply near the grain surface. Moreover, the available analytical models are time-independent, whereas in the problem under study, an important point is that the field oscillates at a high frequency. At present, numerical simulations are a unique method for calculating the electric field distribution near the grain surface.

The simulation results presented in Fig. 3 demonstrate a rather complicated character of the spatial distribution of the electric field. At the instant shown in Fig. 3c, when the external alternating field is close to zero, the spatial distributions of the radial components of the electric field differ insignificantly from one another for different azimuthal angles θ (the angle is counted from the direction of the external field). It can be seen that the field is fairly high at the grain surface. Note that these distributions are similar to the electric field distribution in the cathode sheath of a glow discharge.

As the external field increases, the field distribution can change radically, depending on the ratio between the external electric field and the dust grain charge, which determines the field strength at the grain surface. Figure 3b corresponds to the case where the external electric field is high and the field profile along the ray $\theta = 0$ is substantially redistributed. Note, the external field is not merely added to the grain's field, but the field profile is radically redistributed and becomes similar to the anode sheath of a glow discharge.

Figure 3a corresponds to an intermediate case in which the external field is even somewhat higher than in the previous case, but the dust grain charge is also larger. As a result, the radial component of the electric
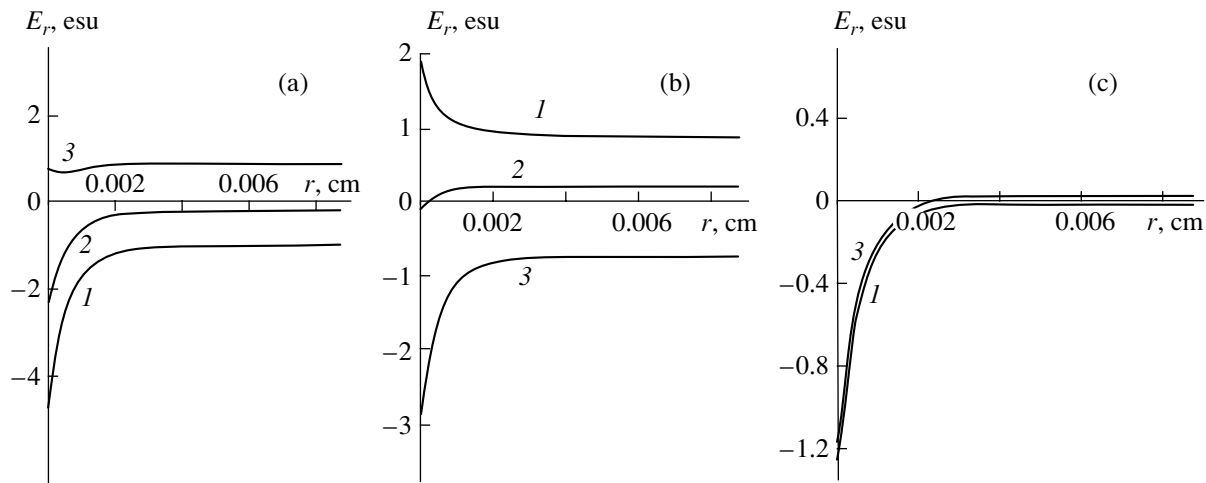
Fig. 3. Profiles of the radial component of the electric-field vector at different azimuthal angles (θ = (*1*) 0, (*2*) 0.46π, and (*3*) 0.86π) and different microwave fields E_{ex} and grain charges Q: (a) E_{ex} = −0.999 esu and Q = −5.22 × 10^3 au, (b) E_{ex} = 0.862 esu and Q = −1.9 × 10^3 au; and (c) E_{ex} = −2.21 × 10^{-2} esu and Q = −3.66 × 10^3 au.

field at a certain azimuthal angle (in this case, at an angle of $\theta = 0.86\pi$) does not increase as the grain surface is approached; i.e., the field distribution is almost uniform.

Figure 4 shows the density distribution of the charged plasma particles near a charged dust grain. A characteristic feature of the ion density distribution in this case is that the ion density is almost constant up to the grain surface. Such behavior is quite different from the cases where an external field is absent or a steady-state electric field is applied; in both these cases, the ion density decreases as the grain surface is approached (see, e.g., [2]). The constant ion density profile may be explained by the alternating motion of ions from the dust grain and backward in the alternating external electric field. In such a situation, the ion flux has no time to reach its steady-state value, because the ion velocity is determined only by the electric field strength. As a result, the ions are mixed and their density near the dust grain equalizes.
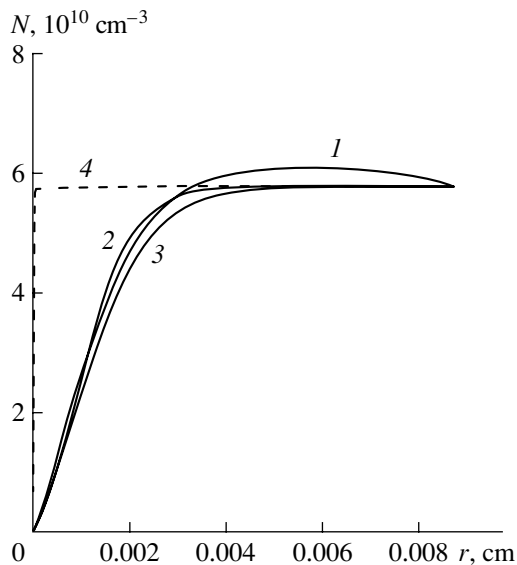

Fig. 4. Densities of charged plasma particles as functions of the distance from the grain surface: electron density profiles for azimuthal angles of θ = (*1*) 0, (*2*) 0.46π, and (*3*) 0.86π and (*4*) the ion density distribution (almost independent of the azimuthal angle).

4. CONCLUSIONS

The effect of microwave radiation on a complex plasma has been studied using numerical simulations. It is shown that the problem can be solved in a quasistatic model. The simulations have been performed for a microwave frequency higher than the plasma frequency, because, at lower frequencies, radiation does not penetrate into the plasma. It is shown that, in choosing the radiation frequency at a fixed power of the ionization source, the effect of depletion of the electron component due to the absorption of electrons by dust grains should be taken into account. In this way, it is possible to expand the frequency range in experimental studies.

Our simulations have shown that the main contribution to the dipole moment of a metal grain in plasma comes from the polarization of the grain in the microwave field. This contribution is described by the Mee theory. The higher the microwave intensity, the larger the contribution from radiation scattering related to the charge polarization on dust grains. The intensity of the scattered radiation is shown to increase nonlinearly with increasing microwave field. At high microwave intensities, the grain charge is found to oscillate at the second harmonic of the incident radiation. This results

in the appearance of the second-harmonic component in the scattered spectrum.

It is shown that such an important parameter as the dust grain charge increases substantially (by more than one order of magnitude) as the microwave intensity increases to ~1 MW/cm^2. This rather simple method of controlling the grain charge can be used in experimental studies of plasma crystals.

It is found that, at a high microwave intensity, the distribution of the electric field near a dust grain changes so radically that the field component normal to the grain's surface can even change its sign. This effect should substantially influence the attraction forces between grains in a dusty plasma.

ACKNOWLEDGMENTS

REFERENCES

1. V. N. Tsytovich, G. E. Morfill, and H. Thomas, Fiz. Plazmy **28**, 675 (2002) [Plasma Phys. Rep. **28**, 623 (2002)]

2. Yu. V. Petrushevich, Fiz. Plazmy **29**, 508 (2003) [Plasma Phys. Rep. **29**, 473 (2003)].

3. A. F. Pal', D. V. Sivokhin, A. N. Starostin, *et al.*, Fiz. Plazmy **28**, 32 (2002) [Plasma Phys. Rep. **28**, 28 (2002)].

4. M. Born and E. Wolf, *Principles of Optics* (Pergamon, Oxford, 1969; Nauka, Moscow, 1970).

5. A. P. Nefedov, O. F. Petrov, and V. E. Fortov, Usp. Fiz. Nauk **167**, 1215 (1997) [Phys. Usp. **40**, 1163 (1997)].

6. V. E. Fortov, A. G. Khrapak, S. A. Khrapak, *et al.*, Usp. Fiz. Nauk **174**, 495 (2004) [Phys. Usp. **47**, 447 (2004)].

7. A. V. Zobnin, A. P. Nefedov, V. A. Sinel'shchikov, and V. E. Fortov, Zh. Éksp. Teor. Fiz. **118**, 554 (2000) [JETP **91**, 483 (2000)].

8. J. Vranies, M. Y. Tanaka, B. P. Pandey, and M. Kono, Phys. Rev. E **66**, 037401 (2002).

Translated by N.F. Larionova

Effect of the Global Topology of the Interplanetary Magnetic Field on the Properties of Impulsive Acceleration Processes in Distant Regions of the Earth's Magnetospheric Tail

E. E. Grigorenko[1, 2], L. M. Zelenyi[2], A. O. Fedorov[3], and J.-A. Sauvaud[3]

[1]*Skobeltsyn Institute of Nuclear Physics, Moscow State University, Vorob'evy gory, Moscow, 119899 Russia*
[2]*Institute for Space Research, Russian Academy of Sciences, Profsoyuznaya ul. 84/32, Moscow, 117810 Russia*
[3]*Centre d'Etude Spatiale des Rayonnements, 4346 31028 Toulouse, France*
Received January 22, 2004; in final form, March 17, 2004

Abstract—The paper is devoted to a statistical study of high-speed ion beams (beamlets) observed by the *Interball-1* and *Interball-2* satellites in the boundary region of the plasma sheet of the geomagnetic tail and in the high-latitude auroral regions of the Earth's magnetosphere. Beamlets result from nonlinear acceleration processes occurring in the current sheet in the distant regions of the geomagnetic tail. They propagate toward the Earth along the magnetic field lines and are detected in the boundary region of the plasma sheet and near the high-latitude boundary of the plasma sheet in the auroral region in the form of short (with a duration of 1–2 min) bursts of high-energy (with energies of about several tens of keV) ions. The sizes of the latitudinal zones where the beamlets are localized in the tail and in the auroral region are determined using the epoch superposition method. The relationship between the frequency of beamlet generation in the boundary region of the plasma sheet and the prehistory of the direction of the interplanetary magnetic field (the magnitude of a clock angle) is investigated. It was established that this direction exerts a global effect on the beamlet generation frequency; moreover, it was found that the beamlet generation frequency in the midnight local time sector of the tail and at the flanks depends differently on the direction of the interplanetary magnetic field. In the midnight sector, the beamlets are observed at almost all directions of the interplanetary field, whereas the frequency of their generation at the flanks is maximal only when the interplanetary magnetic field has a large *y* component. © *2005 Pleiades Publishing, Inc.*

1. INTRODUCTION

Since its discovery in the late 1960s, the geomagnetic tail of the Earth's magnetosphere has been attracting attention as one of the most complicated and interesting objects in space physics. The tail forms at the Earth's night side as a result of the stretching of the geomagnetic field lines by the solar wind (SW) plasma fluxes, which are permanently flowing from the Sun (Fig. 1). Hence, the geomagnetic tail can be regarded as *mobilis in mobile*, because it is a very dynamic magnetoplasma structure capable of responding to any changes in the external (interplanetary) medium, such as changes in the SW parameters (the SW plasma velocity and density) and in the direction of the interplanetary magnetic field (IMF). From the standpoint of plasma physics, the geomagnetic tail is a huge self-consistent plasma configuration that keeps its equilibrium only at the expense of the currents flowing within it. It is characterized by the coexistence of various plasma regimes and the occurrence of different nonlinear processes on different spatiotemporal scales. Some processes develop as a result of a direct response of the system to changes in the interplanetary medium, and the others occur after a certain time interval during which

the energy that comes with the SW into the Earth's magnetosphere and that is accumulated in the geomagnetic tail reaches a critical level. This energy is released either in an explosive manner to give rise to magnetic substorms or in small amounts, by accelerating the particles. In the latter case, the tail can persist in a quasisteady state for a long time. Such acceleration processes, which occur in distant tail regions (at distances of more than $100R_E$ from the Earth, where R_E is the Earth's radius), manifest themselves as transient plasma structures observed very close to the boundary between the quasi-isotropic hot medium of the plasma sheet (PS) and a comparatively vacuous (at least, devoid of hot plasma) high-latitude tail region. The existence of this transient region, called the PS boundary layers (PSBL), and its role in the energy and momentum transfer from the distant tail regions to the inner magnetosphere were recognized in the middle of 1970s. It was originally thought that the onset of transient plasma structures at the PS boundary is associated with the development of a substorm, i.e., that the PSBL exists only during active periods [1]. Later, numerous observations carried out in the geomagnetic tail by the *ISEE-1* and *ISEE-2* satellites have revealed that the
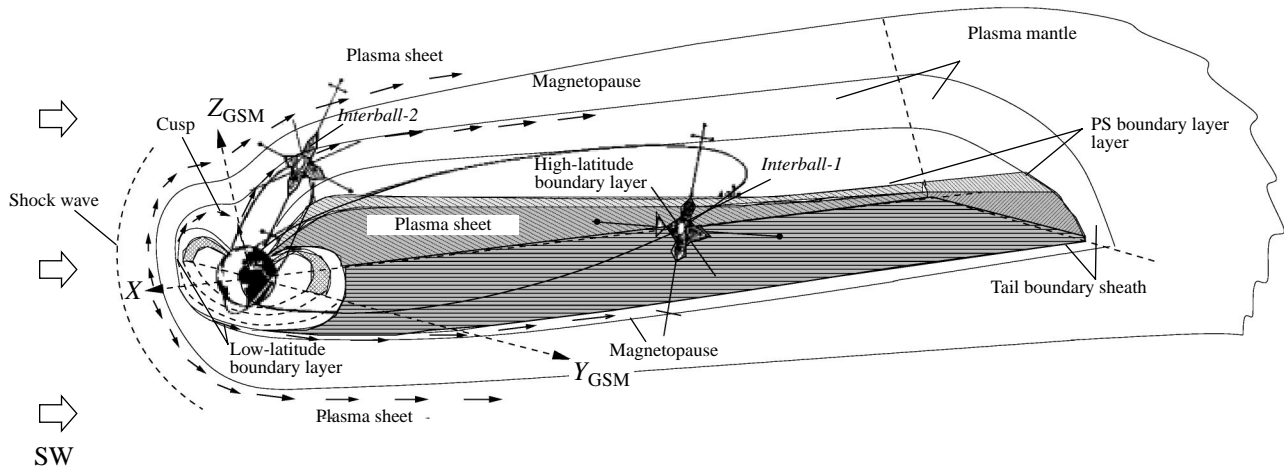
Fig. 1. Schematic structure of the Earth's magnetosphere and schematic positions of the orbits of the *Interball-1* and *Interball-2* satellites. The *X* axis of the GSM coordinate system lies in the ecliptic plane and points in the positive direction along the Earth–Sun line, the *Z* axis is directed along the axis of the geomagnetic dipole, and the *Y* axis is such that the basic vectors form a right-hand triple.

PSBL is a permanently existing domain of the tail, because it is also observed to be present during long-term quiescent periods [2–6].

The structures that are most often observed within the PSBL are short-duration (1–2 min) high-energy (with energies E of about several tens of keV) ion beams, called beamlets, which propagate toward the Earth along the magnetic field lines [7–9]. According to the theory, the beamlets are generated due to nonadiabatic ion acceleration in the current sheet of the distant tail regions (at distances of more than $100R_E$ from the Earth). The possibility of nonadiabatic ion acceleration in current sheets (in regions where the normal magnetic-field component B_z is small) was considered in early studies (see, e.g., [10]). In the late 1980s, the theory of nonadiabatic ion acceleration received additional impetus [7, 11] from numerous new experimental data indicating that, in the PSBL, there exist ion distributions with highly regular structures in physical and phase spaces. It was proved that, in the region where the magnetic field changes its sign, particle acceleration is resonant in character [7, 8, 12, 13]. The behavior of a particle after its interaction with the current sheet is determined by the value of the so-called adiabaticity parameter $K = \dfrac{B_n}{B_0}\sqrt{\dfrac{L}{r_0}}$, where L is the sheet thickness, r_0 is the particle gyroradius, B_n is the normal component of the magnetic field of the current sheet at the place of acceleration, and B_0 is the magnetic field strength in the high-latitude tail region.

Depending on the K value, the particles either can be strongly scattered and be trapped by the current sheet or they can leave the sheet, moving along open (Speiser) trajectories in the PSBL [8, 14] (Fig. 2). The nonmonotonic dependence of scattering on the parameter K leads

to a structuring of the plasma in phase space. However, numerical simulations of the acceleration of a large particle ensemble in a current sheet were hindered by the fact that, because of the complexity of the magnetic field topology in the geomagnetic tail, neither the MHD methods nor the guiding-center approximation can provide an adequate description of the motion and dynamics of the tail ions, which exhibit a pronounced nonadiabatic behavior, especially in the region where the magnetic field reverses its direction [7–9, 14–16]. The nonadiabatic interaction of the ions with the current sheet in the magnetospheric tail and the resulting ion distributions in the PSBL and PS were described for the first time in [8, 9] by the method of large-scale kinetic simulations. It was found that the nonadiabatic interaction of the ions with the current sheet results in the formation of two ion populations, one of which consists of the ions that were strongly scattered and were trapped within the central plasma sheet (CPS) and the other consists of the ions that were scattered only slightly in the current sheet and move at a high speed toward the Earth along the magnetic field lines (Fig. 3). It is the ions of the second population that form the beamlets detected within the PSBL. Numerical simulations also revealed that the PSBL has a complicated structure: there are beamlets that move toward the Earth, beamlets that are reflected from the Earth, and bidirectional beams, which form as a result of the interference between direct (downward propagating) and reflected beamlets (Fig. 4). These results were confirmed by numerous experimental investigations carried out with the *Galileo*, *Geotail*, *Wind*, and *Interball* satellites [17–19]. Hence, the complicated structure of the PSBL reflects the nonlinear self-consistent magnetoplasma configuration of the magnetospheric tail, which is in stable equilibrium because of the balance between the plasma inflow from the source in the plasma mantle and
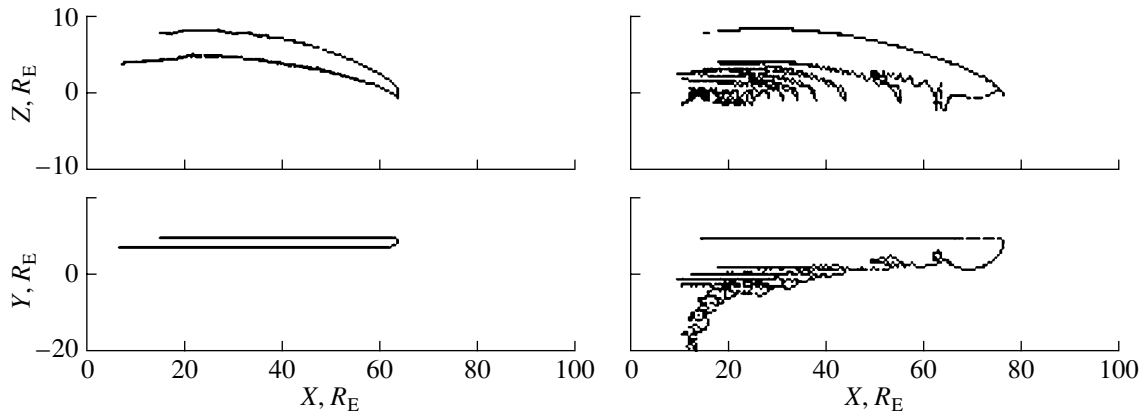
Fig. 2. Calculated trajectories of the particles that move toward the current sheet, interact with it, and then are convected to the Earth [7]. The projections of the particle trajectories onto the (X, Y) and (X, Z) planes are shown. The two left panels of the figure display the projections on the (X, Z) and (X, Y) planes of a representative Speiser trajectory of a particle that interacts with the current sheet in far regions of the geomagnetic tail, leaves the sheet, and moves toward the Earth in the PSBL. The two right panels display the projections on the (X, Z) and (X, Y) planes of the trajectory of a particle trapped within the current sheet.
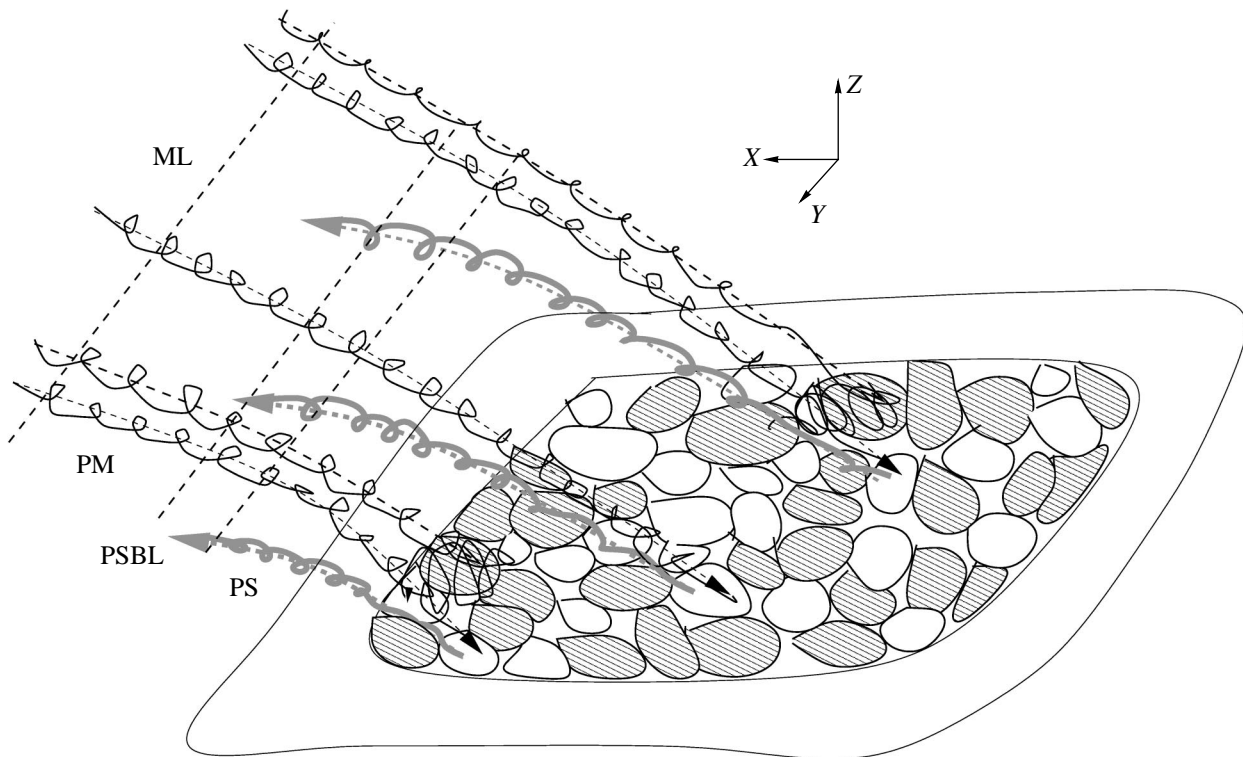

Fig. 3. Schematic illustration of the generation of beamlets in localized regions of the current sheet of the distant magnetospheric tail. The particles move from the plasma mantle (PM) and interact with the current sheet. Depending on the conditions in the interaction region, the particles either are strongly scattered and are trapped within the current sheet (hatched ovals) or they come into the regions of slight scattering (open ovals), where they are accelerated and move toward the Earth along the magnetic field lines to form beamlets that are detected within the PSBL or in the magnetotail lobe (ML) that is adjacent to the PSBL.

the loss of particles due to their nonadiabatic motion in the tail. Quasi-equilibrium oscillations that occur in the system as a result of instantaneous imbalances between the inflow of the particles and their loss have a period of about 1–5 min [20]. This corresponds to the characteristic time scales on which the beamlets are observed

in the PSBL. The question that remains open is whether the onset of beamlets in the PSBL is a consequence of the release of an excess energy that comes from outside and is accumulated in the tail (or, in other words, a consequence of a certain prehistory in the interplanetary medium, in particular, of a certain direction of the IMF) or whether this is an internal response (characteristic of the lifestyle of the geomagnetic tail) that the system makes in order to eliminate the above imbalances. The theoretical and experimental results obtained by now confirm that the structurization of the ion distributions observed in the PSBL is a permanent feature of the tail plasma [21] and that the onset of beamlets is independent of the level of geomagnetic activity [19]. However, systematic studies of the relation between the observations of beamlets in the tail and the conditions in the interplanetary medium have not yet been made. In the present paper, an attempt is made to apply a statistical approach to find whether or not the onset of beamlets in the PSBL is related to a certain direction of the IMF prior to their generation. This relationship should indeed exist, if for no other reason than the particles that move nonadiabatically in the current sheet are in fact accelerated by the tail's electric field as a result of the penetration of the interplanetary electric field $\mathbf{V}_{SW} \times \mathbf{B}$ (where V_{SW} is the solar wind speed and $\mathbf{B}$ is the IMF strength) into the Earth's magnetosphere. At a southward IMF, the electric field within the tail is fairly strong: it is directed across the tail from dawn to dusk and can nonadiabatically accelerate the moving particles to energies on the order of several tens of keV. At a northward IMF, the tail is free of such an electric field. Nevertheless, there is evidence that the electric field is always present in the magnetosphere owing to the viscous friction between the two plasmas having different properties: the SW plasma and the plasma of the boundary sheath of the magnetosphere. This electric field is, however, far weaker. We can, therefore, anticipate that, at a northward IMF, either nonadiabatic ion acceleration in the magnetospheric tail is less efficient or the ions are not accelerated at all.

The transient plasma structures that move in the PSBL toward the Earth partially precipitate into the auroral region. The remaining part of the plasma is reflected from the strong magnetic field regions near the Earth, returns to the tail, and later becomes isotropized. Different structures observed at the PS boundary in the auroral region have been studied in many papers. Among these structures, we should mention, first of all, the dispersive structures: the so-called velocity dispersed ion structures (VDIS) and time-dispersed ion structures (TDIS). VDIS, being typical spatial structures, are observed for tens of minutes. It is thought that such structures form in far tail regions and their internal latitudinal dispersion results from the $\mathbf{E} \times \mathbf{B}$ drift of the ions as they fly at different velocities from their source to the Earth [22]. TDIS are time-of-flight structures whose source is in the equatorial plane at a comparatively small distance from the Earth: $(7–40)R_E$. The
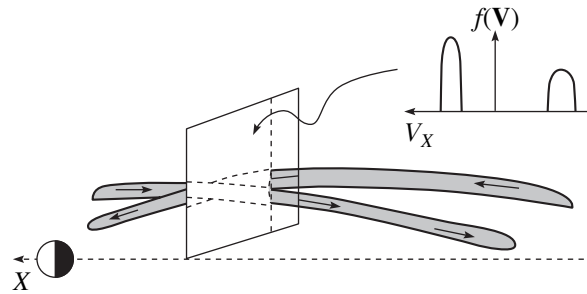

Fig. 4. Schematic illustration of the interference between two beamlets: a direct beamlet propagating from the tail toward the Earth and a reflected beamlet reflected in the strong magnetic field region near the Earth and propagating in the opposite direction toward the tail. The ion velocity distribution function measured in the region where the two beamlets interfere is also shown schematically.

onset of such structures in the auroral region is, as a rule, associated with a substorm [23, 24]. Here, however, we are going to describe observations of one more type of structures. We consider these structures separately because they differ from those just mentioned: in contrast to TDIS, they are also observed during absolutely quiescent periods and, in contrast to VDIS, their duration is short (no longer than several minutes) and they have essentially no internal dispersion. This is why we call these structures nondispersive structures. In what follows, we will carry out a comparative statistical analysis of nondispersive structures in the auroral region and beamlets observed in the tail. We will also try to prove that the phenomena observed in these two magnetospheric regions have the same nature, i.e., that the relevant structures are beamlets.

In Section 2, we briefly describe the experimental data from the *Interball-1* and *Interball-2* Earth orbiting satellites that are analyzed in our work. In Section 3, we present the results from satellite observations of beamlets in the PSBL and near the high-latitude PS boundary in the auroral region. In Sections 4 and 5, we statistically investigate the spatial distributions of beamlets and try to clarify whether the prehistory of the IMF direction affects the frequency of beamlet generation in the midnight sector of the magnetosphere and at the flanks. In Section 6, we discuss the results obtained and outline the questions that remain to be answered.

2. EXPERIMENTAL DATA

The *Interball-1* satellite was launched on August 3, 1995. The primary goal of its mission was to investigate the boundary regions of the Earth's magnetosphere (in particular, the PSBL), which are extremely important and interesting from the standpoint of plasma physics. The satellite orbit was an ellipse with an initial apogee of $30R_E$, a perigee of 800 km, and an inclination of $63°$ to the Earth's equatorial plane. This orbit provided
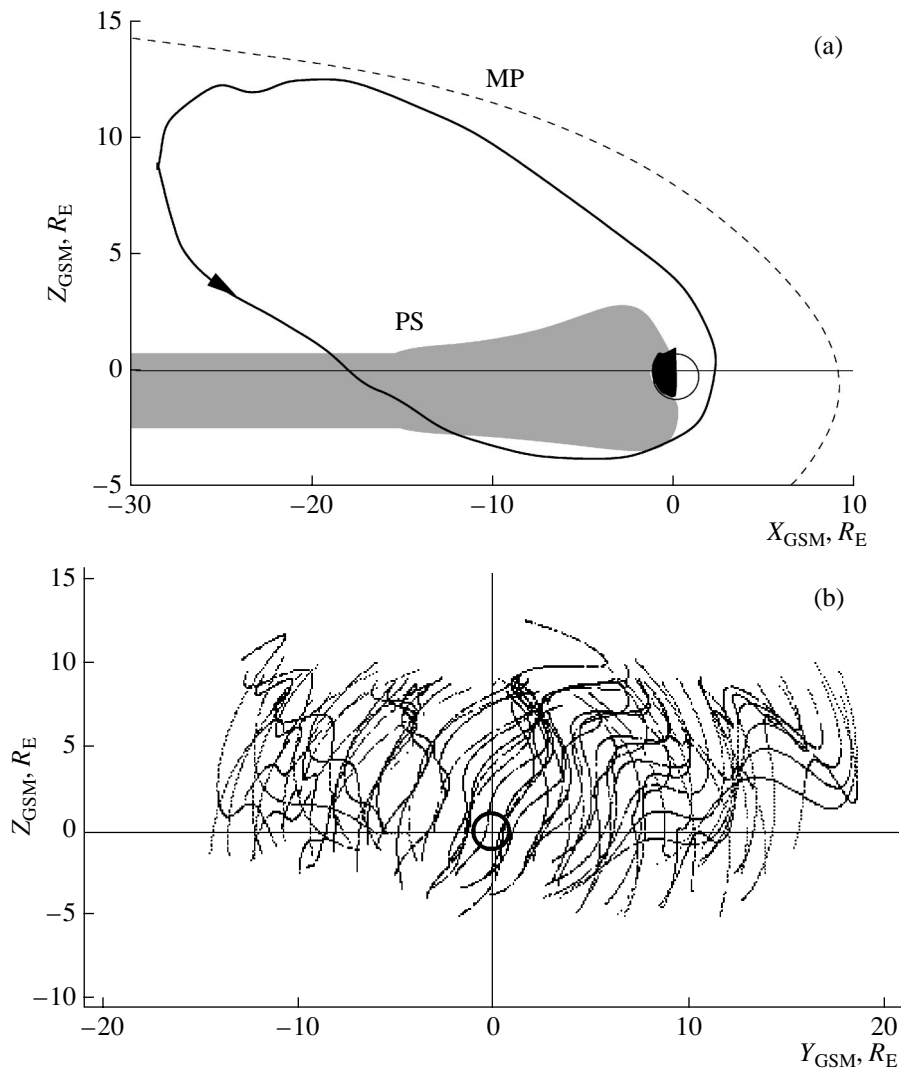
Fig. 5. (a) Representative projection of one of the actual orbits of the *Interball-1* satellite onto the XZ_{GSM} plane (the dashed curve shows the magnetopause (MP)) and (b) projections of all the *Interball-1* orbits analyzed in the present study onto the YZ_{GSM} plane.

long-term observations in the high-latitude tail regions and within the PSBL. In this sense, *Interball-1* offered an obvious advantage for the study of the PSBL over other space vehicles that performed measurements in the tail at that time. The satellite rotated about an axis directed toward the Sun, the rotation period being 118 s. An example of an actual orbit of *Interball-1* in the XZ plane is shown in Fig. 5a. The satellite orbit covered the tail cross section fairly widely; this provided measurements at the flanks at distances from $-20R_E$ to $20R_E$ in the Y direction (Fig. 5b). During each passage through the tail, *Interball-1* crossed the high-latitude tail region, the PSBL, and the PS. We analyzed 70 crossings of the PSBL by *Interball-1* at a distance of $X \sim -25R_E$ from the Earth. We used the measurement data from Russian devices, specifically the data on the magnetic field obtained with a MIF magnetometer [25]

and on the plasma parameters obtained with a CORALL ion spectrometer [26]. The spectrometer provided measurements of the three-dimensional ion distribution function (without mass resolution) within a time of about 2 min (which was determined by the period of rotation of the satellite around its axis). The total ion energy spectrum was measured in the range 0.03–25 keV (in 32 steps) within a time of 3.6 s. The field of view of the spectrometer, $5° \times 110°$, was divided into five sectors.

Measurements in the auroral region were carried out by the *Interball-2* satellite. The data on plasma were obtained with a Russian–French ION spectrometer [27]. We have analyzed 52 crossings of the high-latitude PS boundary by *Interball-2* at altitudes of about $\sim 3R_E$ under quiescent geomagnetic conditions. We also used the data on the IMF from the CDA WEB database

that were obtained by the *Wind* satellite (http://cdaweb.gsfc.nasa.gov). In analyzing the measurement data from the *Wind* satellite, we took into account the times of propagation of the SW from the position of this satellite to the positions of the *Interball-1* and *Interball-2* satellites.

3. EXPERIMENTAL OBSERVATIONS OF BEAMLETS

3.1. Observations of Beamlets in the Magnetospheric Tail

In the spectrograms of the magnetospheric tail that were measured in the PSBL, the beamlets look like short bursts of high-energy (with energies E of about several tens of keV) ions with a duration of about 1–2 min. As a rule, within an individual beamlet event, no velocity dispersion was observed. In all observations, the beamlet events in the PSBL were accompanied by a reduction in the magnetic field strength (the diamagnetic effect). The distribution functions of the beamlets in velocity space have the characteristic shape of a Peruvian bean [19, 28–31]. In spectrograms, the beamlets are seen to be isolated from the PS or to occur just at the PS boundary. In this sense, since all the *Interball-1* measurements were carried out at a single point, we cannot definitely establish whether the beamlets were actually isolated from the PS or they were spatially confined to the PS and, thus, were phenomena that occur only at the PS boundary. (Later, the measurement data from four artificial satellites launched as part of the CLUSTER project confirmed that the beamlets were isolated from the main structure of the PS. This result will be discussed in our future paper that is being prepared for publication.) Figure 6 shows a representative example of beamlets observed by the *Interball-1* satellite in the magnetospheric tail. The satellite moved from the high-latitude tail region toward the neutral sheet (NS). In the spectrogram measured by a tail-oriented detector when the satellite was still within the high-latitude region (as is seen from the data on the magnetic field), we observe several short ion beams (beamlets) with energies of about 10 keV and a duration of about 1 min, accompanied by a reduction in the magnetic field strength. From the shape of the distribution function, we see that the beamlets move very rapidly toward the Earth, preferentially along the magnetic field lines. Unfortunately, the dead angle of the KORALL spectrometer was just along the rotation axis (the Sun–Earth line); this is why, in the sector corresponding to the velocity exactly aligned with the magnetic field, the distribution function is not plotted.

3.2. Observation of Nondispersive Structures in the High-Latitude Auroral Region

An observation made by *Interball-2* from 21:02 to 21:09 on Aug. 26, 1997, is illustrated in Fig. 7, which shows the nondispersive structure of the ions precipi-
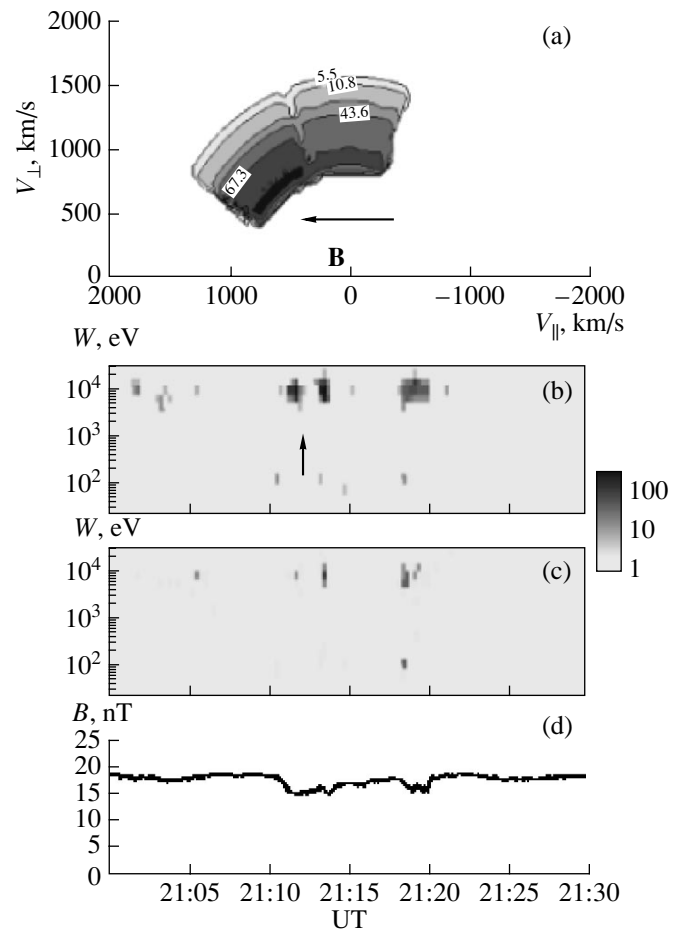
Fig. 6. Representative beamlet observed by the *Interball-1* satellite in the high-latitude part of the Earth's magnetospheric tail: (a) the characteristic shape of the ion velocity distribution function measured within a time of 2 min and plotted in the parallel–perpendicular (to the magnetic field) ion velocity coordinates, (b) a representative ion spectrogram measured by a tail-oriented detector and plotted in the time–energy coordinates (the counting rate in s^{-1} is shown by shades of gray in accordance with the scale given on the right of the panel), (c) a spectrogram measured by a Sun-oriented detector, and (d) the time evolution of the magnetic field strength B. The arrow shows the beamlet.

tated into the auroral region near the high-latitude PS boundary. The precipitation event lasted for seven minutes, a time that is extremely long for this class of structures. The observation was made under absolutely quiescent geomagnetic conditions. An interesting feature of such events is that they are accompanied by the precipitation of comparatively cold electrons with energies of $E \sim 300$–400 eV, which are lower than the energies of the electrons in the PS (~1 keV or more). This is more evidence that the events in question actually occur in the boundary region, i.e., outside the PS. Such events resemble the beamlets detected in the magnetospheric tail. In the next section, we will try to prove that the beamlets in the tail and nondispersive events in the
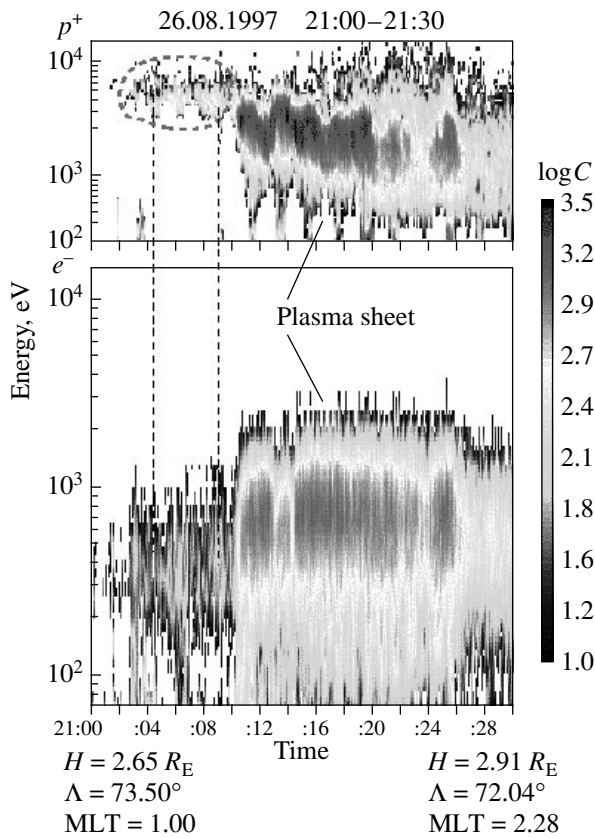
p^+ 26.08.1997   21:00–21:30

Fig. 7. Example of a nondispersive structure observed by the *Interball-2* satellite near the high-latitude PS boundary in the auroral region: an ion (top) and electron (bottom) spectrograms plotted in the time–energy coordinates. At the bottom of the figure, the positions of the *Interball-2* satellite at the beginning and the end of the observational time interval are also given (here, *H* is the radial distance from the Earth, Λ is the invariant latitude, and MLT is the magnetic local time). The dashed lines show the interval of interest where beamlets are observed: to the left, there are empty lobes, and to the right, there is the hot dense plasma sheet. The counting rate C (in s^{-1}) is shown by shades of gray in accordance with the scale given on the right of the figure.

auroral region actually belong to the same class of structures.

4. STATISTICAL INVESTIGATIONS OF BEAMLETS OBSERVED IN THE TAIL AND NONDISPERSIVE STRUCTURES OBSERVED IN THE AURORAL REGION

In order to carry out a statistical analysis of the spatial distributions of beamlets in the tail and of nondispersive structures in the high-latitude area of the auroral region, we started by considering the time intervals during which the *Interball-1* and *Interball-2* satellites crossed the corresponding magnetospheric zones in the midnight sector ($|Y_{GSM}| \leq 7 R_E$ for the tail, and a local time interval of $21.00 < \text{MLT} < 03.00$ for the auroral

region) and during which the geomagnetic conditions were quiescent (the AE index was less than 100 nT). As a result, we have chosen 42 crossings of the PSBL in the magnetospheric tail and 52 crossings of the high-latitude PS boundary in the auroral region.

Figure 8 shows spectrograms obtained by applying the epoch superposition method to all of the chosen crossings of the PSBL in the tail. The spectrograms are plotted in the *dZ*–energy coordinates, where *dZ* is the distance between the satellite and the PS boundary (along the Z_{GSM} direction). The PS boundary was determined separately for each crossing of the PSBL according to the following criteria: (i) the ion temperature is $T_i > 1$ keV and (ii) the counting rates in all five polar channels of the CORALL spectrometer should be approximately the same (the difference between the rates should be no more than 30%). Having determined the PS boundary for each particular crossing, we assigned the value $dZ = 0$ to it; as a result, the range $dZ > 0$ corresponded to the high-latitude part of the tail, and the range $dZ < 0$ corresponded to the internal part of the PS. Figure 8a refers to the data from a tail-oriented detector, and Fig. 8b displays the data from a Sun-oriented detector. On the side of the high-latitude region in Fig. 8a, we clearly see beamlets moving from the tail. We thus can statistically estimate the size of the region (in the Z_{GSM} direction) where the beamlets are observed: this size is about $0.5 R_E$.

An analogous method was applied to the crossings of the auroral region by the *Interball-2* satellite. Figures 9b and 9c show the ion and electron spectrograms, respectively, plotted in the *d*Λ–energy coordinates, where *d*Λ is the distance between the PS boundary and the satellite in the latitudinal direction. The PS boundary was also determined separately for each of the crossings, and the value $d\Lambda = 0$ was assigned to it. Thus, the range $d\Lambda > 0$ corresponded to the latitudinal zone above the PS, and the range $d\Lambda < 0$ corresponded to the internal part of the PS. The PS boundary in the auroral region is also clearly seen in the electron spectrogram. The size of the latitudinal zone occupied by nondispersive structures was estimated from the auroral data and was found to be about ~0.8°.

In order to compare the size of the tail region occupied by beamlets with the size obtained from the auroral data, we projected all the crossings of the PSBL in the tail onto the ionosphere (with allowance for convection) and thereby determined the invariant latitude Λ for each of the positions of *Interball-1* in the tail. We then again applied the epoch superposition method to all the crossings of the PSBL but plotted Fig. 9b in terms of *d*Λ (rather than *dZ*). As a result, the size of the latitudinal zone where the beamlets were localized in the tail was estimated to be 0.5° (see Fig. 9a).

Next, we found out whether or not the mean energy of a beamlet depends on the height of its localization region above the NS or, equivalently, on its invariant latitude. To do this, all the beamlets observed in the tail
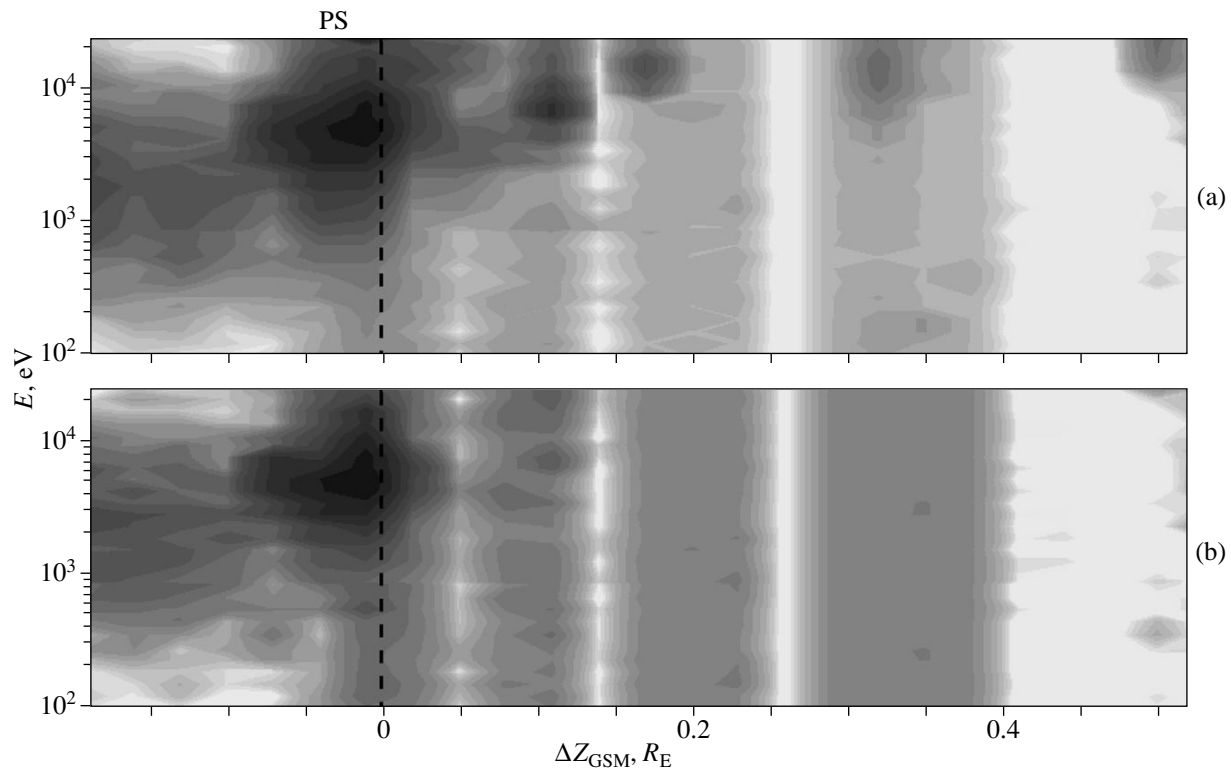
Fig. 8. Ion spectrograms obtained by applying the epoch superposition method to 42 crossings of the PSBL by the *Interball-1* satellite during quiescent geomagnetic periods: (a) the data from the tail-oriented detector, and (b) the data from the Sun-oriented detector. The spectrograms are plotted in the ion energy–ΔZ coordinates (where ΔZ is the distance between the satellite and the PS boundary). The PS boundary is shown by the dashed curve. The counting rate in the detectors is shown by shades of gray in accordance with the scale given in Fig. 6.

during the above crossings of the PSBL (in the midnight sector and under quiescent geomagnetic conditions) and nondispersive structures observed in the auroral region during approximately the same periods were plotted in the same figure in the Λ–energy coordinates. In plotting the figure, the invariant latitudes for the beamlets observed in the tail were determined by the above method. All the events were divided into two groups in accordance with the mean direction of the IMF. The IMF direction was averaged over 1.5 h before the observation of each of the beamlets. In Fig. 10a, we plotted the mean energy of the tail beamlets (gray circles) and of the auroral events (black circles) versus the latitude Λ for a southward IMF. We can see that, in this case, the mean energies of the beamlets and nondispersive auroral events increase with Λ. The events observed at a northward IMF are illustrated in the same manner in Fig. 10b. In this case, the energy and latitude are seen to be in inverse relationship to one another: the higher the latitude, the lower the energy of the beamlets and auroral events.

Figure 11 shows how the probability distributions of nondispersive auroral structures (Fig. 11a) and tail beamlets (Fig. 11b) depend on the duration of these events. We see that the distributions in both of the magnetospheric regions are similar to one another: the

mean duration of beamlets in the tail and of nondispersive structures in the auroral region is about 1 min, and the high-energy tails of the distributions are well approximated by the power law $F(\tau) \sim \tau^{-0.5}$, where τ is the duration of the event.

Hence, the beamlets observed in the tail and nondispersive structures detected in the auroral region have much in common. Specifically, the beamlets and nondispersive structures are observed near the high-latitude PS boundary; moreover, the sizes of the latitudinal zones where they are localized in both magnetospheric regions are comparable in magnitude. In addition, these two types of structures have approximately the same energy and duration and possess similar dependences of the energy on the latitude at south- and northward IMFs. These factors allow us to conclude that nondispersive structures observed in the auroral region are beamlets precipitating from the tail. Hence, beamlets are stable plasma structures because they reach the Earth and then partially precipitate near the high-latitude PS boundary in the auroral region and are partially reflected in the strong magnetic field region near the Earth, moving back toward the tail and forming bidirectional beams that are detected in the PSBL.
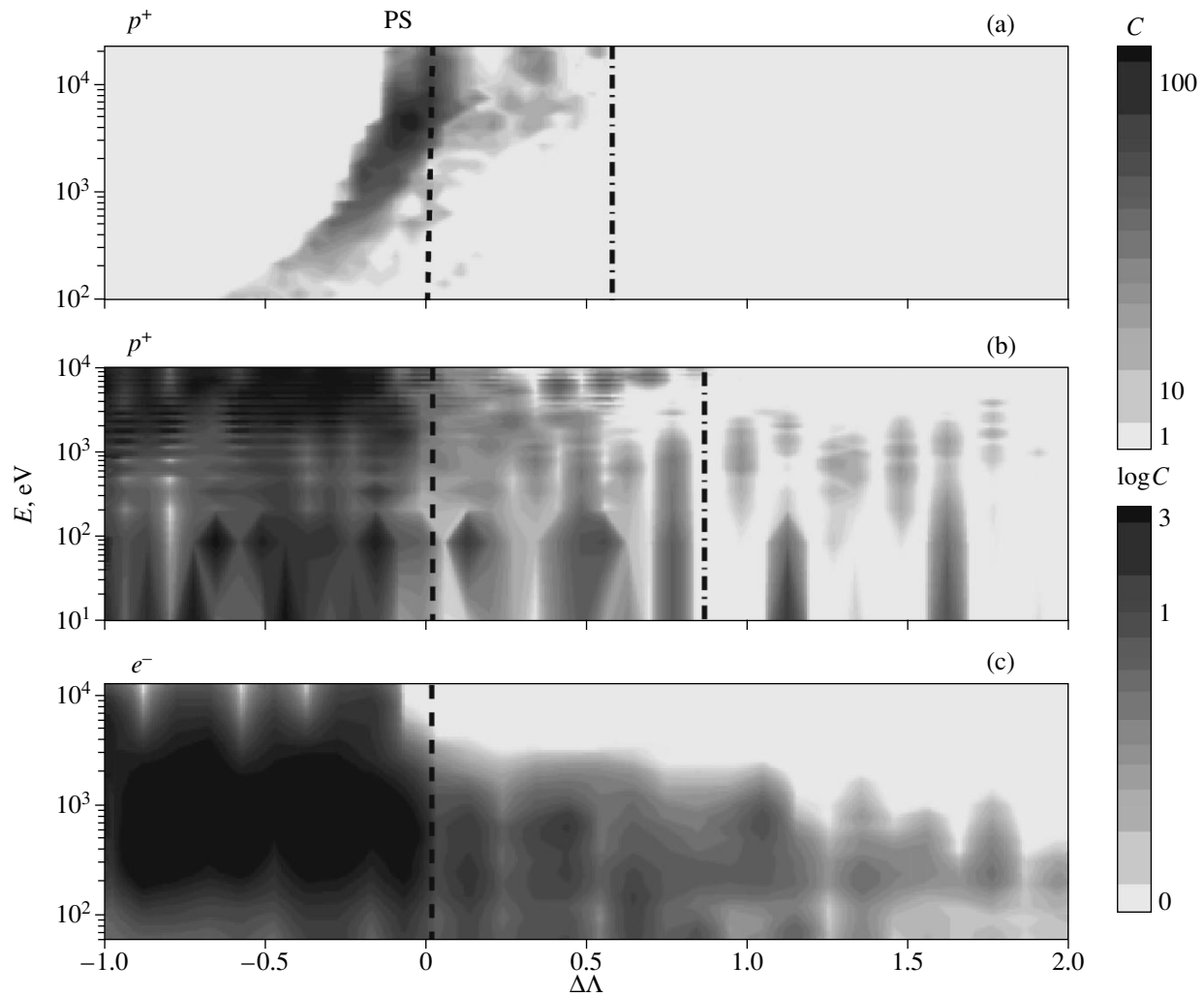
Fig. 9. (a) Ion spectrogram of Fig. 7, projected onto the auroral region (with allowance for convection); (b) ion spectrogram obtained by applying the epoch superposition method to 52 crossings of the high-latitude PS boundary in the auroral region by the *Interball-2* satellite during quiescent geomagnetic periods; and (c) electron spectrogram obtained by applying the epoch superposition method to the same crossings of the auroral region by the *Interball-2* satellite as those illustrated in plot (b). The spectrograms are plotted in the energy–$\Delta\Lambda$ coordinates, where $\Delta\Lambda$ is the distance between the *Interball-1* satellite and the PS boundary in the latitudinal direction. The counting rate C (in s^{-1}) is shown by shades of gray in accordance with the scale given on the right of the figure.
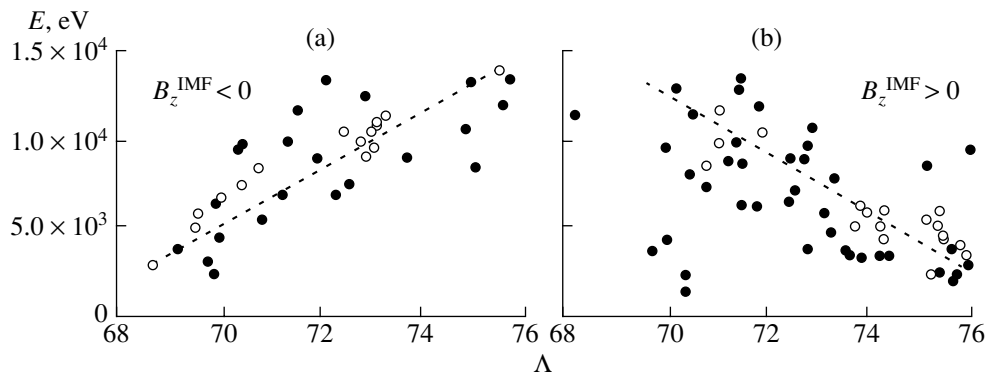

Fig. 10. Mean energy of the beamlets in the tail (gray circles) and in the auroral region (black circles) vs. latitude Λ at which they were detected: (a) beamlets observed at a preferentially southward IMF and (b) beamlets observed at a preferentially northward IMF. The IMF was measured and averaged over a time interval of 1.5 h before the observation of each of the beamlets.
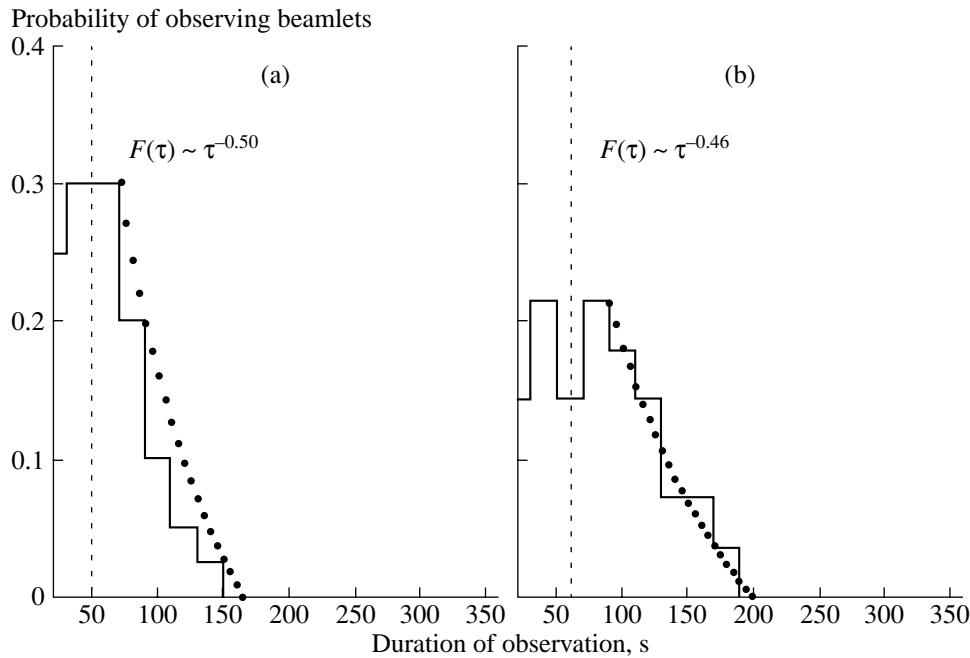
Fig. 11. Probability of observing beamlets as a function of the duration of their observation: (a) distribution obtained for beamlets observed in the auroral region (according to the data from the *Interball-2* satellite) and (b) distribution obtained for beamlets observed in the tail (according to the data from the *Interball-1* satellite).

5. INVESTIGATION OF THE EFFECT OF THE INTERPLANETARY MAGNETIC FIELD ON THE OCCURRENCE FREQUENCY OF BEAMLETS AND ON THEIR LOCALIZATION IN THE MAGNETOSPHERIC TAIL

In this section, we will attempt to find out whether the beamlet occurrence frequency depends on the prehistory of the IMF direction. To do this, we will use only the results from measurements in the tail (because of the large amount of relevant experimental data) and will no longer restrict ourselves to considering the midnight sector and quiescent geomagnetic conditions. In total, for a statistical analysis, we have chosen the data on 504 beamlets detected during 70 crossings of the PSBL by the *Interball-1* satellite. In each crossing, the PSBL was scanned over a time interval of $dt_i = 10$ min. For each next time interval, the mean direction of the IMF was determined by averaging over 1.5 h before its beginning, regardless of whether the beamlets were observed during it or not. Figure 12 shows how the beamlet occurrence frequency depends on the mean IMF direction so determined. The beamlet occurrence frequency was determined as follows: The entire range of directions of the IMF in the YZ plane was divided into twelve 30° sectors. For each sector, the total observational time (in hours) of the IMF directions within it was determined by superposing the corresponding 10-min intervals (regardless of whether beamlets were observed during them). The number of beamlets preceded by the IMF directions from this sector was then determined and was divided by the total time of obser-

vation of the IMF direction within the sector. This procedure was carried out separately for the dawn ($Y_{GSM} \leq -7R_E$), midnight ($|Y_{GSM}| < 7R_E$), and dusk ($Y_{GSM} \geq 7R_E$) sectors of the tail. The diagrams of Fig. 12 show how the beamlet occurrence frequency depends on the IMF direction in these three sectors of the tail. The diagrams are plotted on the same scale. Each sector of the diagram corresponds to a certain interval of the IMF directions, and its radial size is proportional to the beamlet occurrence frequency at a given direction of the IMF. We can see from Fig. 12 that, in the midnight sector of the tail, the beamlet occurrence frequency depends on the IMF direction to the smallest extent: the beamlets are observed at arbitrary IMF directions, but when the IMF is oriented exactly northward, the beamlet occurrence frequency is substantially lower than that for the southward direction. At the flanks, the beamlet occurrence frequency is distributed in a somewhat different fashion. In contrast to the midnight sector, the beamlets are not observed at the flanks at a northward IMF. At the dusk flank, the beamlets are not observed even at a southward IMF. At the same time, the beamlet occurrence frequency at the flanks increases with the y component of the IMF. This effect is especially pronounced at the dawn flank ($Y_{GSM} \leq -7R_E$).

In order to determine how the spatial distributions of beamlets depend on the height ΔZ above the NS, we divided the entire range of directions of the IMF in the YZ plane into four (rather than twelve) 90° sectors. We thus dealt with the following four sectors of the IMF directions: the northward, southward, and two azi-
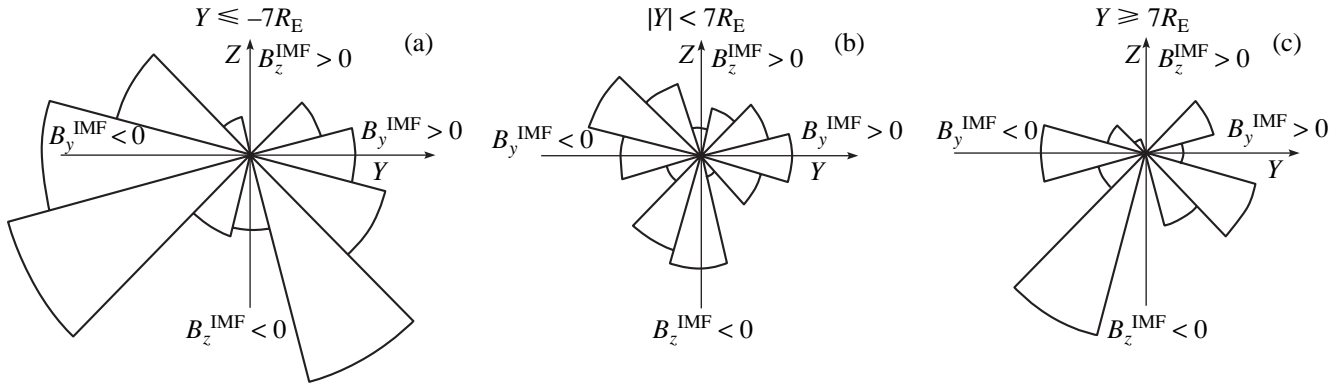
Fig. 12. Frequency of beamlet occurrence in the tail (according to the data from the *Interball-1* satellite) as a function of the mean direction of the IMF (the clock angle in the YZ_{GSM} plane), averaged over 1.5 h before the observation of each of the beamlets, for three sectors of the tail: (a) the dawn sector ($Y_{GSM} \leq -7R_E$), (b) the midnight sector ($|Y_{GSM}| < 7R_E$), and (c) the dusk sector ($Y_{GSM} \geq 7R_E$). The entire range of clock angles, ($0°$, $360°$), is divided into twelve $30°$ sectors. The radius of each of the $30°$ sectors of the diagrams is proportional to the beamlet occurrence frequency that was calculated for a given sector of the IMF directions.

muthal (with $B_y^{IMF} > 0$ and $B_y^{IMF} < 0$) sectors. The directions of the IMF were determined in the above manner. However, the beamlet occurrence frequency was calculated with allowance not only for the mean direction of the IMF but also for the height ΔZ of the satellite above the NS. For each time interval dt_i, this height was determined as the difference between the coordinate Z_{GSM} of the *Interball-1* satellite and the coordinate Z_{GSM} of the NS that was found by using the Tsyganenko-96 model. The beamlet occurrence frequency was now a function of two variables: the IMF direction and the height ΔZ. The value of this frequency was determined as the ratio of the number of beamlets observed within a given interval of ΔZ (the height of the interval being $1R_E$) and at the IMF directions within a given sector to the total time (in hours) during which the satellite remained within this interval of ΔZ under the same IMF conditions. The beamlet occurrence frequency as a function of ΔZ for the above four main directions of the IMF is shown in Fig. 13 in the form of histograms. The black circles show the number of beamlets (plotted on the lower scale) detected at a given height ΔZ and at a given direction of the IMF. In order to distinguish between the cases in which the beamlets were actually absent and those in which the beamlets were absent because they were not detected, the heights ΔZ at which no measurements were carried out at that time are marked by gray rectangles for each of the IMF directions under consideration. We can see from Fig. 13 that, in the midnight sector of the tail, the beamlets are most often observed at heights of about $\Delta Z \sim (3-5)R_E$. Moreover, at preferentially northward and azimuthal IMFs, the beamlets are detected at great heights above the NS (up to $10R_E$). At a southward IMF, the beamlets are observed at comparatively small heights above the NS (at most $6R_E$). The situation at the dusk flank of the tail is seen to be analogous, the only difference being that, at a northward IMF, the beamlets are not observed at all

and, when the IMF possesses a large negative y component, the beamlet occurrence frequency in the vicinity of the NS is highest. Interestingly, the situation at the dawn flank is the opposite. First, at all IMF directions, the beamlets at the dawn flank are observed at great heights above the NS (up to $\Delta Z \sim 12R_E$). Second, when the IMF possesses a large negative y component, the beamlet occurrence frequency even increases with ΔZ. At a preferentially northward IMF, essentially no beamlets are observed at both dawn and dusk flanks. That the beamlet occurrence frequency at $\Delta Z = 11R_E$ is high is presumably an artifact because it was determined only from two events.

Hence, the beamlet occurrence frequency in the midnight sector of the tail and at its flanks depends differently on the IMF direction. All the three sectors of the tail possess one common property: a sharp decrease in the beamlet occurrence frequency at a northward IMF. When the IMF is oriented exactly northward, there are no beamlets at all at the flanks. The beamlet occurrence frequency at the flanks is also strongly affected by the y component of the IMF.

The spatial distributions of beamlets over the NS in the dawn and dusk sectors of the tail depend differently on the IMF direction. This difference is especially pronounced when the IMF points preferentially in the azimuthal direction. Thus, for $B_y^{IMF} > 0$, the beamlet occurrence frequency at the dawn flank is maximal near the NS, i.e., at lower heights ΔZ in comparison to those at the dusk flank. For $B_y^{IMF} < 0$, the situation is the opposite: at the dusk flank, beamlets are observed predominantly at small heights ΔZ, whereas, at the dawn flank, the beamlets occurrence frequency increases with ΔZ, so the beamlets are detected at heights of up to $12R_E$ above the NS.
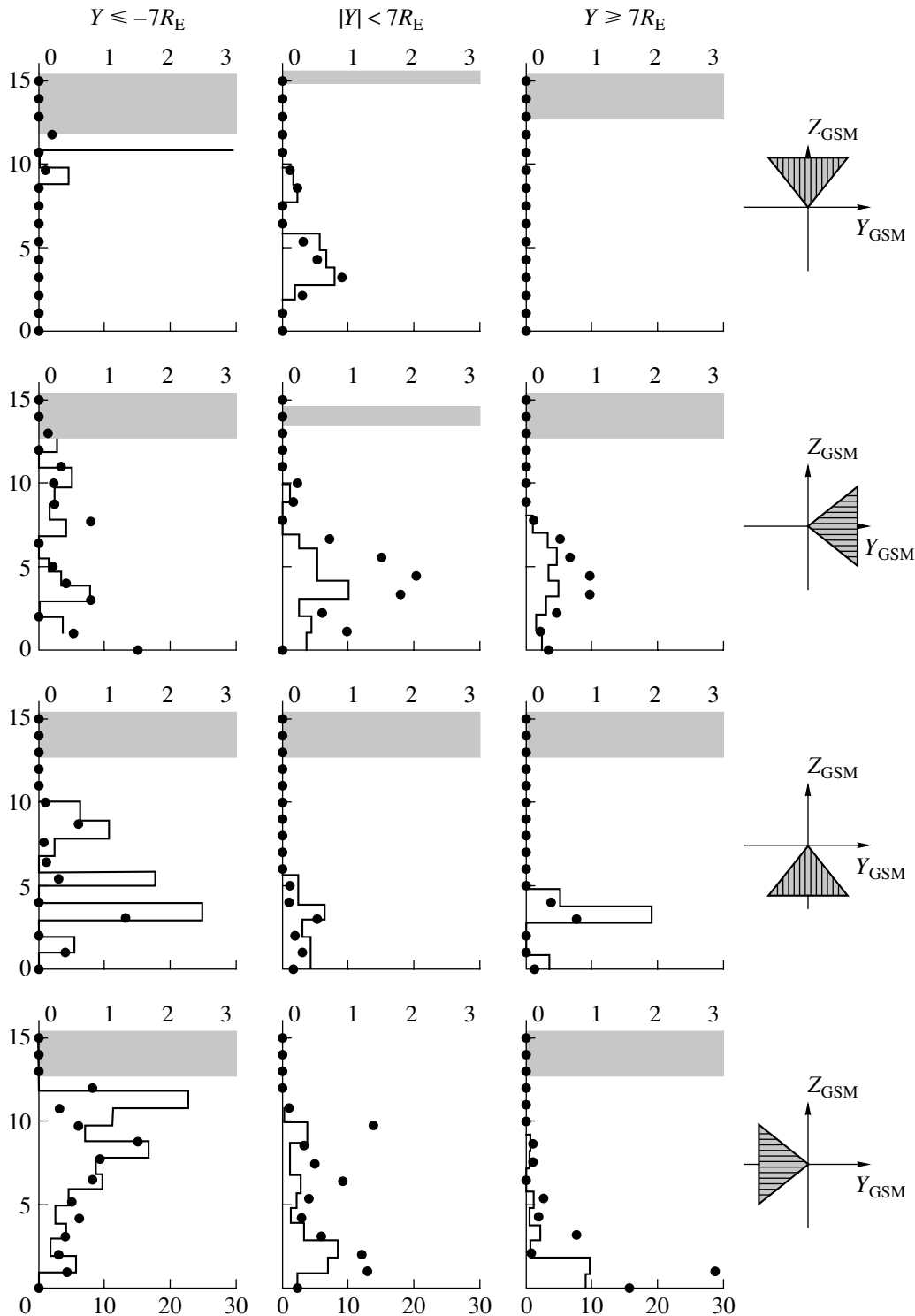
Fig. 13. Beamlet occurrence frequency in h^{-1} (upper horizontal scale) for different mean directions of the IMF (the clock angle in the YZ_{GSM} plane) as a function of the height above the neutral sheet (NS) (left vertical scale). The symbols indicate the number of observed beamlets (lower horizontal scale) within a given range of heights above the NS and within a given IMF sector. The entire range of clock angles was divided into four 90° sectors corresponding to the main directions of the IMF: the northward direction, the azimuthal direction with $B_y^{IMF} > 0$, the southward direction, and the azimuthal direction with $B_y^{IMF} < 0$ (each of the IMF sectors is shown schematically on the right of the corresponding histograms). The histograms are plotted for three sectors of the tail: the dawn sector, $Y_{GSM} \leq -7R_E$ (left column); the midnight sector, $|Y_{GSM}| < 7R_E$ (central column); and the dusk sector, $Y_{GSM} \geq 7R_E$ (right column).

6. DISCUSSION

The onset of beamlets in the PSBL is attributable to complicated acceleration processes occurring in the current sheet in distant regions of the geomagnetic tail. The ions in the tail are accelerated over a wide energy range, from several hundreds of eV to several tens of keV. Although there exists a substantial literature on the problem of beamlet generation, many questions concerning particle acceleration in the tail still remain open. In particular, the physical nature of the beamlet sources has not yet been clarified in full measure. At present, this problem can be looked at from at least two points of view. From the first point of view, for the ions to be accelerated nonadiabatically within the current sheet of the tail, it is sufficient that there be localized regions in which the normal component B_z of the magnetic field is small [7, 32, 33]. Due to the magnetic field fluctuations in the distant current sheet, such regions always form spontaneously in different parts of the tail. As a result of nonadiabatic ion acceleration in such regions, spatially localized accelerated ion beams (beamlets) form in the PSBL; these beamlets may be isolated from the PS. From the second point of view, the acceleration of beamlets observed in the PSBL and high-speed ion fluxes observed in the CPS stems from macroscopic magnetic field reconnection that occurs in the distant tail regions and near the Earth, respectively. In this case, beamlet structures cannot be isolated from the PS. Thus, Keiling *et al.* [34] showed that accelerated ion beams that arose during the explosive phase of a substorm, moved in the PSBL and PS to (or from) the Earth, and were observed for about 1 min (according to the data from the *ISEE-1* and *ISEE-2* satellites) were associated with a spatially localized perturbation that passed by the satellite when moving along the PS boundary toward (or away from) the Earth. In the model used by the authors of that paper, such perturbations form as a result of a reconnection event that occurs in the PS at a distance from the Earth that is larger than the distance to the satellite (or occurs between the satellite and the Earth). The authors suggested that the high-speed ion fluxes observed in the PSBL during quiescent periods were also accelerated as a result of magnetic field line reconnection that was localized in the distant tail regions. Hence, in solving the problem about the mechanism for magnetic field reconstruction and its geometry, it may be helpful to answer the question of whether the beamlets are isolated structures or they are structures confined to the PS boundary. Unfortunately, given only the data from single-point measurements, it is difficult to answer this question. We have succeeded only in showing by means of statistical analysis that the beamlets are actually localized within a fairly narrow region near the PS boundary; this result, however, does not provide a conclusive answer to the question of whether the beamlet are isolated from the PS or are spatially confined to it. We hope to answer this question by using multipoint measurement data from many satellites, like those launched as a part of the CLUSTER project.

The problem of beamlet sources and their properties is also related to the question about the internal dispersion of beamlets. According to the results presented in Section 4, beamlets observed in the tail and nondispersive structures detected in the auroral region belong to the same class of structures. In this sense, the morphology of the beamlets differs strongly from that of more steady dispersive structures observed at the PS boundary in the auroral region [22–24]. This is clearly illustrated by the example of a structure shown in Fig. 7. Hoshino *et al.* [35] considered the structures that were observed by the CLUSTER satellites in one crossing of the high-latitude area of the auroral region during a substorm. The high time resolution of those measurements enabled the authors of that paper to show that these structures consisted of smaller-scale substructures exhibiting internal dispersion. The authors identified these substructures with the beamlets that were accelerated nonadiabatically in the current sheet of the tail. Based on the fact that the energy W acquired by the ions in this acceleration process is inversely proportional to the squared value of the normal component $B_z(X)$ of the magnetic field present at that time in the current sheet, $W \propto \left(\dfrac{E}{B_z(X)} \right)^2$ (where E is the electric field component that is directed perpendicularly to the tail and is associated with the penetration of the interplanetary electric field into the tail), the authors of [35] explained the dispersion observed inside the beamlet as caused by the existence in the tail's current sheet (during acceleration) of a $B_z(X)$ profile monotonically decreasing with increasing distance from the Earth. Taking into account that the maximal energy of the structures considered in [35] often exceeded the upper energy threshold (35 keV) of a detector and that the minimal energy was about 7 keV, we see that, in the source of accelerated ions, the B_z component should vary monotonically within the range (B_{z1}, B_{z2}) such that $\dfrac{B_{z2}}{B_{z1}} \approx \sqrt{5}$. However, the measurements made by the *Geotail* satellite in far tail regions (at distances of more than $100R_E$ from the Earth) showed that the magnetic field in these regions is turbulent and undergoes strong fluctuations [36]. Consequently, we can speak only of the monotonic dependence of the averaged $B_z(X)$ component and only for a source of accelerated ions that is greatly extended in the X direction, because the general tendency for the B_z component to increase toward the Earth manifests itself only on long spatial scales. In many theoretical studies, however, it has been shown that the beamlet sources should be spatially localized [7, 32, 37–39]. Consequently, it is only in a statistical sense (i.e., based on numerous observations of beamlet structures at different latitudes and at different times) that we can speak of the latitude dependence of the

beamlet energy due to the presence of a magnetic field with such a $B_z(X)$ profile (Fig. 10). Figure 10 shows how the mean beamlet energy depends on latitude. The events illustrated in this figure were observed in quiescent periods and were collected from measurements carried out by the *Interball-1* satellite in the geomagnetic tail over four years (1995–1998) and by the *Interball-2* satellite in the auroral region over two years (1996–1997). The mean beamlet energies are seen to be statistically dependent on the latitude, but this dependence is inferred not from a particular event but from a series of events that were observed over a long time and were analyzed in the latitude–energy coordinates. The question about the internal dispersion of beamlets still remains unclear. It may be that the time resolution of the data from the *Interball* satellites is too low to observe the internal dispersion. It is also possible that the internal dispersion can only be observed during substorms. To answer this question, it is necessary to carry out a detailed examination of the data from the CLUSTER satellites and, of course, to analyze more than one beamlet event.

It was proved experimentally that beamlets in the PSBL occurred over a fairly short time (about 1–2 min). However, experimental observations so far have not succeeded in determining what the reason is for such a short duration of beamlet structures: whether this is a temporal or a spatial effect. In the theoretical model of [8], the beamlets were assumed to be long-lived but spatially localized structures with a vertical size of about ~$0.1R_E$. Under this assumption, the short time during which beamlets were observed is explained by the fact that, because of the permanent vertical oscillations of the PS boundary (the so-called flapping of the PS), the satellite within the PSBL sees a beamlet only for a short time. On the other hand, it has already been mentioned that the beamlets are echoes of high-power impulsive energy-conversion processes in distant regions of the geomagnetic tail; therefore, they should certainly be transient structures. Figure 11 shows that the probability distributions of observing beamlets in the tail and in the auroral region are well described by the same power function $F(\tau)$. The mean time of observation of beamlets in both these magnetospheric regions is the same and is approximately equal to 1–1.5 min, in spite of the facts that the conditions under which they are detected in the tail and in the auroral region are different: the *Interball-1* and *Interball-2* satellites travel at different speeds, and the convection rates are also different. This supports the suggestion that the beamlet duration (i.e., the characteristic time for the pulsed acceleration of particles in far tail regions) is actually about 1–1.5 min. Watanable *et al.* [40] attempted to simulate sporadic particle acceleration in these regions by self-consistently calculating the large-scale structure of the geomagnetic tail. The problem here is that the particles accelerated in distant tail regions to energies on the order of several tens of keV cannot be regarded as test particles because they drive a current that makes a substantial (if not dominant) contribution to the main current that flows across the tail and maintains the tail in a quasisteady state. The accelerated particles move nonadiabatically and undergo strong scattering, which may terminate the acceleration process. In [8, 9], it was shown that the ion acceleration in the current sheet of the tail can only be efficient under certain local resonance conditions; but the current of the accelerated ions can, in turn, violate these very sensitive conditions, thereby terminating the acceleration process. In order for the ions to gain energies on the order of 10–20 keV (i.e., characteristic beamlet energies), they should travel a distance of about ~(15–20)R_E across the tail over a time of ~1–1.5 min. It is this time that determines the lower limit on the acceleration time of the beamlet ions in the simplest case, and it corresponds approximately to the observed beamlet duration. Hence, we can suggest that the physical picture of sporadic impulsive particle acceleration is as follows: the spatially localized acceleration regions are short-lived channels in the current sheet, which decay just after the generation of beamlets and then arise repeatedly in new places within the tail.

Finally, let us discuss the question of whether there exist special conditions required for the generation of beamlets in the magnetospheric tail. It is known that beamlets are observed during both active and completely quiescent geomagnetic periods [19]. In our study, we have tried to analyze the problem of how the interplanetary conditions (in particular, the IMF direction) affect beamlet generation. The results shown in Fig. 12 imply that the beamlet generation frequency in the tail depends on the prehistory of the IMF. The diagrams of Fig. 12 were obtained for an IMF whose direction was averaged over 1.5 h before the observation of each next beamlet. We also used other averaging intervals, namely, 2 and 1 h and 30 and 15 min (the corresponding diagrams are not presented here), and found that the relevant distributions are similar to those shown in Fig. 12, provided that the averaging interval is no less than 1 h. The dependence on the IMF direction becomes less pronounced for shorter averaging intervals (30 and 15 min). Hence, the IMF presumably has a global effect on the processes occurring in the magnetospheric tail, in particular, on the processes responsible for beamlet generation. Analogous results were obtained in [41, 42], where it was shown that the state of the magnetosphere at a given time is governed by the IMF history during at least the preceding hour. We can see from Fig. 12 that the beamlet generation frequency in the midnight sector of the tail and at its flanks depends differently on the IMF direction. All these three sectors of the tail share one common property: a sharp decrease the beamlet generation frequency at a northward IMF. At the exactly northward IMF, the beamlets at the flanks are completely absent, probably because, at a northward IMF, the dawn-to-dusk electric field, which accelerates beamlets, is weak. An interesting feature of the distributions obtained is that the

y component of the IMF exerts a significant influence on the beamlet generation frequency, especially at the flanks. This effect can be associated with the onset of conditions favorable for the acceleration of ions in the current sheet at the flanks of the tail. The role of the *y* component of the IMF in the tail dynamics was discussed by Petrukovich *et al.* [43], who showed that the onset of low-intensity magnetic substorms (such that the magnetic field fluctuations at the night side was about 100–300 nT) was associated with the azimuthal IMF. On the other hand, there are indications that SW ions can effectively penetrate into the magnetospheric tail through its flanks, especially when the IMF has a nonzero *y* component [44]. In interacting with the current sheet, the penetrating SW ions can form beamlets. In order to answer the question of what might be the actual cause of an increase in the beamlet occurrence frequency in an azimuthal IMF (either favorable conditions for acceleration in the current sheet or an additional influx of the accelerated SW ions), it is necessary to carry out special experimental and theoretical investigations.

As for the spatial distributions of beamlets above the NS, they are very different at the dawn and dusk flanks. For $B_y^{\mathrm{IMF}} > 0$, the beamlet generation frequency at the dawn flank is maximal at lower heights ΔZ in comparison to those at the dusk flank, and vice versa for $B_y^{\mathrm{IMF}} < 0$. This result can hardly be explained as being due to the twisting of the tail, because the distributions shown in Fig. 13 are plotted as functions of ΔZ, i.e., of the height ΔZ of the satellite above the NS. Therefore, the tail twisting does not manifest itself in our results (to within an error resulting from the determination of the position of the NS). It may be that the difference in the spatial distributions of beamlets above the NS at the dawn and dusk flanks stems from the fact that, at the given IMF direction, the sources of accelerated beamlet ions in the tail are at different distances from the Earth. An IMF with a strong *y* component can set up convection in the *Y* direction within the tail [45]; moreover, for $B_y^{\mathrm{IMF}} > 0$, the convection velocity is positive, $V_y^{\mathrm{conv}} > 0$, whereas for $B_y^{\mathrm{IMF}} < 0$, we have $V_y^{\mathrm{conv}} < 0$. Hence, in moving toward the Earth, the beamlets that have been accelerated in far tail regions are convected toward the dusk flank at $B_y^{\mathrm{IMF}} > 0$ and toward the dawn flank at $B_y^{\mathrm{IMF}} < 0$. In the first case, the beamlets that are observed at the dawn flank at large $|Y|$ values should be accelerated closer to the Earth (in comparison to the beamlets detected at the dusk flank) in order for the effect of convection on them to be smaller; otherwise, their source would be at larger $|Y|$ values, i.e., in the low-latitude boundary sheath or even outside the Earth's magnetosphere. Accordingly, at the dawn flank, the beamlets will be observed at lower heights ΔZ in comparison to

those at the dusk flank, and vice versa for an IMF with a large negative azimuthal component ($B_y^{\mathrm{IMF}} < 0$).

7. CONCLUSIONS

(i) High-speed ion beams (beamlets) in the form of short plasma bursts, which usually have no dispersion and have energies amounting to several tens of keV, the duration being 1–2 min, have been observed in the PSBL of the magnetospheric tail and near the high-latitude PS boundary in the auroral region.

(ii) In the geomagnetic tail, as well as in the auroral region, the beamlets are localized near the PS boundary in a zone whose size in the latitudinal direction is about 0.5°–0.8°.

(iii) In both these magnetospheric regions, the mean time during which beamlets are observed is the same and is approximately equal to 1–1.5 min, even though they are detected under different conditions. It can thus be suggested that the short time during which beamlets are observed is most probably governed by a temporal rather than by a spatial effect; i.e., it is determined by the short time of beamlet generation in the current sheet of the tail.

(iv) The frequency of beamlet generation in the tail depends on the prehistory of the interplanetary conditions, in particular, on the mean IMF direction averaged over at least one hour before the observation of a beamlet. Moreover, this dependence is different for the midnight sector of the tail and for its flanks.

In the midnight sector, the beamlets are observed at almost all directions of the IMF. At a strong northward IMF, the beamlet generation frequency is considerably lower than at other IMF directions:

At a strong northward IMF, no beamlets are observed at the flanks.

The frequency of beamlet generation at the flanks is maximal when the IMF has a strong *y* component.

(v) The spatial distribution of beamlets above the NS also depends on the mean IMF direction.

At a preferentially southward IMF, beamlets in the midnight sector are observed at heights of no more than $5R_{\mathrm{E}}$ (in the Z_{GSM} direction) above the NS, whereas, at a preferentially northward IMF, the beamlets are observed at greater heights (up to $10R_{\mathrm{E}}$) above the NS.

At the same direction of an IMF with a strong *y* component, the spatial distributions of beamlets at the dawn and dusk flanks are different. For $B_y^{\mathrm{IMF}} > 0$, the beamlet generation frequency at the dawn flank is highest near the NS, while at the dusk flank, the beamlets are mostly observed at heights of about 3–5R_{E} above the NS. For $B_y^{\mathrm{IMF}} < 0$, the situation is opposite: the beamlet generation frequency at the dawn flank increases with height above the NS, while the fre-

quency of observing them at the dusk flank is maximal near the NS.

On the whole, our results confirm the validity of the model in which impulsive plasma acceleration leads to the generation of beamlets during transient processes that occur sporadically in different tail regions even under absolutely quiescent geomagnetic conditions. Such short-lived fast ion beams (beamlets) are not necessarily associated with magnetic reconnection (i.e., with a change in the sign of B_z within the current sheet); in the regions where the normal magnetic-field component is small and positive ($B_z > 0$), they can also be driven by a purely nonadiabatic mechanism. Of course, if beamlets are indeed generated by the reconnection mechanism, then reconnection events should be localized in space and be pulsed in character. It is these properties of magnetic reconnection in the magnetospheric tail that have been actively discussed in the literature over the past decade [33, 34, 38, 39]. Since the Earth's magnetospheric tail is a very dynamic system, the different structures that occur within it are characterized by different spatiotemporal scales. Presumably, when favorable conditions arise (e.g., when the IMF at the dayside magnetopause acquires a large negative normal component, $B_z^{\mathrm{IMF}} < 0$, which promotes an energy influx into the tail), sporadic localized acceleration regions can be self-organized into a coherent pattern that corresponds to a macroscopic magnetic reconnection event in the tail [46]. In this case, the acceleration processes acquire new properties; this may lead to the generation of higher-power longer-duration (≥ 10 min) fluxes of accelerated particles. It is presumably the vast diversity of possible dynamic magnetospheric processes that can give rise to different types of structures in the geomagnetic tail and in the auroral region that have been discussed in our study: dispersive and nondispersive, local and global, permanent and transient.

ACKNOWLEDGMENTS

REFERENCES

1. J. D. Winningham, F. Yasuhara, S.-I. Akasofu, and W. J. Heikkila, J. Geophys. Res. **80**, 3148 (1975).

2. T. E. Eastman, L. F. Frank, W. K. Peterson, and W. Lennartsson, J. Geophys. Res. **89**, 1553 (1984).

3. T. E. Eastman, L. A. Frank, and C. Y. Huang, J. Geophys. Res. **90**, 9541 (1985).

4. K. Amano and T. Tsuda, J. Geomagn. Geoelectr. **30** (1), 27 (1978).

5. G. K. Parks, M. McCarthy, R. J. Fitzenreiter, *et al.*, J. Geophys. Res. **89**, 8885 (1984).

6. K. Takahashi and E. W. Hones, J. Geophys. Res. **93**, 8558 (1988).

7. J. Buchner and L. M. Zelenyi, J. Geophys. Res. **94**, 11821 (1989).

8. M. Ashour-Abdalla, J. P. Berchem, J. Buchner, and L. M. Zelenyi, J. Geophys. Res. **98**, 5651 (1993).

9. M. Ashour-Abdalla, L. M. Zelenyi, V. Peroomian, *et al.*, J. Geophys. Res. **100**, 19191 (1995).

10. L. R. Lyons and T. W. Speisen, J. Geophys. Res. **87**, 2276 (1982).

11. J. Chen and P. J. Palmadesso, J. Geophys. Res. **91**, 1499 (1986).

12. G. R. Burkhart and J. Chen, J. Geophys. Res. **96**, 14033 (1991).

13. J. Buchner, Geophys. Res. Lett. **18**, 1595 (1991).

14. T. W. Speiser, J. Geophys. Res. **70**, 4219 (1965).

15. J. S. Wagner, P. C. Gray, J. R. Kan, *et al.*, Planet. Space Sci. **29**, 391 (1981).

16. L. A. Frank and W. R. Paterson, Geophys. Res. Lett. **21**, 2963 (1994).

17. G. Parks, L. Chen, M. McCarthy, *et al.*, Geophys. Res. Lett. **25**, 3285 (1998).

18. E. E. Grigorenko, A. O. Fedorov, and L. M. Zelenyi, Ann. Geophys. **20**, 329 (2002).

19. V. Peroomian, M. Ashour-Abdalla, and L. M. Zelenyi, J. Geophys. Res. **105**, 18807 (2000).

20. L. A. Frank, W. R. Paterson, and M. G. Kivelson, J. Geophys. Res. **99**, 14877 (1994).

21. L. M. Zelenyi, R. A. Kovrazkhin, and J. M. Bosqued, J. Geophys. Res. **95**, 12119 (1990).

22. J.-A. Sauvaud, D. Popescu, D. C. Delcourt, *et al.*, J. Geophys. Res. **104**, 28565 (1999).

23. V. A. Sergeev, J.-A. Sauvaud, D. Popescu, *et al.*, J. Geophys. Res. **105**, 18465 (2000).

24. S. Klimov, S. Romanov, E. Amata, *et al.*, Ann. Geophys. **15**, 514 (1997).

25. Yu. I. Yermolaev, A. O. Fedorov, O. L. Vaisberg, *et al.*, Ann. Geophys. **15**, 533 (1997).

26. J.-A. Sauvaud, H. Barthe, C. Aoustin, *et al.*, Ann. Geophys. **16**, 1056 (1998).

27. R. J. DeCoster and L. A. Frank, J. Geophys. Res. **84**, 5099 (1979).

28. T. G. Onsager, M. F. Thomsen, R. C. Elphic, and J. T. Gosling, J. Geophys. Res. **96**, 20999 (1991).

29. L. M. Zelenyi, A. L. Taktakishvili, E. M. Dubinin, *et al.*, in *Proceedings of the 9th COSPAR Colloquium "Magnetospheric Research with Advanced Techniques," Beijing, 1996*, p. 125.

30. E. Dubinin, L. Yu. Budnik, N. Pissarenko, *et al.*, in *Proceedings of the 3rd International Conference on Substorms, Versailles, 1996*, p. 533.

31. M. Ashour-Abdalla, L. M. Zelenyi, V. Peroomian, *et al.*, J. Geophys. Res. **101**, 15287 (1996).

32. W. Liu, J. Geophys. Res. **106**, 289 (2001).

33. V. A. Sergeev, R. C. Elphic, F. S. Mozer, *et al.*, Planet. Space Sci. **40**, 1551 (1992).

34. A. Keiling, H. Reme, I. Dandouras, *et al.*, in *Proceedings of the EGS–AGU–EUG Joint Assembly, 2003, Nice*, p. 1059.

35. M. Hoshino, A. Nishida, and T. Yamamoto, Geophys. Res. Lett. **21**, 2935 (1994).

36. M. Ashour-Abdalla, M. El-Alaoui, V. Peroomian, and R. Walker, Geophys. Res. Lett. **26**, 3545 (1999).

37. A. J. Klimas, J. A. Valdivia, D. Vassiliadis, *et al.*, J. Geophys. Res. **105**, 18765 (2000).

38. T. Nagai, I. Shinohara, M. Fujimoto, *et al.*, J. Geophys. Res. **106**, 25929 (2001).

39. V. Peroomian and L. Zelenyi, Space Sci. Rev. **95**, 257 (2001).

40. M. Watanabe, N. Sato, R. Greenwald, *et al.*, J. Geophys. Res. **105**, 22955 (2000).

41. W. Baumjohann, G. Paschmann, N. Sckopke, *et al.*, J. Geophys. Res. **93**, 11507 (1988).

42. N. C. Maynard, W. J. Burke, J. Moen, *et al.*, J. Geophys. Res. **108**, 1006 (2003).

43. A. A. Petrukovich, W. Baumjohann, R. Nakamura, *et al.*, J. Geophys. Res. **105**, 21109 (2000).

44. G. Rostoker, J. Geophys. Res. **101**, 12955 (1996).

45. A. Nishida, T. Mukai, T. Yamamoto, *et al.*, J. Geophys. Res. **103**, 4409 (1998).

46. T. Wiegelmann and J. Buchner, Nonlin. Processes Geophys. **8**, 127 (2001).

Translated by O.E. Khadin

<center>

PLASMA OSCILLATIONS
AND WAVES

</center>

Electromagnetically Induced Transparency in a Magnetized Plasma during Oblique Propagation of Radiation

A. Yu. Kryachko and M. D. Tokman

Institute of Applied Physics, Russian Academy of Sciences, ul. Ul'yanova 46, Nizhni Novgorod, 603950 Russia

Received February 4, 2004

Abstract—The parametric effect of electromagnetically induced transparency (EIT) is studied in the case of quasi-transverse propagation of an extraordinary wave in the vicinity of the upper hybrid resonance in a cold plasma. The question is investigated of whether the waves that propagate in a smoothly inhomogeneous medium (from the transparency region in the vicinity of the upper hybrid resonance into vacuum or in the opposite direction) can reach the EIT region. The features of the quasi-transverse propagation of an extraordinary wave at the electron cyclotron resonance frequency in the quasi-EIT regime are also considered. It is shown that, in this situation, the parametric effects modify the polarization of the wave, with the result that its absorption increases substantially (by one to two orders of magnitude). © 2005 Pleiades Publishing, Inc.

1. INTRODUCTION

In recent years, considerable attention has been devoted to the effect of electromagnetically induced transparency (EIT) in plasmas [1–3]—a classical analogue of the EIT effect in three-level quantum systems [4, 5]. This phenomenon consists in the formation of a transparency window in the resonant absorption line of a quantum or a classical system in the presence of a high-power pump wave, accompanied by an extremely strong slowing down of the signal wave. The characteristic feature of plasma systems in the EIT regime is efficient excitation of the electrostatic oscillations by the beating between the signal wave and the pump wave. In the EIT regime, the power thresholds for most of the known nonlinear optical effects are appreciably lower than the usual threshold [4, 5]. It has been proposed to use the EIT phenomenon when working with plasma accelerators [3, 6, 7].

The EIT effect in plasma systems was investigated for electromagnetic waves in the electron cyclotron resonance (ECR) frequency range that propagate in a magnetized plasma along the external magnetic field. In [1, 3], this effect was investigated for a cold plasma, and, in [2], it was considered with allowance for thermal motion of the plasma particles. In addition, the case in which the role of the pump system is played by a magnetic undulator was studied in [3, 6, 7].

In the present paper, we investigate the EIT effect in a plasma in the case of obliquely propagating waves. Besides being of general theoretical significance, studies of an oblique (or, more precisely, quasi-transverse) wave propagation are important from the standpoint of possible applications of the EIT effect in controlled fusion research. In a toroidal plasma, this effect can be used to the output intrinsic radiation from the cutoff region [1, 2] in the vicinity of the upper hybrid reso-

nance (UHR) at the center of the plasma column into vacuum; in this case, the quasi-transverse wave propagation is forced by the toroidal geometry. We consider the propagation of waves in a cold magnetized plasma and confine our attention to the case in which the frequency of the signal wave corresponds to the UHR frequency range, another subject of analysis being the case of the ECR frequency range.

Our paper is organized as follows. In Section 2, we present the basic equations and derive the expression for the effective refractive index of the plasma for a signal wave. In Section 3, we consider a signal wave in the UHR region. Namely, we investigate the dispersion of this wave and its absorption, as well as the possibility of achieving the EIT regime during its propagation in a smoothly inhomogeneous plasma medium. In Section 4, we study the propagation of a signal wave in the ECR region.

2. FORMULATION OF THE PROBLEM AND BASIC EQUATIONS

We consider the propagation of two extraordinary electromagnetic waves—a signal wave and a pump wave—in a cold collisional magnetized plasma. For simplicity, we assume that the wave vectors of the waves and the vector of the external magnetic field $\mathbf{H} = H\mathbf{z}_0$ lie in the same plane xz (see Fig. 1):

$$
\begin{aligned}
\mathbf{E}(x, z, t) = \mathrm{Re}\{ & \mathbf{E}_1 \exp(-i\omega_1 t + ik_{1x}x + ik_{1z}x) \\
& + \mathbf{E}_2 \exp(-i\omega_2 t + ik_{2x}x + ik_{2z}z) \}.
\end{aligned}
\tag{1}
$$

Here, $\mathbf{E}(x, z, t)$ is the total electric field of the propagating bichromatic electromagnetic wave and the subscripts 1 and 2 refer, respectively, to the signal wave and the pump wave. In [1, 2, 8], it was shown that the fundamental condition for the onset of the EIT effect is the
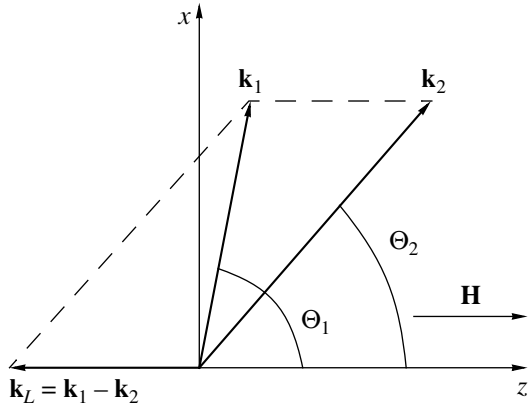
Fig. 1. Coordinate system and propagation directions of the waves.

effective excitation of a quasi-electrostatic mode by the beatings between the pump wave and the signal wave. In what follows, we will also require that this condition be satisfied:

$$|\omega_L - \omega_p| \ll \omega_L, \omega_p, \qquad (2a)$$

$$|k_{Lx}| = |k_1 \sin\Theta_1 - k_2 \sin\Theta_2| \ll |k_{Lz}| \qquad (2b)$$
$$= |k_1 \cos\Theta_1 - k_2 \cos\Theta_2|.$$

Here, $\Theta_{1,2}$ are the angles at which the waves propagate with respect to the magnetic field, $\omega_L = \omega_1 - \omega_2$ and $\mathbf{k}_L = \mathbf{k}_1 - \mathbf{k}_2$ are the frequency of the beat wave and its wave vector, $\omega_p = (4\pi e^2 N_e/m)^{1/2}$ is the electron plasma frequency, N_e is the electron density, and e and m are the charge and mass of an electron ($e > 0$). The most interesting case is that of the quasi-transverse propagation of a signal wave. In this case, as can be seen from condition (2b), the angle Θ_2 is other than 0 or $\pi/2$.

Note that, in the case of oblique propagation of a signal and a pump wave, the beating between them can generally excite quasi-electrostatic oscillations, which propagate at arbitrary angles to the magnetic field (in particular, at a right angle to the field, which indicates that the propagation of the pump wave can also be considered to be quasi-transverse). However, it is known [9] that the refractive index for such waves is high, $ck_L/\omega_L \gg 1$; in this case, condition (2b) implies that the effective refractive index for the signal wave, ck_1/ω_1, should also be high. On the other hand, moderate values of the refractive index are preferable for extracting radiation into vacuum (or for exciting it by a wave incident from vacuum). This is why we will be interested in the excitation of quasi-electrostatic oscillations having the plasma frequency and propagating at a small angle to the magnetic field.

We will consider the problem in terms of hydrodynamic theory. The oscillations of the velocity $\mathbf{V}$ of the plasma electrons are described by the Euler equations

with allowance for the Lorentz force exerted on them by the wave fields:

$$\frac{\partial \mathbf{V}}{\partial t} + \omega_H (\mathbf{V} \cdot \mathbf{z}_0) + \gamma \mathbf{V} + V_x \frac{\partial \mathbf{V}}{\partial x} + V_z \frac{\partial \mathbf{V}}{\partial z}$$
$$= -\frac{e}{m}\mathbf{E}(x, z, t) + \frac{e}{m}\left(\mathbf{V} \times \int_{-\infty}^{t} \nabla \times \mathbf{E}(x, z, t)dt\right). \qquad (3)$$

Here, $\omega_H = eH/mc$ is the electron gyrofrequency and γ is the effective collision frequency. Equation (3) should be supplemented with the continuity equation

$$\frac{\partial N_e}{\partial t} + \nabla \cdot (N_e \mathbf{V}) = 0 \qquad (4)$$

and with the wave equation

$$\frac{\partial^2 \mathbf{E}}{\partial t^2} + c^2 (\nabla \times (\nabla \times \mathbf{E})) - 4\pi e \frac{\partial}{\partial t}(N_e \mathbf{V}) = 0. \qquad (5)$$

We assume that the ion density N_i is constant and that the plasma is quasineutral,

$$N_i = N_0 = \text{const},$$
$$|n| = |(N_e - N_i)/N_i| \ll 1, \qquad (6)$$

these conditions allow us to express the electron plasma frequency in terms of N_0 rather than N_e. We also assume that the signal wave amplitude E_1 is small in comparison to the pump wave amplitude E_2; this assumption makes it possible to treat the problem using the approximation linear in the signal wave amplitude E_1.

The set of equations (3)–(5) can be solved by the so-called method of reduced equations, which was described in [2, 8] with regard to analogous problems. In this method, the complex amplitudes of the corresponding quantities are introduced,

$$(\mathbf{E}, \mathbf{V}, n) = \text{Re} \sum_{j=1,2,L} (\mathbf{E}_j, \mathbf{V}_j, n_j)$$
$$\times \exp(-i\omega_j t + ik_{jx}x + ik_{jz}z), \qquad (7)$$

and the only terms that are retained in Eqs. (3)–(5) are those containing resonant frequencies. As a result, we arrive at the following set of equations:

$$-i\omega_1 \mathbf{V}_1 + \omega_H (\mathbf{V}_1 \times \mathbf{z}_0) + \gamma \mathbf{V}_1$$
$$+ \frac{i}{2}(\mathbf{k}_L \cdot \mathbf{V}_2)\mathbf{V}_L + \frac{i}{2}(\mathbf{k}_2 \cdot \mathbf{V}_L)\mathbf{V}_2$$
$$= -\frac{e}{m}\mathbf{E}_1 - \frac{e}{2m}\left\{\frac{\mathbf{k}_2}{\omega_2}(\mathbf{V}_L \cdot \mathbf{E}_2) - \mathbf{E}_2\left(\frac{\mathbf{k}_2}{\omega_2} \cdot \mathbf{V}_L\right)\right. \qquad (8.1)$$
$$\left. + \frac{\mathbf{k}_L}{\omega_L}(\mathbf{V}_2 \cdot \mathbf{E}_L) - \mathbf{E}_L\left(\frac{\mathbf{k}_L}{\omega_L} \cdot \mathbf{V}_2\right)\right\},$$

$$-\omega_1 n_1 + (\mathbf{k}_1 \cdot \mathbf{V}_1) + n_2(\mathbf{k}_1 \cdot \mathbf{V}_L)/2$$
$$+ n_L(\mathbf{k}_1, \mathbf{V}_2)/2 = 0, \qquad (8.2)$$

$$-\omega_1^2 \mathbf{E}_1 - c^2\{\mathbf{k}_1(\mathbf{k}_1 \cdot \mathbf{E}_1) - k_1^2 \mathbf{E}_1\}$$
$$+ 4\pi e N_0 i\omega_1(\mathbf{V}_1 + n_2\mathbf{V}_L/2 + n_L\mathbf{V}_2/2) = 0, \qquad (8.3)$$

$$-i\omega_L \mathbf{V}_L + \omega_H(\mathbf{V}_L \times \mathbf{z}_0) + \gamma \mathbf{V}_L$$
$$-\frac{i}{2}(\mathbf{k}_2 \cdot \mathbf{V}_1)\mathbf{V}_2^* + \frac{i}{2}(\mathbf{k}_1 \cdot \mathbf{V}_2^*)\mathbf{V}_1$$

$$= -\frac{e}{m}\mathbf{E}_L - \frac{e}{2m}\left\{\frac{\mathbf{k}_2}{\omega_2}(\mathbf{V}_1 \cdot \mathbf{E}_2^*) - \mathbf{E}_2^*\left(\frac{\mathbf{k}_2}{\omega_2} \cdot \mathbf{V}_1\right)\right. \qquad (8.4)$$
$$\left. + \frac{\mathbf{k}_1}{\omega_1}(\mathbf{V}_2^* \cdot \mathbf{E}_1) - \mathbf{E}_1\left(\frac{\mathbf{k}_1}{\omega_1} \cdot \mathbf{V}_2^*\right)\right\},$$

$$-\omega_L n_L + (\mathbf{k}_L \cdot \mathbf{V}_L) + n_1(\mathbf{k}_L \cdot \mathbf{V}_2^*)/2$$
$$+ n_2^*(\mathbf{k}_L \cdot \mathbf{V}_1)/2 = 0, \qquad (8.5)$$

$$-\omega_L^2 \mathbf{E}_L - c^2\{\mathbf{k}_L(\mathbf{k}_L \cdot \mathbf{E}_L) - k_L^2 \mathbf{E}_L\}$$
$$+ 4\pi e N_0 i\omega_L(\mathbf{V}_L + n_1\mathbf{V}_2^*/2 + n_2^*\mathbf{V}_1/2) = 0. \qquad (8.6)$$

By virtue of the condition $E_1 \ll E_2$, we can assume that the parametric wave interaction does not affect the propagation of a pump wave; hence, the refractive index for this wave and its polarization can be described by the well-known linear relationships [9].

From Eqs. (8.1), (8.2), and (8.4)–(8.6) we can find the expressions for the quantities $V_{1x,y,z}$, $V_{Lx,y,z}$, n_1, n_L,

and $E_{Lx,y,z}$ as (obviously linear) functions of the electric field components $E_{1x,y,z}$ of the signal wave. As for Eq. (8.3), it yields the following expression for the effective refractive index for the signal wave:

$$\frac{c^2 k_1^2}{\omega_1^2} = 1 - \frac{2(a-b+c)}{2a - b \pm \sqrt{b^2 - 4ac}}, \qquad (9)$$

where we have introduced the notation

$$a = \varepsilon_{xx}\sin^2\Theta_1 + \varepsilon_{zz}\cos^2\Theta_1 + (\varepsilon_{zx} + \varepsilon_{xz})\sin\Theta_1\cos\Theta_1,$$
$$b = \varepsilon_{xx}\varepsilon_{zz} + \varepsilon_{yy}\varepsilon_{zz}\cos^2\Theta_1$$
$$+ (\varepsilon_{xx}\varepsilon_{yy} - \varepsilon_{xy}\varepsilon_{yx})\sin^2\Theta_1 \qquad (10)$$
$$+ (\varepsilon_{yy}\varepsilon_{zx} - \varepsilon_{yx}\varepsilon_{zy} + \varepsilon_{yy}\varepsilon_{xz} - \varepsilon_{xy}\varepsilon_{yz})\sin\Theta_1\cos\Theta_1,$$
$$c = \varepsilon_{zz}(\varepsilon_{xx}\varepsilon_{yy} - \varepsilon_{xy}\varepsilon_{yx}).$$

The dielectric tensor elements ε_{jk} are determined by the relationship

$$\varepsilon_{jk} = \varepsilon_{0jk} + \frac{A_{jk}(\omega_1, k_1, \Theta_1)\xi_{EC}}{D(\omega_L, k_L) - B(\omega_1, k_1, \Theta_1)\xi_{EC}}. \qquad (11)$$

Here, ε_{0jk} are the elements of the "linear" dielectric tensor of a cold magnetized plasma [9] in the coordinate system shown in Fig. 1 and $\xi_{EC} = |V_2|^2/(2\omega_2/k_2)^2$ is the square of the ratio of the electron oscillatory velocity to the phase velocity of the pump field. The determinant $D(\omega_L, \mathbf{k}_L)$ describes the familiar linear dispersion relation of a wave whose frequency and wave vector correspond to those of the beat wave:

$$D(\omega_L, \mathbf{k}_L) = \begin{vmatrix} -c^2 k_{Lz}^2/\omega_L^2 + \varepsilon_{0xx}(\omega_L) & \varepsilon_{0xy}(\omega_L) & c^2 k_{Lx}k_{Lz}/\omega_L^2 \\ \varepsilon_{0yx}(\omega_L) & -c^2 k_L^2/\omega_L^2 + \varepsilon_{0yy}(\omega_L) & 0 \\ c^2 k_{Lz}k_{Lx}/\omega_L^2 & 0 & -c^2 k_{Lx}^2/\omega_L^2 + \varepsilon_{0zz}(\omega_L) \end{vmatrix}. \qquad (12)$$

The matrix $A(\omega_1, k_1, \Theta_1)$ and scalar $B(\omega_1, k_1, \Theta_1)$ are independent of ξ_{EC}. The expressions describing them are quite lengthy and are thus presented separately in Appendix 1.

For a finite pump field amplitude, the plus and minus signs in the denominator in expression (9) cannot be unambiguously assigned to the ordinary (O) and extraordinary (X) waves because, in different ranges of parameter values, the signs for them are chosen according to different rules. Because of the complexity of expressions (9)–(11), we failed to find the boundaries of these ranges analytically; however, they can be uniquely determined for each particular shape of the dispersion curves of the signal wave. In what follows, we will discuss, among other things, the dispersion

curves that were calculated numerically based on formulas (9)–(11) and correspond to the X wave (i.e., those that approach the dispersion curve of the X mode in the limit in which the pump field intensity is zero).

3. SIGNAL WAVE IN THE VICINITY OF THE UPPER HYBRID RESONANCE

Our further discussion will focus primarily on the case in which the frequency of the signal wave is close to the upper hybrid frequency $\omega_{uh} = (\omega_p^2 + \omega_H^2)^{1/2}$ because, for this frequency range, there are the resonant absorption line [9] and the cutoff region for a transversely propagating extraordinary electromagnetic wave.
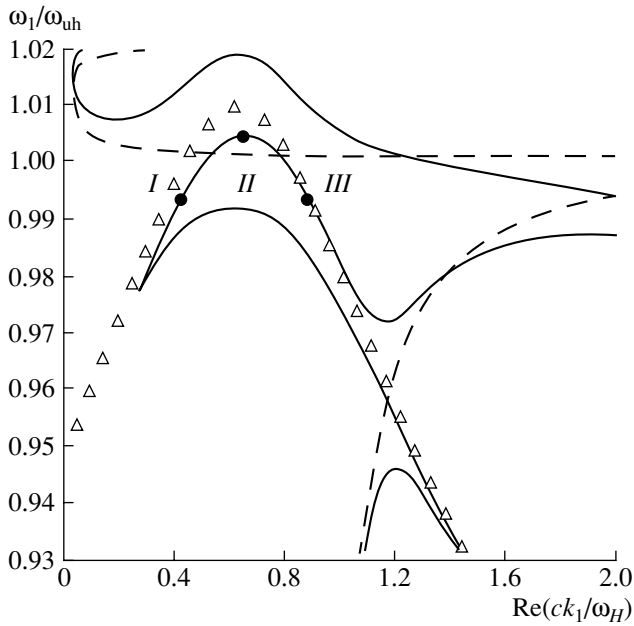
Fig. 2. Characteristic behavior of the dispersion curve of a signal wave under the EIT conditions: $\xi_{EC} = 3 \times 10^{-3}$ (solid curve), $\xi_{EC} = 0$ (dashed curve), and $\mathrm{Re}\,D = 0$ (triangles). The calculations were carried out for $\omega_p/\omega_H = 0.2$, $\gamma/\omega_H = 5.0 \times 10^{-4}$, $\omega_2/\omega_H = 0.83$, $\Theta_2 = 45°$, and $\Theta_1 = 90°$.
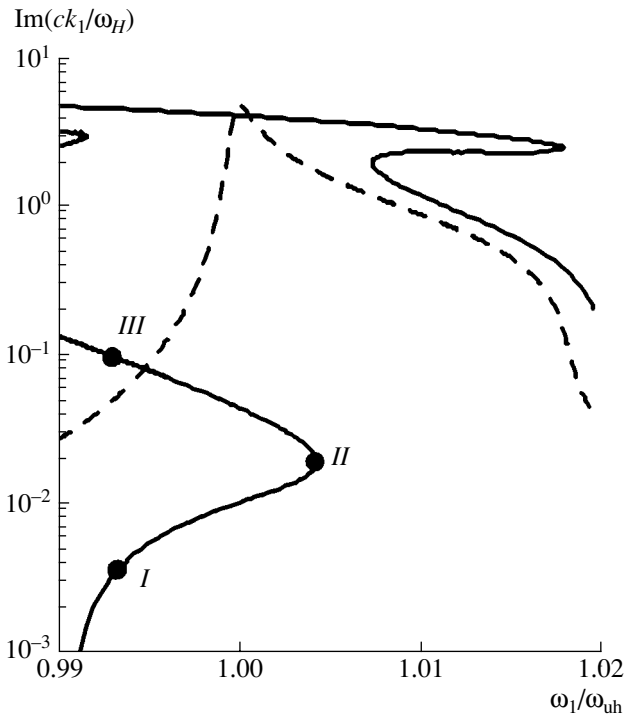

Fig. 3. Characteristic behavior of the absorption line profile of a signal wave. The parameters are the same as in Fig. 2.

The squared ratio ξ_{EC} is a small parameter: for reasonable values of the pump field intensity (on the order of 10 kW/cm^2 in the microwave frequency range), it is on the order of 10^{-7}. Consequently, in relationship (11), the contribution of the second term, which accounts for the EIT effect, is significant only when the determinant $D(\omega_L, \mathbf{k}_L)$ in it is also small. This indicates that the behavior of the dispersion curves of the signal wave in the EIT regime is determined by the linear dispersion relation of the beat wave, $\mathrm{Re}\,D(\omega_L = \omega_1 - \omega_2, \mathbf{k}_L = \mathbf{k}_1 - \mathbf{k}_2) = 0$. Below, we will present the results of numerical investigation of expression (9). Figure 2 shows the dispersion curves of the signal wave in the UHR region. We can see that, at finite intensities of the pump field, the behavior of the dispersion curves is indeed determined by the dispersion relation of the beat wave.

The absolute value of the group velocity of the signal wave is determined as follows. In contrast to the case of purely longitudinal waves, this group velocity has two mutually orthogonal components: one of which, $V_k = \partial\omega_1/\partial k_1$, is oriented along the wave vector $\mathbf{k}_1$ [10] and the other is determined by the relationship $V_\perp = -(1/k_1)\partial\omega_1/\partial\Theta_1$. Accordingly, the absolute value V_{gr} of the group velocity is given by the expression

$$V_{\mathrm{gr}} = (V_k^2 + V_\perp^2)^{1/2}.$$

Figure 3 shows the profiles of the absorption line of the signal wave. This figure, as well as the calculations based on formula (9), implies that, over a certain portion of the dispersion curve of the signal wave (see Fig. 2, portion *I–III*), the wave energy dissipation decreases substantially and at the same time the wave group velocity is strongly slowed down. These are two main features of the EIT regime. An important point is that the range of characteristic parameter values where the EIT effect is observed corresponds to the effective excitation of plasma oscillations at the beat frequency (see conditions (2)):

$$\begin{aligned} \omega_1 &= \omega_2 + \omega_p + O(\xi_{EC}), \\ \mathrm{Re}\,k_1 &= k_2\sin\Theta_2/\sin\Theta_1 + O(\xi_{EC}). \end{aligned} \qquad (13)$$

This result agrees with the result obtained earlier in [1, 2] for a classical system, specifically, the condition for the EIT effect to occur is the effective excitation of the collective degrees of freedom of the electron ensemble.

In order to provide the best illustration of the main features of the behavior of the dispersion curves and absorption line in the EIT regime, the plots shown in Figs. 2 and 3 were calculated for such values of the pump field intensity I_2 and collision frequency γ that are significantly higher than those in actual experiments. The results of calculations carried out for the actual values of these parameters are illustrated in Figs. 4 and 5, which show how the portions of the dispersion curve and absorption line behave under the EIT conditions.

For the same parameter values, the table illustrates the dependence of the main parameters of the propaga-
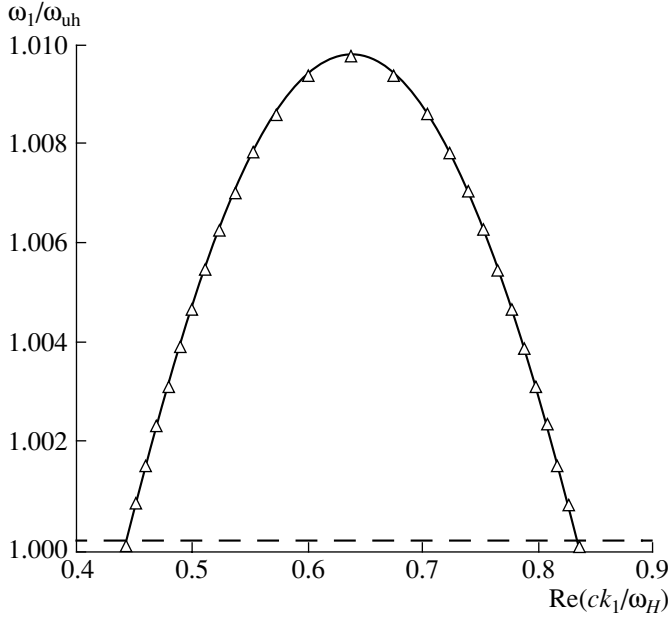
Fig. 4. Dispersion relations for the actual parameter values $I_2 = 10$ kW/cm^2 (solid curve), $I_2 = 0$ (dashed line), and $\mathrm{Re}\,D = 0$ (triangles), the remaining parameters being $N_0 = 2.5 \times 10^{12}$ cm^{-3}, $H = 35$ kG ($\omega_{uh}/2\pi = 100$ GHz, $\omega_p/\omega_H = 0.2$), $T = 1$ keV ($\gamma/\omega_H = 1 \times 10^{-8}$), $\omega_2/\omega_H = 0.83$, $\Theta_2 = 45°$, and $\Theta_1 = 90°$.

Fig. 5. Absorption line profile for the same parameter values as in Fig. 4.

tion of the signal wave on the pump field intensity. Here, $\Delta\omega$ is the width of the transparency region in the EIT regime (calculated as the difference between the frequencies at points *I* and *II*), $L = (2\,\mathrm{Im}\,k_1)^{-1}$ is the length over which the wave is absorbed at point *II*, and $V_{gr\,min}$ is the minimal value of the group velocity (at extremal point *II*). The quantity $\Delta\Theta$ is defined as the maximal allowable width of the angular spectrum of the signal wave and is obviously determined by the maximum allowable deviation Δk_1 of the wave vector k_1 from its optimal value $k_{opt} = k_2\sin\Theta_1/\sin\Theta_2$ (see conditions (13)): $\Delta\Theta = \arccos(1 - \Delta k_1/k_{opt})$. From the table, we see that the quantities $\Delta\omega$, L, and $V_{gr\,min}$ increase with pump field intensity; moreover, they increase according to the same laws as they do in the case of longitudinal propagation of waves in a cold plasma [8]:

$$\Delta\omega \propto I_2^{1/2}, \quad L \propto I_2, \quad V_{gr\,min} \propto I_2. \quad (14)$$

The above results were obtained for a homogeneous plasma. However, it is also important to consider the EIT effect in a spatially inhomogeneous medium. In this context, one possible application of the EIT effect in diagnostics-related problems is the transport of intrinsic radiation from the overcritical plasma region (the cutoff region in the vicinity of the UHR) toward the periphery of the system and then into vacuum.

Without going into the details of a rigorous theory of the EIT effect in an inhomogeneous medium, we inves-
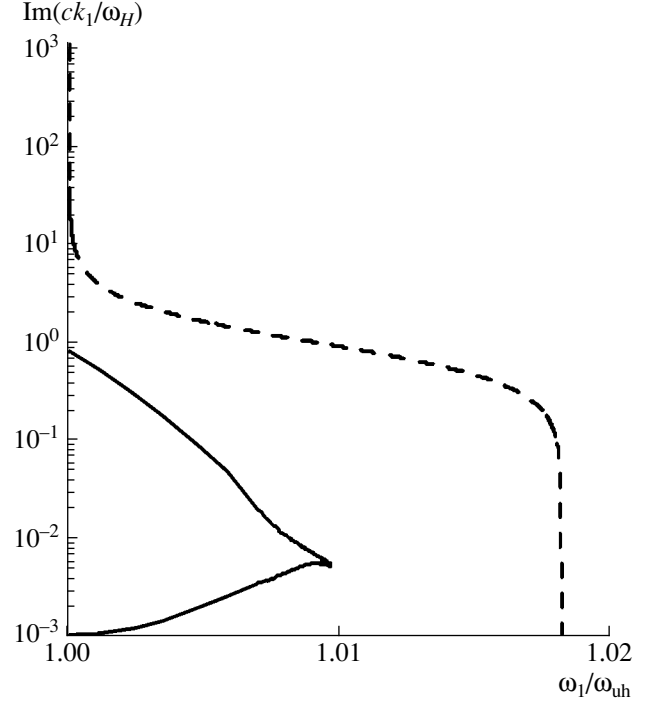
tigate the propagation of a signal wave in the EIT regime in the geometrical-optics approximation under the assumption that the wave propagates in the direction of the density gradient. To do this, we consider how the refractive index of the signal wave behaves as the plasma density N_0 varies. This behavior is illustrated in Fig. 6. We can see that, when the pump field intensity is finite, the dispersion curve includes two branches, *AB* and *CD*, which provide a coupling between the cutoff region (point *A*) and the vacuum region (point *D*). On both branches, the absorption of the signal wave is weak, $\mathrm{Im}\,k_1 \ll \mathrm{Re}\,k_1$ (along the branch *AB*, the absorption is weak due to the EIT effect, and, along the branch *CD*, it is weak because the absorption coefficient is nearly equal to its linear value). Strictly speaking, the branches *AB* and *CD* do not constitute a continuous portion of the dispersion curve; the wave, however, can transform from one branch to another in the region where they come close together (at the points *B* and *C*).

Main parameters of the propagation of a signal wave in the EIT regime

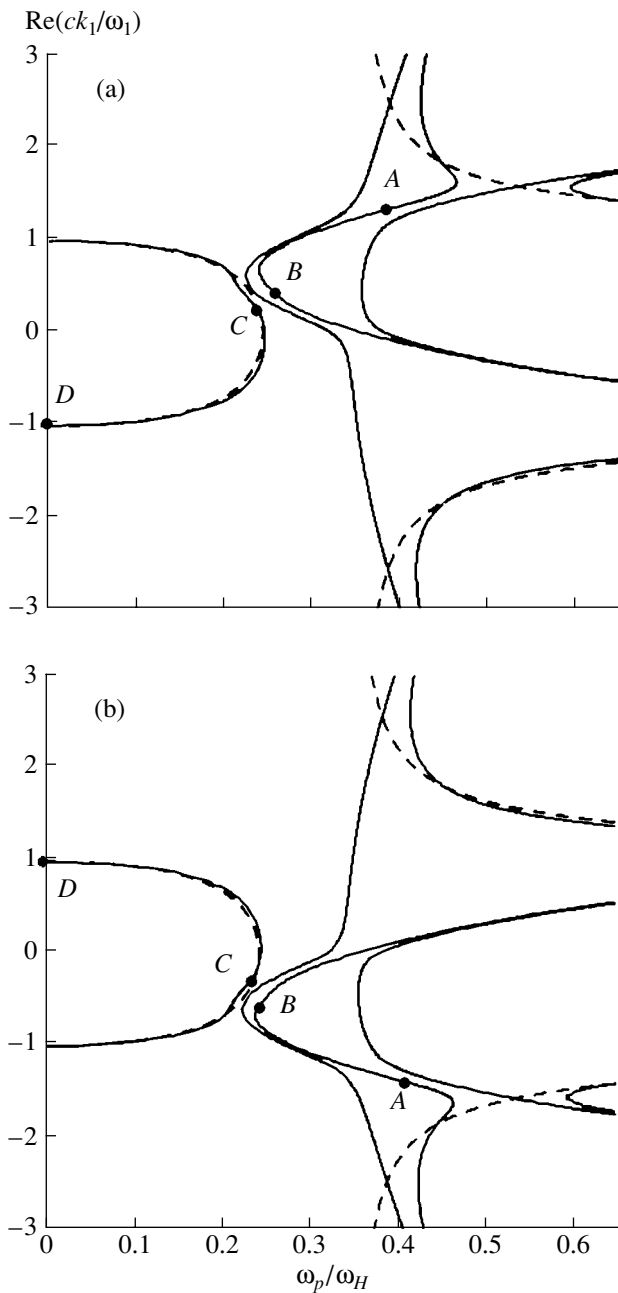| I_2, kW/cm^2	10	3	1	0
$\Delta\omega/\omega_{uh}$	5×10^{-3}	3×10^{-3}	1.5×10^{-3}	–
L, cm	20	5	1.5	2.5×10^{-4}
$V_{gr\,min}$/s	6×10^{-7}	2×10^{-7}	6×10^{-8}	–
$\Delta\Theta$, deg	38	33	28	–

Fig. 6. Behavior of the refractive index for a signal wave in an inhomogeneous ($\omega_1/\omega_H = 1.06$) plasma for $\Theta_2(\omega_p) =$ (a) 45° and (b) −45°, the remaining parameters being the same as in Fig. 2.

The wave transformation coefficient D_1 can be estimated (see Appendix 2), and the requirement for the transformation to be efficient ($D_1 \geq 90\%$) can be used to estimate the spatial scale on which the plasma density should vary. Thus, for a pump field intensity on the order of 10 kW/cm², the spatial scale should not exceed several tens of meters (for advanced controlled fusion devices, this condition is satisfied by a large margin).

For parameters corresponding to Fig. 6a, the signal wave can only propagate from the overcritical plasma region into vacuum along path *ABCD*. In this case, the reverse process (the propagation of a wave incident from vacuum into the opaque region) is impossible because, along all the portions of the dispersion curves that emerge from the opaque region and on which the absorption is weak, the direction of the group velocity is opposite to that of the plasma density gradient. Nevertheless, it is possible to force the waves to propagate into the dense plasma region by reversing the direction of the wave vector component of the pump wave that is orthogonal to the external magnetic field, i.e., by changing the sign of k_{2x}. In this case, the dispersion curve of the beat wave and, accordingly, the dependence $ck_1/\omega_1(\omega_p)$, which is determined by the position of this dispersion curve, are reflected symmetrically with respect to the abscissa (see Fig. 6b). The value of the group velocity of the signal wave and the extent to which it is absorbed change correspondingly, i.e., in such a way that the wave can propagate from vacuum into the opaque region along path *DCBA* in exactly the same manner as it propagates from the overcritical plasma region into vacuum along path *ABCD* (see Fig. 6a).

It should be noted that, in the EIT regime (in contrast to the linear case [10]), the angle between the wave vector of the signal wave and its group velocity is greater than $\pi/2$. This circumstance stems from the spatial dispersion of dielectric tensor (11) in the high-power pump wave field.

Hence, in the EIT regime, either the transport of the signal wave from the opaque region into vacuum or the opposite process—the injection of radiation from vacuum into the cutoff region—may be possible, depending the parameter values.

4. SIGNAL WAVE IN THE VICINITY OF THE ELECTRON CYCLOTRON RESONANCE

Along with the case of the UHR, we numerically analyzed expressions (9)–(11) in order to investigate the propagation of a signal wave at a frequency close to the electron cyclotron frequency ω_H. This problem provides an important logical connection between the problem of the EIT effect in the case of longitudinal propagation of a signal wave in the vicinity of the ECR [1] and the problem of the EIT effect in the case of quasi-transverse propagation of a signal wave in the vicinity of the UHR.

It is well known [9] that the absorption of a transversely propagating X wave is strongest at the upper hybrid frequency. As for the absorption at the electron cyclotron frequency, it corresponds to the wing of the absorption line of an X wave and is weak in comparison to the maximal absorption:

$$\operatorname{Im} k_1(\omega_1 = \omega_H)/\operatorname{Im} k_1(\omega_1 = \omega_{uh}) \sim (\gamma/\omega_1)^{3/2} \ll 1. (15)$$
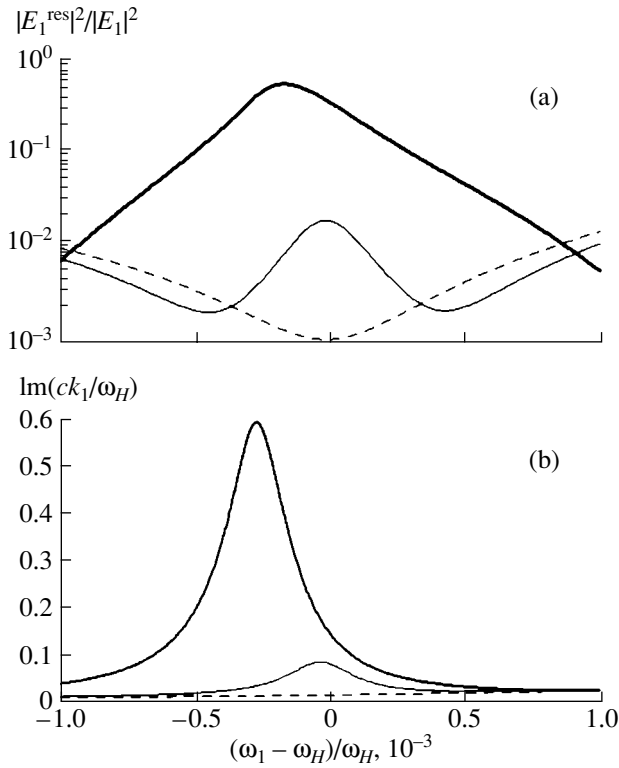
Fig. 7. (a) Amplitudes of the resonant electric-field component and (b) absorption line profiles for a signal wave in the ECR region for $I_2 = 400$ kW/cm^2 (heavy solid curves), $I_2 = 40$ kW/cm^2 (light solid curves), and $I_2 = 0$ (dashed curves). The remaining parameters are $N_0 = 6 \times 10^{11}$ cm^{-3}, $H = 35$ kG ($\omega_H/2\pi = 100$ GHz, $\omega_p/\omega_H = 0.1$), $\gamma/\omega_H = 3.0 \times 10^{-4}$, $\omega_2/\omega_H = 0.9$, $\Theta_2 = 17°$, and $\Theta_1 = 90°$.

The polarization of an obliquely propagating wave with the electron cyclotron frequency in a plane perpendicular to the external magnetic field is nearly circular, with the electric field vector rotating in the direction opposite to that of the electron gyration. The amplitude of the resonant electric-field component $\mathbf{E}_1^{res}$ (which is circularly polarized, with the electric field vector rotating in the direction of the electron gyration) is relatively small. It is determined by dissipative effects,

$$E_1^{res}/E_1 \sim \gamma/\omega_1 \ll 1, \qquad (16)$$

and also by the particle thermal motion, provided that spatial dispersion is taken into account. This is the so-called effect of depression of the resonant electric-field component. It serves, in particular, to explain why the absorption of an obliquely propagating wave with the cyclotron frequency is relatively weak [11].

However, in the case of a finite-amplitude pump wave, its nonlinear interaction with plasma oscillations gives rise to an electromagnetic field whose frequency is equal to the frequency of the signal wave and whose polarization vector generally has a larger resonant com-

ponent (see Fig. 7a). In turn, it is quite clear that the enhancement of this resonant component of the polarization vector is accompanied by an increase in the dissipation of the energy of the signal wave (Fig. 7b). The shift of the peak in the absorption line toward lower frequencies is obviously associated with the fact that, as the pump field intensity increases, the resonant component of the polarization vector is enhanced most efficiently at lower frequencies (see Fig. 7a).

Hence, this regime of the parametric interaction between the waves is not, strictly speaking, the EIT regime because, in this case, the absorption of the signal wave increases (rather than decreases). Nevertheless, the regime just considered has one interesting feature: the nonlinear parametric interaction between the waves leads to the efficient excitation of the collective degrees of freedom (in analogy with the ordinary EIT effect in plasma), thereby giving rise to strong polarization effects and significantly changing the propagation conditions of a signal wave.

5. CONCLUSIONS

In the present paper, we have investigated the EIT effect in plasma in the case of electromagnetic radiation propagating obliquely to the external magnetic field. In the parameter range corresponding to the efficient excitation of longitudinal plasma oscillations at the beat frequency, the group velocity of the signal wave in the vicinity of the UHR is strongly slowed down and the dissipation of its energy decreases substantially. The main parameters of the propagation of the signal wave (the absorption length, the width of the transparency window, and the maximum extent to which the wave group velocity is slowed down) depend on the pump field intensity in the same manner as in the case of longitudinal wave propagation that was studied earlier. It has been predicted that a signal wave can propagate in a smoothly inhomogeneous plasma in the EIT regime (from the overcritical plasma region into vacuum, and vice versa).

Possible applications of the EIT effect in a magnetized plasma may be associated with the problems of diagnosing fusion plasmas by extracting the intrinsic plasma radiation from the cutoff region. In connection with this, it seems worthwhile to further investigate the EIT effect in a spatially inhomogeneous plasma in which the plasma frequency is higher than the electron gyrofrequency. It is known [11] that, in such a plasma, the cutoff region in the cross section of the torus is closed; hence the intrinsic plasma radiation cannot be extracted from the central regions of the system. In the EIT regime, however, the extraction of radiation is in principle possible.[1]

Another problem that seems to be important enough to require further study is that in which, in addition to a

---

[1] Under certain conditions, the extraction of plasma radiation can also be provided by the so-called OXB (or z) transformation [11].

signal wave at the frequency $\omega_2 + \omega_p$ (an anti-Stokes satellite), account is taken of a wave mode at the frequency $\omega_2-\omega_p$ (a Stokes satellite). This wave mode also can exist in the system and generally can have an appreciable impact on the dispersion properties of the signal wave. On the other hand, analogous investigations carried out for isotropic [12] and magnetized [3] plasmas showed that accounting for this mode does not significantly alter the EIT effect. This permits us to hope that, in a more rigorous analysis of the problems in question, the EIT effect will be at least no less pronounced and the main results obtained above will remain valid.

APPENDIX 1

The matrix $A(\omega_1, k_1, \Theta_1)$ and scalar $B(\omega_1, k_1, \Theta_1)$, which were introduced in relationship (11), have the following form:

$$A = \frac{\omega_p^2}{\omega_1\omega_H|\mu_{xx}|^2(|1 - i(\omega_1/\omega_H)K_y|^2 + |i(\omega_1/\omega_H) + K_y|^2) + |K_z|^2}\left\{\frac{\omega_2}{\omega_H}M_1^{-1}M_{21}C_1\right.$$

$$\left. - \frac{\omega_p^2}{\omega_1\omega_H}\frac{\omega_2^2}{\omega_L^2}M_1^{-1}M_{22}\overline{\left(\frac{\omega_2}{\omega_H}M_L^{-1} - M_{L2}\right)}M_L^{-1}M_{24} + BM_1^{-1} + M_{26}(C_1 + C_2M_1^{-1}) - \frac{\omega_p^2}{\omega_1\omega_H}C_4\right\},$$

$$B = \frac{C_{3zz}/M_{1zz} + [M_{1xx}(C_{3xx} + C_{3xy}) + M_{1xy}(C_{3xy} - C_{3yx})]/(M_{1xx}^2 + M_{1xy}^2)}{|\mu_{xx}|^2(|1 - i(\omega_1/\omega_H)K_y|^2 + |i(\omega_1/\omega_H) + K_y|^2) + |K_z|^2}.$$

Here, $\mu = im\omega_2\mu_2/e$, with μ_2 being the mobility tensor for the pump wave, and $K_{y,z} = E_{2y,z}/E_{2x}$ are the polarization coefficients for the pump wave [9]. For convenience, the following notation is introduced: $\overline{M} = M^{-1}\det M$. The 3×3 matrices M_1, M_L, M_{L2}, M_{21}, M_{22}, M_{23}, M_{24}, M_{25}, M_{26}, and $C_{1,2,3,4}$ are defined as follows:

$$C_1 = \frac{\omega_2}{\omega_1}M_L^{-1}\left[\frac{\omega_p^2}{\omega_L\omega_H}\overline{\left(\frac{\omega_2}{\omega_H}M_L^{-1} - M_{L2}\right)}M_L^{-1} + D\right]M_{24}$$

(where the determinant D is defined by relationship (12)),

$$C_2 = \frac{\omega_p^2}{\omega_L\omega_H}M_L^{-1}\overline{\left(\frac{\omega_2}{\omega_H}M_L^{-1} - M_{L2}\right)}\left(\frac{\omega_2}{\omega_H}M_L^{-1}M_{23} - M_{25}\right)$$

$$- \frac{\omega_2}{\omega_H}M_L^{-1}M_{23}D,$$

$$C_3 = -\frac{\omega_p^2}{\omega_L\omega_H\omega_L}\frac{\omega_2}{\omega_L}M_{22}\left(\frac{\omega_2}{\omega_H}M_L^{-1}M_{23} - M_{25}\right)$$

$$+ \frac{\omega_2}{\omega_H}M_{21}C_2,$$

$$C_{4xx} = M_{1yy}C_{3zz} + M_{1zz}C_{3yy},$$

$$C_{4xy} = -M_{1zz}C_{3xy} - M_{1xy}C_{3zz},$$

$$C_{4xz} = M_{1xy}C_{3yz} - M_{1yy}C_{3xz},$$

$$C_{4yx} = -M_{1yx}C_{3zz} - M_{1zz}C_{3yx},$$

$$C_{4yy} = M_{1zz}C_{3xx} + M_{1xx}C_{3zz},$$

$$C_{4yz} = M_{1yx}C_{3xz} - M_{1xx}C_{3yz},$$

$$C_{4zx} = M_{1yx}C_{3zy} - M_{1yy}C_{3zx},$$

$$C_{4zy} = M_{1xy}C_{3zx} - M_{1xx}C_{3zy},$$

$$C_{4zz} = M_{1xx}(C_{3xx} + C_{3yy}) + M_{1xy}(C_{3xy} - C_{3yx}).$$

$$M_{1,L}$$

$$= \begin{pmatrix} (\omega_{1,L} + i\gamma)/\omega_H & i & 0 \\ -i & (\omega_{1,L} + i\gamma)/\omega_H & 0 \\ 0 & 0 & (\omega_{1,L} + i\gamma)/\omega_H \end{pmatrix},$$

$$M_{L2}$$

$$= \begin{pmatrix} 1 - c^2k_{Lz}^2/\omega_L^2 & 0 & (ck_{Lx}/\omega_L)(ck_{Lz}/\omega_L) \\ 0 & 1 - c^2k_L^2/\omega_L^2 & 0 \\ (ck_{Lx}/\omega_L)(ck_{Lz}/\omega_L) & 0 & 1 - c^2k_{Lx}^2/\omega_L^2 \end{pmatrix},$$

$$M_{21xx} = (k_{1x}/k_2)(\mu_{xx} + \mu_{xy}K_y) + (k_{Lz}/k_2)K_z,$$

$$M_{22xx} = -(k_{Lz}/k_2)K_z,$$

$$M_{21xy} = K_y\sin\Theta_2,$$

$M_{22xy} = (k_{Lx}/k_2)(\mu_{yx} + \mu_{yy}K_y),$

$M_{21xz} = (\mu_{xx} + \mu_{xy}K_y - 1)\cos\Theta_2 + K_z\sin\Theta_2,$

$M_{22xz} = (k_{Lx}/k_2)K_z,$

$M_{21yx} = (\mu_{yx} + \mu_{yy}K_y - K_y)\sin\Theta_2,$

$M_{22yx} = 0,$

$M_{21yy} = (k_{Lx}/k_2)(\mu_{xx} + \mu_{xy}K_y) + (k_{Lz}/k_2)K_z,$

$M_{22yy} = -(k_{Lx}/k_2)(\mu_{xx} + \mu_{xy}K_y) - (k_{Lz}/k_2)K_z,$

$M_{21yz} = (\mu_{yx} + \mu_{yy}K_y - K_y)\cos\Theta_2,$

$M_{22yz} = 0,$

$M_{21zx} = \cos\Theta_2,$

$M_{22zx} = (k_{Lz}/k_2)(\mu_{xx} + \mu_{xy}K_y),$

$M_{21zy} = K_y\cos\Theta_2,$

$M_{22zy} = (k_{Lz}/k_2)(\mu_{yx} + \mu_{yy}K_y),$

$M_{21zz} = (k_{Lx}/k_2)(\mu_{xx} + \mu_{xy}K_y).$

$M_{22zz} = -(k_{Lx}/k_2)(\mu_{xx} + \mu_{xy}K_y).$

$M_{23xx} = -(k_{Lx}/k_2)(\mu_{xx}^* + \mu_{xy}^*K_y^*) - (k_{1z}/k_2)K_z^*,$

$M_{24xx} = -(k_{1z}/k_2)K_z^*,$

$M_{23xy} = K_y^*\sin\Theta_2,$

$M_{24xy} = (k_{1x}/k_2)(\mu_{yx}^* + \mu_{yy}^*K_y^*),$

$M_{23xz} = (\mu_{xx}^* + \mu_{xy}^*K_y^* - 1)\cos\Theta_2,$

$M_{24xz} = (k_{1x}/k_2)K_z^*,$

$M_{23yx} = (\mu_{yx}^* + \mu_{yy}^*K_y^* - K_y^*)\sin\Theta_2,$

$M_{24yx} = 0,$

$M_{23yy} = -(k_{1x}/k_2)(\mu_{xx}^* + \mu_{xy}^*K_y^*) - (k_{1z}/k_2)K_z^*,$

$M_{24yy} = -(k_{1x}/k_2)(\mu_{xx}^* + \mu_{xy}^*K_y^*) - (k_{1z}/k_2)K_z^*,$

$M_{23yz} = (\mu_{yx}^* + \mu_{yy}^*K_y^* - K_y^*)\cos\Theta_2,$

$M_{24yz} = 0,$

$M_{23zx} = \cos\Theta_2,$

$M_{24zx} = (k_{1z}/k_2)(\mu_{xx}^* + \mu_{xy}^*K_y^*),$

$M_{23zy} = K_y^*\cos\Theta_2,$

$M_{24zy} = (k_{1z}/k_2)(\mu_{yx}^* + \mu_{yy}^*K_y^*),$

$M_{23zz} = (\mu_{yx}^* + \mu_{yy}^*K_y^*)\cos\Theta_2 - (k_{1z}/k_2)K_z^*$
$\qquad - (k_{1x}/k_2)(\mu_{xx}^* + \mu_{xy}^*K_y^*).$

$M_{24zz} = -(k_{1x}/k_2)(\mu_{xx}^* + \mu_{xy}^*K_y^*).$

$M_{25xx} = (k_{1x}\omega_2/k_2\omega_1 + \sin\Theta_2)$
$\qquad \times (\mu_{xx}^* + \mu_{xy}^*K_y^*) + K_z^*\cos\Theta_2,$

$M_{26xx} = (k_{Lx}\omega_2/k_2\omega_L + \sin\Theta_2)$
$\qquad \times (\mu_{xx} + \mu_{xy}K_y) + K_z\cos\Theta_2,$

$M_{25xy} = 0,$

$M_{26xy} = 0,$

$M_{25xz} = (k_{1z}\omega_2/k_2\omega_1)(\mu_{xx}^* + \mu_{xy}^*K_y^*),$

$M_{26xz} = (k_{Lz}\omega_2/k_2\omega_L)(\mu_{xx} + \mu_{xy}K_y),$

$M_{25yx} = (k_{1x}\omega_2/k_2\omega_1)(\mu_{yx}^* + \mu_{yy}^*K_y^*),$

$M_{26yx} = (k_{Lx}\omega_2/k_2\omega_L)(\mu_{yx} + \mu_{yy}K_y),$

$M_{25yy} = (\mu_{xx}^* + \mu_{xy}^*K_y^*)\sin\Theta_2 + K_z^*\cos\Theta_2,$

$M_{26yy} = (\mu_{xx} + \mu_{xy}K_y)\sin\Theta_2 + K_z\cos\Theta_2,$

$M_{25yz} = (k_{1z}\omega_2/k_2\omega_1)(\mu_{yx}^* + \mu_{yy}^*K_y^*),$

$M_{26yz} = (k_{Lz}\omega_2/k_2\omega_L)(\mu_{yx} + \mu_{yy}K_y),$

$M_{25zx} = (k_{1x}\omega_2/k_2\omega_1)K_z^*,$

$M_{26zx} = (k_{Lx}\omega_2/k_2\omega_L)K_z,$

$M_{25zy} = 0,$

$M_{26zy} = 0,$

$M_{25zz} = (\mu_{xx}^* + \mu_{xy}^*K_y^*)\sin\Theta_2$
$\qquad + (k_{1z}\omega_2/k_2\omega_1 + \cos\Theta_2)K_z^*.$

$M_{26zz} = (\mu_{xx} + \mu_{xy}K_y)\sin\Theta_2$
$\qquad + K_z(k_{Lz}\omega_2/k_2\omega_L + \cos\Theta_2).$

APPENDIX 2

Here, we estimate the characteristic value of the transformation coefficient D_1 for a signal wave when it transforms from point B to point C, at which the two branches of the dispersion curve come close together (see Fig. 6). This value can be estimated, e.g., by using the method of phase integrals [10]. In this way, the transformation coefficient is given by the expression $D_1 = \exp(-\delta)$ with

$$\delta = \left| \frac{\omega_1}{c} L_N \oint_L \frac{N_1 - N_2}{2} d\nu \right|. \qquad (17)$$

Here, $\nu = \omega_p^2/\omega_1^2$, N_1 and N_2 are the values of the refractive index at the two branches of the dispersion curve
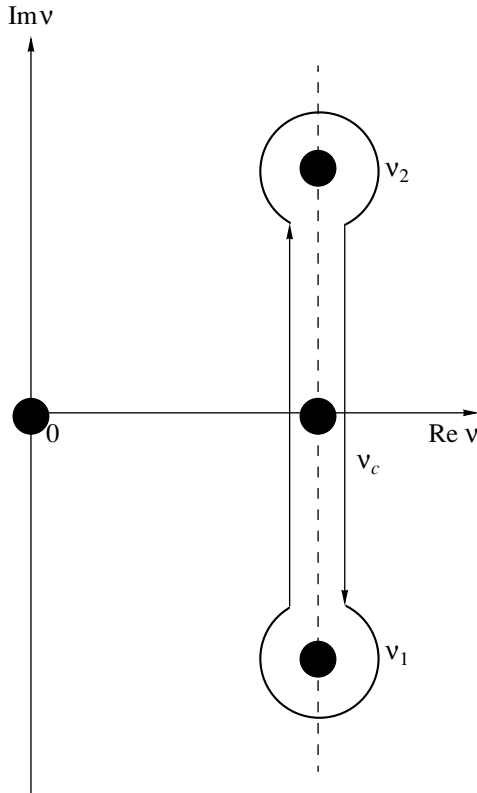
Imν

ν₂

ν_c

Re ν

0

ν₁

Fig. 8. Integration contour in formula (17).

under consideration, and L_N is the characteristic spatial scale on which the plasma density varies. It is assumed that the direction of the plasma density gradient coincides with the propagation direction of the signal wave. In expression (17), the integration is carried out along a contour that encircles the branch points of the function $G(\nu) = N_1(\nu) - N_2(\nu)$, whose positions are determined by the relationship $G(\nu) = 0$.

With the exact expressions for the refractive indices $N_{1,2}(\nu)$, the positions of the singular points cannot be determined analytically. This is why we approximate the branches of the dispersion curves in the region where they come close together by the dependence

$$[N - N_c - a_1(\nu - \nu_c)][N - N_c - a_2(\nu - \nu_c)] = \mu, \quad (18)$$

which is the equation for the two hyperbolas such that (ν_c, N_c) are the coordinates of the intersection point of their asymptotes, a_1 and a_2 are the tangents of the angles of inclination of the asymptotes, and μ is a small parameter characterizing the distance between the asymptotes (for the dispersion curves shown in Fig. 6, we have $\mu > 0$). These parameters of the model dispersion curve are determined from the condition for the root-mean-square deviation from the actual dispersion curve to be minimal. Equation (18) can easily be

resolved in terms of $N(\nu)$ to yield the following expression for $G(\nu)$:

$$G(\nu) = \sqrt{(a_1 - a_2)^2(\nu - \nu_c)^2 + 4\mu}. \quad (19)$$

We thus see that the function $G(\nu)$ has two branch points:

$$\nu_{1,2} = \nu_c \pm i\frac{2\sqrt{\mu}}{|a_1 - a_2|}. \quad (20)$$

If we choose the integration contour like that shown in Fig. 8, we can readily take the integral in formula (17) to obtain the following expression for δ:

$$\delta = \frac{\omega_1}{c}L_N\frac{2\pi\mu}{|a_1 - a_2|}. \quad (21)$$

From the requirement for the transformation to be efficient, $\delta \leq 0.1$ (which corresponds to $D_1 \geq 90\%$), we can estimate the maximum allowable spatial scale of the plasma density variations:

$$L_N \leq 0.1\frac{c}{\omega_1}\frac{|a_1 - a_2|}{2\pi|\mu|}. \quad (22)$$

From this estimate, we find that, for a pump field intensity of 10 kW/cm² and for parameters corresponding to Fig. 4 ($\mu \sim 10^{-5}$, $|a_1 - a_2| \sim 10$), the characteristic spatial scale of the plasma density variations should not exceed 10 meters.

It should be noted that this method for estimating the transformation coefficient is rather approximate and thus should be used with a great deal of care because of the exponential dependence of D_1 on δ. Instead of considering the actual dependence $G(\nu)$, we have approximated it by a known function without allowance for the fact that, in the vicinity of points B and C in Fig. 6, three (rather than merely two) branches of the dispersion curve come close together. There are, however, two particular reasons why the proposed method is quite adequate for purposes of obtaining rough estimates. First, the third branch of the dispersion curve corresponds to a strongly absorbed signal wave ($\mathrm{Im}k_1 \sim \mathrm{Re}k_1$); hence, such a wave is not generated during the transformation. Second, the form of expression (21) seems to be fairly reasonable (as is clear from dimensionality considerations): the wave transformation coefficient increases with decreasing scale L_N of plasma density variations and/or distance (proportional to μ) between the branches of the dispersion curve. Note that, although the minimum distance between the branches decreases with pump wave power, there exists a certain threshold pump power, which is governed by dissipative effects.

REFERENCES

1. A. G. Litvak and M. D. Tokman, Phys. Rev. Lett. **88**, 095003 (2002).

2. A. Yu. Kryachko, A. G. Litvak, and M. D. Tokman, Zh. Éksp. Teor. Fiz. **122**, 805 (2002) [JETP **95**, 697 (2002)].

3. M. S. Hur, J. S. Wurtele, and G. Shvets, Phys. Plasmas **10**, 3004 (2003).

4. S. E. Harris, Phys. Today **50**, 36 (1997).

5. S. E. Harris, Phys. Rev. Lett. **82**, 4611 (1999).

6. G. Shvets and J. S. Wurtele, Phys. Rev. Lett. **89**, 115003 (2002).

7. M. Tushentsov, G. Shvets, A. Kryachko, and M. Tokman, IEEE Trans. Plasma Sci. **33** (2005) (in press); A. Yu. Kryachko, M. D. Tokman, G. Shvets, and M. Tushentsov, in *Proceedings of the 13th Joint Workshop on ECE and ECRH, Nizhni Novgorod, 2004* (in press).

8. A. G. Litvak and M. D. Tokman, Izv. Vyssh. Uchebn. Zaved., Radiofiz. **44**, 407 (2001) [Radiophys. Quant. Electron. **44**, 375 (2001)].

9. *Plasma Electrodynamics*, Ed. by A. I. Akhiezer, I. A. Akhiezer, R. V. Polovin, *et al.* (Nauka, Moscow, 1974; Pergamon, Oxford, 1975).

10. V. L. Ginzburg, *The Propagation of Electromagnetic Waves in Plasmas* (Nauka, Moscow, 1967; Pergamon, Oxford, 1970).

11. V. V. Alikaev, A. G. Litvak, E. V. Suvorov, and A. A. Fraĭman, in *High-Frequency Plasma Heating*, Ed. by A. G. Litvak (IPF AN SSSR, Gorki, 1983; AIP, New York, 1991).

12. D. F. Gordon, W. B. Mori, and C. Joshi, Phys. Plasmas **7**, 3145 (2000).

Translated by O.E. Khadin

Electromagnetic Plasma Acceleration in an Inverse Z-Pinch Geometry

S. A. Sorokin

Institute of High-Current Electronics, Siberian Division, Russian Academy of Sciences,
Akademicheskiĭ pr. 4, Tomsk, 634055 Russia
Received February 10, 2004; in final form, April 1, 2004

Abstract—Results are presented from experimental studies of the electromagnetic acceleration of a hydrogen or deuterium plasma in an inverse Z-pinch geometry. The acceleration dynamics of the plasma shell was simulated in a zero-dimensional model and was measured with magnetic probes. The ion energy spectrum in the plasma flow was determined with the help of ion collectors by the time-of-flight technique. © *2005 Pleiades Publishing, Inc.*

1. INTRODUCTION

In [1, 2], the possibility was analyzed of using intense plasma flows generated with the help of pulsed plasma accelerators to study the interaction between low-Z nuclei at low energies. To implement this idea in practice, it is necessary to have such an accelerator scheme that would make it possible to vary the mean ion energy and the intensity of the ion flux onto a target, as well as to separate the processes of plasma acceleration and plasma–target interaction in space and time. The limitation on the intensity of the ion flux onto the target is dictated by the requirement that the physical properties of the target must remain unchanged in the course of interaction. In particular, the energy (per atom) released in the interaction with a solid target should be substantially lower than the sublimation energy. The spatial and temporal separation of the processes of plasma acceleration and plasma–target interaction facilitates the extraction of the valid signal against the background signal, which is caused primarily by the processes occurring in the accelerated plasma. In this paper, we study the formation of a radially expanding flow of a hydrogen or deuterium plasma in an inverse Z-pinch geometry [3]. The radial expansion of the flow allows us to meet almost all the above requirements by properly positioning the target. The objective of the study is to determine the design and initial parameters of a plasma accelerator that would be capable of transporting the generator current to the plasma shell, to accelerate the radially expanding plasma flow up to $v \sim 10^8$ cm/s, and to measure the energy spectrum of the accelerated ions.

2. EXPERIMENTAL SETUP AND DIAGNOSTIC TECHNIQUE

Experiments were carried out on the SGM and MIG high-current generators with a current pulse duration of

~100 ns and current amplitudes of ~0.9 and 1.6 MA, respectively [4, 5]. A schematic of the experimental setup is shown in Fig. 1. The working gas was fed to annular nozzle *3* through a fast electrodynamic valve. The gas jet formed by the nozzle passed through high-transparency grid *2* (a set of 48 radially oriented wires 120 μm in diameter). Thus, an annular gas shell was produced in the gap between the nozzle and the grid. The average radius of the annular nozzle was ~15 mm, and the radius of the central rod was 6 mm. The load unit was connected to the high-current generator through a vacuum magnetically insulated line (electrodes *5* and *6*). After the breakdown of the gas jet, the generator current flowed through the plasma shell and the grid and returned back through the central rod, thus accelerating the plasma shell away from the axis. A current-hogging structure (CHS) in the form of a squirrel cage made of 24 steel rods 2 mm in diameter was
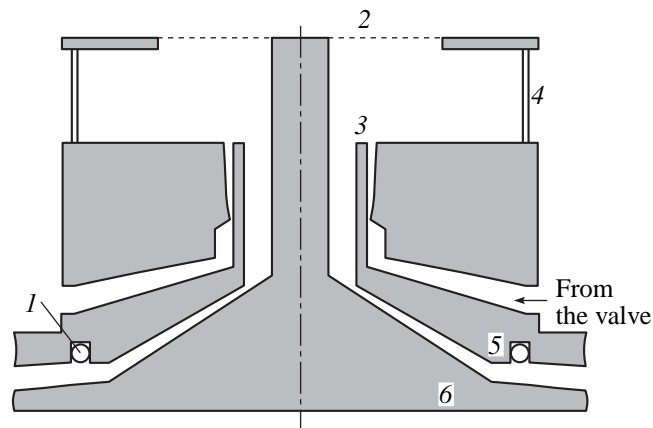

Fig. 1. Schematic of the experimental setup: (*1*) Rogowski coil, (*2*) grid, (*3*) nozzle, (*4*) current-hogging structure, (*5*) anode, and (*6*) cathode.

placed at a radius of 45 mm. When the plasma shell passed through the CHS region, the current switched to the CHS rods. The mass per unit length of the gas get was controlled by varying the pressure in the valve plenum and the delay time of triggering the generator. The efficiency of current transport to the load and the propagation dynamics of the current shell were measured with a Rogowski coil and magnetic probes. The angular energy distribution in the plasma flow and the time-integrated energy density deposited in the target were measured with a resistive bolometer. The ion energy spectrum in the plasma flow was measured with the help of ion collectors by the time-of-flight technique [6]. To separate the ion component, a negative bias (>200 V) was applied to the collector. For ions with a charge z and density n, the current density at the collector is equal to

$$j = e(z + \gamma)n\upsilon,$$

where e is the electron charge, γ is the coefficient of secondary ion–electron emission, and υ is the ion velocity. For a hydrogen (deuterium) plasma, in which only one ion component is present, time-of-flight measurements allow one, in principle, to unambiguously measure the ion energy spectrum, provided that the parameters of secondary ion–electron emission are known. To reduce the ion flux onto the collector (i.e., to reduce the plasma density), we used an entrance pinhole located at a certain distance from the collector. In our experiments, we used three ion collectors. In spite of the limited number of the high-current generator shots, the use of three collectors allowed us to test the diagnostics and to determine the operating parameters of the detectors (the optimal distance from the ion source to the collector, the optimal diameter of the entrance pinhole of the ion flux attenuator, the sensitivity of the measuring channel, etc.).

3. EXPERIMENTAL RESULTS AND DISCUSSION

3.1. Electromagnetic Plasma Acceleration

The propagation dynamics of the current-carrying shell was measured with the help of magnetic probes. It was assumed that the instant at which the probe signal began to rapidly grow corresponded to the arrival of the shell at the radius where the probe was installed. Figure 2 shows signals from the Rogowski coil and from the magnetic probe located at a radius of 28 mm for a typical shot of the MIG generator. The probe measurements were compared to the results of zero-dimensional simulations of the plasma dynamics in the snowplow approximation. The current through the load was calculated for the specific parameters of the electric circuit. It should be noted that the magnetic probes served merely to determine the instant at which the current-carrying shell arrived at a given radius. Thereafter, the probe signals could not be used to adequately determine the current flowing through the accelerated shell and the efficiency of the current transport through the
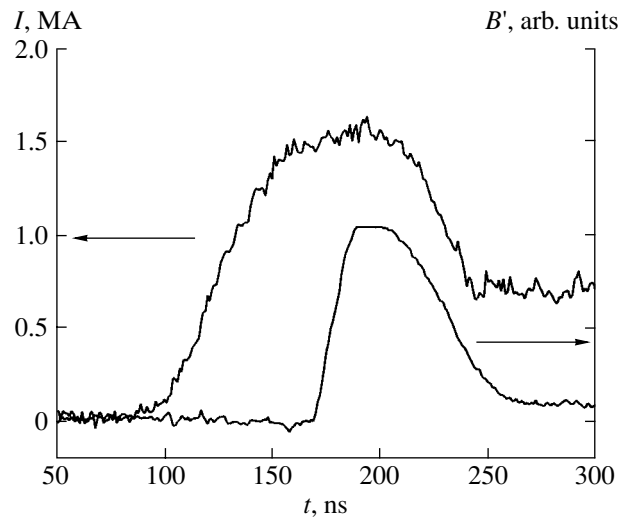

Fig. 2. Signals from the Rogowski coil (I) and the magnetic probe (B') located at a radius of 28 mm.

narrow coaxial channel with an outer and inner radii of 11 and 6 mm, respectively. A test shot in the absence of a gas jet was also performed. In this case, the current flowed through the CHS, and the generator load was purely inductive. The currents measured with the Rogowski coil and magnetic probes coincided within the measurement errors. Although this test was not quite correct, it confirmed the possibility of efficiently transporting the current to the load. Moreover, the propagation dynamics of the shell (to a radius of 35 mm) measured with the probes agrees with the results of zero-dimensional simulations; this also confirms the absence of appreciable current losses in the course of the current transport to the plasma shell. At the same time, the fact that the probe signal is zero until the current-carrying shell arrives at the probe (Fig. 2) means that no current flows through the CHS; i.e., the CHS is efficiently shielded by the shell. To determine the efficiency with which the current is switched to the CHS, we placed a probe beyond the CHS, at a radius of 50 mm. In this case, no component above the noise level was detected in the probe signal, whereas the signals from the probes located at radii less than 45 mm exceeded the noise level by one to two orders of magnitude. Hence, there are good reasons to believe that, beyond the CHS, the magnetic field is absent and the plasma expands freely.

The main drawback of schemes for axial plasma acceleration is that the magnetic field in the gap between the coaxial electrodes of the accelerator is radially nonuniform; as a result, the current-carrying shell is inclined and the plasma velocity has a radial component. The inverse pinch scheme is free of this drawback. However, in practice, due to the radial divergence of the gas jet, the current-carrying shell turns out to be inclined in the course of dragging the gas jet and may also remain inclined after dragging. In our experi-
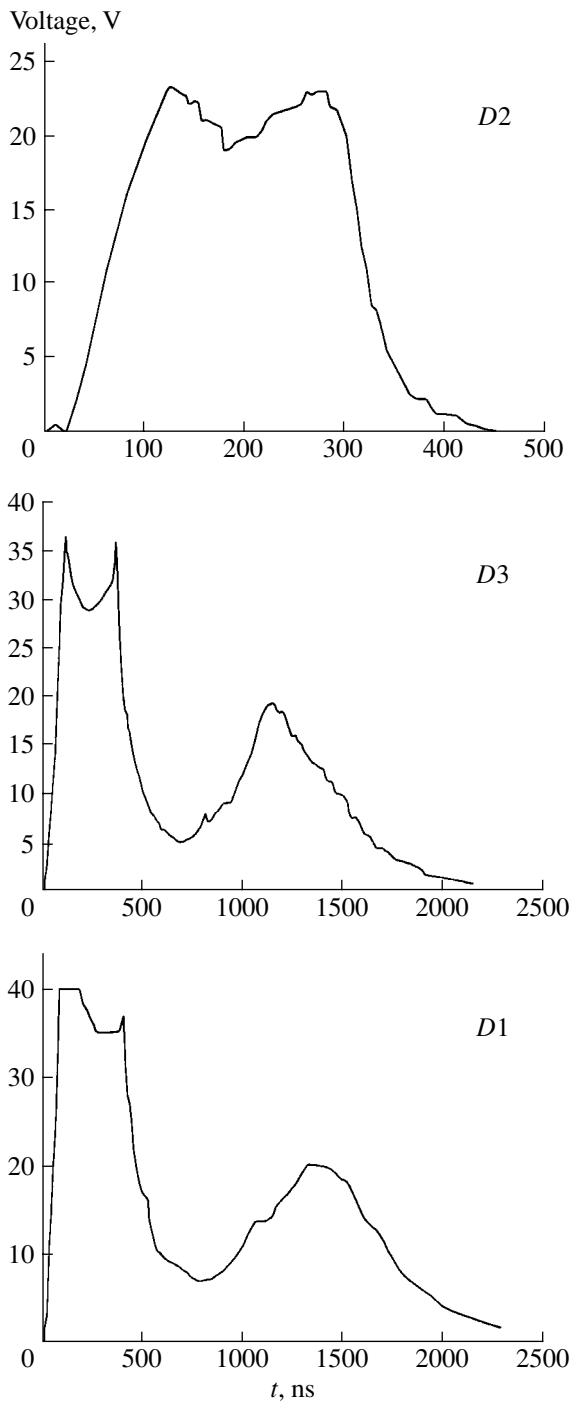
Fig. 3. Signals from three ion collectors located at radii of 30 cm (*D*2), 129 cm (*D*3), and 157 cm (*D*1).

ments, the divergence of the gas jet was compensated for by properly choosing the inclination of the jet nozzle to the *z* axis. The inclination of the current-carrying shell after jet dragging was estimated by using two magnetic probes positioned at the same radius near the cathode and anode. The time interval between the arrival of the shell to a radius of 35 mm at the positions of these probes was no longer than 2 ns, which corre-

sponded to $\Delta r \leq 1$ mm. Note that, using the waveforms of the signals from the probes positioned at a radius of more than 35 mm, it was difficult to unambiguously determine the time at which the current-carrying shell arrived at this radius. Moreover, the instant at which the probe signal appeared did not agree with the zero-dimensional simulations of the propagation dynamics of the plasma liner and with probe measurements at radii of less than 35 mm. This is probably related to the onset of Rayleigh–Taylor instability and to the breakdown of the cylindrical symmetry of the shell in the final stage of its acceleration.

3.2. Measurement of the Ion Energy Spectrum

Ion collector measurements showed that the photoelectric current caused by UV plasma radiation contributed substantially to the collector current at times of $t <$ 350 ns from the start of the current through the liner. For this reason, the collectors were placed at a radius of $r > 42$ cm, i.e., outside the vacuum chamber, because the transit time of the bulk ions to the vacuum chamber wall was 300–500 ns. Figure 3 shows the signals from three ion collectors positioned at radii of 30 cm (*D*2), 129 cm (*D*3), and 157 cm (*D*1) for one of the shots with a hydrogen liner. It can be seen that, as the distance between the collector and the ion source increases, the peak associated with the bulk ions can first be distinguished against the background of the photoelectric emission signal (*D*2, $r = 30$ cm) and then the peak produced by fast ions appears (*D*1 and *D*3).

The ion energy spectrum can be determined using the time-of-flight technique. Ignoring the radial size of the plasma bunch near the CHS and measuring time from the instant at which the current-carrying shell passes through the CHS in zero-dimensional simulations, we obtain

$$\frac{dN}{d\varepsilon} \propto \frac{1}{1 + \gamma(\varepsilon)} I(\varepsilon)\varepsilon^{-3/2},$$

where $I(\varepsilon)$ is the collector current at a time t corresponding to the arrival of the ions with energy ε,

$$\varepsilon = \frac{m_p v^2}{2} = \frac{m_p l^2}{2 t^2},$$

l is the distance from the CHS to the collector; m_p is the proton mass; and $\gamma(\varepsilon)$ is the coefficient of secondary ion–electron emission. The coefficient γ depends on the sort and charge of an ion, the ion velocity, the material of the collector, and the quality of its surface and requires calibrating in each particular case. In our experiments, we used an aluminum collector and used γ values obtained by extrapolating the available experimental data [7]. For proton energies of 4–30 keV, $\gamma(\varepsilon)$ can be approximated by the following expression (with deviations of no more than 2.5% from the measured values):
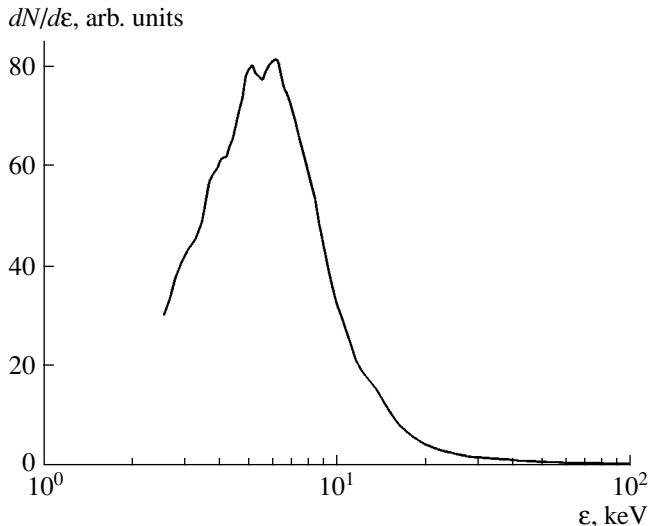
$$\gamma = 0.24\sqrt{\varepsilon \text{ (keV)}} - 0.07.$$

$dN/d\varepsilon$, arb. units

Fig. 4. Ion energy spectrum recovered from the signal measured with collector $D1$ (Fig. 3).

Figure 4 shows the spectrum determined from the signal measured with detector $D1$ (Fig. 3). The bulk of the accelerated ions has a rather broad energy spectrum (3–10 keV). It should be noted that, near the CHS, the velocity of the plasma shell calculated using signals from the probes located at a radius <3 cm corresponds to the lower boundary (~3 keV) of the ion energy spectrum. This allows us to suggest that, in the final stage of plasma acceleration ($r > 3$ cm, $v > 5 \times 10^7$ cm/s), the propagation dynamics of the shell is significantly affected by instabilities. Presumably, instabilities lead to the formation of a plasma flow with a broad energy spectrum and a fraction of the plasma does not undergo radial acceleration. In addition to the bulk ions with energies of 3–10 keV, fast ions with energies at least of up to 200 keV ($v \sim 6 \times 10^8$ cm/s) are also observed. The relative amount of these ions is difficult to estimate because the ions with velocities of $v > 4 \times 10^8$ cm/s reach a radius of 120 cm over a time shorter than 300 ns and the ion current is masked by the photoelectric current. Since the current of high-energy ions cannot be separated from the photoelectric current, the recovered spectrum at energies of >40 keV is qualitative in character. However, ions with velocities of 5×10^8 cm/s and higher are certainly present in the spectrum because the corresponding peak in the current signals shifts over time proportionally to the distance between the detector and the ion source (see Fig. 3). The presence of fast particles may be attributed to the ion acceleration by an ambipolar electric field at the boundary of the expanding plasma flow [8].

From the expression for the collector current $I = e(z + \gamma)nvs$ (where s is the area of the entrance pinhole of the collector), we can estimate the plasma density n at the entrance pinhole. The maximal density near collector $D3$, located at a radius of 129 cm, is ~4 $\times$ 10^{11} cm^{-3}. The collector current and the plasma density

near the collector were controlled by varying the diameter of the entrance pinhole located a distance of 5 cm from the collector.

The energy density in the radially expanding plasma was measured with a foil bolometer. Such measurements are justified because of the low reflection coefficient of ions from the foil and the low coefficient of the foil sputtering by light ions [9]. In the above shot, the bolometer foil (a strip of length $l = 4.5$ cm and width of ~2 mm) was placed parallel to the z axis at a radius of $r = 36$ cm. Assuming that the plasma flow is axially symmetric, the energy passing through a cylindrical surface with an area of $S = 2\pi rl = 6.28 \times 36 \times 4.5 \sim 1000$ cm^2 around the liner turned out to be about 1 kJ; i.e., the average energy density was about 1 J/cm^2. The measured energy density allows us to normalize the energy spectrum of ions arriving at the target.

4. CONCLUSIONS

The process of the formation of a radially expanding plasma flow in an inverse Z-pinch geometry has been studied. It is shown that, when the plasma is accelerated to a velocity of ~10^8 cm/s, the bulk of the accelerated ions has a rather broad energy spectrum (3–10 keV). In addition to the bulk ions, fast ions with energies at least of up to 200 keV are also observed. The presence of fast particles may be attributed to the ion acceleration in an ambipolar electric field at the boundary of the expanding plasma flow.

REFERENCES

1. V. B. Belyaev, V. M. Bystritsky, O. I. Kartavtsev, *et al.*, Preprint No. D15-92-324 (JINR, Dubna, 1992).
2. V. B. Belyaev, A. Bertin, V. M. Bystritsky, *et al.*, Nucleonics **40**, 85 (1995).
3. O. A. Anderson, H. P. Furth, J. M. Stone, and R. E. Wright, Phys. Fluids **1**, 489 (1958).
4. A. V. Luchinskiĭ, V. I. Makhrin, N. A. Ratakhin, *et al.*, Izv. Vyssh. Uchebn. Zaved., Fiz. **38**, 52 (1995).
5. A. V. Luchinskiĭ, N. A. Ratakhin, V. F. Fedushchak, *et al.*, Izv. Vyssh. Uchebn. Zaved., Fiz. **38**, 58 (1995).
6. N. G. Basov, Yu. A. Zakharenkov, A. A. Rupasov, *et al.*, *Diagnostics of Dense Plasmas* (Nauka, Moscow, 1989).
7. R. A. Baragiola, E. A. Alonso, and A. Oliva Florio, Phys. Rev. B **19**, 121 (1979).
8. A. V. Gurevich and L. P. Pitaevskii, in *Reviews of Plasma Physics*, Ed. by M. A. Leontovich (Atomizdat, Moscow, 1980; Consultants Bureau, New York, 1986), Vol. 10.
9. N. V. Pleshivtsev, *Cathode Sputtering* (Atomizdat, Moscow, 1968).

Translated by N.F. Larionova

Unsteady Processes during Stimulated Emission from a Relativistic Electron Beam in a Quasi-Longitudinal Electrostatic Pump Field

I. N. Kartashov*, M. V. Kuzelev*, and N. Sepehri Javan**

*Moscow State University, Vorob'evy gory, Moscow, 119992 Russia
**Zanjan University, Zanjan, Islamic Republic of Iran
Received January 26, 2004; in final form, March 29, 2004

Abstract—The problem of stimulated emission from a relativistic electron beam in an external electrostatic pump field is studied. A set of nonlinear time-dependent equations for the spatiotemporal dynamics of the undulator radiation amplitude and the amplitude of the beam space charge field is derived. The beam electrons are described by a modified version of the macroparticle method. The regimes of the single-particle and collective Cherenkov effects during convective and absolute instabilities are considered. The nonlinear dynamics of radiation pulses emitted during the instabilities of the beam in its interaction with the forward and backward electromagnetic waves is investigated. © *2005 Pleiades Publishing, Inc.*

A relativistic electron beam moving in a static periodic field can emit short-wavelength coherent electromagnetic radiation, which is called undulator radiation [1, 2]. The stimulated undulator radiation underlies the operation of such promising sources of electromagnetic waves as free-electron lasers [3–5]. The most widely recognized type of undulators seems to be a magnetostatic wiggler, which was successfully implemented and investigated in experiments [6]. The objective of the present paper is to consider an electrostatic undulator in which an external electrostatic field stimulates an electron beam to emit radiation. Note that the theory of stimulated emission from relativistic electron beams in electrostatic undulators has already been described in the literature (see, e.g., [7]). To the best of our knowledge, however, theoretical investigations in this direction were restricted to solving the so-called boundary- or initial-value problems; this makes it possible to consider only steady-state phenomena in systems with an electrostatic pump field. This approach, of course, does not enable one to investigate various unsteady and transient processes in free-electron lasers. Among the most important unsteady phenomena whose description requires the development of a far more complete spatiotemporal mathematical model are the self-excitation of oscillations in the electrodynamic system of a laser, the relaxation of oscillations in the system, the formation of the radiation spectrum, the dynamics of electromagnetic radiation pulses, and the interaction and competition between electromagnetic modes of different structure. In what follows, we will derive time- and coordinate-dependent nonlinear equations and use them to investigate some of these unsteady transient processes, which occur during the dynamic evolution of

a relativistic electron beam stimulated to emit radiation by an electrostatic pump field.

Let us consider the radiation emitted by a straight relativistic monoenergetic electron beam in a waveguide in the presence of a static electric field,

$$E_{z0} = \frac{1}{2}[E_0(r_\perp)\exp(i\chi z) + \text{c.c.}], \quad E_0 = E_0^*, \quad (1)$$

and an infinitely strong external longitudinal magnetic field (here, the z axis is assumed to coincide with the longitudinal waveguide axis and $r_\perp$ is the radial coordinate in the waveguide cross section).

We start with the following general equations, which are widely used in microwave electronics [8]:

$$\frac{\partial}{\partial z}\left(\Delta_\perp + \frac{\partial^2}{\partial z^2} - \frac{1}{c^2}\frac{\partial^2}{\partial t^2}\right)\psi = 4\pi\rho_b,$$

$$E_z = \left(\frac{\partial^2}{\partial z^2} - \frac{1}{c^2}\frac{\partial^2}{\partial t^2}\right)\psi,$$

$$\rho_b = en_{0b}\frac{\lambda}{N}S_b\delta(\mathbf{r}_\perp - \mathbf{r}_b)\sum_j \delta(z - z_j(t)), \quad (2)$$

$$\frac{dz_j}{dt} = v_j, \quad \frac{dv_j}{dt} = \frac{e}{m}\left(1 - \frac{v_j^2}{c^2}\right)^{3/2}(E_z + E_{z0}),$$

$$z_j|_{t=0} = z_{0j}, \quad v_j|_{t=0} = u.$$

Here, E_z is the total self-consistent microwave field, which is the sum of the undulator radiation field and the

field of the beam space charge, and E_{z0} is the electrostatic pump field (1). The first of Eqs. (2) is the wave equation for the polarization potential ψ [9], which is related to the total microwave field by the second of Eqs. (2). The right-hand side of the wave equation contains the perturbed charge density ρ_b, which is calculated from the third of Eqs. (2). This third equation, in turn, was obtained by transforming the familiar expression for the macroscopic electron phase density [8, 10, 11]. The rest of the notation in Eqs. (2) is as follows: n_{0b} is the unperturbed beam electron density, S_b is the beam cross-sectional area, $\mathbf{r}_b$ is the radial coordinate in the beam cross section, $\Delta_\perp$ is the transverse Laplace operator, λ is the characteristic scale length, N is the number of macroparticles (electrons) within a portion of an unperturbed beam of length λ, $z_j(t)$ and $v_j(t)$ are the coordinate and velocity of the jth electron, and u is the unperturbed beam velocity.

Equations (2) are written under the assumption that the electron beam in the waveguide cross section is infinitely thin (needle-shaped). The characteristic scale length λ will be determined below; it should obviously satisfy the equality $\lambda S_b n_{0b} = N$. This equality makes it possible to write the main physical relationships in terms of a purely physical quantity—the actual beam electron density n_{0b}—and, at the same time, to operate in fact with a fictitious auxiliary parameter—the number of macroparticles N.

The polarization potential ψ of the total microwave field can be represented in the form

$$\psi = \tilde{\psi} + \psi_b,$$

$$\tilde{\psi} = \frac{1}{2}\varphi_s(\mathbf{r}_\perp)[A_s(z,t)\exp(-i\omega_0 t + ik_0 z) + \text{c.c.}], \quad (3)$$

$$\psi_b = \frac{1}{2}[A_b(r_\perp, z, t)\exp[-i\omega_0 t + i(k_0 + \chi)z] + \text{c.c.}].$$

Here, $\tilde{\psi}$ refers to the component of the total microwave field that describes the undulator radiation and the potential ψ_b describes the high-frequency variations in the space charge of the relativistic electron beam. The rest of the notation in representations (3) is as follows: $\varphi_s(\mathbf{r}_\perp)$ are the eigenfunctions of the waveguide cross section ($k_{\perp s}^2$ being the corresponding eigenvalues of the equation $\Delta_\perp \varphi_s + k_{\perp s}^2 \varphi_s = 0$ with $s = 1, 2, \ldots$); $A_s(z,t)$ is the slowly varying amplitude; and the frequency and wave vector of the wave emitted in the undulator, ω_0 and k_0, are related by the dispersion relation $D_s(\omega_0, k_0) \equiv k_{\perp s}^2 + k_0^2 - \omega_0^2/c^2 = 0$. Solution (3) does not take into account a distortion of the transverse structure of the waveguide field by the beam (there is only one waveguide mode with the transverse number s), but it describes the spatiotemporal dynamics of the radiation field (the amplitude $A_s(z,t)$ depends on both t and z). The second of representations (3), which determines

the potential of the radiation field, implies that the relativistic beam resonantly emits radiation at the frequency of only one transverse waveguide wave, namely, that with the number s. The resonance condition for this emission process will be discussed below.

The motion of relativistic beam electrons can be described as the sum of a slow and a fast motion. In the approximation linear in the wave amplitudes, the motion in pump field (1) is characterized by the frequency $\Omega_\chi = \chi u$ and the motion in the field with the potential $\tilde{\psi}$ occurs with the characteristic frequency $\Omega_0 = \omega_0 - k_0 u$. Both these frequencies are nonzero and thereby refer to fast electron motions. In the next approximation (i.e., to second order in the wave amplitudes), there are two frequencies, $\Omega_0 + \Omega_\chi$ and $\Omega_0 - \Omega_\chi$, one of which is low.

We assume that the lower frequency is $\Omega_0 - \Omega_\chi$; this means that the following inequalities are satisfied:

$$|\Delta| \ll |\omega_0 - k_0 u|, \quad |\chi u|, \quad (4)$$

where

$$\Delta = \Omega_0 - \Omega_\chi = \omega_0 - k_0 u - \chi u \quad (5)$$

is the detuning. The requirement that detuning (5) be small is a necessary resonance condition for the stimulated emission of the undulator radiation. Inequalities (4), in turn, make it possible to describe the motion of relativistic electrons as the sum of a slow and a fast motion.

It is necessary to point out the following circumstance: the high-frequency space charge field of the relativistic beam is driven at the frequency $\Omega_0 - \Omega_\chi$; i.e., it is associated with the modulation resulting from a nonlinear interaction between the radiation fields and the electrostatic pump field. Consequently, the polarization potential of the high-frequency beam space charge can be described by the third of relationships (3); in this case, the amplitude $A_b(r_\perp, z, t)$ is a slowly varying function of z and t (by virtue of inequalities (4), the motion of electrons in the field of the high-frequency beam space charge occurs at a frequency close to frequency (5) and is therefore slow).

We represent the coordinates and velocities of the electrons of a relativistic beam in the form

$$z_j = z_j' + ut + \tilde{z}_j, \quad v_j = v_j' + \tilde{v}_j, \quad (6)$$

where z_j' and v_j' correspond to a slow motion and $\tilde{z}_j$ and $\tilde{v}_j$ refer to fast oscillations. We assume that the coordinates and velocities satisfy the inequalities $|k_0 \tilde{z}_j| \ll 1$; $|\chi \tilde{z}_j| \ll 1$, and $|\gamma^2 \tilde{v}_j/c| \ll 1$; this implies that fast oscillations are small and nonrelativistic. Here, $\gamma = (1 - u^2/c^2)^{-1/2}$ is the relativistic factor of the unperturbed beam electrons. Substituting representations (6) into the equations of motion of the beam electrons (the fourth and fifth of Eqs. (2)), we obtain, to first order in

the amplitudes $E_0(r_\perp)$ and $A_s(z, t)$, the following expression for the coordinate $\tilde{z}_j$ of an electron in its fast motion:

$$
\tilde{z}_j = -\frac{1}{2}\frac{e}{m}\gamma_j^{-3}\left\{ k_{\perp s}^2 \left[\frac{\varphi_s(\mathbf{r}_b)A_s(z_j, t)}{(\omega_0 - k_0 u)^2} \right.\right.
$$

$$
\times \exp[ik_0 z_j' - i(\omega_0 - k_0 u)t] + \text{c.c.} \bigg]
\tag{7}
$$

$$
+ \left[\frac{E_0(\mathbf{r}_b)}{(\chi u)^2} \exp(i\chi z_j' + i\chi u t) + \text{c.c.} \right] \bigg\},
$$

where $\gamma_j = (1 - (v_j'/c)^2)^{-1/2}$ is the relativistic factor of the jth electron. Note that the high-frequency beam space charge field does not contribute to expressions (7) because, on a time scale corresponding to conditions (4), the motion in this field is slow.

The equation for the slowly varying amplitude $A_s(z, t)$ of the radiation field can be derived by using formulas (3) and (7). We insert the second of representations (3) into the first of Eqs. (2), multiply the resulting equation by $\varphi_s(\mathbf{r}_\perp)\exp(i\omega_0 t - ik_0 z)$, and integrate it over the waveguide cross section and over z from $z - \lambda/2$ to $z + \lambda/2$. In this way, we obtain

$$
\frac{\partial A_s}{\partial t} + V_{gs}\frac{\partial A_s}{\partial z}
$$
$$
= -4\pi e n_{0b}\frac{c^2}{\omega_0}\frac{k_0^{-1}}{N}S_b\frac{\varphi_s(r_b)}{\|\varphi_s\|^2}\sum_j \exp(i\omega_0 t - ik_0 z_j).
\tag{8}
$$

Here, $V_{gs} = c^2(k_0/\omega_0)$ is the group velocity of the sth transverse mode of the waveguide under consideration and $\|\varphi_s\|^2$ is the squared norm of the eigenfunction. The summation in Eq. (8) is carried out only over the electrons with coordinates in the range $z_j \in [z - \lambda/2, z + \lambda/2)$, where z is the independent (running) variable. The right-hand side of Eq. (8) contains both slowly and rapidly varying terms. Expanding the right-hand side in powers of $\tilde{z}_j$ and omitting the rapidly varying terms yields the following equation for the slowly varying amplitude $A_s(z, t)$ of the undulator radiation field:

$$
\frac{\partial A_s}{\partial t} + V_{gs}\frac{\partial A_s}{\partial z} = -i\frac{c^2\omega_b^2}{4\omega_0}G_s\frac{E_0}{(\chi u)^2}\hat{R}.
\tag{9}
$$

In writing Eq. (9), we ignored the effect of the beam on the dispersion of the electromagnetic waves of the waveguide and made a change of variable $\varphi_s(r_b)A_s(z, t) \longrightarrow A_s(z, t)$.

We also introduced the notation $G_s = S_b\varphi_s^2(\mathbf{r}_b)\|\varphi_s\|^{-2}$ and the quantity

$$
\hat{R} = \frac{2}{N}\sum_j \gamma_j^{-3}\exp(i\Delta t)\exp[-i(k_0 + \chi)z_j'],
$$

which depends on the perturbed beam electron density.

Based on the right-hand side Eq. (9), we can now determine the value of the formally introduced characteristic scale length λ. The phase of the beam electrons is determined by the exponential $\exp[-i(k_0 + \chi)z_j']$, which governs the spatial scale of modulation of the emitting beam. Consequently, it is natural to set $\lambda = 2\pi(k_0 + \chi)^{-1}$, which is equal to the combinational wavelength.

In accordance with representations (3) and the second of Eqs. (2), the solution to Eq. (9) determines the radiation field:

$$
\tilde{E}_z = \frac{1}{2}k_{\perp s}^2[A_s\exp(-i\omega_0 t + ik_0 z) + \text{c.c.}].
\tag{10}
$$

The high-frequency beam space charge field can be determined in the one-dimensional potential approximation [8, 11] with allowance for the inequality $\omega_0 \sim (k_0 + \chi)u \gg k_{\perp s}c$:

$$
\frac{\partial E_{zb}}{\partial z} = 4\pi e n_{0b}\frac{\lambda}{N}\sum_j \delta(z - z_j(t)),
\tag{11}
$$

where the high-frequency beam space charge field E_{zb} has the same mathematical structure as the potential ψ_b. Substituting a solution having such a structure into expression (11), we find

$$
E_{zb}
$$
$$
= -i\frac{1}{2}\frac{4\pi e n_{0b}}{(k_0 + \chi)}\{R\exp[-i\omega_0 t + i(k_0 + \chi)z] - \text{c.c.}\},
\tag{12}
$$

where $R = \frac{2}{N}\sum_j \exp(i\Delta t)\exp[-i(k_0 + \chi)z_j']$ is the amplitude of the space charge density wave of the beam.

The equations of motion of the relativistic beam electrons can be averaged in two steps. First, we substitute into them the already calculated electric fields, namely, the radiation field $\tilde{E}_z$ (10), the high-frequency space charge field E_{zb} (12), and the electrostatic pump field E_{z0} (1):

$$
\frac{dv_j'}{dt} = \frac{e}{m}\gamma_j^{-3}\langle(\tilde{E}_z + E_{zb} + E_{z0})\rangle,
\tag{13}
$$

where the angle brackets stand for time averaging. Second, we substitute into Eqs. (13) the relationships $z_j = z_j' + ut + \tilde{z}_j$, take into account expressions (7), and merely discard the rapidly varying terms on the right-hand side of Eq. (13). As a result, omitting fairly laborious intermediate manipulations, we obtain [7, 11]

$$\frac{dz_j'}{dt} = v_j' - u,$$

$$\frac{dv_j'}{dt}$$

$$= -\frac{1}{2}i\frac{\omega_b^2}{k_0 + \chi}\gamma_j^{-3}\{R\exp[-i\Delta t + i(k_0 + \chi)z_j'] - \text{c.c.}\} \quad (14)$$

$$-\frac{1}{4}iE_0\left(\frac{e}{m}\right)^2 k_{\perp s}^2\gamma_j^{-6}\left(\frac{k_0}{(\chi u)^2} + \frac{\chi}{(\omega_0 - k_0 u)^2}\right)$$

$$\times \{A_s\exp[-i\Delta t + i(k_0 + \chi)z_j'] - \text{c.c.}\}.$$

For further analysis, it is worthwhile to transform Eqs. (9) and (14) in a certain way. Representations (6) for z_j are convenient for the purpose of averaging, i.e., for deriving the averaged equations. The investigation of an actual physical laser system with the entrance and exit ends, however, implies the use of the laboratory frame of reference. This is why we will describe the straight-line translational motion (characterized by the coordinate ut) and the nonoscillating motion (characterized by the coordinates z_j') in the same terms. In this way, we also introduce the following dimensionless quantities and variables:

$$y_j = (k_0 + \chi)(z_j' + ut), \quad \eta_j = \frac{v_j'}{u},$$

$$w_j = \frac{\gamma}{\gamma_j} = \sqrt{\frac{1 - (u/c)^2\eta_j^2}{1 - (u/c)^2}},$$

$$x = (k_0 + \chi)z, \quad \tau = \omega_0 t, \quad \tilde{v}_g = \frac{V_{gs}}{u}, \quad (15)$$

$$\tilde{v}_b = \frac{(k_0 + \chi)u}{\omega_0},$$

$$\Phi(x, \tau) = \frac{1}{2}E_0\left(\frac{e}{mu^2}\right)^2\gamma^{-6}\frac{k_{\perp s}^2}{\chi^2}A_s(x, \tau).$$

The quantity $\tilde{v}_b$, which is introduced in formulas (15), obviously plays the role of detuning (5). Under resonance conditions (4), we have $\tilde{v}_b \approx 1$. In terms of the new quantities and variables, the equations transform to [8, 12]

$$\frac{\partial\Phi}{\partial\tau} + \tilde{v}_g\frac{\partial\Phi}{\partial x} = -\frac{1}{2}i\alpha_b\Theta\hat{R},$$

$$\frac{dy_j}{d\tau} = \tilde{v}_b\eta_j,$$

$$(16)$$

$$\frac{d\eta_j}{d\tau} = -\frac{1}{2}i\alpha_b w_j^3\{R\exp[-i(\tau - y_j)] - \text{c.c.}\}$$

$$-\frac{1}{2}iw_j^6\{\Phi\exp[-i(\tau - y_j)] - \text{c.c.}\},$$

where

$$R = \frac{2}{N}\sum_{j(x)}\exp[i(\tau - y_j)];$$

$$\hat{R} = \frac{2}{N}\sum_{j(x)}w_j^3\exp[i(\tau - y_j)], \quad (17)$$

$$\alpha_b = \frac{\omega_b^2\gamma^{-3}}{\omega_0^2}; \quad \Theta = \frac{1}{4}G_s\frac{k_{\perp s}^2 c^2}{\chi^2 u^2}\left(\frac{eE_0}{\chi mu^2\gamma^3}\right)^2. \quad (18)$$

The quantities R and $\hat{R}$, defined by expressions (17), are functions of the independent temporal and spatial variables, namely, the time τ and coordinate x. The dependence on the spatial coordinate x is determined by the following rule: the summation in the expressions for R and $\hat{R}$ is carried out over those macroparticles (electrons) whose coordinates lie within the region $y_j \in [x - \pi, x + \pi)$, where x is an arbitrary coordinate value from the region over which the problem is solved. It is in this sense that the symbolic notation $\sum_{j(x)}(\ldots)$ should be understood. The parameter α_b, which is determined by the beam electron density, is very small. This is because, in all existing microwave radiation sources and those at the design stage, the Langmuir frequency ω_b of the beam is the lowest of all the characteristic frequencies of the system [13]. In order to estimate the value of the parameter Θ, we assume that the beam is relativistic ($u \sim c, \gamma \gg 1$). We also assume that the inequality $mc^2\gamma > |eE_0/\chi|$ is satisfied. The reason for this is that, when the latter inequality fails to hold, the electrostatic pump wave traps the beam electrons, so they are simply reflected from the humps of its electric field potential; this is unacceptable from the standpoint of the generation of undulator radiation. Note also that the geometric factor in the parameter Θ contains the small ratio S_b/S_w (where S_w is the waveguide cross-sectional area). We thus see that both of parameters (18) are small.

The initial conditions for the coordinates and velocities of the beam electrons are stated in accordance with the "history" of their appearance in the region where they interact with the radiation field and pump field. For

the electrons that enter the system through the entrance boundary $x = 0$, we have

$$y_j(\tau = \tau_j) = 0, \quad \eta_j(\tau = \tau_j) = 1, \qquad (19)$$

where $\tau_j \geq 0$ is the time at which the jth electron flies (is injected) into the system. The electrons that were present in the interaction space from the beginning of interaction satisfy other initial conditions:

$$y_j(\tau = 0) = y_{0j}, \quad \eta_j(\tau = 0) = 1, \qquad (20)$$

where $y_{0j} \in (0, X)$ and X is the total dimensionless length of the interaction region. Note that the averaging procedure used above to derive Eqs. (16) and formulas (17) requires that the length of the system be equal to an integer number of wavelengths λ. In other words, we have $X = 2\pi N_\lambda$, where N_λ is the (sufficiently large) number of wavelengths that fit along the entire length of the system.

In the most general terms, additional conditions for the radiation field amplitude $A_s(x, \tau)$ are formulated as follows:

$$A_s(0, \tau) = f_1(\tau), \quad \tau \geq 0;$$
$$A_s(x, 0) = f_2(x), \quad 0 \leq x < X; \quad f_1(0) = f_2(0), \qquad (21)$$

where $f_{1,2}$ are continuous functions.

In the linear approximation, we have $R, \Phi \sim \exp(-i\Omega\tau + i\kappa x)$ and Eqs. (16) yields the following dispersion relation for the dimensionless frequency Ω and dimensionless wavenumber κ:

$$(\Omega - \kappa\tilde{v}_g)(\Omega - \kappa\tilde{v}_b)[(\Omega - \kappa\tilde{v}_b) + 2(\pm\sqrt{\alpha_b})]$$
$$= \frac{1}{2}\alpha_b\Theta. \qquad (22)$$

It can be shown that the imaginary part of the frequency Ω is maximal at $\kappa = 0$. Restricting the analysis to this important particular case, we write the dispersion relation in the form

$$\Omega^2(\Omega \pm 2\sqrt{\alpha_b}) = \frac{1}{2}\alpha_b\Theta. \qquad (23)$$

Under the condition

$$\Theta \gg \sqrt{\alpha_b}, \qquad (24)$$

we find from this dispersion relation the growth rate of the instability due to the emission of undulator radiation by the beam in the regime of the stimulated single-particle Cherenkov effect [14]:

$$\Omega = \frac{-1 + i\sqrt{3}}{2}\left(\frac{1}{2}\alpha_b\Theta\right)^{1/3}. \qquad (25)$$

Under the inequality opposite to inequality (24), it is only dispersion relation (23) with the minus sign that possesses complex values of the frequency Ω; this indicates a resonance between the radiation field and the slow beam space charge wave. In this case, dispersion

relation (23) yields the growth rate of the instability due to the emission of undulator radiation by the beam in the regime of the stimulated collective Cherenkov effect [14]:

$$\Omega = i\frac{1}{2}(\sqrt{\alpha_b}\Theta)^{1/2}. \qquad (26)$$

We now turn to the solutions to nonlinear equations (16), restricting ourselves to studying the problem about the dynamics of a solitary electromagnetic radiation pulse. In this way, we consider an electromagnetic field perturbation that is created at the initial time $\tau = 0$ against the background of an unperturbed electron beam infinite in the longitudinal direction and that has the spatial size $n_\lambda = 6$ (in wavelength units) and the amplitude $a_0 = 10^{-4}$.

We begin by analyzing the pulse dynamics during the instability of the beam in its interaction with the forward wave in the regime of the single-particle Cherenkov effect. To do this, we choose the parameter values satisfying inequality (24), namely, $\alpha_b = 0.005$ and $\Theta = 0.5$. For numerical simulations, we set the number of macroparticles per unit wavelength to be $N = 500$ and specify the computation region by setting $N_\lambda = 40$.

Recall (see [11, 12]) that, in the linear approximation, the radiation pulse during the convective instability in the regime of the single-particle Cherenkov effect grows at rate (25) and is transported in space with the velocity

$$U_g = \frac{2}{3}u + \frac{1}{3}V_{gs}. \qquad (27)$$

In terms of the dimensionless variables used here, velocity (27) determines the following law for the momentum transport in space: $x \approx (2/3 + \tilde{v}_g/3)\tau + \text{const}$.

In the initial (linear) stage, the pulse evolution is seen to be well described by linear theory. In the later stages, the pulse amplitude grows at a progressively decreasing rate and approaches a certain maximal quasi-steady value. This is because the beam electrons are trapped in the spatial region where the pulse intensity is the highest. Another reason is that, at low group velocities such that $\tilde{v}_g \ll 1$, the pulse becomes wider in space because its leading edge moves faster than its trailing edge. This latter circumstance stems from the fact that, at $\tilde{v}_g \ll 1$, transport velocity (27) is about 2/3 (in dimensionless units), while the velocity of the perturbations within the beam, as well as the velocity of the beam as a whole, is about $\tilde{v}_b \approx 1$. For $\tilde{v}_g \approx 1$, there is no spatial widening of the pulse at the expense of its leading edge.

Some results of numerical simulations of the pulse dynamics during the convective instability in the regime of the single-particle Cherenkov effect are illustrated in Fig. 1. Figure 1a shows the dependence of the
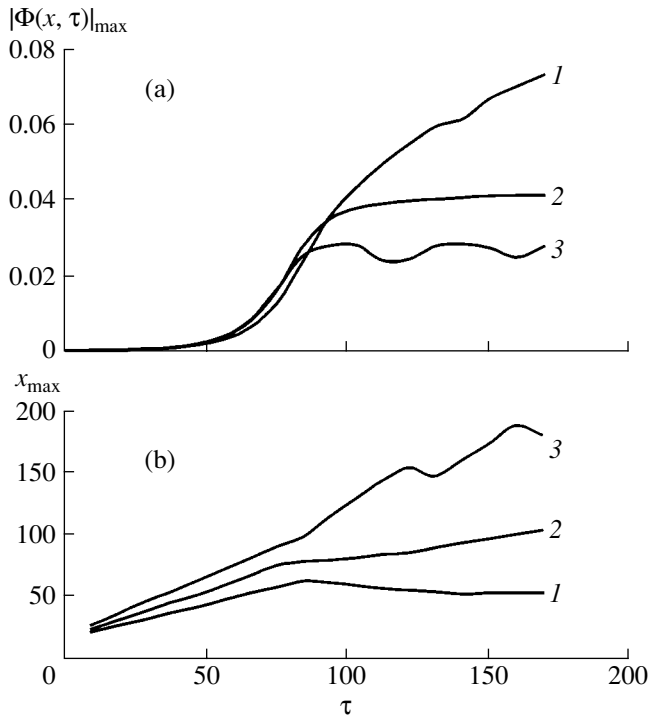
Fig. 1. Time evolutions of (a) the maximal amplitude of the radiation pulse envelope and of (b) the position of the point of the maximal amplitude during the convective instability in the regime of the single-particle Cherenkov effect for $\alpha_b = 0.005$; $\theta = 0.5$; and $1 - \tilde{v}_g = (1)$ 0.1, (2) 0.5, and (3) 0.95.

maximal pulse amplitude on the dimensionless time τ for three different values of the group velocity: $\tilde{v}_g = $ 0.1, 0.5, and 0.95. In the initial stage ($\tau < 80$–90), the pulse amplitude in these three cases grows at approximately the same rate, namely, rate (25), which is thus independent of the value of the group velocity. In the nonlinear stage, the maximal pulse amplitude approaches a certain quasi-steady value, which is larger for lower group velocities $\tilde{v}_g$.

Figure 1b shows the dependence of the coordinate of the point at which the pulse amplitude is maximal on the time τ for three different values of the group velocity $\tilde{v}_g$. In the initial stage ($\tau < 80$–90), this point coincides with the central point of the pulse and is displaced as predicted by linear theory. In later stages, the point of the maximal pulse intensity deviates from the pulse center and, as a result, the velocity at which this point is displaced changes according to a complicated law. In turn, the deviation of the point of the maximal pulse intensity from the pulse center is due to the fact that the beam electrons within the pulse are trapped nonuniformly.

Figure 2 displays the phase planes of the beam electrons at three different times. The vertical axis in the phase plane represents the dimensionless coordinates y_j
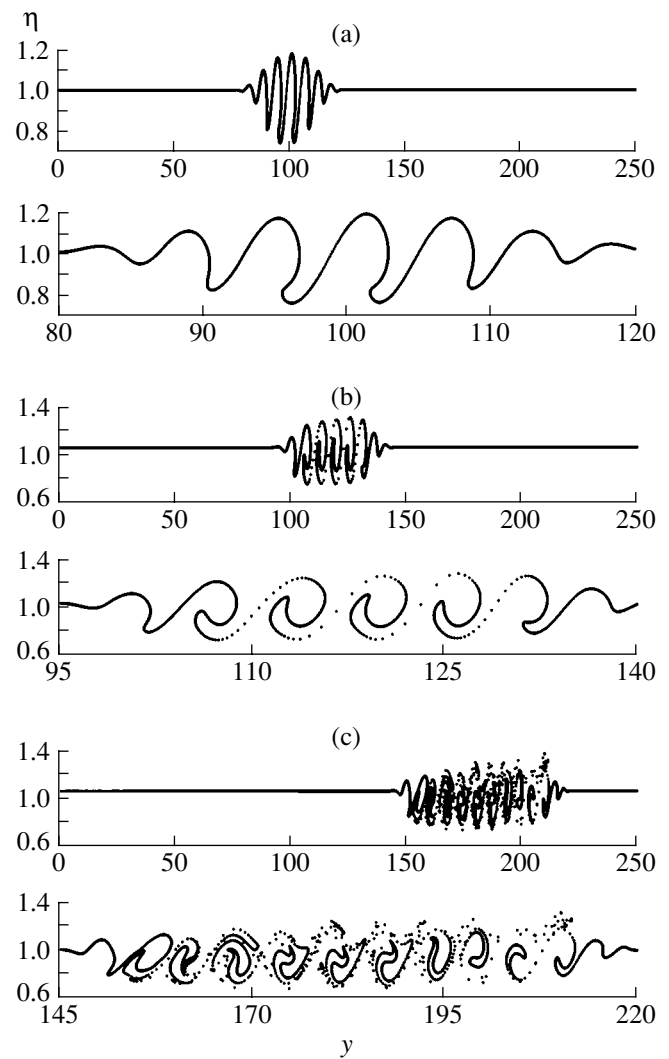

Fig. 2. Phase planes of the beam electrons during the convective instability in the regime of the single-particle Cherenkov effect for $\alpha_b = 0.005$, $\theta = 0.5$, and $\tilde{v}_g = 0.95$ at the times $\tau = $ (a) 85, (b) 104, and (c) 170. Each second image is a magnified fragment of the previous one.

and the horizontal axis represents the dimensionless velocities η_j. An analysis of the phase planes makes it possible to reveal the main mechanism responsible for nonlinear suppression of the instability in the regime of the single-particle Cherenkov effect. The initial phase plane ($\tau = 85$) corresponds to the very beginning of the nonlinear saturation process. The electrons that are slowed down are seen to predominate over those that are accelerated, and slower electrons in the central pulse region, where the field is stronger, are decelerated at a progressively decreasing rate. This is most clearly seen in the magnified fragment of the phase plane at $\tau = 85$ (the second image in Fig. 2). This fragment illustrates the very beginning of the trapping of beam electrons by a compact wave pulse (the phenomenon of the trapping of particles by a harmonic wave has been thor-
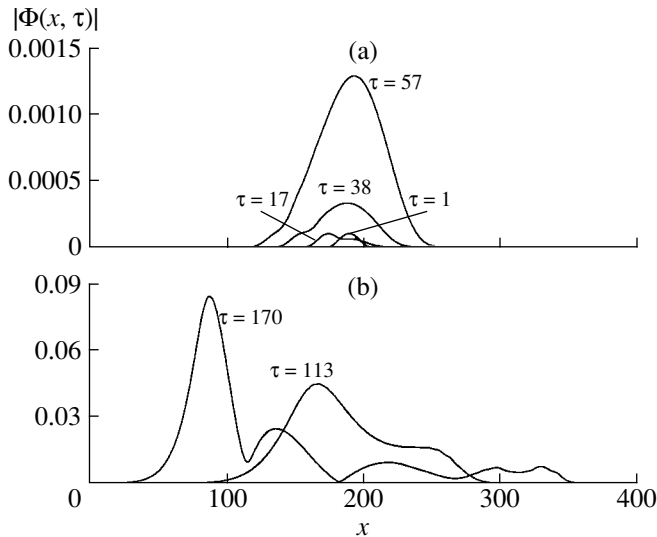
Fig. 3. Dynamics of the radiation pulse envelope during the absolute instability in the regime of the single-particle Cherenkov effect for $\alpha_b = 0.005$, $\theta = 0.5$, and $\tilde{v}_g = -0.95$.

oughly investigated in the literature, see, e.g., [11, 15]). The developed stage of the trapping process is illustrated in the last four images in Fig. 2, which show the entire phase planes and their magnified fragments at the time $\tau = 104$ (by this time, all the beam electrons have been trapped and the beam has already broken up into bunches) and at the time $\tau = 170$ (by this time the electrons have completed several oscillations in the field of the combinational wave).

We now consider the pulse dynamics during the instability of the beam in its interaction with the backward wave in the regime of the single-particle Cherenkov effect (the absolute instability [16]). To do this, we adopt the above parameter values $\alpha_b = 0.005$ and $\Theta = 0.5$ and set the group velocity to be $\tilde{v}_g = -0.95$. We also keep the above number of macroparticles N and the above size of the computation region N_λ. Note that, in contrast to the convective instability, the dynamics of a short pulse during the absolute instability of the beam in its interaction with the backward wave has not yet been thoroughly investigated in the literature.

We can see from Fig. 3a that, in the initial stage, the pulse grows linearly in amplitude at rate (25) and becomes wider, the position of the point of its maximal intensity being essentially unchanged. In later stages (Fig. 3b), the pulse amplitude grows at a progressively decreasing rate, the pulse width increases to a larger extent, and the point of the maximal pulse amplitude is displaced to the left. The pulse amplitude stops growing because of the trapping of the beam electrons (see Fig. 4). The widening of the pulse and the displacement of the point of its maximal amplitude result from the "splitting" of the perturbation: the electromagnetic field
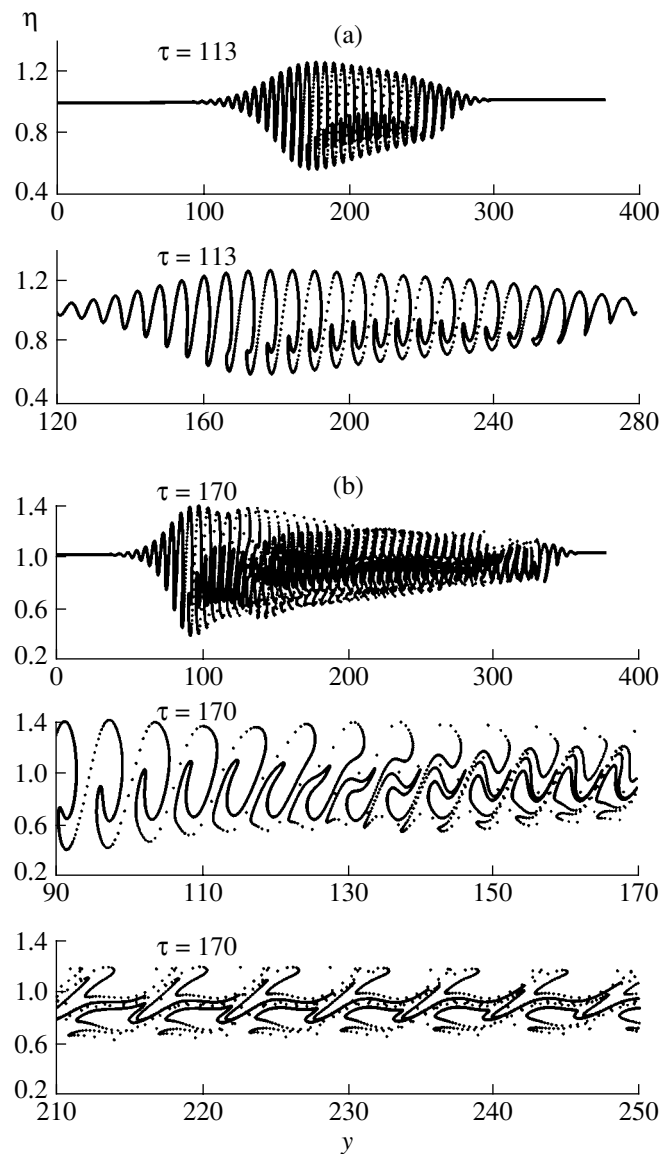

Fig. 4. Phase planes of the beam electrons during the absolute instability in the regime of the single-particle Cherenkov effect for $\alpha_b = 0.005$, $\theta = 0.5$ and $\tilde{v}_g = -0.95$ at the times $\tau = $ (a) 113 and (b) 170. The second plot in panel (a) is a magnified fragment of the first plot, and the second and third plots in panel (b) are magnified fragments of the first plot.

propagates leftward, while the beam modulation region is displaced rightward.

The trapping phenomenon during the absolute instability is illustrated in Fig. 4, which shows the phase planes of the beam electrons at two different times. We can see that the perturbation grows considerably over an increasingly wider region. We also see the formation of fairly complicated regular structures within the beam: the characteristic spatial scale of the structures increases and the structures themselves remain regular.
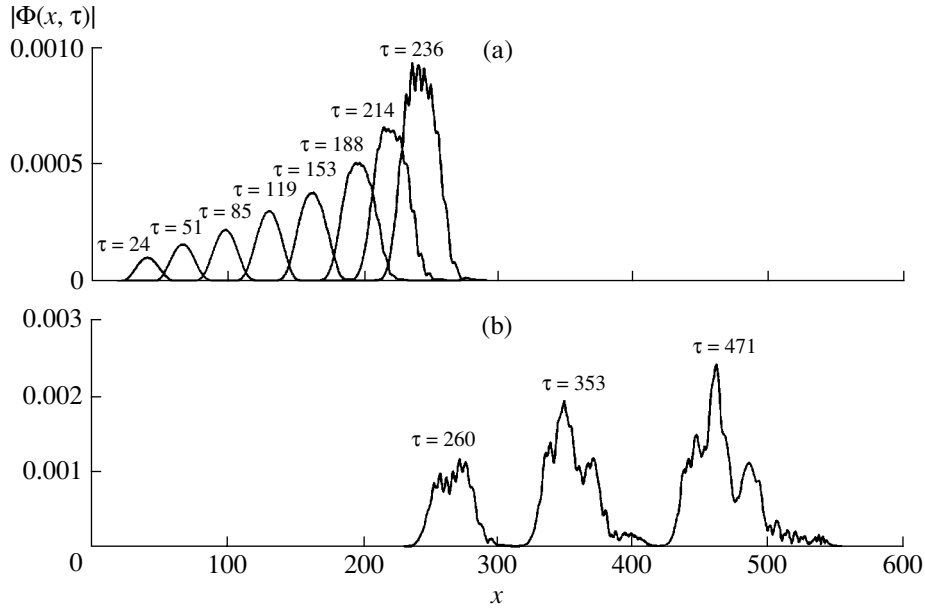
Fig. 5. Dynamics of the radiation field pulse envelope during the convective instability in the regime of the collective Cherenkov effect for $\alpha_b = 0.01$, $\theta = 0.05$, and $\tilde{v}_g = 0.95$.

We now turn to an analysis of the undulator radiation in the regime of the collective Cherenkov effect. To do this, we choose the parameter values satisfying the inequality opposite to inequality (24), namely, $\alpha_b = 0.01$ and $\Theta = 0.05$. We restrict ourselves to considering the instability of the beam in its interaction with the forward wave; in this case, we set $\tilde{v}_g = 0.95$. For numerical simulations, we set the number of macroparticles per unit wavelength to be $N = 300$ and specify the computation region by setting $N_\lambda = 90$.

In the linear approximation, the pulse during the convective instability in the regime of the collective Cherenkov effect grows at rate (26) and is transported in space with the velocity

$$U_g = \frac{1}{2}u + \frac{1}{2}V_{gs}. \qquad (28)$$

In terms of the above dimensionless variables, velocity (28) determines the following law for the momentum transport in space: $x \approx (1/2 + \tilde{v}_g/2)\tau + \text{const}$.

Figure 5 illustrates the pulse dynamics in the regime of the collective Cherenkov effect. In the initial (linear) stage (Fig. 5a), the pulse evolution is seen to be well described by linear theory. At $\tau < 250$, the pulse amplitude grows at rate (26). According to Fig. 5a, it is as late as at the time $\tau = 214$ that the pulse shape is distorted (because of the nonlinear effects). Thereafter (Fig. 5b), the pulse amplitude grows at a progressively decreasing rate and approaches a certain quasi-steady value. In the late stages, the pulse shape is strongly distorted and the pulse itself becomes substantially wider. Throughout the evolution, the point of the maximum pulse ampli-

tude is displaced almost uniformly (in accordance with the law $x \approx \tau + \text{const}$), as is predicted by linear theory.

The mechanism that leads to nonlinear saturation of the instability in the regime of the collective Cherenkov effect is the trapping of the beam electrons by the field of the beam charge density wave. Actually, this mechanism appears to be even more complicated because of the additional effect of the field of the combinational wave. In this case, the beam electrons usually exhibit a very stochastic behavior [11]. Figure 6 shows the phase planes of the beam electrons at three different times. In all the stages, the position and size of the perturbed beam region coincide exactly with those of the region where the radiation pulse is localized. In the saturation stage, the beam structure in phase plane is essentially irregular, which provides evidence of a strong beam stochastization within the pulse. This stochastization is especially pronounced in the phase plane calculated for $\tau = 471$ and is best seen in its magnified fragment (the last image in Fig. 6).

To conclude, we note that averaged equations (16) provide an efficient tool for a description and investigation of unsteady and transient processes occurring during the resonant emission of electromagnetic waves by an electron beam in an electrostatic pump field. That a similar approach, based on analogous equations, can be successfully applied to solve a nonlinear problem was demonstrated in simulating relativistic plasma microwave oscillators [8]. In the present paper, we have restricted ourselves to solving the problem of the nonlinear dynamics of a solitary pulse emitted by the beam in different regimes of its interaction with the field. In our subsequent studies, we will apply Eq. (16) to solve
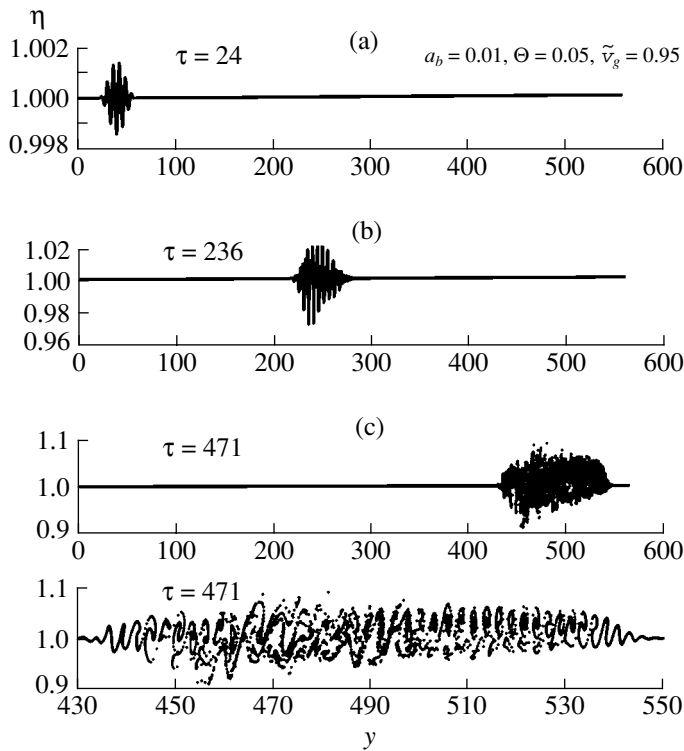
Fig. 6. Phase planes of the beam electrons during the convective instability in the regime of the collective Cherenkov effect at the times τ = (a) 24, (b) 236, and (c) 471. The second plot in panel (c) is a magnified fragment of the first plot.

boundary-value problems about the emission of electromagnetic waves by beams in electrodynamic systems equipped with units for extracting microwave radiation.

ACKNOWLEDGMENTS

REFERENCES

1. V. L. Ginzburg, *Theoretical Physics and Astrophysics* (Nauka, Moscow, 1981; Pergamon, Oxford, 1979).
2. D. F. Alferov, Yu. A. Bashmakov, and E. G. Bessonov, Tr. Fiz. Inst. im. P.N. Lebedeva AN SSSR **80**, 100 (1975).
3. M. V. Fedorov, Usp. Fiz. Nauk **135**, 213 (1981) [Sov. Phys. Usp. **24**, 801 (1981)].
4. V. L. Bratman, N. S. Ginzburg, and M. I. Petelin, Izv. AN SSSR. Fizika **44**, 1593 (1980).
5. *Free-Electron Generators of Coherent Radiation*, Ed. by A. A. Rukhadze (Mir, Moscow, 1983).
6. N. A. Vinokurov and F. N. Skrinskiĭ, in *High-Frequency Relativistic Electronics* (IPF, Gorki, 1981), p. 204.
7. M. V. Kuzelev, Zh. Tekh. Fiz. **53**, 1029 (1983) [Sov. Phys. Tech. Phys. **28**, 623 (1983)].
8. M. V. Kuzelev, A. A. Rukhadze, and P. S. Strelkov, *Plasma Relativistic Microwave Electronics* (MGTU im. Baumana, Moscow, 2002).
9. M. Born and E. Wolf, *Principles of Optics* (Pergamon, Oxford, 1969; Nauka, Moscow, 1970).
10. Yu. L. Klimontovich, *Kinetic Theory of Nonideal Gases and Nonideal Plasmas* (Nauka, Moscow, 1975; Pergamon, Oxford, 1982).
11. M. V. Kuzelev and A. A. Rukhadze, *Electrodynamics of Dense Electron Beams in Plasma* (Nauka, Moscow, 1990).
12. I. N. Kartashov, M. V. Kuzelev, and I. B. Rudyak, Kratk. Soobshch. Fiz., No. 12, 14 (2002).
13. M. V. Kuzelev, O. T. Loza, A. A. Rukhadze, *et al.*, Fiz. Plazmy **27**, 710 (2001) [Plasma Phys. Rep. **27**, 669 (2001)].
14. M. V. Kuzelev and A. A. Rukhadze, Usp. Fiz. Nauk **152**, 285 (1987) [Sov. Phys. Usp. **30**, 507 (1987)].
15. A. A. Ivanov, *Physics of Highly Nonequlibrium Plasma* (Atomizdat, Moscow, 1977).
16. E. M. Lifshitz and L. P. Pitaevskii, *Physical Kinetics* (Nauka, Moscow, 1979; Pergamon, Oxford, 1981).

Translated by I.A. Kalabalyk

NONIDEAL
PLASMA

The Search for Rydberg Matter: Beryllium

A. V. Popov

Altai State University, ul. Dimitrova 66, Barnaul, 656099 Russia
Received October 8, 2003; in final form, January 21, 2004

Abstract—Results are presented from theoretical investigations of condensed excited states of beryllium by the Hartree–Fock method with allowance for the width of the atomic levels. It is shown that, during the excitation of a beryllium atom in the X-ray energy range, the $2p$ states split, the one-electron energy levels are shifted by unequal amounts, the $2s$ and $2p$ states mix at excitation energies of 10 and 14 Ry, and the atom is stabilized at energies higher than 6.7 Ry. In the optical range of excitation energies, a condensed excited state of beryllium with a lifetime on the order of 0.1 fs is revealed. © *2005 Pleiades Publishing, Inc.*

1. INTRODUCTION

By Rydberg matter (RM) is usually meant a condensed state of highly excited atoms at a gas density. RM was first mentioned by Manykin *et al.* [1]. The general theory of condensed excited states (CESs) of atoms, molecules, and impurity centers in solids was presented in [2] by the same authors. In [3], they reported experimental and theoretical results on condensed states in a system of excited cesium atoms. The existence of an isolated region of a metastable nonideal plasma [4] is not peculiar to cesium alone [5]. Yarygin *et al.* [6] pointed out that, at excitation energies close to the ionization energy, the alkali metal atoms can be as large as 10^{-6}–10^{-5} cm in diameter and can form a metastable condensate at an atomic density of about $\sim 10^{17}$–10^{18} cm^{-3}. Holmlid and Manykin [7] noticed RM hydrocarbon clusters and also RM hydrogen surface layers. It may be that CESs form in a natural way as well. Thus, ball lightning can be interpreted as RM [8].

In my opinion, the most important experiments are those with excited cesium atoms (see [3, 5–7, 9] and the literature cited therein). In this context, of particular note are experiments carried out by Sweden investigators with a thermionic converter of thermal energy into electric energy. The converter consisted of a cesium diode, an emitter, and a collector, all held at different temperatures. Cesium vapors were supplied through a mesh collector into the interelectrode gap, where they condensed on the wall of a bell jar in which the thermionic converter was installed. Decisive evidence for the onset of CESs was provided by the unusual shape of the current–voltage characteristics of the thermionic converter during the dynamic supply of cesium vapors into the interelectrode gap, specifically, a decrease in the work function of the collector to less than 0.7 eV and a substantial increase in the output voltage. A mass-spectrometric analysis showed that, in the interelectrode gap, there were clusters, each containing up to 1000 atoms. Yarygin *et al.* [6], carried out analogous experiments, but with a more sophisticated equipment

and technique. They, however, failed to completely reproduce the CESs parameters that were obtained in the above Sweden experiments. Thus, when switching from equilibrium to dynamic supply of cesium vapors, the work function of the collector was found to drop to only 1 eV. Estimates made it possible to establish that the clusters produced in the RM contained about 100 atoms, the decay times of the CESs being longer than those of a cluster-free plasma by a factor of 10 to 100.

On the whole, the conclusion made in review [3] seems to be right: indeed, the idea of the condensation of excitations, being so simple, has not yet been sufficiently appreciated by theoreticians and experimentalists and, in recent years, has received only little attention.

The present paper reports the results of theoretical investigation of the CESs of beryllium. The excitations will be described in terms of the Hartree–Fock method with allowance for the width of the atomic levels. The idea of taking the width of the atomic levels into account was first used by Yanavichus and Shuchurov [10] in calculating the excited hydrogen wave functions. In what follows, this idea will be pursued further: it will be applied to calculate the wave functions of the excited states of multielectron atoms. The Hartree–Fock method will be used as the basic one, because, in my opinion, this method is the most systematic of all one-electron methods. It provides precise formulations of all the assumptions and makes it clear, at least in principle, how to go beyond them in order to obtain more and more exact final results.

2. CALCULATION METHOD

We consider the standard method of solving the spectral problem for a multielectron atom in the ground state in the Hartree–Fock approximation,
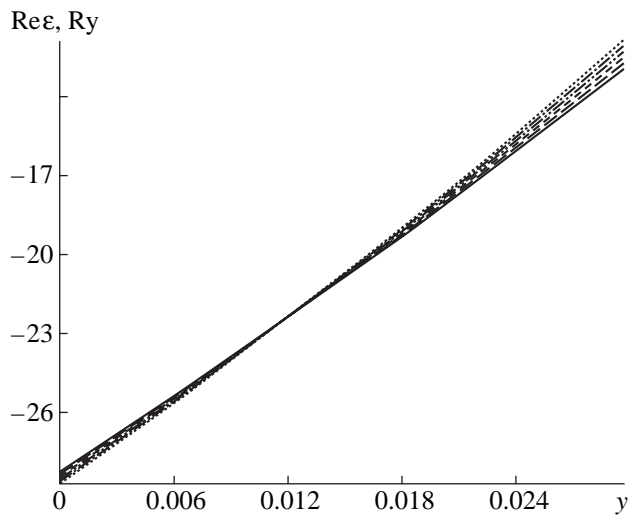
$$F\psi = E\psi. \tag{1}$$

Reε, Ry

Fig. 1. Dependence of the real part of the total energy of a beryllium atom on the parameter y for $x = 0$, 0.005, 0.010, 0.015, 0.020, and 0.025. Curves with gentler slopes correspond to larger values of the parameter x.

Using the central-field approximation, we can separate the radial and angular variables and seek the eigenfunctions of the Fock operator F in the form of the product of the radial function $R(r)$ and azimuthal function $Y(\theta, \varphi)$,

$$\psi = R(r)Y(\theta, \varphi), \qquad (2)$$

where the azimuthal function satisfies the equations

$$-\Delta Y = l(l+1)Y, \quad -i\frac{\partial Y}{\partial \varphi} = mY. \qquad (3)$$

Here, Δ is the Laplace operator in spherical coordinates. If we require that the solutions to Eqs. (3) be regular on the sphere ($0 \le \theta \le \pi$, $0 \le \varphi \le 2\pi$), be continuous at $\theta = 0$ and $\theta = \pi$, and satisfy the condition $Y(\theta, \varphi + 2\pi) = Y(\theta, \varphi)$ then we arrive at an eigenvalue problem that admits solutions only with the integer values $l = 0$, 1, 2, … and $m = 0, \pm 1, \pm 2, …, \pm l$.

Let us now consider the excited states of an atom in an equilibrium field. All the particles surrounding the atom in question are regarded as a thermostat. The uncertainty relation implies that, in such excited states, which can spontaneously decay over a short time τ, the energy level characterizing the quasistatic system has a finite width $\Gamma \sim \hbar/\tau$ (where $\hbar$ is Planck's constant). The wave function describing this system should contain such an exponential factor that all the probabilities determined by the square of the absolute value of the wave function decrease according to the law $\exp(-\Gamma t/\hbar)$:

$$\Psi(\mathbf{r}, t) = \psi(\mathbf{r})\exp\left\{-i\left(E - \frac{i\Gamma}{2}\right)\frac{t}{\hbar}\right\}. \qquad (4)$$

We assume that the use of the central-field approximation to describe excitations is justified just as it is for partially occupied shells of the ground state of a multielectron atom. It is then convenient to seek the function $\psi(\mathbf{r})$, which enters into the right-hand side of relationship (4), in form (2). Moreover, let the angular function satisfy the same equations (3). Since $Y(\theta, \varphi)$ is a single-valued function of φ, we can restrict ourselves to the integer values of the number m. In this case, however, electron orbital transitions should be allowed in our model; consequently, we are forced to rule out the constraints on the number l in Eqs. (3) and to treat it as a complex number, $L = l + x + iy$, where l is, as before, integer and $|x| < 1$, $|y| < 1$. The problem of searching the spectrum of the excited states of an atom can thus be reduced to the eigenvalue problem for the time-independent equation

$$\left(F + \frac{u + iv}{r^2}\right)\psi = \varepsilon\psi, \qquad (5)$$

where $u = x(x + 2l + 1) - y^2$, $v = y(2x + 2l + 1)$, and F is the Fock operator for an atom in the ground state. Note that, for $y \ne 0$, Eq. (5) is essentially non-Hermitian, with complex values of $\varepsilon = E - i\Gamma/2$. By searching through all possible values $|x|, |y| < 1$ in seeking self-consistent solutions to Eq. (5), we can determine the spectral parameters of an excited atom from the minimum value of the real part of its total energy. In particular, based on the uncertainty relation, we can estimate the decay time of the calculated excited state with an energy equal to the real part of the total energy of an atom.

3. CALCULATED RESULTS

Equation (5) was solved numerically in a basis of Gaussian functions that consists of nine functions from the expansion for $l = 0$, six functions from the expansion for $l = 1$, and three functions from the expansion for $l = 2$. Estimates showed that such a basis is full enough for Eq. (5) to be solved for a beryllium atom by the Roothaan method, provided that $|x|, |y| < 0.03$.

The results of self-consistent calculations show that the real part of the total energy of an atom, Reε, increases monotonically as the parameter y increases from 0 to 0.03 and depends weakly on the parameter x in the range of its values from 0 to 0.025 (Fig. 1). The dependence of the imaginary part of the total energy of an atom, Imε (note that the absolute value of this quantity is the probability for an excited state to decay in unit time), on the parameter y for six different values of the parameter x (0, 0.005, 0.010, 0.015, 0.020, and 0.025) is shown in Fig. 2. An important point is that the beryllium atom is stabilized in the region where the decay probability for an excited state decreases at excitation energies above 6.7 Ry. The fact that this region indeed exists agrees, at least qualitatively, with the data reported by Delone and Kraĭnov [11].
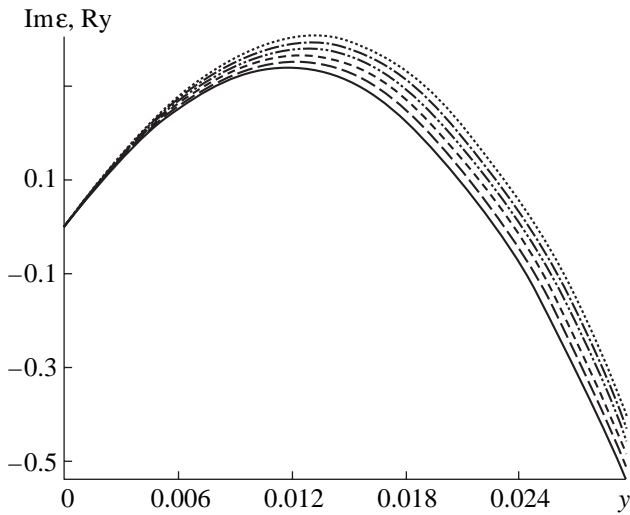
Imε, Ry

Fig. 2. Dependence of the imaginary part of the total energy of a beryllium atom on the parameter y for $x = 0$, 0.005, 0.010, 0.015, 0.020, and 0.025. A lower position of the curve corresponds to a larger value of the parameter x.

The spectral parameters of a beryllium atom, namely, the levels of the one-electron energy states E_n, the widths of these levels Γ_n, and the probabilities of filling of the states w_n, also depend weakly on x. The above dependence, in fact, makes it possible to follow the changes in the spectral parameters as functions of the excitation energy of an atom, $\Delta\varepsilon = \mathrm{Re}(\varepsilon - \varepsilon_0)$ (relative to the energy ε_0 of its ground state), instead of following the changes in the parameters x and y, which are physically meaningless.

Hence, from Fig. 3, which illustrates the results of self-consistent calculations of the energy levels E_n, whose positions change depending on $\Delta\varepsilon$, we see that
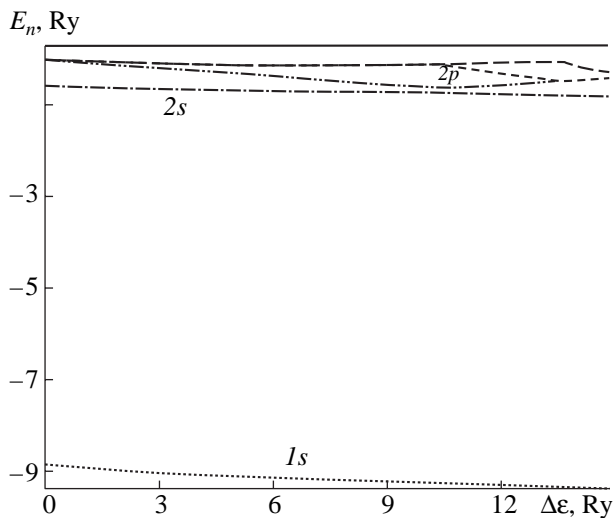
the energy of the 1s state decreases as $\Delta\varepsilon$ increases. On the whole, this conclusion, as well as the behavior of the external 2s state when the perturbations are small and the excited states have not yet mixed, agrees with the results that were reported by Delone and Kraĭnov [12] and were later confirmed experimentally by Bondar' and Suran [13].

As for the mixing of the 2s and 2p states, it is observed at excitation energies in the range $\Delta\varepsilon > 10$ Ry. The 2p states split at excitation energies close to zero. Figure 4 displays the dependence of the width of each energy level, Γ_n, on $\Delta\varepsilon$. This dependence shows that, as the excitation energy of a beryllium atom increases, the widths Γ_{1s} and Γ_{2p} change fairly abruptly, i.e., the decay probabilities for the 1s and 2p states increase. The widths Γ_{2s} and Γ_{3s} are nearly zero; consequently, the probabilities of transitions to the 2s and 3s states are low. This is confirmed by the selection rules, which were deliberately abandoned in the calculation method used here.

Figure 5 presents the dependence of the electron occupancy of one-electron states of a beryllium atom on $\Delta\varepsilon$. This dependence shows that the probability for electrons to jump from lower to higher energy levels increases with excitation energy of the atom. The slopes of the curves shown in Fig. 5 changes at the accidental degeneracy points, at which the external states mix at excitation energies of 10 and 14 Ry.

4. EXCITATIONS IN THE OPTICAL RANGE

Here, we consider the excitation of a beryllium atom in the optical range of energies. To do this, it is sufficient to assume that electron transitions from the 1s states are forbidden. In this case, the electron occupancies of these states remain unchanged and equal to
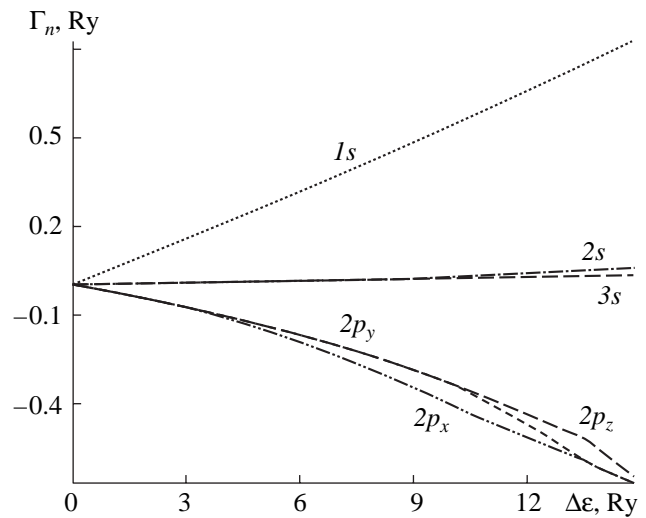
E_n, Ry

Fig. 3. Dependence of the energies of the one-electron levels of a beryllium atom on the excitation energy.

Γ_n, Ry

Fig. 4. Dependence of the width of the one-electron energy levels on the excitation energy of a beryllium atom.
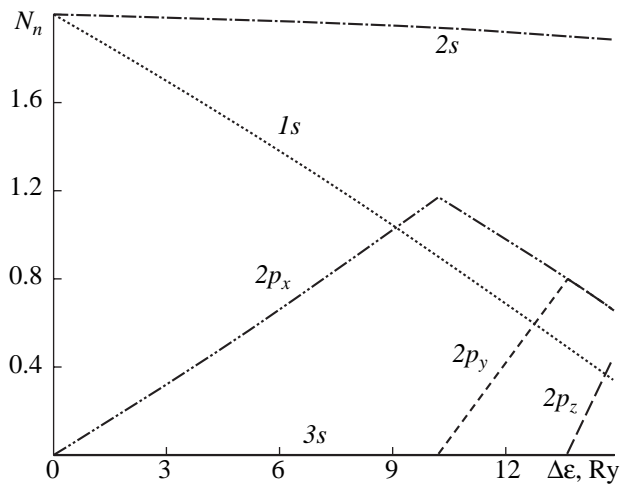
Fig. 5. Dependence of the electron occupancy of the one-electron states of a beryllium atom on the excitation energy.
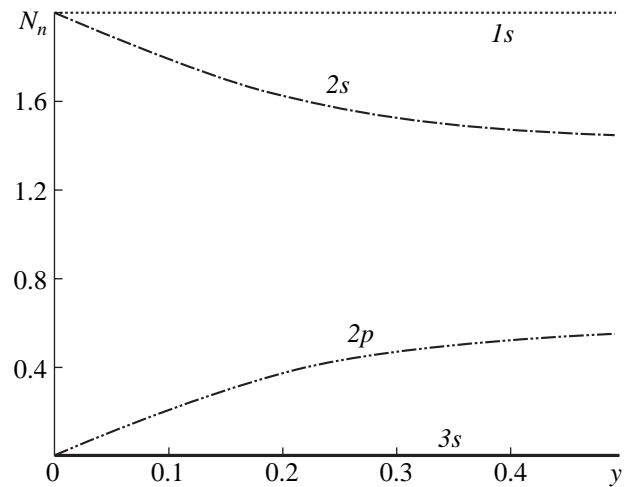

Fig. 6. Dependence of the electron occupancy of the one-electron states of a beryllium atom on the parameter y in the optical range of excitation energies.
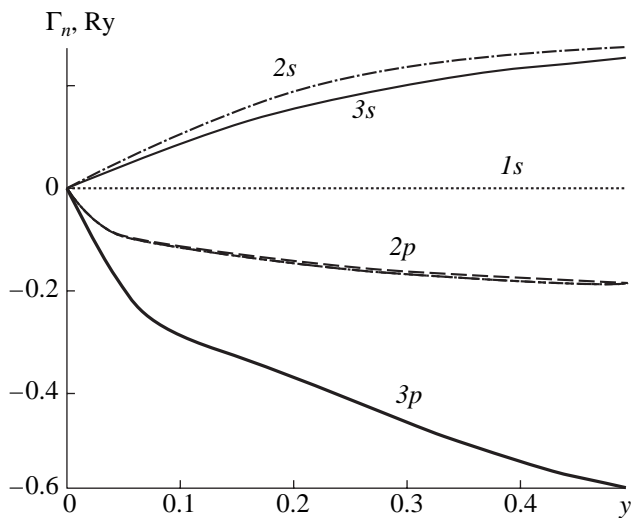

Fig. 7. Dependence of the width of the one-electron energy levels of a beryllium atom on the parameter y in the optical range of excitation energies.
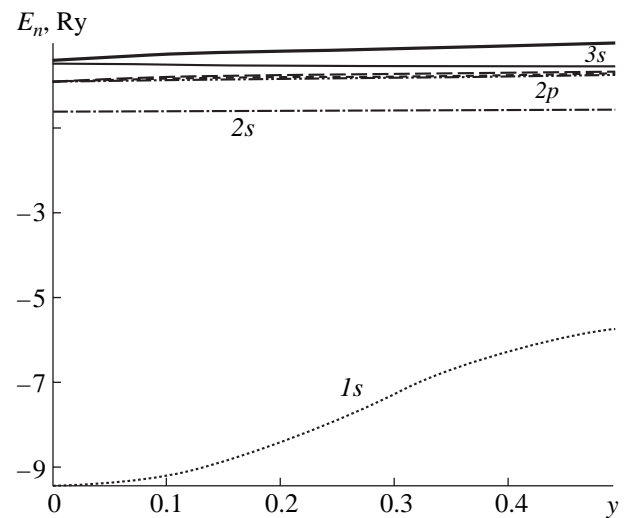

Fig. 8. Dependence of the energies of the one-electron levels of a beryllium atom on the parameter y in the optical range of excitation energies.

two (with allowance for the spin degeneracy). The dependence of the electron occupancies of all the states, N_n, on the parameter y is depicted in Fig. 6. The electron occupancies of the $2s$ and $2p$ states are seen to change to the greatest extent. The electron occupancies of the $3s$ states are close to zero because the $2s$–$3s$ transitions are forbidden by the selection rules and the probabilities of the $2p$–$3s$ transitions are low because the short-lived $2p$ states are populated by only a few electrons. The lifetimes of all these states can be estimated using the uncertainty relation and knowing the widths of the energy levels, Γ_n, presented Fig. 7, which illustrates the results of calculations carried out for the $1s$, $2s$, $2p$, $3s$, and $3p$ orbitals and for $|y| < 0.5$. The posi-

tions of these levels are displayed in Fig. 8. Note that, as the parameter y increases, the $1s$ state is seen to substantially rise upward along the energy scale; this effect is here regarded as the collapse of an atom—a phenomenon that was thoroughly discussed by Delone and Kraĭnov [11], who considered a hydrogen atom as an example.

Figure 9 depicts the real part $\mathrm{Re}\,\varepsilon$ of the total energy of a beryllium atom calculated as a function of the parameter y, which describes excitations in the optical range of energies. These and all other calculations of the excitations in the optical range were carried out for $x = 0$ because it is at this value of the parameter x that the imaginary part of the total energy of an atom is min-
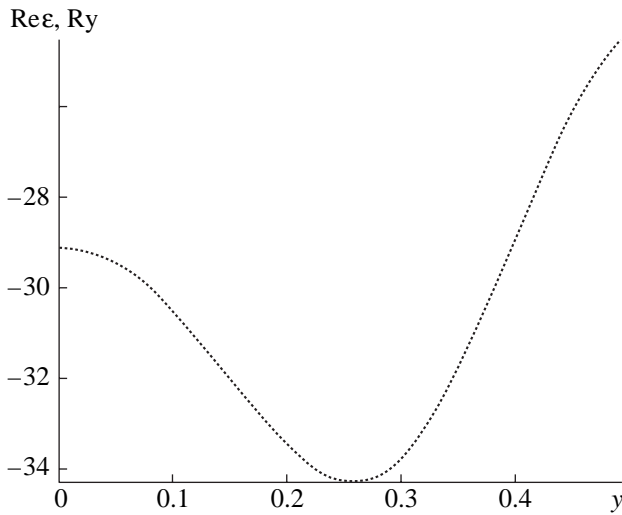
Reε, Ry

Fig. 9. Dependence of the real part of the total energy of a beryllium atom on the parameter y in the optical range of excitation energies.
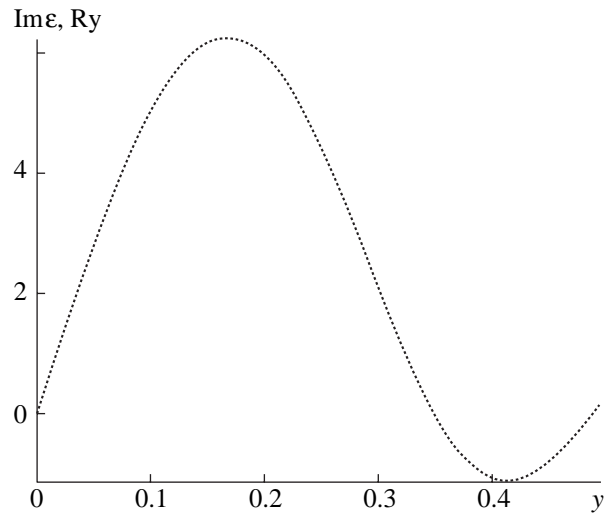
Imε, Ry

Fig. 10. Dependence of the imaginary part of the total energy of a beryllium atom on the parameter y in the optical range of excitation energies.

imal and because an increase in x leads to a corresponding increase in Reε at each fixed value of y. The dependence shown in Fig. 9 is essentially nonlinear, in contrast to an almost linear dependence in the case of excitations in the X-ray energy range (Fig. 1). For y values from 0 to 0.01, the real part Reε increases very gradually. An important point is that, for fairly large y values (from 0.02 to 0.26), the real part of the total energy of an atom decreases considerably and becomes lower than the energy of the ground state. The lifetimes of an atom in such states are very short because the imaginary part of the total energy, Imε, which is inversely proportional to the lifetime, is fairly large (see Fig. 10). The calculated results illustrated in Fig. 10 show that the imaginary part vanishes, Imε = 0, at certain y values, in particular, at $y = 0.35$ and 0.49. This indicates that there exist at least two long-lived states of a highly excited atom. One of these excited states, namely, that with $y = 0.35$, is stable because its total energy is lower than the energy of the ground state at $y = 0$. It is very unlikely, however, that, in the optical range, an atom can be excited to such a high state (with $y = 0.35$). With the strengths of the fields used in practice, it is only possible to change the parameter y within a few thousandths or, at least, a few hundredths.

Nevertheless, it is possible to make an excited state stable, e.g., by placing the atom in the field of another atom. In order to verify this hypothesis, the total energy of two beryllium atoms was calculated as a function of the distance between them for small values of the parameter y. The results of these calculations are illustrated in Fig. 11, from which we can see that the energy of the ground state of a system of two atoms (see Fig. 11, the curve with $y = 0$) at any distance d between them (in particular, at a distance of 2.5–9 au) is higher than the energy of the ground state of atoms isolated

from one another. This indicates that a Be_2 system in the ground state is unstable. At low excitation energies (up to 0.1 Ry), the total energy of a system of two beryllium atoms is seen to increase with distance between them. At higher excitation energies ($y \geq 0.009$), the total energy appears to have a pronounced minimum. The higher the excitation energy, the deeper the minimum and the shorter the distance between the atoms. The fact that the imaginary part Imε of the total energy of a system of two beryllium atoms decreases with distance between them (see Fig. 12) indicates that the system becomes stable. Let a slight but pronounced minimum occur within the above range of distances between the
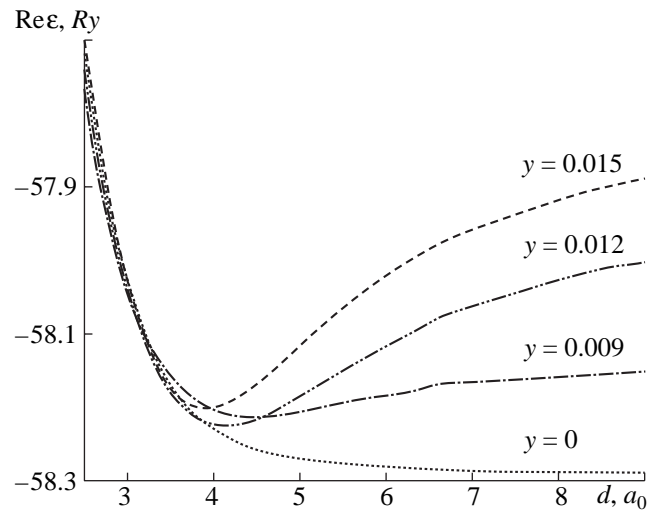
Reε, Ry

Fig. 11. Dependence of the real part of the total electron energy of two beryllium atoms on the distance d between them for four different values of the parameter y in the optical range of excitation energies. The distance d is expressed in units of the Bohr radius a_0.

Imε, Ry

y = 0.015

0.56

y = 0.012

0.46

y = 0.009
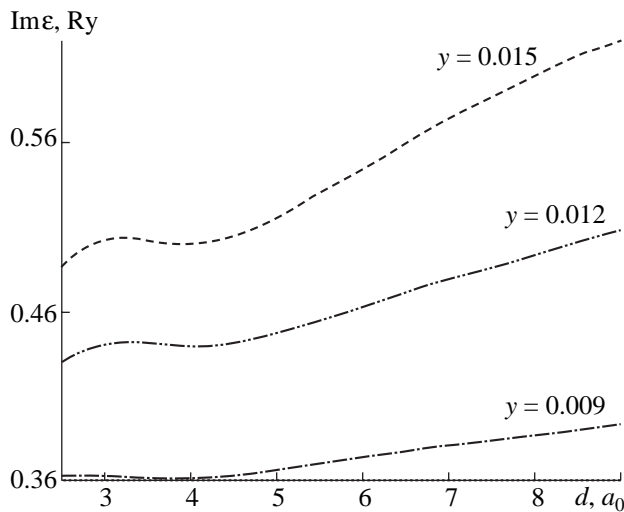
0.36

3   4   5   6   7   8 d, a_0

Fig. 12. Dependence of the imaginary part of the total electron energy of two beryllium atoms on the distance d between them for three different values of the parameter y in the optical range of excitation energies. The distance d is expressed in units of the Bohr radius.

atoms (i.e., within a range around 4 au). The derived dependence of the lifetime τ of excitations on the excitation energy $\Delta\varepsilon$ of a Be$_2$ system is essentially non-monotonic. For instance, the values $\Delta\varepsilon = 0.08$, 0.09, and 0.10 Ry and the corresponding values $\tau = 0.11$, 0.13, and 0.10 fs imply that there is a maximum lifetime of 0.13 fs at an excitation energy of 0.09 Ry. The phenomenon just described for beryllium can be treated as photocondensation with the CES lifetime on the order of 0.1 fs.

Hence, the results of the calculations show that a CES can be achieved by placing the beryllium atom in question in the field of another beryllium atom at a distance on the order of four Bohr radii from the latter. In this case, the Be$_2$ system is subject to short-lived excitations accompanied by intense electron transitions to the $2p$ symmetric state. The data on excitations in heavier Rb$_2$ dimers [14] and in cesium clusters consisting of up to a hundred atoms [4, 5, 9] provide evidence of the existence of long-lived excitations with electron transitions to the states with principal quantum numbers of 8 to 20. The results obtained above (in particular, those presented in Figs. 9 and 10) lead to the suggestion that, if the beryllium atom in question were placed in the field of two, three, or a larger number of beryllium atoms, then CESs could form in which the minima are deeper than those shown in Figs. 11 and 12 for a Be$_2$ system and, consequently, the excitations are more stable energetically and are longer lived.

5. CONCLUSIONS

In the present paper, the suggestion about the existence of CESs of beryllium has been checked. The spec-

tral parameters of the excited states have been calculated by the Hartree–Fock method with allowance for the width of the atomic energy levels.

It has been shown that, during the excitation of a beryllium atom in the X-ray energy range, the following processes occur:

(i) the splitting of te $2p$ states increases with excitation energy;

(ii) the probability for the excited state of an atom to decay decreases with excitation energy in the range above $\Delta\varepsilon = 6.7$ Ry (i.e., the excited state is observed to be stabilized); and

(iii) the $2s$ and $2p$ states are observed to mix at excitation energies $\Delta\varepsilon$ of 10 and 14 Ry.

In the optical range of excitation energies, a condensed excited state of beryllium with a lifetime on the order of 0.1 fs has been revealed.

REFERENCES

1. É. A. Manykin, M. I. Ozhovan, and P. P. Poluéktov, Dokl. Akad. Nauk SSSR **260**, 1096 (1981) [Sov. Phys. Dokl. **26**, 974 (1981)].
2. É. A. Manykin, M. I. Ozhovan, and P. P. Poluéktov, Zh. Éksp. Teor. Fiz. **84**, 442 (1983) [Sov. Phys. JETP **57**, 256 (1983)].
3. É. A. Manykin, M. I. Ozhovan, and P. P. Poluéktov, Khim. Fiz. **18** (7), 87 (1999).
4. L. Holmlid, Phys. Rev. A **63**, 013817 (2001).
5. G. É. Norman, Pis'ma Zh. Éksp. Teor. Fiz. **73**, 13 (2001) [JETP Lett. **73**, 10 (2001)].
6. V. I. Yarygin, V. N. Sidel'nikov, I. I. Kasikov, *et al.*, Pis'ma Zh. Éksp. Teor. Fiz. **77**, 330 (2003) [JETP Lett. **77**, 280 (2003)].
7. L. Holmlid and É. A. Manykin, Zh. Éksp. Teor. Fiz. **111**, 1601 (1997) [JETP **84**, 875 (1997)].
8. G. É. Norman, Khim. Fiz. **18** (7), 78 (1999).
9. R. Svensson and L. Holmlid, Phys. Rev. Lett. **83**, 1739 (1999).
10. A. Yanavichus and V. Shuchurov, Litov. Fiz. Sb. **8** (1–2), 47 (1968).
11. N. B. Delone and V. P. Kraǐnov, Usp. Fiz. Nauk **165**, 1295 (1995) [Phys. Usp. **38**, 1247 (1995)].
12. N. B. Delone and V. P. Kraǐnov, Usp. Fiz. Nauk **169**, 753 (1999) [Phys. Usp. **42**, 669 (1999)].
13. I. I. Bondar' and V. V. Suran, Pis'ma Zh. Éksp. Teor. Fiz. **71**, 3 (2000) [JETP Lett. **71**, 1 (2000)].
14. C. Boisseau, I. Simbotin, and R. Cóte, Phys. Rev. Lett. **88**, 133004 (2002).

Translated by G.V. Shepekina

PARTICLE ACCELERATION
IN PLASMA

Generation of Superthermal Electrons
in a Micropinch Discharge

A. N. Dolgov* and V. V. Vikhrev**

Moscow Engineering Physics Institute, Kashirskoe sh. 31, Moscow, 115409 Russia
**Institute of Nuclear Fusion, Russian Research Centre Kurchatov Institute,
pl. Akademika Kurchatova 1, Moscow, 123182 Russia
Received May 16, 2003; in final form, December 26, 2003

Abstract—Results are presented from experimental studies of the formation of the superthermal electron component in a micropinch discharge plasma. Radiative collapse in a Z-pinch is found to affect the energy of the accelerated electrons. That the radiative collapse has been reached may be inferred from the energy of the emitted hard X-ray photons. © 2005 Pleiades Publishing, Inc.

1. INTRODUCTION

It is known [1] that the collapse of a high-temperature plasma column caused by radiative energy losses leads to an increase in the $n\tau$ parameter. This allows one to suggest that the radiative collapse can be used to initiate a self-sustained fusion reaction in a Z-pinch. It is expected that, in this case, the deposited energy that is required for attaining positive energy balance can be substantially reduced.

Creating conditions under which the Z-pinch current is high enough to reach radiative collapse is a rather complicated technical problem. The radiative collapse of a Z-pinch is threshold in nature. For instance, radiative collapse in a hydrogen plasma can occur only if the current exceeds the so-called Pease–Braginskii critical current $I_{cr} \cong 1.4$ MA. In carrying out experiments on the radiative collapse of micropinch discharges, it is reasonable to use plasmas of high-Z elements because, in such plasmas, the collapse occurs at much lower currents.

Pinch discharges in high-Z plasmas are characterized by intense line emission. This emission can be partially trapped even before the onset of radiative collapse; therefore, the critical current corresponding to radiative collapse is a rather complicated function of the discharge parameters. Because of the partial trapping of radiation, a transition to the regime of radiative collapse is determined, in particular, by the number of particles per unit length of the pinch. It was found that, for Fe plasma, there is a definite linear density at which a micropinch most easily turns into the regime of radiative collapse.

In [2], the following model for the onset of radiative collapse in a micropinch was proposed: Since the micropinch plasma is produced due to the evaporation of the electrodes, the linear plasma density varies along the pinch; specifically, it is maximum near the electrodes and gradually decreases away from them. In a

certain cross section, the linear plasma density turns out to be best suited for the onset of radiative collapse. It is this cross section in which radiative collapse begins. Since, in other cross sections, conditions for the onset of radiation collapse are not satisfied, it occurs within a narrow region along the plasma column. In experiments, it looks like a bright X-ray spot. Thus, for a given plasma composition, there is a critical pinch current corresponding to the onset of radiative collapse. For a plasma produced in the explosion of iron electrodes, this current is ~50 kA. For subcritical discharge currents, radiative energy losses only slightly affect the discharge dynamics, whereas for supercritical currents, the pinch discharge can collapse down to a micron size.

Therefore, in order to make a comparison between theoretical results and experimental data complete and reliable, it is necessary to determine general scaling laws according to which the processes in a pinch plasma depend on the current, rather than to deal with a narrow parameter range of any specific experiment.

The aim of this study is to investigate the formation of the superthermal electron component in a micropinch plasma.

2. EXPERIMENTAL RESULTS

The experiments were performed in a low-inductance vacuum spark facility (Fig. 1). The working medium was the erosion products of the electrode material (iron). The discharge was supplied from a low-inductance high-voltage capacitor bank. The electrons emitted from the discharge were recorded with the help of a compact analyzer in which the electron beam was turned by 180° and then focused onto a photoemulsion particle detector [3]. Nearly one hundred shots were needed to provide the necessary exposure. The analyzer was calibrated with monoenergetic electron beams formed by an ÉG-100M electron chronograph. The dis-
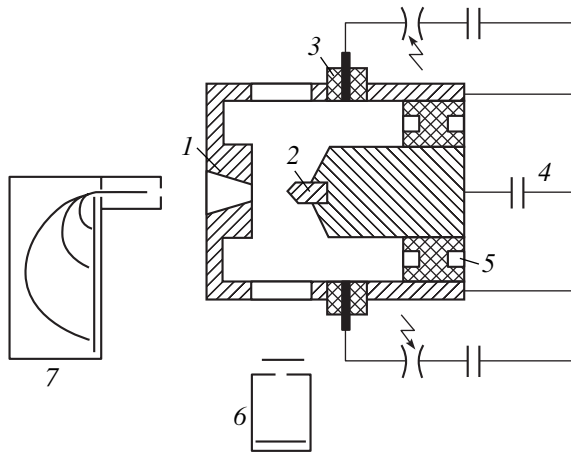
Fig. 1. Schematic of the experimental setup: (*1*) cathode, (*2*) anode, (*3*) discharge ignition system, (*4*) high-voltage capacitor bank, (*5*) insulator, (*6*) pinhole chamber, and (*7*) magnetic analyzer.
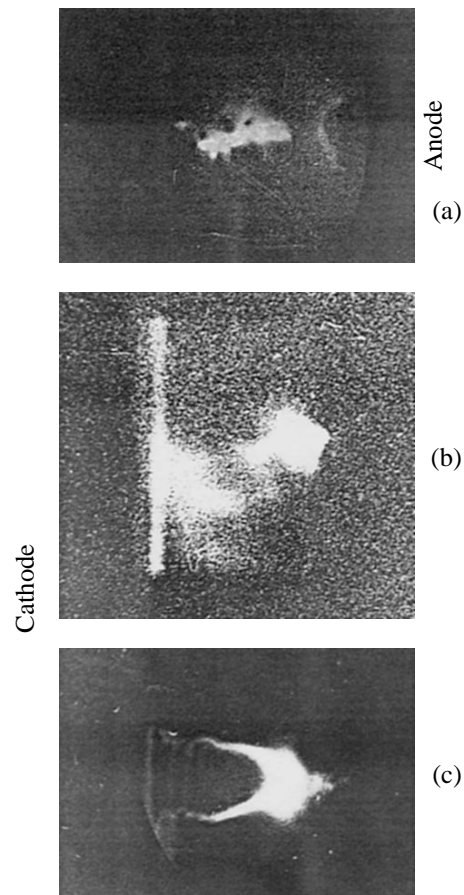

Fig. 2. X-ray pinhole images of discharges with different electrode configurations: (a, b) discharges with a conical anode and flat cathode and (c) a discharge with a conical anode and conical cathode.

charge was monitored using an X-ray pinhole camera, which recorded the structure of the emitting plasma in the spectral ranges of $\lambda < 18$ Å and $\lambda < 3$ Å. Pinhole images recorded in the spectral range of $\lambda < 3$ Å indicated the formation of a directed high-energy electron beam in each discharge.

The electrons with energies sufficient for the excitation of X-ray emission with $\lambda < 3$ Å propagated from the micropinch either to the anode or to the cathode (Fig. 2). The propagation direction was determined by the parameters of the discharge circuit.

The high-energy electrons moving toward the cathode were seemingly the hot component of the plasma expanding in the axial direction with a supersonic speed. Estimates of the Mach number by the shape of a standing shock wave that arises when a point obstacle is placed at the cathode surface give $M = 3$–4. At the anode surface, no supersonic plasma flow was observed. We failed to measure the electron energy spectrum in the regime in which the electron beam propagated toward the hollow anode. The energy spectrum of a cathode-directed electron beam was recorded using a cathode with an axial channel. Such asymmetry was probably related to different conditions of the electron beam transportation to the recording apparatus. The ratio h/d of the channel length to its diameter was ~10 for the anode and ~2 for the cathode.

The experimental results (see Fig. 3) show that the particle spectra change radically when passing from subcritical currents $I_{max} < I_{cr}$ (regimes with no radiative collapse) to supercritical currents $I_{max} > I_{cr}$ (regimes with a radiative collapse). At subcritical currents, both the shape and amplitude of the recorded energy spectrum are well reproducible. At $I_{max} > I_{cr}$, the number of the recorded particles increases greatly. In this case, the shape of the spectrum varies significantly in different

experiments and there is no definite dependence of the spectrum on I_{max} and the charging voltage U_0. Measurements of the emitted electrons with the help of a scintillation detector showed that, even at fixed values of I_{max} and U_0, the number of the emitted electrons varied within one order of magnitude and the particle spectrum also changed significantly from shot to shot [4].

When passing from subcritical to supercritical currents, the recorded electron spectrum shifted in a jump-like manner toward higher energies. Note that the degrees of plasma compression and heating in a micropinch only slightly affected the generation of high-energy electrons.

It was experimentally observed that the electron spectrum depends on the length of the electrode insulators. The longer the insulator, the larger the fraction of high-energy electrons (Fig. 4). The spectrum of electrons emitted from the micropinch plasma depends on the insulating properties of the interelectrode gap. This indicates that the generation of high-energy electrons is related to the presence of quasistatic electric fields [5].
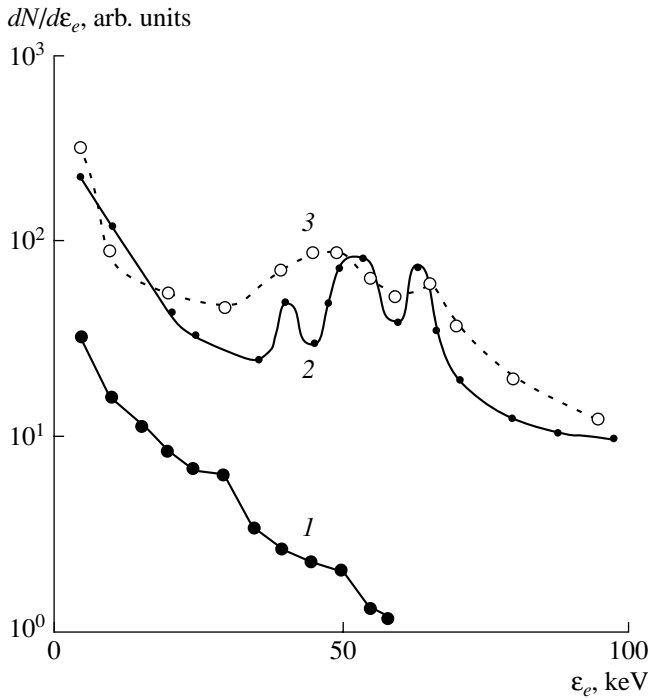
$dN/d\varepsilon_e$, arb. units

Fig. 3. Electron energy spectra $dN/d\varepsilon_e$ for different discharge currents: (*1*) $I_{max} < I_{cr}$ and (*2, 3*) $I_{max} > I_{cr}$.

$dN/d\varepsilon_e$, arb. units
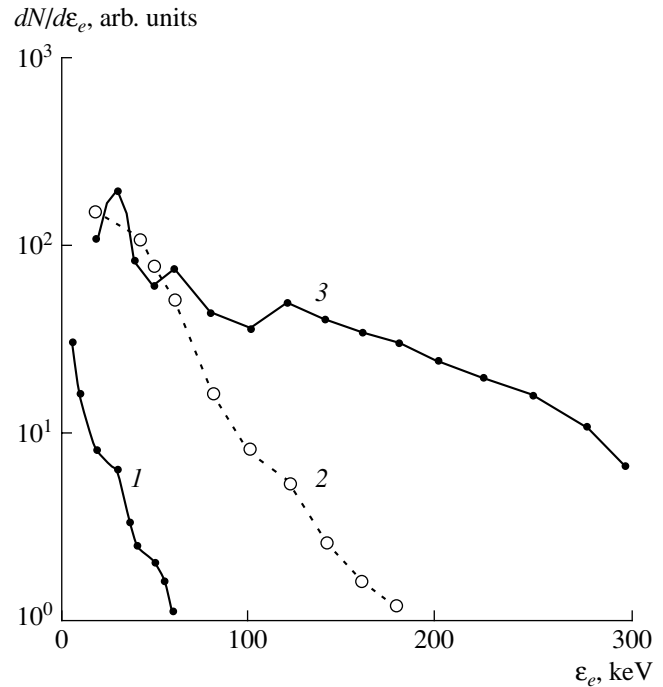

Fig. 4. Electron energy spectra $dN/d\varepsilon_e$ for different lengths L of the discharge insulator: (*1*) $L = 8$ cm ($I_{max} < I_{cr}$), (*2*) $L = 2$ cm ($I_{max} > I_{cr}$), and (*3*) $L = 8$ cm ($I_{max} > I_{cr}$).

These fields exist on time scales of $>10^{-8}$ s, which is much longer than the time of electron acceleration ($\sim 10^{-11}$–10^{-10} s) in the interelectrode gap.

Note that some factors can mask the actual dependence of the spectrum of electrons generated in a micropinch on I_{max} and U_0. Studying the structure of a fast Z-pinch in a high-Z medium showed that, at $I_{max} < I_{cr}$, the plasma column is axisymmetric. In the micropinch regime ($I_{max} > I_{cr}$), the plasma column is subject to firehose instability [6], which can substantially affect the propagation direction of the accelerated electrons. Moreover, the magnitude of the quasistatic electric field arising in a micropinch discharge depends on the properties of the insulator and the state of it surface and is probably affected by the peripheral plasma in the discharge gap.

To minimize the effect of the above factors, the spectra of the emitted electrons were recorded in one series of discharges (without reevacuating the discharge chamber) at a fixed charging voltage ($U_0 = 15$ kV) and two amplitudes of the discharge current ($I_{max} = 90$ and 150 kA). The surface of the electrode insulator was cleaned from the deposited material and polished. A set of dielectric shields protecting the insulator surface from plasma flows and discharge emission was set between the electrodes. It was found that, under these conditions, the spectrum in the energy range of 10–100 keV depended slightly of the discharge current and the number of the emitted electrons was nearly pro-

portional to I_{max} (Fig. 5). It should be noted, however, that the fast-electron tail was somewhat heavier at high currents. The measurements of the electron spectra for a larger number of I_{max} values at a fixed charging voltage U_0 was restricted by the finite lifetime of the electrodes and the limited range within which the discharge current amplitude I_{max} could be varied by varying the capacitance of the capacitor bank.

The relative hard X-ray (HXR) yield from the discharge plasma was measured for currents of $50 \leq I_{max} \leq 250$ kA (for the charging voltage varying in the range $5 \leq U_0 \leq 25$ kV). HXR emission in the photon energy range of $20 \leq h\nu \leq 300$ keV was recorded by a scintillation detector and a photomultiplier, the signal from which was integrated over time. The scintillation detector was oriented in the radial direction with respect to the discharge and monitored HXR emission from both the discharge plasma and the electrode surfaces. The lower boundary of the spectral sensitivity range of the detector was determined by the thickness of the copper filter, and the upper boundary was determined by the scintillator size. It was found that the HXR yield is proportional to the amplitude of the discharge current I_{max} (see Fig. 6). The results obtained showed that the high-energy tail of the electron spectrum contributed insignificantly to the pinch energy balance.
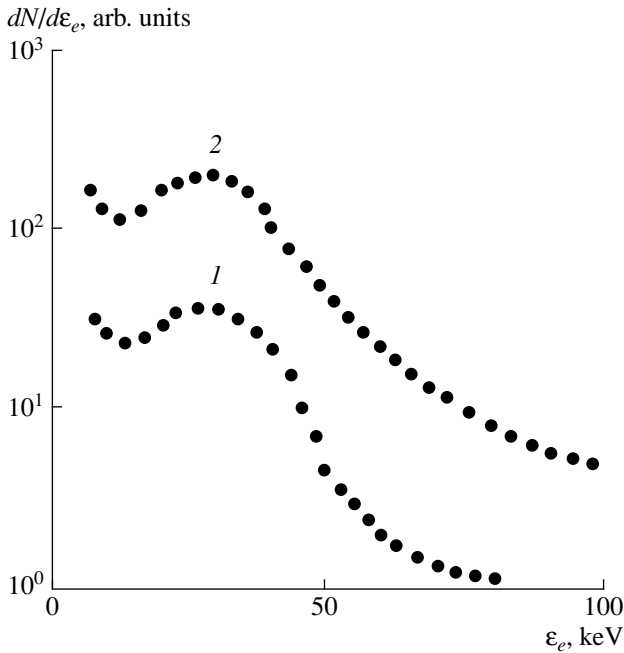
$dN/d\varepsilon_e$, arb. units

Fig. 5. Electron energy spectra recorded in one series of discharges with $I_{max} > I_{cr}$ for $I_{max} = $ (*1*) 90 and (*2*) 150 kA.

$E_{h\nu}$, arb. units

Fig. 6. HXR photon energy vs. discharge current.

3. GENERATION OF A HIGH VOLTAGE ALONG THE PINCH

In [7, 8], the acceleration of particles in a pinch was attributed to the abrupt termination of the conduction current and the onset of a displacement current in the final stage of pinching. Note, however, that estimates and simulations of the plasma dynamics in the final stage of a Z-pinch show that the displacement current is low compared to the conduction current. Moreover, it can be shown that taking the displacement current into account leads to a decrease in the longitudinal electric field in the pinch plasma; hence, this mechanism cannot be responsible for the generation of high-energy particles in a pinch.

Indeed, according to the model proposed in [7, 8], the onset of a displacement current is equivalent to including a capacitor in parallel to the plasma resistance in the waist region. The equivalent capacitance is on the order of $C \approx \varepsilon_0 r$, where r is the waist radius. After the first compressions, the waist radius is $r_1 \approx 2 \times 10^{-4}$ m and after the second compression, it is $r_2 \approx 5 \times 10^{-6}$ m [2]. The reactance of the capacitor is

$$Z_{C1,2} \approx \frac{\Delta t_{1,2}}{\varepsilon_0 r},\qquad(1)$$

where $\Delta t_1 \approx 10^{-8}$ s and $\Delta t_2 \approx 10^{-10}$ s are the durations of the first and second compressions, respectively [8]. Thus, we have $Z_{C1} \approx 10^7\ \Omega$ and $Z_{C2} \approx 10^6\ \Omega$ in the first and second compressions, respectively. It will be shown below that $Z_C \gg R$, where R is the plasma resistance in
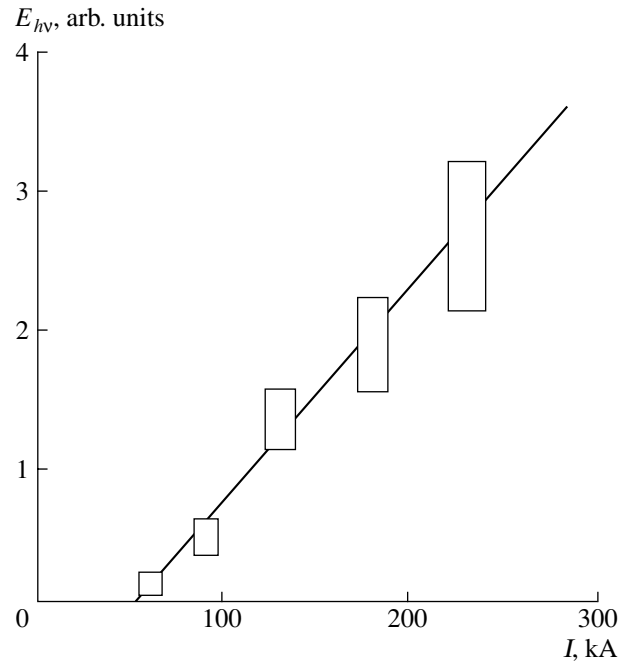
the waist region. Including the equivalent capacitor in the discharge circuit decreases the total impedance of the circuit segment under consideration and, hence, the voltage drop across this segment. This effect, however, turns out to be negligibly small:

$$U \cong \frac{IR}{\sqrt{1 + (R/Z_C)^2}}.\qquad(2)$$

4. EXPERIMENTAL DATA ON THE Z-PINCH RESISTANCE

It was established experimentally that, in linear discharges and plasma focus facilities, one of the reasons for an increase in the voltage drop across the plasma column up to values exceeding the initial discharge voltage is an increase in the plasma column impedance. At the instants when the radial motion of the plasma column boundary stops for a moment, the inductive component of the voltage is absent and the voltage drop across the pinch is entirely determined by its ohmic resistance [9, 10]; as a result, the current decreases. The magnitude of the ohmic resistance can be experimentally estimated by a decrease in the pinch current at these instants.

Let us make such estimates for a micropinch discharge. The inductance of the low-inductance vacuum

spark facility is $L_p \approx 10^{-8}$ H, and the inductance of the discharge plasma in different stages of pinching is

$$L_i = \frac{\mu_0}{4\pi} h_i \ln\frac{r}{r_i}, \quad i = 0, 1, 2. \qquad (3)$$

Here, $r = 1.5$ cm is the radius of the external current conductor of the discharge unit; $h_0 = 1$ cm is the length of the discharge gap; $r_0 \approx 1$ mm is the plasma column radius; and $h_1 \approx r_1 \approx 0.1$ mm and $h_2 \approx r_2 \approx 5 \times 10^{-3}$ mm are the characteristic micropinch sizes after the first and second compressions, respectively.

The measured change in the discharge current in the course of micropinch formation was $\Delta I \approx 10^4$ kA at a current amplitude of $I_{max} \approx 10^5$ kA. Therefore, the pinch resistance at the instants of the first and second compressions was $R_1 \approx \dfrac{(L_1 + L_0)\Delta I}{I_{max}\Delta t_1} \approx 10^{-2}\ \Omega$ and $R_2 \approx \dfrac{(L_2 + L_0)\Delta I}{I_{max}\Delta t_2} \approx 1\text{--}10\ \Omega$, respectively.

The measured ohmic resistance of the plasma column in plasma focus facilities was found to be 0.2–0.5 Ω [11–13]. At currents of 0.5–1 MA, this leads to overvoltages of 100–500 kV across the pinch.

5. PINCH RESISTANCE CALCULATED BY A SIMPLE MODEL

The plasma resistance in the waist region can be determined using a simple model of the final stage of Z-pinch [14, 15]. According to this model, the plasma in the pinch waist keeps collapsing while the power P_{in} input in the waist is lower than the total loss power, which is the sum of the radiative loss power P_{rad} and the loss power P_{esc} related to the escape of plasma from the waist (i.e., while $P_{in} < P_{rad} + P_{esc}$). At $P_{in} > P_{rad} + P_{esc}$, the pinch plasma expands in the radial direction. At the instant of maximum plasma compression (i.e., when the waist radius is minimum), we have

$$P_{in} = P_{rad} + P_{esc}. \qquad (4)$$

The dissipation power of magnetic energy in plasma is determined by the voltage drop U across the waist and the current I: $P_{in} = UI$. Thus, the maximum resistance of the pinch waist is determined by the total power of thermal losses from the waist:

$$R = U/I = UI/I^2 = P_{in}/I^2 = (P_{rad} + P_{esc})/I^2. \qquad (5)$$

The reason for the existence of the maximum waist resistance is as follows [10]: When the waist resistance is lower than that determined by Eq. (5), the total loss power is higher than power input in the waist and the pinch plasma collapses under the action of the magnetic field pressure. As a result, the radius of the conducting plasma channel decreases and, accordingly, the resis-

tance of the channel increases. The resistance increases until the ohmic heating power in the waist becomes equal to the total loss power. At the instant of maximum plasma compression, the waist resistance reaches its maximum.

If, for some reason, the resistance of the pinch channel becomes higher than that determined by Eq. (5), then the total loss power will be insufficient to balance ohmic heating in the waist and the pinch radius will increase. The increase in the cross-sectional area of the pinch is accompanied by a decrease in the waist resistance and, accordingly, in the voltage drop across the pinch.

The loss power related to the escape of plasma from the waist region is determined by the velocity V_s with which the plasma flows out through the waist ends, the waist length h, and the plasma enthalpy W: $P_{esc} = 2WV_s/h$. The plasma enthalpy within the pinch region of length h is $W = (5/2)kNTh$, where N is the number of particles (ions and electrons) per unit length of the pinch, T is the plasma temperature, and k is the Boltzmann constant. The velocity with which the plasma flows out of the waist in the axial direction is close to the ion acoustic velocity $V_s = \sqrt{\dfrac{5(z + 1)kT}{3m_i}}$, where z is the average ion charge number and m_i is the ion mass. Hence, the loss power related to the escape of plasma is equal to

$$P_{esc} = 5kNT\sqrt{\frac{5(z + 1)kT}{3m_i}}. \qquad (6)$$

The waist resistance can easily be determined in the case of low radiative losses ($P_{rad} \ll P_{esc}$). At the instant of maximal plasma compression, the Bennett condition for the radial plasma equilibrium, $NkT = \dfrac{\mu_0 I^2}{8\pi}$ (where μ_0 is the permeability of free space), holds with good accuracy. Therefore, the waist resistance at the instant of maximum compression can be written as

$$R = \frac{U}{I} = \frac{5\mu_0 V_s}{8\pi} = \frac{5\mu_0}{8\pi}\sqrt{\frac{5(z + 1)kT}{3m_i}}. \qquad (7)$$

Thus, when radiative losses are low, the waist resistance at the instant of maximum compression is determined only by the plasma temperature T in the waist. For $T = 1$ keV, the waist resistance is 0.1 Ω and, for a temperature of $T = 10$ keV (which is usually reached in plasma focus experiments at the instant of maximum plasma compression), it is 0.3 Ω.

In the case of radiative collapse ($P_{rad} > P_{esc}$) [15], the waist resistance at the instant of maximum compression is

$$R = P_{rad}/I^2. \tag{8}$$

This resistance is higher than that given by formula (7) for the case where energy losses related to the plasma escape prevail. Therefore, the overvoltage across the pinch and the energy of the accelerated electrons in pinch discharges dominated by radiative energy losses are much higher than those in discharges in which these losses play a minor role.

At the instant when radiative collapse terminates, radiation is usually strongly trapped in the plasma and its intensity outside the plasma is equal to the intensity of blackbody radiation. Thus, in the case of strong radiative collapse, the maximum pinch resistance is determined by the formula

$$R = \frac{2\pi r h \sigma T^4}{I^2},$$

where r is the minimum radius of the waist, h is the waist length, and σ is the Stefan–Boltzmann constant.

6. DISCUSSION OF RESULTS

The above model allows one to estimate the ohmic resistance of the micropinch plasma. The required parameters can be taken from [2, 16]. For the resistance of a quasistatic plasma column with $I \approx 10^5$ A, $z \approx 3$, and $T \approx 20$ eV, and a lifetime of $\tau \approx 5 \times 10^{-7}$ s, we obtain $R_0 = 0.02$ Ω.

In the stage between the first and second compressions, we have $z \approx 6$ and $T \approx 50$ eV. In this stage, which lasts for a time of $\tau \approx 5 \times 10^{-8}$ s, the plasma emits an energy of about 100 J. This is approximately ten times higher than the energy lost due to the escape of plasma from the waist. In accordance with formula (8), the pinch resistance in this stage is equal to ~0.2 Ω.

During the second (maximum) compression, which is caused by radiative energy losses, the energy emitted from the plasma (mainly in the soft X-ray range) over a time of $\tau \approx 5 \times 10^{-10}$ s is $E \approx 10$ J. The discharge current in this stage is ~10^5 A. Therefore, in accordance with formula (8), the pinch resistance reaches ~10 Ω during the second compression. The overvoltage across the pinch at the instant of maximum compression is $U = 10^6$ V, which agrees with experimental results.

The above considerations are also confirmed by a substantial change in the electron spectra (see Fig. 3) when passing from subcritical ($I_{max} < I_{cr}$) to supercritical currents ($I_{max} > I_{cr}$). In the former case, there is no radiative collapse and the pinch resistance is determined only by the escape of plasma from the waist (see formula (7)). Therefore, the energy of the accelerated electrons turns out to be much lower than that in the case of supercritical currents, when the Z-pinch undergoes radiative collapse and the maximum resistance is determined by radiative energy losses (see formula (8)). The observed dependence of the number of the accelerated electrons on the discharge gap length (Fig. 4) can merely be explained by an increase in the number of waists formed in the interelectrode space.

An analysis of X-ray images of the discharge plasma shows that high-energy electrons are generated only in the micropinch region, where the plasma resistance is high, rather than throughout the entire plasma column. This allows us to explain the dependences shown in Figs. 5 and 6. The electron component of the pinch plasma is accelerated most efficiently during the formation and decay of a micropinch. The electrons acquire energy in the course of the current drift with an average velocity of $V_d = 10^5$ m/s; therefore, the acceleration time is on the order of the duration of the second compression. In this case, the beam current is proportional to the discharge current. The characteristic acceleration time and the accelerating voltage depend slightly on the discharge current because of the influence of the peripheral plasma and the insulation of the discharge unit. The beam energy turns out to be proportional to the discharge current, whereas the efficiency with which it is converted into radiation depends slightly on the current.

The above considerations and estimates provide an explanation for the substantial change in the recorded electron spectra from a micropinch discharge when passing from subcritical to supercritical currents, as well as for the dependences of the electron energy spectrum and the HXR yield on the micropinch current.

REFERENCES

1. V. V. Vikhrev and G. A. Rozanova, Fiz. Plazmy **19**, 79 (1993) [Plasma Phys. Rep. **19**, 40 (1993)].

2. V. V. Vikhrev, V. V. Ivanov, and K. N. Koshelev, Fiz. Plazmy **8**, 1211 (1982) [Sov. J. Plasma Phys. **8**, 688 (1982)].

3. M. A. Gulin, A. N. Dolgov, O. V. Nikolaev, and A. S. Savelov, Fiz. Plazmy **16**, 1015 (1990) [Sov. J. Plasma Phys. **16**, 590 (1990)].

4. E. O. Gorbunov, M. A. Gulin, A. N. Dolgov, *et al.*, Prib. Tekh. Eksp., No. 5, 56 (1990).

5. M. A. Gulin, A. N. Dolgov, N. N. Kirichenko, and A. S. Savelov, Zh. Éksp. Teor. Fiz. **108**, 1309 (1995) [JETP **81**, 719 (1995)].

6. J. Fukai and E. J. Clouthiaux, Phys. Rev. Lett. **34**, 863 (1975).

7. B. A. Trubnikov, in *Plasma Physics and the Problem of Controlled Thermonuclear Reactions*, Ed. by M. A. Leontovich (Izd. Akad. Nauk SSSR, Moscow, 1958; Pergamon Press, New York, 1960), Vol. 4.

8. B. A. Trubnikov, Fiz. Plazmy **12**, 468 (1986) [Sov. J. Plasma Phys. **12**, 271 (1986)].

9. V. V. Vikhrev, Fiz. Plazmy **12**, 454 (1986) [Sov. J. Plasma Phys. **12**, 262 (1986)].

10. V. V. Vikhrev, V. V. Ivanov, and G. A. Rozanova, Nucl. Fusion **33**, 311 (1993).

11. A. Bernard, P. Cloth, H. Conrads, *et al.*, Nucl. Instrum Methods **145**, 191 (1977).

12. L. Bertalot, R. Deutsch, H. Herold, *et al.*, Plasma Phys. Controlled Nucl. Fusion Res. **2**, 177 (1980).

13. A. Gentilini, C. Maisonnier, and J. P. Rager, Comm. Plasma Phys. Controlled Fusion **2**, 41 (1978).

14. V. V. Vikhrev, Fiz. Plazmy **3**, 981 (1977) [Sov. J. Plasma Phys. **3**, 539 (1977)].

15. V. V. Vikhrev and S. I. Braginskii, in *Reviews of Plasma Physics*, Ed. by M. A. Leontovich (Atomizdat, Moscow, 1980; Consultants Bureau, New York, 1986), Vol. 10.

16. A. N. Dolgov, Candidale's Dissertation (Moscow Engineering Physics Inst., Moscow, 1988).

Translated by N.N. Ustinovskiǐ

BRIEF
COMMUNICATIONS

Experimental Modeling of a Novel Magnetic Confinement System: Galathea with a Myxine in the Shape of a Convex Polyhedron

V. A. Gordienko, A. E. Dubinov, S. S. Zhuravlev, M. M. Ivanov, and P. B. Repin

Sarov Physicothechnical Institute, Sarov, Nizhni Novgorod oblast, 607188 Russia
Received February 9, 2004

Abstract—A new type of magnetic confinement system—a Galathea with a myxine in the shape of a convex polyhedron—is proposed. The system was modeled experimentally by passing an RF current through the myxine. On the one hand, the myxine acts as an inductor whose electric field ionizes the gas and, on the other, it acts as an RF magnetic confinement system. A steady-state plasma produced and confined in this system is almost spherical in shape. The electron density and specific (per unit volume) glow intensity of the plasma produced are found to be higher than those in conventional helical inductors. © 2005 Pleiades Publishing, Inc.

To provide compact plasma confinement, A.I. Morozov proposed magnetic confinement systems with current conductors embedded in the plasma. These confinement systems were called "Galatheas," and the current conductors were named "myxines." In [1], various simple configurations of this type ("dipole," "string-bag," "belt," "tornado," etc.) were described.

In [2], a confinement system based on current circuits arranged on the frame of a convex polyhedron was proposed and theoretically analyzed. A truncated icosahedron with twenty hexagonal and twelve pentagonal faces (similar in shape to the C_{60} fullerene molecule) was used as a basic polyhedron.

In our opinion, the use of a truncated icosahedron as the frame of the confinement system has the following disadvantages: Each vertex of this polyhedron connects three edges; hence, it is impossible to traverse its edges around a single contour passing along each edge only once. In other words, the graph of the polyhedron is not unicursal. As a result, the feed system should have several parallel-connected circuits of different length and different inductance (in [2], there were five circuits of different length); this requires additional means for balancing the feed system, especially, in the pulsed operating mode. Moreover, each face has edges along which no current flows; this deteriorates plasma confinement. On the other hand, an advantage of the confinement system proposed in [2] is that all the faces can be traversed along their working edges in the same direction.

In this paper, we consider new types of current circuits laid out along the edges of a convex polyhedron. Among the known convex polyhedrons, we chose those whose edges can be traversed around a single contour passing along each edge only once and returning to the starting point (the so-called unicursal line or Eulerian graph). According to theorem IV.1 in [3], the number of edges converging in each vertex (i.e., the valence $d(v)$ of each vertex) of such a polyhedron must be even.

Among the variety of polyhedrons described in [4], there are only five that satisfy this condition. Of these polygons, only the octahedron (a polyhedron whose faces are eight identical equilateral triangles) is classed among Platonic bodies, whereas the other four are classed among Archimedean bodies, which have faces of different types—cuboctahedron, icosidodecahedron, rhombicuboctahedron, and rhombicosidodecahedron.

It turns out that the contour along the edges of these polyhedrons can always be laid out so that, for each face, the current flows in the same direction along all the edges of this face, which is important in focusing the RF field inside the polyhedron and confining the plasma produced. This follows from theorem III.68 in [3], which states that a graph is bicolored if and only if it is Eulerian. In fact, two colors can be interpreted as two opposite directions in which the edges of the face can be traversed.

Taking into account the above considerations, we manufactured myxine inductors shaped like the five polygons mentioned above. For comparison, we also manufactured inductors in the shape of a flat Archimedean spiral, cylindrical and conical helices, and a "tornado."

The inductor was placed inside a gas-discharge chamber filled with air at a pressure of 0.1–1 torr and was connected through a coaxial cable to a 200-W IKV-4 continuous-wave medical-purpose generator operating at a frequency of 13.56 MHz.

Figures 1a–1c show photographs of discharges produced by spiral inductors. A distinctive feature of these discharges is that the shape of the plasma produced is similar to the shape of the inductor itself: for a flat Archimedean spiral, the plasma has the shape of two
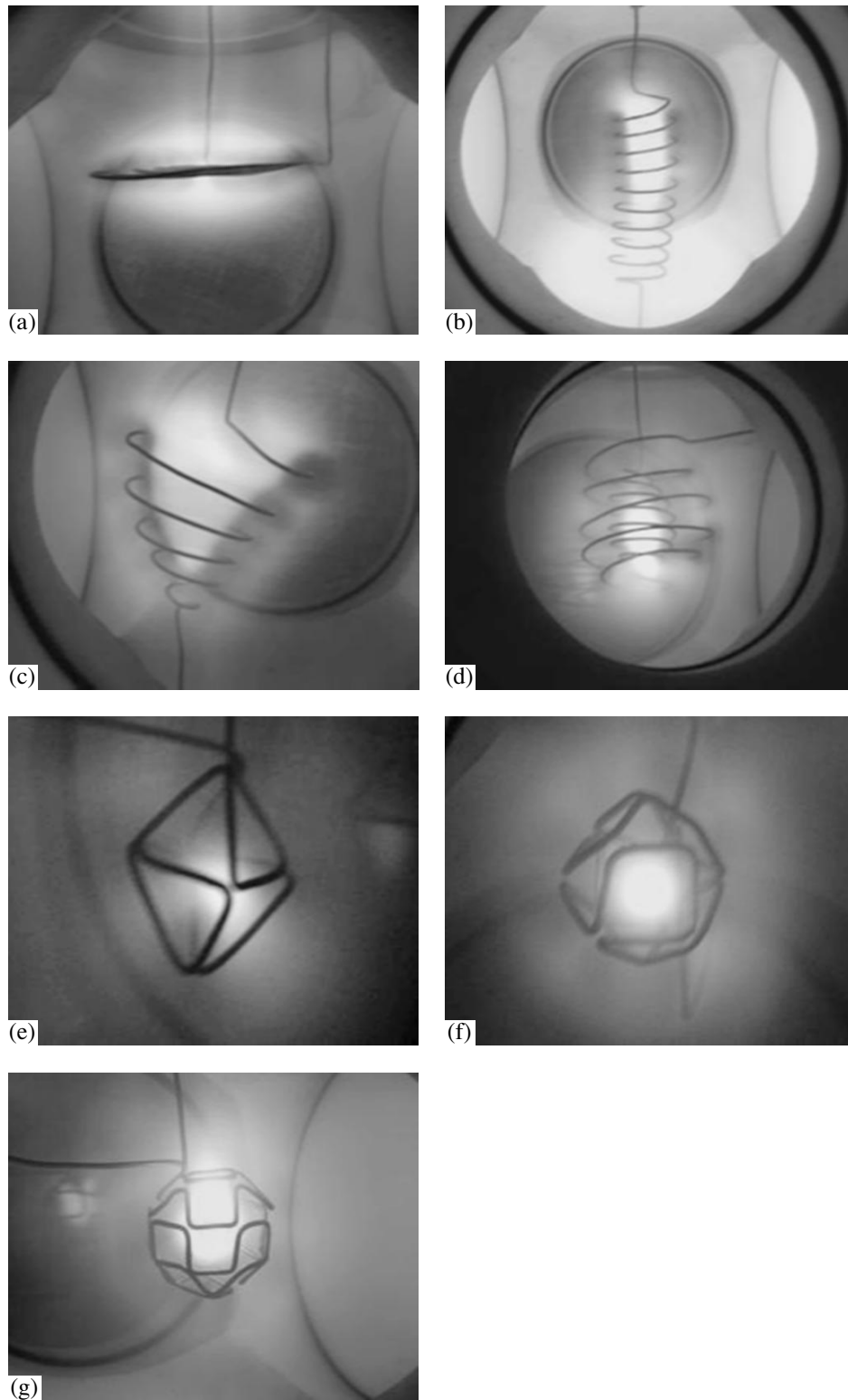
Fig. 1. Photographs of plasma configurations for different types of inductors: (a) Archimedean spiral, (b) cylindrical helix, (c) conical helix, (d) tornado, (e) octahedron, (f) cuboctahedron, and (g) rhombicuboctahedron.

layers arranged almost parallel to the inductor plane; for a cylindrical helix, the plasma is nearly cylindrical in shape; and for a conical helix, the plasma is nearly conical in shape. In all these configurations, the electrode sheaths responsible for plasma localization are clearly seen.
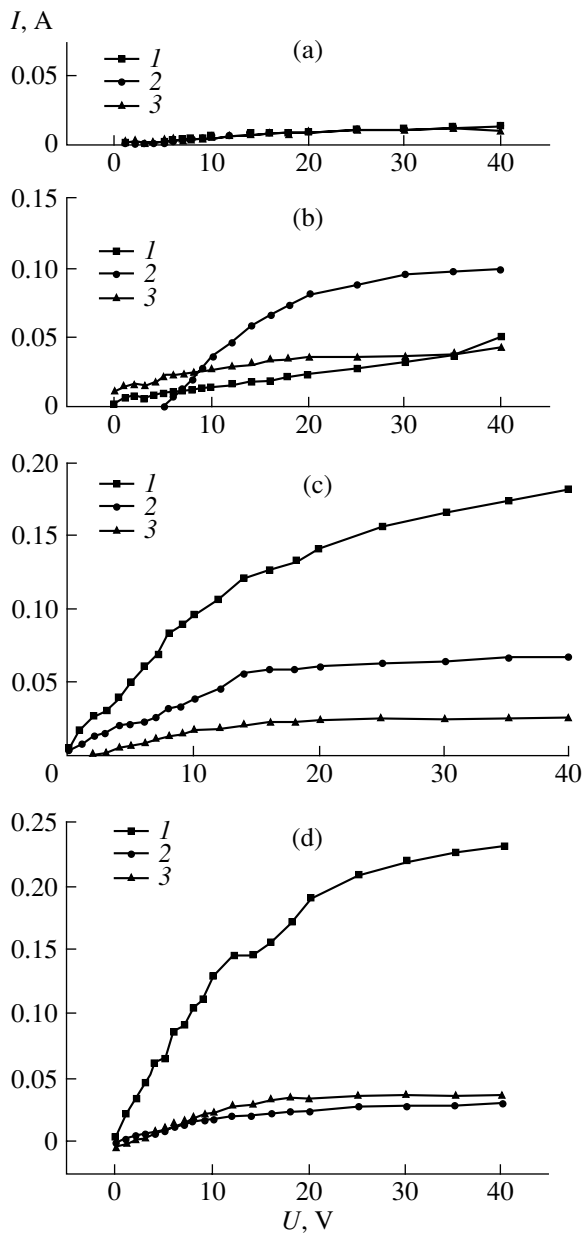
Fig. 2. Probe *I–V* characteristics for different types of inductors: (a) conical helix, (b) tornado, (c) octahedron, and (d) rhombicuboctahedron. Curves *1* show the characteristics measured at the center of the inductor and curves *2* and *3* show the characteristics measured outside the inductor at distances of 1 cm and 3 cm from its surface, respectively.

The total length of the inductor is several tens of centimeters, whereas at a frequency of 13.56 MHz, the electromagnetic wavelength is longer than 22 m; hence, all the inductor points are approximately in phase. If such an inductor is placed entirely into the working chamber, then it acts not only as an RF inductor, but also as an electrode, around which electrode sheaths arise. Thus, in addition to the properties of an RF inductive discharge, the discharge acquires the properties of an RF electrode discharge.

In a tornado inductor, the plasma is almost spherical in shape and is located at the center of the inner spherical helix (Fig. 1d). However, near the poles of the inductor, the spherical shape of the plasma is disturbed.

The dimensions of the myxine inductors in the shape of polyhedrons were chosen such that the electrode sheaths formed a closed quasi-spherical shell without holes. For larger polyhedrons, the shell formed by the electrode sheaths would have windows, through which the plasma would escape from the system, as is the case with a tornado inductor. Recall that, in the electrode sheaths, there is a considerable electric field, which elastically reflects electrons.

Thus, on the one hand, the myxine acts as an inductor whose electric field ionizes the gas and, on the other hand, it acts as an RF magnetic confinement system.

Figures 1e–1g show examples of compact plasma configurations inside inductors in the shape of an octahedron, a cuboctahedron, and a rhombicuboctahedron. The plasma configurations are seen to be compact and nearly spherical. The specific glow intensity of the plasma produced is rather high.

The plasma parameters were measured by a double probe consisting of two copper cylinders 0.3 mm in diameter and 7 mm in length, the distance between the cylinders being 3 mm. The measurements were performed at three points for each inductor: at the inductor center and outside the inductor at distances of 1 cm and 3 cm from its surface.

As a result, we obtained probe current –voltage (*I–V*) characteristics (three characteristics for each inductor). Some of these are shown in Fig. 2. In can be seen in Fig. 2a that, for conventional helical inductors (specifically, for a conical helix), the *I–V* characteristics measured at different points are similar to one another, whereas for a tornado inductor (Fig. 2b) and, in particular, for inductors in the shape of a convex polyhedron, the *I–V* characteristics measured at the center of the system lie far above those measured at the periphery of the discharge (Figs. 2c, 2d). This indicates that, in polyhedrons, the plasma is localized much stronger than in helical inductors.

It should be noted that the plasma produced does not reach thermodynamic equilibrium; i.e., the electron distribution function differs from Maxwellian and the average electron energy is much higher than the ion and neutral energies. The reasons for this are as follows:

(i) Under our experimental conditions, the working pressure in the chamber is low and collisional energy exchange between particles is too feeble.

(ii) Electrons reflecting from the electrode sheaths repeatedly cross the plasma volume (the so-called hollow cathode effect [5]).

(iii) The boundaries of the electrode sheathes oscillate at the frequency of the RF generator, thus causing the well-known stochastic Fermi–Ulam heating of elec-

trons, whose distribution function becomes enriched with fast electrons [6].

By processing the *I–V* characteristics, we determined the effective electron temperature, which turned out to be from 6 to 9 eV for different inductors and different points. It was found that the temperature was usually higher inside the inductor.

For myxine inductors in the shape of a polyhedron, the central electron density was nearly one order of magnitude higher than that for helical inductors (3.2×10^{10} cm^{-3} for a rhombicuboctahedron against 1.4×10^{9} cm^{-3} for a conical helix). At the same time, the density decreased toward the periphery more rapidly for polyhedrons than for helices.

Thus, we have developed a new type of myxine inductors in the shape of convex polyhedrons. With these inductors, steady-state compact quasi-spherical plasma configurations have been produced. The electron density and specific (per unit volume) glow intensity of the plasma produced are found to be higher than those in conventional helical inductors.

REFERENCES

1. A. I. Morozov and V. V. Savel'ev, Usp. Fiz. Nauk **168**, 1153 (1998) [Phys. Usp. **41**, 1049 (1998)].

2. V. P. Budaev, Vopr. At. Nauki Tekh., Ser. Termoyad. Sintez, No. 1, 36 (1999).

3. H. Fleischner, *Eulerian Graphs and Related Topics* (North-Holland, Amsterdam, 1971; Mir, Moscow, 2002).

4. M. Wenninger, *Polyhedron Models* (Cambridge Univ. Press, London, 1971; Mir, Moscow, 1974).

5. G. Stockhausen and M. Kock, J. Phys. D **34**, 1683 (2001).

6. C. G. Goedde, A. J. Lichtenberg, and M. A. Lieberman, J. Appl. Phys. **64**, 4375 (1988).

Translated by N.F. Larionova

BRIEF COMMUNICATIONS

Spectropolarimetry of Hydrogen-Containing Plasma by the H_α and H_β Lines

Yu. B. Pankrashkin and M. B. Shapochkin

Moscow Power Engineering Institute, Krasnokazarmennaya ul. 14, Moscow, 111250 Russia
Received March 24, 2004

Abstract—The degree of linear polarization of the H_α and H_β atomic lines in a hydrogen-containing plasma is measured. The dependence of the degree of linear polarization on the spatial anisotropy of a discharge is investigated. © *2005 Pleiades Publishing, Inc.*

1. INTRODUCTION

The anisotropy of the electron distribution function can be determined by measuring the degree of polarization of the spectral lines of an ionized gas excited by electron impact [1, 2]. An ionized hydrogen-containing gas is a frequent object in astrophysical and technical issues. It was shown in [3] that the degree of linear polarization of the H_α line of atomic hydrogen excited by an electron beam is about 28% near the excitation threshold. Hence, it may be expected that the degree of linear polarization of the H_α line in an ionized hydrogen-containing gas will also be high. The theoretical aspects of quantitative collisional spectropolarimetry of atomic hydrogen radiation (first of all, in studying astrophysical objects) were analyzed in [4–6].

A significant difference between the diagnostics of ionized hydrogen-containing gases by the H_α and H_β lines and the spectropolarimetry diagnostics based on measurements of the degree of linear polarization of the singlet transition [2] is that the former diagnostics operate, in fact, with seven closely spaced transitions. For diagnostic purposes, it is of interest to develop a technique in which the fine structure of the H_α and H_β lines is unresolved, i.e., each of these lines is recorded as a single whole. The present study was motivated by the lack of experimental data on the degree of linear polarization of the H_α and H_β lines in an ionized gas.

2. EXPERIMENTAL TECHNIQUE

If the transitions corresponding to the of H_α (656.5 nm) and H_β (486.3 nm) lines are unresolved, i.e., when each of these lines is recorded as a single whole, then it is reasonable to introduce the concept of the effective degree of linear polarization for these lines. Let us consider as an example a spectral line including three transitions with known polarizations. In this case, the

effective degree of linear polarization can be introduced as

$$
\begin{aligned}
P &= \frac{(I_\parallel^1 + I_\parallel^2 + I_\parallel^3) - (I_\perp^1 + I_\perp^2 + I_\perp^3)}{(I_0^1 + I_0^2 + I_0^3)} \\
&= \frac{P_1 I_0^1 + P_2 I_0^2 + P_3 I_0^3}{(I_0^1 + I_0^2 + I_0^3)},
\end{aligned} \tag{1}
$$

where

$$
P_i = \frac{I_\parallel^i - I_\perp^i}{I_0^i} \tag{2}
$$

is the degree of linear polarization of the *i*th spectral transition [7], $I_\parallel^i$ is the intensity of the spectral transition component polarized along the discharge axis, $I_\perp^i$ is the intensity of the spectral transition component polarized across the discharge axis, and I_0^i is the total intensity of the spectral transition.

We assume that the dependence of the effective degree of linear polarization (1) of the spectral line (as well as of the degree of linear polarization of each spectral transition (2)) on the energy of incident electrons can be determined both experimentally [3] and theoretically [7]. In this case, in order to diagnose hydrogen-containing ionized gases by the degree of linear polarization of the H_α and H_β lines, we can employ the previously developed theory [1, 2]. Of course, in addition to the effective degree of linear polarization of the spectral line, we should also introduce the effective cross section for the line excitation [8].

The determination of the effective degree of linear polarization (1) of the H_α and H_β lines is then reduced to the measurements of the line intensities in the direction perpendicular to the anisotropy axis of the discharge. In the case of electron-impact excitation, the H_α and H_β lines emitted in this direction should be linearly

polarized [1]. With allowance for the spectral transmission of the optical system of the experimental setup, the effective degree of linear polarization can be written as [9]

$$P = \frac{I_\parallel - I_\perp k_0}{I_\parallel + I_\perp k_0}, \qquad (3)$$

where

$$k_0 = \frac{k_\parallel}{k_\perp} \qquad (4)$$

is the relative spectral transmission coefficient [9] and $k_\parallel$ and $k_\perp$ are the spectral transmission coefficients of radiation polarized along and across the discharge axis, respectively. In measuring the $k_\parallel$ and $k_\perp$ coefficients, a TRU spectral incandescent lamp was used as a source of unpolarized emission.

3. EXPERIMENTAL SETUP

A schematic of the experimental setup is shown in Fig. 1. As a source of the H_α and H_β lines, we used a TVS-15 hydrogen lamp (Fig. 2), whose spectrum is dominated by the atomic hydrogen lines. The anisotropy axis of the plasma in this lamp coincides with the lamp axis. There are two regions in the wide (point *1*) and narrow (point *2*) parts of the lamp that are characterized by different degrees of spatial anisotropy. The lamp diameters in these parts are 13 mm and 2 mm, respectively. A glow discharge in the lamp operates at a voltage of 1700 V, current of 18 mA, and gas pressure of about 1 torr.

The intensities of the line emission components polarized along and across the discharge axis, $I_\parallel$ and $I_\perp$, were measured at points *1* and *2* (see Fig. 2). When measuring the relative spectral transmission coefficient, the TVS-15 lamp was replaced with a TRU lamp. The hydrogen emission was projected by a quartz lens with a 750-mm focal length onto the entrance slit of an MDR-23 monochromator equipped with a 1200-groove/mm diffraction grating. The vertical size of the 0.02-mm-wide entrance slit of the monochromator was limited by a 1-mm pinhole placed in front of the slit. The dimensions of the region from which the emission was collected (the region over which the degree of linear polarization was averaged) were 1 mm along the optical axis and 0.1 mm along the discharge anisotropy axis. The angle within which the emission was collected (and, accordingly, the angle within which the degree of linear polarization was averaged) in the planes perpendicular and parallel to the discharge axis did not exceed 3°. The line emission components polarized along and across the discharge axis were separated by a polaroid film placed in front of the entrance slit of the monochromator.

The emission was recorded by a low-noise FÉU-106 photomultiplier operating in the linear photon counting mode. The intrinsic noise of the photomultiplier was
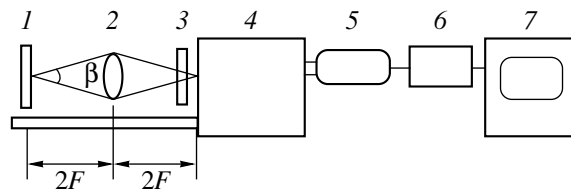

Fig. 1. Schematic of the experimental setup: (*1*) TVS-15 lamp, (*2*) lens (*F* = 750 mm), (*3*) polarizer, (*4*) MDR-23 monochromator, (*5*) FÉU-106 photomultiplier, (*6*) pulse forming unit, and (*7*) PC.
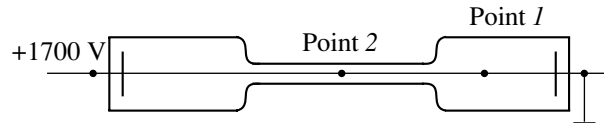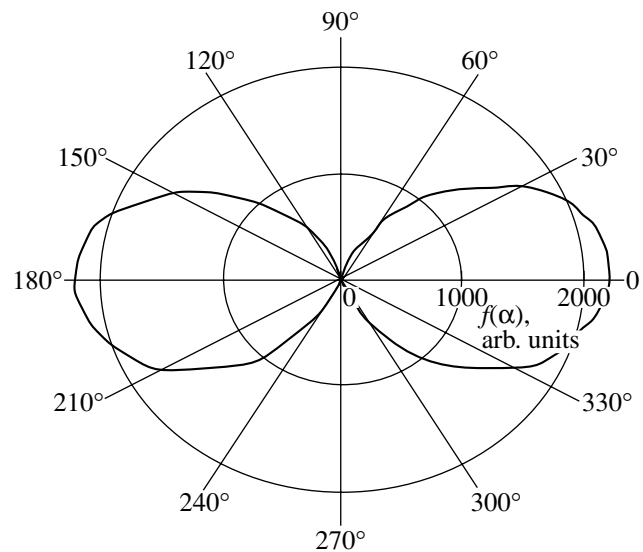

Fig. 2. TVS-15 hydrogen lamp.

Fig. 3. Diagram illustrating the dependence of the quantity $f = I_\parallel^*(\alpha) - I_\perp$ for the H_α line at point 2 on the angle α between the axes of the polarizer and discharge.

100 count/s. After amplifying and discriminating, the photomultiplier pulses were supplied to a BSchTs2-90 counter (in the VECTOR frame) connected to an IBM PC. In calculating the degree of polarization, the noise level was taken into account using a specially developed software.

4. MEASUREMENT RESULTS

The measured degrees of linear polarization of the H_α and H_β lines are shown in the table. Taking into

Table

	$H_\alpha P$, %	$H_\beta P$, %
Point *1*	6.5	7.0
Point *2*	12	12

account that the current was constant along the discharge tube, the current density at point *2* was ten times higher than at point *1*. Hence, the spatial anisotropy of the electron distribution function at point *2* should be higher than at point *1*. This is confirmed by the results of our experiments, because the higher the anisotropy, the larger the degree of linear polarization [1, 2].

At point *2*, the measured degrees of linear polarization of the H_α and H_β lines were 12%, whereas at point *1*, they were 6.5 and 7%, respectively. It is quite expectable since these lines correspond to transitions between levels of the same configuration. The intensity of the H_α line was 2.5 times higher than the intensity of the H_β line.

In the case of linear polarization, the emission should obey the Malus law. To verify this, we measured the emission intensity while rotating the polarizer with a step of 15°. Figure 3 shows the measured dependence $f(\alpha) = I_\parallel^*(\alpha) - I_\perp$ for the H_α line at point *2*. Here, $I_\parallel^*(\alpha)$ is the emission intensity measured behind the polarizer and α is the angle between the axes of the polarizer and discharge. The direction in which $f(\alpha)$ was maximum coincided with the anisotropy axis of the discharge. Similar dependences were obtained for point *1*, as well as for the H_β line at points *1* and *2*.

The degree of linear polarization was measured with an accuracy of no less than 10%.

5. CONCLUSIONS

The measurement results confirm the presence of discharge anisotropy, which is responsible for the linear polarization of the emission lines. The higher the spatial anisotropy of a discharge, the larger the degree of linear polarization. After modifying the existing theory by including the concept of the effective degree of polarization for the H_α and H_β lines, it should be possible to calculate the anisotropy of the electron distribution function [2].

REFERENCES

1. S. A. Kazantsev and J. C. Henoux, *Polarization Spectroscopy of Ionized Gases* (KAP, London, 1995), p. 214.
2. M. B. Shapochkin, Fiz. Plazmy **27**, 734 (2001) [Plasma Phys. Rep. **27**, 692 (2001)].
3. W. R. Ott, W. E. Kauppila, and W. L. Fite, Phys. Rev. Lett. **19**, 1361 (1967).
4. S. A. Kazantsev and A. G. Petrashen', Opt. Spektrosk. **84**, 375 (1998).
5. S. A. Kazantsev and A. G. Petrashen', Opt. Spektrosk. **84**, 551 (1998).
6. S. A. Kazantsev and A. G. Petrashen', Opt. Spektrosk. **85**, 183 (1998).
7. U. Fano and J. H. Macek, Rev. Mod. Phys. **45**, 553 (1973).
8. B. K. Vaĭnshteĭn, I. I. Sobel'man, and E. A. Yukov, *Excitation and Broadening of Spectral Lines* (Nauka, Moscow, 1979), p. 319.
9. M. B. Shapochkin and E. V. Petrov, Phys. Scr. **52**, 52 (1995).

Translated by N.N. Ustinovskiĭ